SEARCHES FOR NEW PHYSICS AT COLLIDERS

A DISSERTATION
SUBMITTED TO THE DEPARTMENT OF PHYSICS
AND THE COMMITTEE ON GRADUATE STUDIES
OF STANFORD UNIVERSITY
IN PARTIAL FULFILLMENT OF THE REQUIREMENTS
FOR THE DEGREE OF
DOCTOR OF PHILOSOPHY

My Phuong Le
August 2011

This dissertation is online at: http://purl.stanford.edu/cc849sr1742

I certify that I have read this dissertation and that, in my opinion, it is fully adequate in scope and quality as a dissertation for the degree of Doctor of Philosophy.

JoAnne L. Hewett, Primary Adviser

I certify that I have read this dissertation and that, in my opinion, it is fully adequate in scope and quality as a dissertation for the degree of Doctor of Philosophy.

Michael Peskin

I certify that I have read this dissertation and that, in my opinion, it is fully adequate in scope and quality as a dissertation for the degree of Doctor of Philosophy.

Jay Wacker

Approved for the Stanford University Committee on Graduate Studies.

Patricia J. Gumport, Vice Provost Graduate Education

This signature page was generated electronically upon submission of this dissertation in electronic format. An original signed hard copy of the signature page is on file in University Archives.

Acknowledgments

I certainly would never have been able to complete my graduate work and this thesis alone, and I would like to thank the many people who provided a lot of help along the way.

First and foremost, I would like to thank my adviser, JoAnne Hewett, for being a wonderful teacher, mentor, and collaborator, and especially for her understanding of my situation. I would also like to express my gratitude to Tom Rizzo for many insightful and enjoyable conversations. I am extremely thankful to my collaborators JoAnne Hewett, Tom Rizzo, Michael Peskin, Jay Wacker, Johan Alwall, Mariangela Lisanti, Randy Cotta, Jamie Gainer, John Conley, and Ahmed Ismail, who have made my time at Stanford and SLAC both pleasant and productive. I also want to thank the many other faculty members, postdocs, and graduate students from whom I've learned so much. In particular, I've been very lucky to benefit from Michael Peskin's teaching and guidance.

I am most indebted to my husband, Jim, who has encouraged me to explore this new path and has been there for me every step of the way through this long journey. I would like to thank my family as well as my mother-in-law for taking good care of Hoai Viet so I would have time to focus on my studies. And to Hoai Viet, you have kept me very happy and well-occupied, and I know you always will. I look forward to when you say some day, "Mommy can do it, so can I"!!!

Chapters 2, 3, 6 and 7 of this thesis have been published previously as:

- J. A. Conley, J. L. Hewett, M. P. Le, Phys. Rev. **D72**, 115014 (2005). [hep-ph/0507198].
- J. A. Conley, J. S. Gainer, J. L. Hewett, M. P. Le, T. G. Rizzo, Eur. Phys. J. **C71**, 1697 (2011). [arXiv:1009.2539 [hep-ph]].
- J. Alwall, M. P. Le, M. Lisanti, J. G. Wacker, Phys. Lett. **B666**, 34-37 (2008). [arXiv:0803.0019 [hep-ph]].
- J. Alwall, M. P. Le, M. Lisanti, J. G. Wacker, Phys. Rev. **D79**, 015005 (2009). [arXiv:0809.3264 [hep-ph]].

Chapters 4 and 5 of this thesis have appeared as preprints:

- J. A. Conley, J. S. Gainer, J. L. Hewett, M. P. Le, T. G. Rizzo, [arXiv:1103.1697 [hep-ph]].
- R. C. Cotta, J. L. Hewett, A. Ismail, M. P. Le, T. G. Rizzo, [arXiv:1105.0039 [hep-ph]].

Contents

List of Tables

List of Figures

Chapter 1

Introduction

The Standard Model (SM) has proven to be a suprisingly successful theory. Despite its rather simple $SU(3)_C \otimes SU(2)_L \otimes U(1)_Y$ gauge structure, it accurately describes many experimental data spanning a large energy range. The (minimal) SM proposes the Higgs mechanism with an elementary scalar field as a way to give mass to all of the other particles in the SM when it spontanously breaks the $SU(2)_L \otimes U(1)_Y$ symmetry down to the $U(1)_{EM}$. However, this Higgs particle still remains experimentally elusive at this time. Thus, we are not certain what the *true* mechanism of spontanous symmetry breaking (SSB) is. In addition, there are many reasons to believe that the SM is not the end of the story. These reasons include the hierarchy problem, *i.e.* the extreme fine-tuning necessary to cancel the quantum correction to the Higgs mass needed to keep it at the electroweak scale, and the lack of a possible candidate to account for the collisionless dark matter (DM) that makes up over 80% of known matter in the universe.

Both of these issues suggest that new physics will be in the TeV energy range, perfectly suited to be discovered in the newest generation of experiments at the Large Hadron Collider (LHC) or the International Linear Collider (ILC). For the fine-tuning associated with the hierarchy problem to be successfully resolved, new physics must enter to stabilize quantum correction to the Higgs mass at or not too far above the electroweak scale. In addition, the well-known "WIMP miracle" shows that if an

electromagnetically neutral particle is weakly interacting, the simple thermal freeze-out mechanism predicts the right thermal relic density of the DM, provided we assume that its mass and couplings are at the weak scale [1].

Therefore, there are plenty of reasons to be excited about the many possibilities that will be explored in many experiments in this era, ranging from studying SSB to producing and studying the particle physics properties of DM at the LHC. There are many possible new physics scenarios which could give very different experimental signatures. One needs to be aware of these possible signatures to be certain that when new physics shows up in the data, we are prepared to detect it. Then naturally, we would like to identify the underlying physics model, and be ready to further study its possibly large parameter space. In this thesis, we will look at some possible extensions to the SM, their signatures at colliders, and possible search strategies to explore the new physics in a model-independent way.

The little Higgs (LH) model [2, 3, 4], which we look at in Chapter 2, features the Higgs as a pseudo Nambu-Goldstone boson of approximately global symmetry. In the SM, at one loop, the Higgs mass recieves quantum correction from the top quark loop, the gauge boson loop, and the Higgs boson loop. LH theories introduce additional particles of the same spin which couple to the Higgs in a specific way to cancel each of these contributions. Then the Higgs mass only recieves quantum correction at two loops, helping to lessen the degree of fine-tuning.

This chapter is based on work done in collaboration with John Conley and JoAnne Hewett. We study the most economical example of a little Higgs model, known as the "Littlest Higgs" [2]. Specifically we focus on its extended neutral gauge sector and its indirect effect in high energy e^+e^- collisions. We find that the search reach in $e^+e^- \to f\bar{f}$ at a $\sqrt{s} = 500$ GeV ILC covers essentially the entire interesting parameter region of the model, and we show that this channel provides an accurate determination of the fundamental model parameters. Furthermore, we show that the couplings of extra gauge bosons to the light Higgs can be observed from the process $e^+e^- \to Zh$ for a significant region of the parameter space. This allows for confirmation of the structure of the cancellation of the Higgs mass quadratic divergence and would verify the little Higgs mechanism.

In chapters 3, 4, & 5 we turn our attention to the most well-studied Beyond-the-Standard-Model scenario, supersymmetry (SUSY). Supersymmetry could help provide answers to many of the unanswered questions, including the abovementioned hierarchy problem and identity of dark matter. A Supersymmetry transformation turns a bosonic state into a fermionic state, and vice versa. The simplest supersymmetric extension of the SM is called the Minimal Supersymmetric Standard Model (MSSM.) In this model, for every particle in the SM, there is a supersymmetric partner with the same mass and SM quantum number with spin different by 1/2 unit. The Higgs mass is protected from quadratic divergences. This can be seen in two ways: *(i)* The Higgs' fermionic partner, the higgsino, has its mass protected by chiral symmetry. By supersymmetry, the Higgs mass is also protected. *(ii)* When one computes the quantum corrections just as in the SM, in addition to the top loop, there is also a (scalar) stop loop which exactly cancels the top loop's contribution if they have similar masses; similar cancellation also occurrs for vector and scalar loop contributions to the Higgs mass. That is the beauty of supersymmetry. In addition, to ameliorate the proton decay problem, it is useful to impose R-parity. This makes the lighest supersymmetric particle (LSP) stable, since it carries an odd R-parity number. This particle provides a good candidate for DM.

SUSY is a simple, clean, minimalist theory, which doesn't require additional parameters beyond the SM. However, if SUSY exists, it needs to be broken, since no supersymmetric partner particles have been observed. The most general SUSY-breaking MSSM contains 105 new parameters. Since a general study of a parameter space of this size is impossible, specific SUSY breaking scenarios have typically been considered in order to reduce the number of parameters. The list of these includes mSUGRA [5], GMSB [6], AMSB [7], Mirage mediation [8] and gaugino mediated supersymmetry breaking [9]. These scenarios, however, are restrictive and predict specific phenomenologies for colliders and cosmology that do not represent the full range of possible SUSY signatures.

In the attempt to study the MSSM more broadly without making any simplifying assumptions about its SUSY-breaking mechanism at high scale, Berger et al [10] chose a minimal set of phenomenologically-motivated assumptions that results in a

model with 19 independent, real, weak-scale, SUSY Lagrangian parameters, called the phenomenological MSSM or pMSSM. They scanned over this 19-dimensional parameter space, subjecting the models in the scan to a number of existing theoretical and experimental constraints. This left them with $\sim$ 70,000 models satistfying all the constraints.

In the work of chapter 3 and 4, in collaboration with John Conley, James Gainer, JoAnne Hewett and Thomas Rizzo, we subject these $\sim$ 70k models to the existing inclusive missing transverse energy (MET) searches by ATLAS [11] to study their sensitivity to this broad class of Supersymmetric models. In chapter 3, we study the ATLAS supersymmetry searches proposed for the 14 TeV pp collider. We find that even though these searches were optimized mostly for mSUGRA signals, they are relatively robust in observing the more general pMSSM models. For the case of models in which squarks and gluinos have mass below 1 TeV, essentially all of these models ($> 99\%$) were observable in at least one of these searches, with 1 fb^{-1} of integrated luminosity allowing for an uncertainty of 50% in the SM background. This coverage was seen to improve significantly when these systematic errors were reduced to 20%. We found that 0-lepton searches are the most powerful searches, while searches with 1-2 leptons do not have coverage as good as has been shown for mSUGRA, mostly due to the fact that only a very small fraction of these models are lepton-rich. We then study possible reasons why a model could not be observed. These difficult models mostly include those with long-lived charginos which lead to small $E_T^{\rm miss}$and models with squeezed spectra which lead to soft jets that fail the jet cuts.

In chapter 4, we study similar searches that have been carried out by ATLAS at the 7 TeV LHC [12]. We found that systematic uncertainty again plays an important role in determining the coverage of the searches. This is especially true for searches with a large SM background, such as n-jet 0 lepton searches. We study the implication of a null result from the 7 TeV LHC. We find that the degree of fine-tuning in the pMSSM depends on the prior in which we scan our 19-dimensional space, but overall it is not as large as in mSUGRA. We find that a null result at the 7 TeV with $10 fb^{-1}$ and 20% systematic errors would imply a need for a higher energy e^+e^- machine than

the 500GeV ILC to study Supersymmetry.

Continuing on along the line of Supersymmetry, in chapter 5 we explore the possibility of adding one more generation to the MSSM (4GMSSM). This chapter is based on the work done in collaboration with Randel Cotta, JoAnne Hewett, Ahmed Ismail and Thomas Rizzo. In particular, we study the Higgs sector and find some surprising results. In most of the 3GMSSM parameter space, the lightest CP-even higgs is ∼115-125 GeV, while all other bosons are much heavier and the value of $tan(\beta)$ is relatively unconstrained. In contrast, the CP-odd A boson in the 4GMSSM can be very light due to the contribution of the heavy 4th generation fermion loops while all other Higgs particles (including the CP-even h) are quite heavy. The parameter $tan(\beta)$ is strongly constrained to be between 0.5 and 2 due to perturbativity requirements on Yukawa couplings. We study the electroweak constraints as well as collider signatures on the possibility of a light A of mass ∼115 GeV. As for an LHC discovery, we find that this light A can be seen in the standard Higgs search channel $h \to \gamma\gamma$ with cross-section more than an order of magnitude greater than that of the SM Higgs.

In the last two chapters, based on work done in collaboration with Johan Alwall, Mariangela Lisanti and Jay Wacker, we study possible search strategies to explore the new physics in a model-independent way. As we mentioned earlier, collider searches are typically optimized to discover some favored, very restrictive models, which could potentially miss the *true* signal entirely. In chapter 6, we attempt to show how one could be largely agnostic about the underlying model in exploring the complete kinematically-allowed parameter space of pair-produced color octet particles (let's call them *gluinos*), that each directly decay into two jets plus a neutral stable particle that would escape the detectors and appear as missing transverse energy E_T^{miss} (let's call it a *bino*). The kinematics of this process can be completely described by two parameters $m_{\tilde{g}}$ and $m_{\tilde{B}}$, and in particular their splitting determines the softness or hardness of jets from the decay products. We model our analysis after the D0 experiment's searches for n-jets plus E_T^{miss} at the Tevatron [13]. In order to cover the whole parameter space, one would need separate searches for different regions. In particular, when the two masses are degenerate, a monojet search is necessary

to look for hard initial state radiation recoiling against the gluinos. The existing D0 experiment's searches use fixed final cuts on E_T^{miss} and H_T (the scalar sum of all visible transverse energy), and we show that optimizing this cut for every ($m_{\tilde{g}}$,$m_{\tilde{B}}$) point, and combining all searches, can extend the coverage significantly. Note that, although we call these two particles *gluino* and *bino*, which are specific to SUSY, our result can be easily reinterpreted for any model with the same decay topology.

In chapter 7, we carry this model-independent approach further in jets plus missing energy searches, by proposing that one should bin the measured data (or simulated SM background) differentially as $\frac{d^2\sigma}{dE_T^{\text{miss}}dH_T}$ for each search, and use them to set limits on any model of interest. We demonstrate this technique by carrying out a search similar to that studied in chapter 6, with one added decay step for the *gluino*, mainly $\tilde{g} \rightarrow q_1 q_2 \tilde{W} \rightarrow q_1 q_2 q_3 q_4 \tilde{B}$. We study different kinematic regions and set bounds in this 3-dimensional parameter space ($m_{\tilde{g}}$,$m_{\tilde{B}}$,$m_{\tilde{W}}$).

Bibliography

[1] G. Jungman, M. Kamionkowski, K. Griest, Phys. Rept. **267**, 195-373 (1996). [hep-ph/9506380].

[2] N. Arkani-Hamed, A. G. Cohen, E. Katz, A. E. Nelson, JHEP **0207**, 034 (2002). [hep-ph/0206021].

[3] N. Arkani-Hamed, A. G. Cohen, H. Georgi, Phys. Lett. **B513**, 232-240 (2001). [hep-ph/0105239].

[4] W. Skiba, J. Terning, Phys. Rev. **D68**, 075001 (2003). [hep-ph/0305302].

[5] A. H. Chamseddine, R. L. Arnowitt, P. Nath, Phys. Rev. Lett. **49**, 970 (1982). A. H. Chamseddine, R. L. Arnowitt, P. Nath, Phys. Rev. Lett. **49**, 970 (1982).

[6] G. F. Giudice, R. Rattazzi, Phys. Rept. **322**, 419-499 (1999). [hep-ph/9801271]. M. Dine, A. E. Nelson, Y. Nir, Y. Shirman, Phys. Rev. **D53**, 2658-2669 (1996). [hep-ph/9507378].

[7] L. Randall, R. Sundrum, Nucl. Phys. **B557**, 79-118 (1999). [hep-th/9810155]. G. F. Giudice, M. A. Luty, H. Murayama, R. Rattazzi, JHEP **9812**, 027 (1998). [hep-ph/9810442].

[8] K. Choi, A. Falkowski, H. P. Nilles, M. Olechowski, Nucl. Phys. **B718**, 113-133 (2005). [hep-th/0503216].

[9] Z. Chacko, M. A. Luty, A. E. Nelson, E. Ponton, JHEP **0001**, 003 (2000). [hep-ph/9911323]. D. E. Kaplan, G. D. Kribs, M. Schmaltz, Phys. Rev. **D62**, 035010 (2000). [hep-ph/9911293].

[10] C. F. Berger, J. S. Gainer, J. L. Hewett, T. G. Rizzo, JHEP **0902**, 023 (2009). [arXiv:0812.0980 [hep-ph]].

[11] G. Aad *et al.* [The ATLAS Collaboration],

[arXiv:0901.0512 [hep-ex]].

[12] ATLAS Note, *Prospects for Supersymmetry discovery based on inclusive searches at a 7 TeV centre-of-mass energy with the ATLAS detector*, Tech. Rep. ATL-PHYS-PUB-2010-010, CERN, Geneva (2010).

[13] V. M. Abazov *et al.* [DO Collaboration], [arXiv:0712.3805 [hep-ex]]; The DO Collaboration, DO Note 5312 (2007). The DO Collaboration, DO CONF 4400 (2007).

Chapter 2

Determination of Littlest Higgs Model Parameters at the ILC

2.1 Introduction

The Standard Model (SM) of particle physics is a remarkably successful theory. It provides a complete description of physics at currently accessible energies, and its predictions have been confirmed to high accuracy by all high energy experiments to date. An important piece of the SM remains unexplained–the mechanism of electroweak symmetry breaking. Precision measurements and direct searches suggest that this mechanism involves a weakly coupled Higgs boson with a mass in the range $114 < m_H < 208\,\mathrm{GeV}$ at 95% CL. The Higgs mass parameter, however, is quadratically sensitive to UV physics. New physics at the TeV scale is therefore necessary to keep the Higgs light without fine-tuning. This is known as the hierarchy problem. Three main classes of models, supersymmetry, extra dimensions, and little Higgs, have been proposed to address the hierarchy problem. Which of these theories, if any, Nature has chosen will be determined in the coming years as the Large Hadron Collider and the International Linear Collider probe the TeV scale.

The little Higgs models [2, 3, 4, 5, 6, 7, 8, 9] feature the Higgs as a pseudo Nambu-Goldstone boson of an approximate global symmetry which is broken by a vev at a scale of a few TeV. The breaking is realized in such a way that the Higgs

mass only receives quantum corrections at two loops. In contrast to supersymmetry, the one-loop contribution to the Higgs mass from a SM particle is canceled by a contribution from a new particle of the *same* spin. Little Higgs theories thus predict the existence of new top-like quarks, gauge bosons, and scalars near the TeV scale. The distinguishing features of this model are the existence of these new particles and their couplings to the light Higgs. Measurement of these couplings would verify the structure of the cancellation of the Higgs mass quadratic divergences and prove the existence of the little Higgs mechanism.

The most economical little Higgs model is the so-called "Littlest Higgs" (LH) [2], which we introduce here and describe in more detail in Sec. 2.2. This scenario is based on a non-linear sigma model with an $SU(5)$ global symmetry, which is broken to the subgroup $SO(5)$ by a vev f. The vev is generated by some strongly coupled physics at a scale $\Lambda_S \sim 4\pi f$; possible UV completions of little Higgs theories are discussed in [8, 9, 10, 11]. The $SU(5)$ contains a gauged subgroup $[SU(2) \times U(1)]^2$ which is broken by the vev to the SM electroweak group $[SU(2)_L \times U(1)_Y]$. The global $SU(5)$ breaking leaves 14 massless Goldstone bosons, four of which are eaten by the gauge bosons of the broken gauge groups, giving these gauge bosons a mass of order f. In particular, we have a heavy Z-like boson Z_H and a heavy photon-like boson A_H which, as we will see, are phenomenologically important. The other ten Goldstone bosons make up a complex doublet and a complex triplet which remain massless at this stage. Masses for the complex triplet are generated at the TeV-scale by one-loop gauge interactions. The neutral component of the complex doublet plays the role of the SM Higgs. Its mass term comes from a Coleman-Weinberg potential and has quadratically divergent corrections only at two loops, giving $\mu^2 \sim f^2/16\pi^2$. Thus the natural scale for f is around a TeV. If f is much higher than a few TeV, the Higgs mass must again be finely tuned and this model no longer addresses the hierarchy problem.

The phenomenological implications of little Higgs models have been explored in [2, 12, 13, 14, 15, 16, 17, 18, 19, 20, 21, 22, 1, 23, 24, 25, 26, 27, 28]. Constraints arise from electroweak precision data as well as from indirect and direct production at LEP-II and the Tevatron. For example, in the Littlest Higgs scenario, the lack of

discovery of the A_H, which is expected to be quite light, puts a lower bound on f in the few TeV range. Significant electroweak constraints come from tree-level and loop deviations of the ρ-parameter and the weak mixing angle $\sin^2\theta_w$ from their SM values. Combining these gives a limit $f \gtrsim 4\,\text{TeV}$ which is relatively parameter independent. Many variants of little Higgs models exist in the literature which lower this bound to $f \gtrsim 1 - 2\,\text{TeV}$.

In this Chapter we use the processes $e^+e^- \to f\bar{f}$ (where f denotes an SM fermion) and $e^+e^- \to Zh$ to investigate experimental limits from LEP II data on the Littlest Higgs parameters, to evaluate the extent of the International Linear Collider's search reach in LH parameter space, and to see how accurately the ILC will be able to determine the LH parameters. We will see that the ILC can substantially extend the discovery reach of the LHC. In addition, we will also see that the bounds from $e^+e^- \to f\bar{f}$ at LEP II exclude a large part of the LHC's search reach in the $pp \to Z_H \to Z_L h \to \ell^+\ell^- b\bar{b}$ channel. Complementary discussions of the Littlest Higgs model at the ILC and LHC can be found in [18, 19, 20, 21, 22, 1, 23, 24, 25, 26, 27, 28]. In Sec. 2.2, we discuss the Littlest Higgs model in detail. In Sec. 2.3, we examine the process $e^+e^- \to f\bar{f}$ at LEP II and the ILC and determine how accurately the ILC will be able to measure the LH parameters. In Sec. 2.4 we explore the LH parameter space using the process $e^+e^- \to Zh$ at the ILC.

2.2 The Littlest Higgs model and its parameters

In this chapter, we are mainly concerned with the extended neutral gauge sector present in the LH model. While this scenario also includes a number of parameters that arise from the top and scalar sectors, in which there are a number of new heavy particles, the observables of concern in our analysis only depend on the three parameters present in the extended heavy gauge sector. These are f, the vev or "pion decay constant" of the nonlinear sigma model, which we discussed in the Introduction, and two mixing angles. Although we focus on the Littlest Higgs model, we note that an enlarged gauge sector with rather generic features is present in all little Higgs scenarios.

The vev f characterizes the scale of the $SU(5) \to SO(5)$ breaking; the effective field theory of the 14 Goldstone bosons has the Lagrangian

$$\mathcal{L}_\Sigma = \frac{1}{2}\frac{f^2}{4}\mathrm{Tr}\left|\mathcal{D}_\mu \Sigma\right|^2, \tag{2.2.1}$$

where Σ is a 5×5 matrix parametrization of the Goldstone boson degrees of freedom [2, 27, 28]. The covariant derivative contains the gauge bosons associated with the gauged subgroup $[SU(2) \times U(1)]^2$, W_1, W_2, B_1, and B_2;

$$\mathcal{D}_\mu \Sigma = \partial_\mu \Sigma - i\sum_{j=1}^{2}\left(g_j(W_j\Sigma + \Sigma W_j^T) + g_j'(B_j\Sigma + \Sigma B_j^T)\right). \tag{2.2.2}$$

At the same time, the $[SU(2) \times U(1)]^2$ is also broken to $[SU(2)_L \times U(1)_Y]$, and the gauge boson mass eigenstates after the symmetry breaking are

$$\begin{aligned} W &= sW_1 + cW_2, \quad W' = -cW_1 + sW_2, \\ B &= s'B_1 + c'B_2, \quad B' = -c'B_1 + s'B_2. \end{aligned} \tag{2.2.3}$$

The W are the massless gauge bosons associated with the generators of $SU(2)_L$ and the B is the massless gauge boson associated with the generator of $U(1)_Y$. The W' and B' are the massive gauge bosons associated with the four broken generators of $[SU(2) \times U(1)]^2$, with their masses being given by

$$m_{W'} = \frac{f}{2}\sqrt{g_1^2 + g_2^2} = \frac{g}{2sc}f, \quad m_{B'} = \frac{f}{2\sqrt{5}}\sqrt{{g_1'}^2 + {g_2'}^2} = \frac{g}{2\sqrt{5}s'c'}f. \tag{2.2.4}$$

The mixing angles

$$s = \frac{g_2}{\sqrt{g_1^2 + g_2^2}} \text{ and } s' = \frac{g_2'}{\sqrt{{g_1'}^2 + {g_2'}^2}} \tag{2.2.5}$$

relate the coupling strengths of the two copies of $[SU(2) \times U(1)]$. These two angles together with f are the three parameters of the model that are relevant to our analysis. As we will see, the factor of $\sqrt{5}$ in the denominator of the expression for $m_{B'}$ will have important phenomenological consequences.

The Higgs sector contains a scalar triplet in addition to a SM-like scalar doublet. The doublet and triplet both obtain vevs. The doublet vev, v, brings about electroweak symmetry breaking (EWSB) as in the SM, and thus $v = 246\,\text{GeV}$. The triplet vev, v', is related to v by the couplings in the Coleman-Weinberg potential. Taking these to be $\mathcal{O}(1)$ gives the relation $v' \simeq v^2/2f$.

After EWSB, the mass eigenstates are obtained via mixing between the heavy (W' and B') and light (W and B) gauge bosons. They include the light (SM-like) bosons $W_L^\pm$, Z_L, and A_L observed in experiment, and new heavy bosons $W_H^\pm$, Z_H, and A_H that could be observed in future experiments. At tree level, the processes $e^+e^- \to f\bar{f}$ and $e^+e^- \to Zh$ involve the exchange of only the neutral gauge bosons. Their masses are given to $\mathcal{O}(v^2/f^2)$ by

$$\begin{aligned}
M_{A_L}^2 &= 0, \\
M_{Z_L}^2 &= m_Z^2 \left[1 - \frac{v^2}{f^2}\left(\frac{1}{6} + \frac{1}{4}(c^2 - s^2)^2 + \frac{5}{4}(c'^2 - s'^2)^2\right) + 8\frac{v'^2}{v^2}\right], \\
M_{A_H}^2 &= m_Z^2 s_w^2 \left[\frac{f^2}{5s'^2c'^2v^2} - 1 + \frac{v^2}{2f^2}\left(\frac{5(c'^2 - s'^2)^2}{2s_w^2} - x_H\frac{g}{g'}\frac{c'^2s^2 + c^2s'^2}{cc'ss'}\right)\right], \\
M_{Z_H}^2 &= m_W^2 \left[\frac{f^2}{s^2c^2v^2} - 1 + \frac{v^2}{2f^2}\left(\frac{(c^2 - s^2)^2}{2c_w^2} + x_H\frac{g'}{g}\frac{c'^2s^2 + c^2s'^2}{cc'ss'}\right)\right],
\end{aligned} \tag{2.2.6}$$

where m_W and m_Z are the SM gauge boson masses, and s_w (c_w) represents the sine (cosine) of the weak mixing angle. Here x_H, given by [27, 28]

$$x_H = \frac{5}{2}gg'\frac{scs'c'(c^2s'^2 + s^2c'^2)}{5g^2s'^2c'^2 - g'^2s^2c^2}, \tag{2.2.7}$$

characterizes the mixing between B' and W'^3 in the A_H and Z_H eigenstates. It is important to note that all but the first term in the square brackets for $M_{A_H}^2$ and $M_{Z_H}^2$ are numerically insignificant. Thus $M_{A_H}^2$ depends strongly on s' and not on s, and vice versa for $M_{Z_H}^2$. This dependence is shown in Fig. 2.1. Note that the A_H is significantly lighter than the Z_H and can be as light as a few hundred GeV; we will discuss the consequences of this below.

After EWSB, the couplings of the gauge bosons Z_L, A_H, and Z_H to fermions

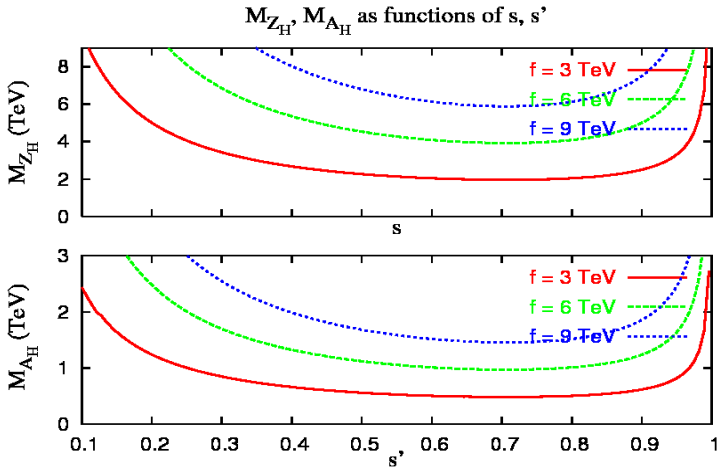

Figure 2.1: Dependence of the heavy gauge boson masses M_{Z_H} and M_{A_H} on s and s', respectively, for different values of f.

similarly depend on s, s' and f because of the mixing between the fields. If we demand that the U(1) be anomaly-free, which requires $y_u = -2/5$ and $y_e = 3/5$ in the notation of [27, 28], the general structure of the couplings is

$$\begin{aligned} g(A_L f\bar{f}) &= g_{SM}(Af\bar{f}), \\ g(Z_L f\bar{f}) &= g_{SM}(Zf\bar{f})\left(1 + \frac{v^2}{f^2}a_i(s,s')\right), \\ g(A_H f\bar{f}) &= b_i \frac{g'}{2s'c'}(\frac{1}{5} - \frac{1}{2}c'^2), \\ g(Z_H f\bar{f}) &= \pm\frac{gc}{4s}, \end{aligned} \tag{2.2.8}$$

where g_{SM} represents the relevant coupling in the SM. A and Z are the SM photon and Z boson, and a_i and b_i are both $\mathcal{O}(1)$ where i labels the species of fermion.

The existence of the heavy gauge boson-Higgs couplings is a hallmark of the Littlest Higgs model. They can be probed using the process $e^+e^- \to Z_L H$ through

the exchange of the Z_L, Z_H, and A_H. The relevant couplings are given by

$$\begin{aligned} g(Z_{L\mu}Z_{L\nu}H) &= g_{SM}(Z_\mu Z_\nu H)\left(1+\frac{v^2}{f^2}a(s,s')\right), \\ g(Z_{L\mu}Z_{H\nu}H) &= \frac{-i}{2}\frac{g^2}{c_W}v\frac{c^2-s^2}{2sc}g_{\mu\nu}, \\ g(Z_{L\mu}A_{H\nu}H) &= \frac{-i}{2}\frac{gg'}{c_W}v\frac{c'^2-s'^2}{2s'c'}g_{\mu\nu}. \end{aligned} \tag{2.2.9}$$

where a is an $\mathcal{O}(1)$ function. The formulae for the couplings can be found in Appendix B of [27].

Certain bounds on s and s' can be obtained by requiring that these couplings remain perturbative. Using the convention that a perturbative coupling g satisfies $g^2/4\pi < 1$ gives $s, s' \gtrsim 0.1 - 0.2$. Using the more conservative convention $g^2 < 1$ would give a smaller allowed range for the parameters. In the analysis that follows, we include the region where $s > 0.16$. As discussed above, expectations for the value of f arise from the requirement of naturalness. For $f \gtrsim 10\,\text{TeV}$, the LH model no longer addresses the hierarchy problem.

As in [27, 28], we write the fermion-boson coupling as $i\gamma^\mu(g_V + g_A\gamma^5)$. It turns out that for the electron-Z_L coupling, $|g_A| \gg |g_V|$, while in general the shifts in the couplings due to mixing are roughly equal, *i.e* $|\Delta g_A| \simeq |\Delta g_V|$. Thus the relative change in g_V is in general much greater than that for g_A, as shown in Fig. 2.2. This relative change in g_V is numerically fairly unimportant for most of the observables in our analysis, as the cross sections are typically functions of $g_V^2 + g_A^2$. The left-right asymmetry A_{LR} in $e^+e^- \to f\bar{f}$, however, has terms directly proportional to g_V. Therefore, for the ILC, which has beam polarization capability, the A_{LR} deviation is important and introduces a surprising s' dependence in our results. We will discuss this in greater detail in Sec. 2.3.

Equation 2.2.6 shows that for generic choices of s and s', $M_{A_H}/M_{Z_H} \simeq s_w m_Z/\sqrt{5}m_W \simeq 1/4$. Figure 2.1 illustrates this, with M_{A_H}, for $f = 3$ TeV, dipping well below 1 TeV for much of the parameter space. As mentioned in Sec. 2.1, this light A_H is responsible for the most stringent experimental constraints on the model [12, 17]. As a result, phenomenologically viable variations of the Littlest Higgs models typically

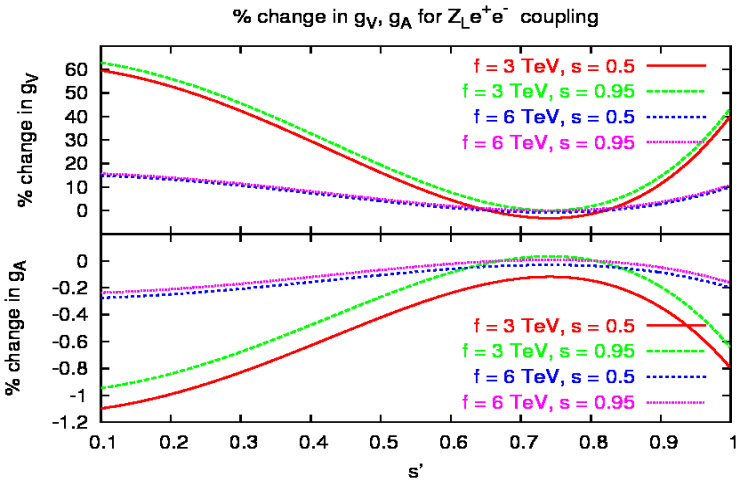

Figure 2.2: The percent deviation of the vector and axial $Z_L e\bar{e}$ couplings from the SM values for $Z_{SM} e\bar{e}$, taking various values for the parameters f and s.

decouple the A_H by modifying the gauge structure of the theory as in [29] and [30]. In this Chapter, however, we analyze the original Littlest Higgs model as it is the most phenomenologically well-studied. To gain some understanding of models in which the A_H decouples we take two approaches in our analysis. One is to choose a parameter value ($s' = \sqrt{3/5}$) for which the coupling of A_H to fermions vanishes. This decouples the A_H from all tree-level electron-positron collider physics. Another approach is to artificially take $M_{A_H} \to \infty$ while letting all other quantities in the theory take on their usual, parameter-dependent values. While not theoretically consistent, this approach gives us a more general picture of the behavior of models in which the A_H decouples. We take both approaches and show the results for each case throughout our analysis.

2.3 Parameter Determination via $e^+e^- \to f\bar{f}$

In this section we examine the process $e^+e^- \to f\bar{f}$, where all of the LH neutral gauge bosons participate via s-channel exchange, at past and future colliders. We first use a χ-squared analysis using the $e^+e^- \to f\bar{f}$ observables measured at LEP II. This

analysis gives the region of LH parameter space excluded (to 95% confidence level) by the LEP II data.

We then perform a similar χ-squared analysis at the energies and luminosity expected at the ILC. We use the same set of observables as in the LEP II analysis as well as the polarization asymmetries that will be measurable due to the beam polarization capability at the ILC. This analysis gives the region of LH parameter space for which the ILC will be able to determine (to 95% confidence level) that the data cannot be explained by the Standard Model, and represents the ILC Littlest Higgs search reach. The two analyses just mentioned are described in Sec. 2.3.1.

Finally, in Sec. 2.3.2, we examine the ability of the ILC to determine the values of the LH parameters from $e^+e^- \to f\bar{f}$. For a few different generic sets of LH parameters, we first generate sample data for the observables, and then perform a χ-squared analysis to map out the region in LH parameter space that is inconsistent (to 95% CL) with the sample data. The size and shape of the remaining region tells us how accurately LH parameters can be determined.

2.3.1 The LEP II exclusion region and ILC search reach

Here we present our numerical analysis of the experimental constraints on the Littlest Higgs parameter space from LEP II data as well as the search reach expected from the ILC. We use the Lagrangian and Feynman rules of the Littlest Higgs model as described in [27, 28]. Note that for our analysis, we follow the notation of [27, 28] and take the values of the U(1) charge parameters $y_u = -2/5$ and $y_e = 3/5$ that, as previously discussed, leave the U(1) anomaly-free and give the couplings shown in Eq. 5.3. The remaining free parameters of the model that are relevant to $e^+e^- \to f\bar{f}$ are the sines of the two $[SU(2) \times U(1)]$ mixing angles, s and s'; and the "decay constant," or vev, f as defined in Eq. 2.2.1 and Eq. 2.2.5.

We first study the constraints on the model from $e^+e^- \to f\bar{f}$ at LEP II, taking as our observables the normalized, binned angular distribution and total cross section for $e^+e^- \to b\bar{b}$, $c\bar{c}$, and $l\bar{l}$, with $l = e$, μ, or τ. We use $\sqrt{s} = 200\,\text{GeV}$ and an integrated luminosity $\mathcal{L}$= 627 pb^{-1}. For the detection efficiencies, we take $\epsilon_e = 97\%$, $\epsilon_\mu = 88\%$,

$\epsilon_\tau = 49\%$, $\epsilon_b = 40\%$, and $\epsilon_c = 10\%$ [31]. We perform a χ-squared analysis and take the SM values for all the observables to correspond to $\chi^2 = 0$, with a nonzero χ^2 representing deviation from the SM. This is a reasonable approach, since there was no detectable deviation from the SM at LEP II [31].

For the ILC analysis, in addition to the above mentioned observables, we also include the angular binned left-right asymmetry A_{LR} for each fermion pair. We use the projected energy $\sqrt{s} = 500$ GeV and luminosity $\mathcal{L}$= 500 fb^{-1}. For the detection efficiencies, we take $\epsilon_e = 97\%$, $\epsilon_{\mu,\tau} = 95\%$, $\epsilon_b = 60\%$, and $\epsilon_c = 35\%$ [32].

Because of the presence of the Z_H and A_H, we use a general formula for the differential cross section for $e^+e^- \to f\bar{f}$ that is valid for any set of extra gauge bosons that can run in the s-channel [33],

$$\frac{d\sigma}{dz} = C_{\rm f}\frac{s}{32\pi}\sum_{ij} P_{ij}^{ss}[B_{ij}(1+z^2) + 2C_{ij}z], \tag{2.3.1}$$

where $z \equiv \cos\theta$, $C_{\rm f}$ is the color factor,

$$P_{ij}^{ss} \equiv \frac{(s-M_i^2)(s-M_j^2) + (\Gamma_i M_i)(\Gamma_j M_j)}{[(s-M_i^2)^2 + (\Gamma_i M_i)^2][(s-M_j^2)^2 + (\Gamma_j M_j)^2]}, \tag{2.3.2}$$

and

$$B_{ij} \equiv (v_i v_j + a_i a_j)_f (v_i v_j + a_i a_j)_e\,,\ C_{ij} \equiv (v_i a_j + a_i v_j)_f (v_i a_j + a_i v_j)_e.$$

Here v and a correspond to the vector and axial couplings g_V and g_A discussed in Sec. 2.2, and the sum runs over the gauge bosons in the s-channel: A_L, Z_L, A_H, and Z_H.

For Bhabha scattering, besides the s-channel, we also have a contribution from

the t-channel, so that

$$\frac{d\sigma}{dz} = \frac{s}{32\pi}\sum_{ij}\Bigg\{P_{ij}^{ss}\left[B_{ij}(1+z^2)+2C_{ij}z\right]+ \\ 2P_{ij}^{tt}\left[B_{ij}\left(1+\frac{1}{4}(1+z)^2\right)-C_{ij}\left(1-\frac{1}{4}(1+z)^2\right)\right]+ \\ P_{ij}^{st}(1+z)^2(B_{ij}+C_{ij})\Bigg\}, \tag{2.3.3}$$

where P_{ij}^{st} and P_{ij}^{tt} are defined similarly to P_{ij}^{ss} with the replacement $s \to t = -\frac{1}{2}s(1-z)$ in Eq. 2.3.2 in the obvious way.

To calculate A_{LR}, we need the cross sections for left- and right-handed electrons. These can be obtained from the above formulae by making the replacements

$$v_{ie} \to \frac{1}{2}\left(v_{ie}+\lambda a_{ie}\right),\ a_{ie} \to \frac{1}{2}\left(a_{ie}+\lambda v_{ie}\right), \tag{2.3.4}$$

with $\lambda = +1(-1)$ corresponding to left- (right-) handed electrons. Then the left-right asymmetry is given by

$$A_{LR}(z) = \mathcal{P}\frac{\frac{d\sigma_L}{dz}-\frac{d\sigma_R}{dz}}{\frac{d\sigma_L}{dz}+\frac{d\sigma_R}{dz}}, \tag{2.3.5}$$

where $\mathcal{P}$ is the degree of e^- beam polarization at the ILC, which we take to be 80%. We assume the e^+ beam is unpolarized.

We compute the χ^2 distribution as follows, where σ^i represents one of the observables mentioned above:

$$\chi^2 = \sum_i\left(\frac{\sigma_{LH}^i-\sigma_{SM}^i}{\delta\sigma^i}\right)^2. \tag{2.3.6}$$

Here, $\delta\sigma$ is the statistical error for each observable, given by

$$\begin{aligned}
\delta\sigma_{tot} &= \sqrt{\frac{\sigma_{tot}}{\mathcal{L}\epsilon}}, \\
\delta(\frac{d\sigma_N}{dz}) &= \sqrt{\frac{\frac{d\sigma_N}{dz} - (\frac{d\sigma_N}{dz})^2}{\mathcal{L}\epsilon\sigma_{tot}}}, \\
\delta A_{LR} &= \sqrt{\frac{1 - A_{LR}^2}{\mathcal{L}\epsilon\sigma_{tot}}},
\end{aligned} \tag{2.3.7}$$

where σ_{tot} is the total cross section and $\frac{d\sigma_N}{dz}$ is the normalized differential cross section:

$$\frac{d\sigma_N}{dz} = \frac{1}{\sigma_{tot}}\frac{d\sigma}{dz} \ . \tag{2.3.8}$$

The efficiency ϵ for each final state is given above.

As previously noted, s, s', f are the free parameters present in the neutral gauge sector of the LH model. In our analysis, we choose a fixed value of s' and scan the parameter space (s, f).

The exclusion region at LEP II and the search reach at the ILC correspond to the regions where χ^2 is greater than 5.99, representing a 95% confidence level for two free parameters. The combined result is shown in Fig. 2.3 for different values of s'. For each value of s', the LEP II exclusion region and the ILC search reach are on the left of the corresponding contour. This is because as f increases, the gauge boson masses (proportional to f) also increase (see Fig. 2.1) and the deviations in the $Z_L f\bar{f}$ couplings (proportional to v^2/f^2) decrease. For the ILC search reach boundary one would expect to see four contours at the upper right corner corresponding to the four different input values of s'. However, there is only one visible contour, for $s' = \sqrt{3/5}$, because in the other three cases, the search reach covers the entire parameter space shown in the figure.

As discussed above, the choice $s' = \sqrt{3/5}$ corresponds to decoupling the A_H from the fermion sector, as verified by the results shown in Eq. 5.3. In this case, the ILC search reach can be as low as $f \sim 2\,\text{TeV}$ for large values of s. For other values of s', the search reach is greater than $f \sim 10\,\text{TeV}$ for all values of s. We thus see how

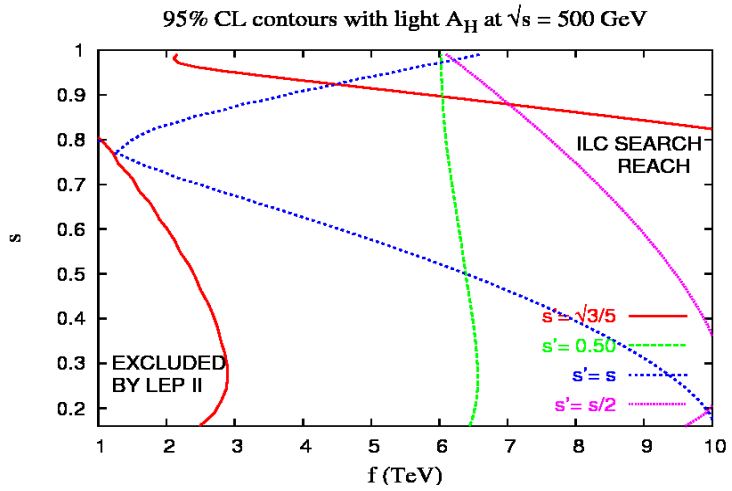

Figure 2.3: LEP II exclusion region from $e^+e^- \to f\bar{f}$ and ILC search reach in the parameter space (s, f) for different input values of s', and including the A_H contribution. For $s' = \sqrt{3/5}$ there are two lines of the same symbol/color, one on the boundary of the LEP II exclusion region, and one on the boundary of the ILC search reach region. For the other values of s' the curve shown is the boundary of the LEP II exclusion region, while the ILC search reach covers the entire parameter region shown.

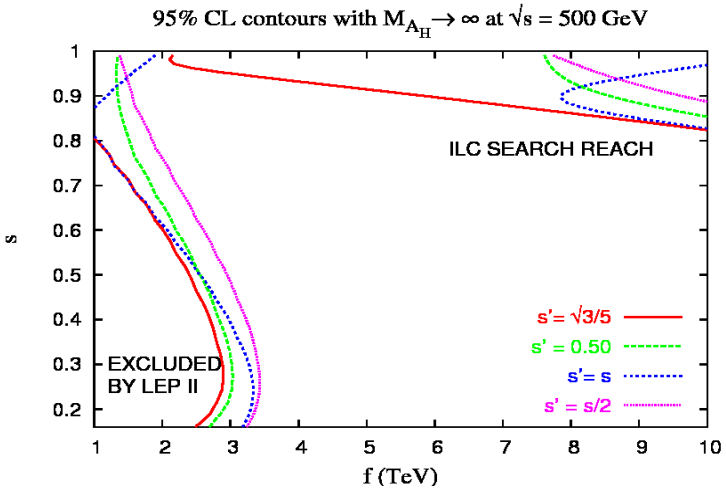

Figure 2.4: LEP II exclusion region and ILC search reach as in Fig. 2.3, but with $M_{A_H} \to \infty$.

strongly the presence of the relatively-light A_H can affect the phenomenology. For LEP II, the story is similar; the exclusion region for $s' = \sqrt{3/5}$ is much smaller than for other values of s'. This is because the observed deviation at $s' = \sqrt{3/5}$ is solely due to the modification in the $Z_L f\bar{f}$ coupling and the presence of the Z_H, which is generally several times heavier than the A_H. For other values of s' the constraints on f can be as high as ~ 6 TeV. Overall, the LEP II exclusion regions have constraints on the parameter f that are roughly consistent with those from precision measurements [2, 12, 13, 14, 15, 16, 17].

As discussed in Sec. 2.2, we also examine the general behavior of models in which the A_H is decoupled by taking $M_{A_H} \to \infty$ while letting all other quantities take on their usual values. The results in this case are presented in Fig. 2.4. It is not surprising that the $s' = \sqrt{3/5}$ contours in Fig. 2.4 are exactly the same as in Fig. 2.3, since the A_H is decoupled for this choice of s'. For other values of s', the contours are very different in the two cases. The s dependence of the contours in Fig. 2.4 is easy to understand. The $Z_H f\bar{f}$ couplings go as gc/s, thus the ILC contours show that the search reach is higher for lower values of s. Similarly, for LEP II, the exclusion region extends farther out in f for lower values of s. There is, however, a "turnover" for

the LEP II exclusion region around $s \sim 0.3$ where the contours start moving towards lower f. This takes place because the mass M_{Z_H} begins to increase (see Fig. 2.1) and the overall contribution from Z_H to the observables starts to decrease as s gets smaller.

With $M_{A_H} \to \infty$, the s'-dependence of the χ^2 is mostly due to the deviation in the $Z_L f\bar{f}$ couplings, since neither the $Z_H f\bar{f}$ couplings (see Eq. 5.3) nor M_{Z_H} (see Eq. 2.2.6) are strongly dependent on s'. This explains why there is less variation among the different contours in Fig. 2.4 than in Fig. 2.3. For values of s close to 1, however, the ILC contours for different values of s' begin to deviate from one another markedly. This s' dependence is due to the s'-sensitive deviation of A_{LR}, as discussed in Sec. 2.2. This is confirmed by Fig. 2.5, which shows the relative contribution of the different observables to the χ^2 at the ILC with $M_{A_H} \to \infty$ and $s = 0.95$. Note that A_{LR} for various final states dominates the χ^2 where it is large.

The fact that the search reach is lowest for $s' = \sqrt{3/5}$ then indicates that the deviations in the $Z_L f\bar{f}$ couplings are smallest for this parameter value. This coincidence arises because both A_H and Z_L are linear combinations of gauge eigenstates. A_H to lowest order is just B', whose couplings to fermions vanish at $s' = \sqrt{3/5}$. As the s'-dependent terms in the deviation of the $Z_L f\bar{f}$ couplings arise from the B' admixture, they also vanish at this value. This is also confirmed by Fig. 2.5, which shows that the relative contribution of A_{LR} and the total χ^2 decrease around $s' = \sqrt{3/5}$.

The search reach at a $\sqrt{s} = 1\,\text{TeV}$ ILC reaches to somewhat higher values of the parameter s, but has essentially the same reach for the parameter f as the $\sqrt{s} = 500\,\text{GeV}$ machine. This is reasonable; as s approaches unity, the contribution from the deviations in the Z_L couplings dominates the search reach, and these contributions are not as important as the center of mass energy increases. The result is that the search reach is very similar for both $\sqrt{s} = 500$ GeV and 1 TeV. We will see later, however, that the $\sqrt{s} = 1\,\text{TeV}$ data can significantly improve the parameter determination.

Figure 2.3 and Fig. 2.4 show that the $\sqrt{s} = 500\,\text{GeV}$ ILC search reach in general covers most of the interesting parameter space where the Littlest Higgs models are relevant to the gauge hierarchy. Thus the $e^+e^- \to f\bar{f}$ process alone is an effective tool for investigating the Littlest Higgs model at a ILC.

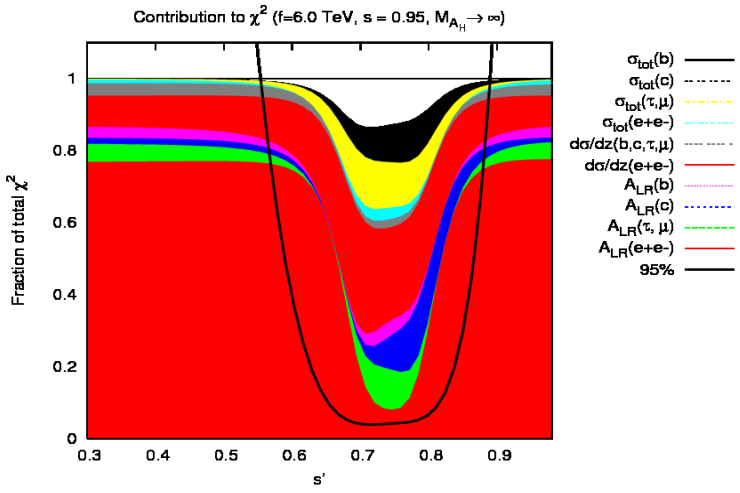

Figure 2.5: Fractional contribution to the total χ^2 for each $e^+e^- \to f\bar{f}$ observable at a 500 GeV ILC for fixed (s, f). The labels on the legend go from top down in one-to-one correspondence with the shaded sections. For example, $A_{LR}(e^+e^-)$ contributes $\sim 78\%$ to the total χ^2 at $s' = 0.4$. The line labeled "95%" is the total $\chi^2/5.99$. This means that the region $s' \sim [0.55, 0.9]$ where this line dips below 1 is outside the $\sqrt{s} = 500$ GeV ILC search reach.

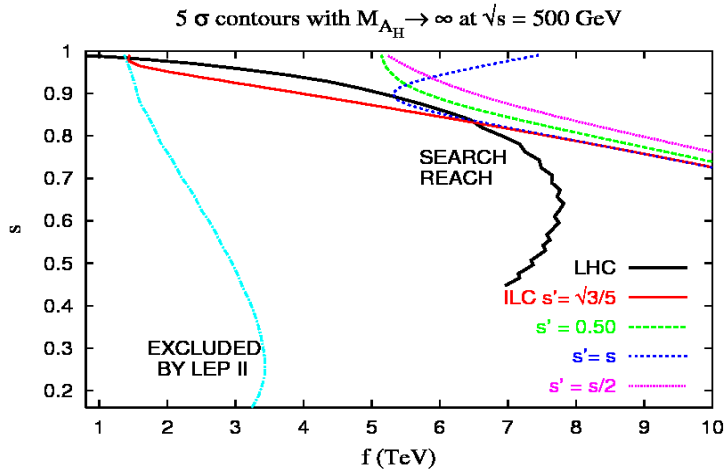

Figure 2.6: Comparison of ILC and LHC search reach. The LHC data was taken from Fig. 8 of [1]. The search reach lies to the left of and underneath the contours.

It is important to compare the ILC search reach to that of the LHC. An ATLAS based analysis of the LHC search reach for the heavy gauge boson Z_H of the Littlest Higgs model was computed in Ref. [1]. The resulting 5σ contour for discovery of the Z_H at the LHC is reproduced in Fig. 2.6 (where we have converted their results to our choices of parameters f and s for the axes). Fig. 2.6 also displays our results for the ILC (taking $M_{A_H} \to \infty$), where we have now employed a statistical significance of 5σ rather than 95% to facilitate an equal comparison. We see that the ILC substantially extends the LHC search reach for $s \lesssim 0.8$.

2.3.2 Parameter Determination: sample fits

We have now determined the available parameter space accessible to the ILC and not already excluded by LEP II. It remains to ask, given the existence of an LH model with parameters in this accessible range, how accurately would the ILC be able to measure them? It is well-known [34, 35, 36, 32, 37, 38, 39, 40] that the ability to precisely measure the couplings of heavy gauge bosons is one of the fortes of the ILC.

We first discuss the capability of the LHC to determine the LH model parameters.

Numerous studies [34, 35, 41, 42, 43] have addressed the ability of the LHC to determine the couplings of new gauge bosons. The results of these studies show that while some model differentiation is possible for Z' bosons with masses $\lesssim 2$ TeV, absolute determination of the Z' couplings is not possible. There are three main reasons for this: (i) the number of observables is limited in the hadron collider environment. The observables are the number of events (*i.e.*, cross section times branching fraction), the forward-backward asymmetry, and the rapidity asymmetry) for leptonic final states only. Other final states are not detectable above background, ($t\bar{t}$ final states are a possible exception, but such events will be heavily smeared and thus not useful for a coupling analysis). (ii) The observables are convoluted with all contributing parton densities. (iii) The statistics are insufficient for $M_{Z'} \gtrsim 2$ TeV. Here, in the case of the LH, our results show that LEP II essentially excludes the region $M_{Z_H} \lesssim 2$ TeV, and thus we do not expect the LHC to contribute to the parameter extraction in any significant way. We note, however, that a very precise mass measurement for Z_H will be obtained at the LHC.

To determine the accuracy of the parameter measurements, we perform some sample fits, using a χ-squared analysis similar to the one described in the preceding section. We use the same ILC observables as before. In some cases we also include data from a $\sqrt{s} = 1\,\text{TeV}$ run, for which we also take an integrated luminosity of $\mathcal{L}=$ 500 fb^{-1}. We note that we can exchange M_{Z_H} for f, so we now take M_{Z_H}, s, and s' as our free parameters. We choose a generic data point (s, s', M_{Z_H}) and use it to calculate the observables, which we then fluctuate according to statistical error. We assume that the Large Hadron Collider would have determined M_{Z_H} relatively well, to the order of a few percent for $M_{Z_H} \lesssim 5 - 6\,\text{TeV}$; we thus fix M_{Z_H} and perform a 2-variable fit to s and s'. Scanning the s-s' parameter space, we calculate the χ^2 at every point. We find the minimum χ^2 point; the 95% CL region surrounding it is the region for which the χ^2 is less than this minimum χ^2 plus 5.99.

Figure 2.7 shows the results of this fit for two sample data points in the contrived scenario with $M_{A_H} \to \infty$. For both of these points, the determination of s is very accurate. This is due to the strong dependence of the $Z_H f \bar{f}$ couplings on s, as discussed in the previous section. The s' determination is worse than that for s because

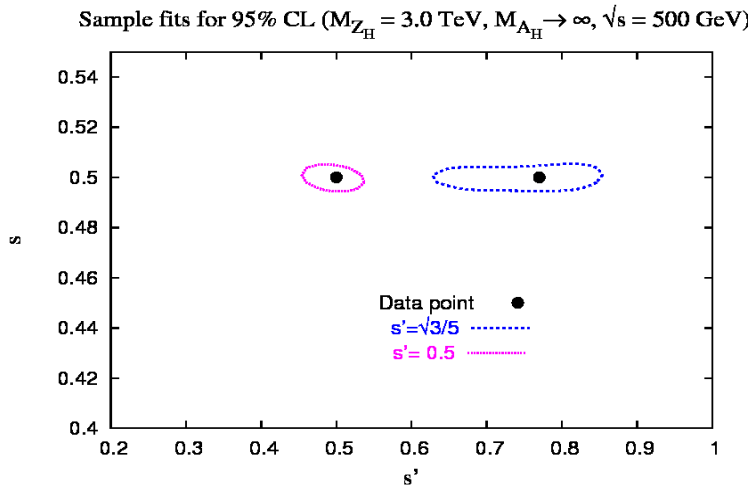

Figure 2.7: 95% CL sample fits to the data points ($s = 0.5$, $s' = 0.5$) and ($s = 0.5$, $s' = \sqrt{3/5}$), using $e^+e^- \to f\bar{f}$ observables at a 500 GeV ILC, taking $M_{Z_H} = 3.0\,\text{TeV}$ and $M_{A_H} \to \infty$.

of our choice $s = 0.5$. At this value of s, the contributions from the Z_L coupling deviations (which carry the s' dependence) are smaller than the Z_H contributions. The reason the s' determination is better for $s' = 0.5$ than it is for $s' = \sqrt{3/5}$ is that the s'-dependent deviations in $g_{V_{Z_L f\bar{f}}}$ vanish for the latter value.

Figure 2.8 shows the results from a similar fit and illustrates how it can be improved with data from a higher-energy run with $\sqrt{s} = 1\,\text{TeV}$ at the ILC. Here, the s determination is not much more accurate than the s' determination, as the s'-independent Z_H contributions no longer dominate the fit for $s = 0.9$.

In Fig. 2.9 we show results from a fit with the full A_H contributions. Not surprisingly, the parameter determination is much more precise, as the A_H contributions, when present, dominate the χ^2. Since the A_H couplings depend only on s', it is also no surprise that here the s' determination is in general much better than that for s.

If, for some reason, the LHC doesn't provide a good measurement of M_{Z_H}, we would need to include that quantity, or equivalently f, in our fits to the data. In Fig. 2.10 we show the results where we have set $s' = \sqrt{3/5}$ and we fit to s and f. Note that for one of the data points, the allowed region doesn't close. This highlights

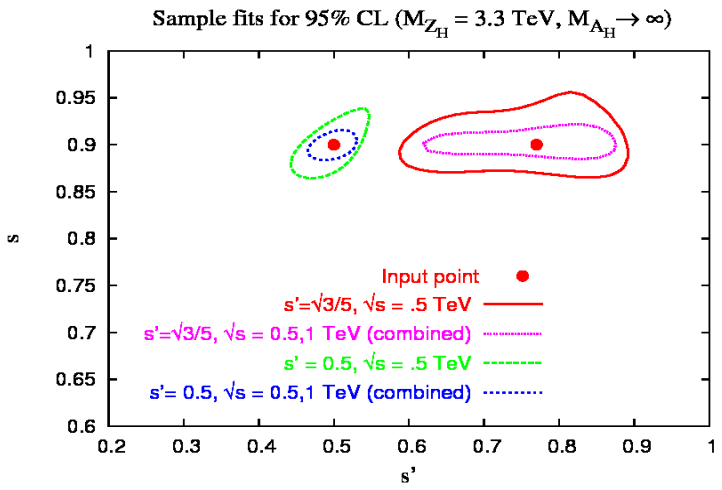

Figure 2.8: Like Fig. 2.7 except $M_{Z_H} = 3.3\,\text{TeV}$ and the data points are ($s = 0.9$, $s' = 0.5$) and ($s = 0.9$, $s' = \sqrt{3/5}$). Also shown for each point is an improved fit from adding data from a $\sqrt{s} = 1\,\text{TeV}$, $\mathcal{L}$= 500 fb^{-1}run at the ILC.

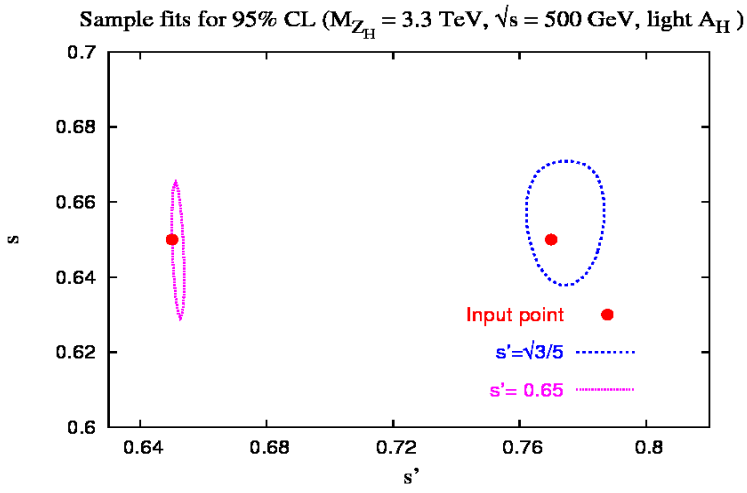

Figure 2.9: Like Fig. 2.7, except $M_{Z_H} = 3.3\,\text{TeV}$ and the data points are ($s = 0.65$, $s' = 0.65$) and ($s = 0.65$, $s' = \sqrt{3/5}$), and the full M_{A_H} contributions are included.

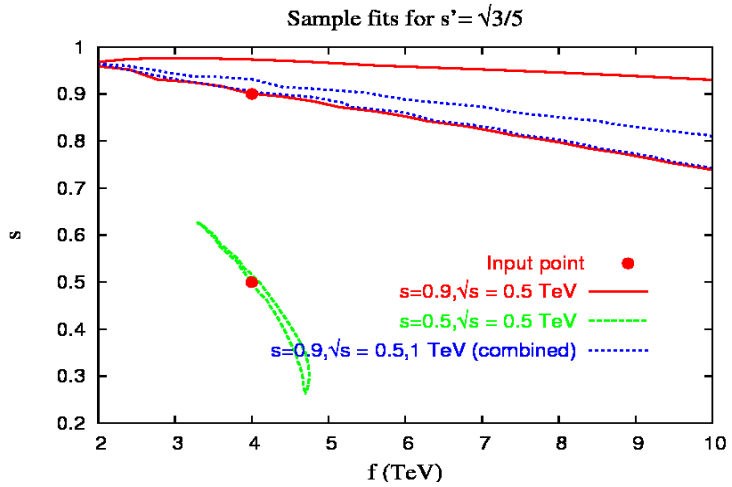

Figure 2.10: Sample fits to the data points ($s = 0.5$, $f = 4\,\text{TeV}$) and ($s = 0.9$, $f = 4\,\text{TeV}$), taking $s' = \sqrt{3/5}$. At the decoupling value of s', the A_H does not contribute.

the importance of using both the LHC and the ILC to reliably determine the model parameters.

2.4 Parameter determination using $e^+e^- \to Z_L h$

In order to confirm that the LH model is the correct description of TeV-scale physics, it is important to test the hallmark of the LH mechanism, namely that the Higgs mass quadratic divergences are canceled by new particles with the same spin as their SM counterparts. The proof lies in the measurement of the new particle couplings to the Higgs. Here we are concerned with the coupling of the heavy Z to the Higgs boson. This coupling can be tested via the process $e^+e^- \to Z_L h$. In the LH model, deviations of observables related to this process from their SM expectations come from three sources: the diagram with the Z_H in the s-channel, the diagram with the A_H in the s-channel, and the deviation of the $Z_L Z_L h$ coupling from its SM value.

In this section we repeat the analysis of Section 2.3, using the process $e^+e^- \to Z_L h$ and taking the total cross section as our observable with $m_h = 120\,\text{GeV}$. We assume that at a $\sqrt{s} = 500\,\text{GeV}$ ILC this cross section will be measured to an accuracy of

1.5% [32].

The cross section, including the effects of additional gauge bosons, can be written as

$$\sigma_{Z_L h} = \frac{|\mathbf{k}|}{8\pi\sqrt{s}}\left(1+\frac{|\mathbf{k}|^2}{3m_Z^2}\right)\sum_{ij} P_{ij}^{ss}[g_{iZ_Lh}g_{jZ_Lh}(v_iv_j+a_ia_j)_e], \tag{2.4.1}$$

where P_{ij}^{ss} was defined in Eq. 2.3.2. The sum runs over the participating gauge bosons in the s-channel: Z_L, A_H, and Z_H. Here, $|\mathbf{k}|$ is the magnitude of the 3-momentum of the outgoing Z_L, given by

$$|\mathbf{k}| = \frac{1}{2\sqrt{s}}\sqrt{(m_H^2 - M_{Z_L}^2)^2 + s(s-2(M_{Z_L}^2+m_H^2))}. \tag{2.4.2}$$

The couplings v_i and a_i are the same as before–the axial and vector couplings of electrons to the ith gauge boson.

We carry out the χ-squared analysis as before. Figure 2.11 shows the ILC search reach in the LH parameter space, where each plot corresponds to a different choice of s'. By comparing to Fig. 2.4 we note that $e^+e^- \to Z_Lh$ gives a much poorer search reach than $e^+e^- \to f\bar{f}$. In particular, when s' is near the decoupling value $\sqrt{3/5}$ the LH model is generally indistinguishable from the SM. Well away from $s' = \sqrt{3/5}$, as shown for $s' = s/2$ and $s' = 0.5$, the search reach covers almost all of parameter space, except for regions of low f where interference between the A_H and Z_H conspire to bring the cross section near its SM value. These regions, however, are ruled out by LEP.

In the case $s' = s$, however, there are regions that exhibit similar interference effects and are not ruled out by LEP data. For example, consider the two data points $f = 4.0\,\text{TeV}$, $s = 0.61$ with (a) $s' = \sqrt{3/5}$ and (b) $s' = 0.61$. With $\sqrt{s} = 500\,\text{GeV}$, (b) is within the search reach while (a) is just outside the search reach. Figure 2.12 shows that at this value of $\sqrt{s}$, the deviation of the cross section from the SM is much greater for $s' = 0.61$ than for $s' = \sqrt{3/5}$, since the A_H decouples in the latter case. With $\sqrt{s} = 1\,\text{TeV}$, this behavior is reversed; point (a) is outside the search reach while (b) is within. At this value of $\sqrt{s}$ the interference between A_H and Z_H brings

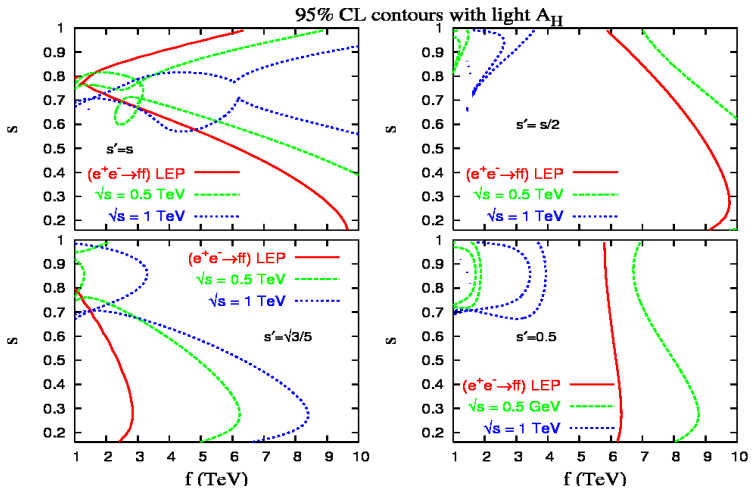

Figure 2.11: LEP II exclusion region from $e^+e^- \to f\bar{f}$ and ILC search reach in the parameter space (s, f) from the process $e^+e^- \to Z_L h$, for various values of s' and including the full A_H contributions. For each value of s' there are three curves; one corresponds to the LEP II exclusion region, and the other two represent the ILC search reach region for $\sqrt{s} = 500$ and 1000 GeV, respectively, taking an integrated luminosity of 500 fb^{-1}at each center-of-mass energy.

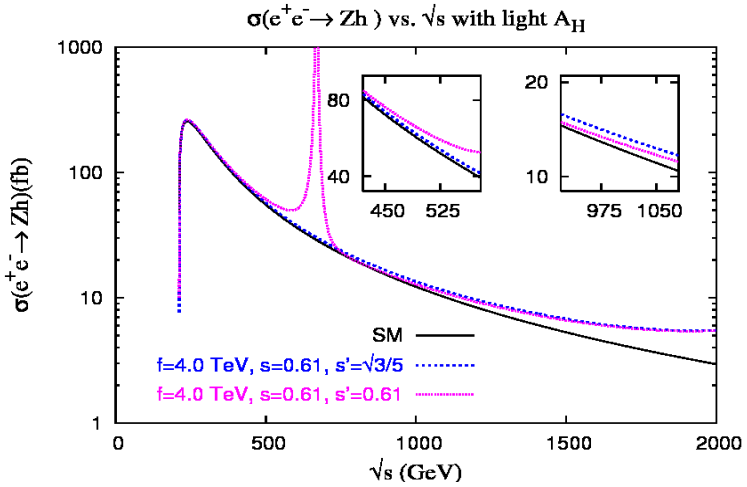

Figure 2.12: The cross section for $e^+e^- \to Z_L h$ as a function of $\sqrt{s}$ for the SM and two different points in LH parameter space. The insets show the behavior near the expected ILC $\sqrt{s}$ values of 500 GeV and 1 TeV. The resonance at about 700 GeV corresponds to the A_H.

the cross section closer to the SM value when the A_H contributes.

Figure 2.13 shows the search reach obtainable with 500 fb^{-1}at a $\sqrt{s} = 500\,\text{GeV}$ ILC, taking $M_{A_H} \to \infty$. Comparing to Fig. 2.3, we see that the search reach here is much smaller than for $e^+e^- \to f\bar{f}$. Figure 2.14 displays the corresponding reach at $\sqrt{s} = 1\,\text{TeV}$ with 500 fb^{-1}. In both cases, and for all choices of s', the search reach decreases markedly around $s = 1/\sqrt{2}$. This is because the $Z_L Z_H H$ coupling vanishes at this value of s, as can be seen in Eq. 2.2.9. It is also interesting to note that the spread in the search reach as s' is varied is larger for $\sqrt{s} = 500\,\text{GeV}$ than it is for 1 TeV. This can be understood if one notes that $\sqrt{s} = 1\,\text{TeV}$ is closer to the Z_H pole (as $M_{Z_H} \simeq$ a few TeV throughout the parameter space) than is 500 GeV. Thus the deviation of σ_{Zh} from its SM value at $\sqrt{s} = 1\,\text{TeV}$ is dominated by the presence of the Z_H, whose mass and couplings are essentially s'-independent. At $\sqrt{s} = 500\,\text{GeV}$, the deviation of σ_{Zh} has a more significant contribution from the deviation of the $e^+e^-Z_L$ coupling, which is strongly dependent on s' (see Fig. 2.2). For both values of $\sqrt{s}$, the sensitivity in the range of parameter space where $s \gtrsim 0.5$ does not reach beyond the general precision electroweak bound of $f \gtrsim 4\,\text{TeV}$.

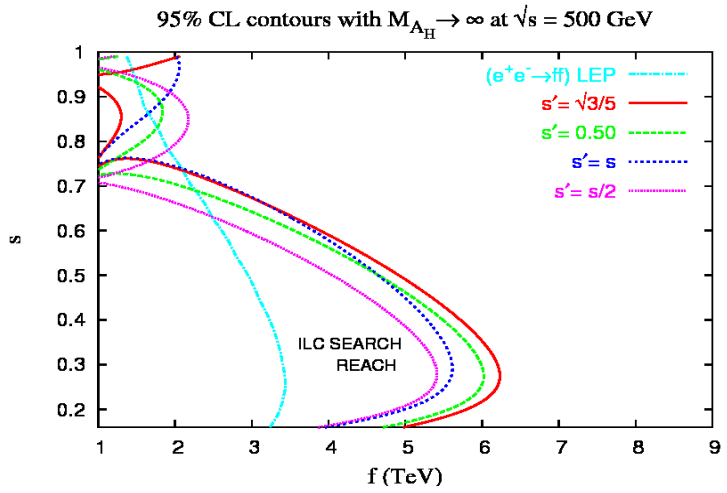

Figure 2.13: The ILC search reach from the process $e^+e^- \to Z_L h$ for various values of s', taking $\sqrt{s} = 500$ and $M_{A_H} \to \infty$. The LEP II exclusion region from $e^+e^- \to f\bar{f}$ is shown for $s' = s/2$ (from Fig. 2.4) for comparison.

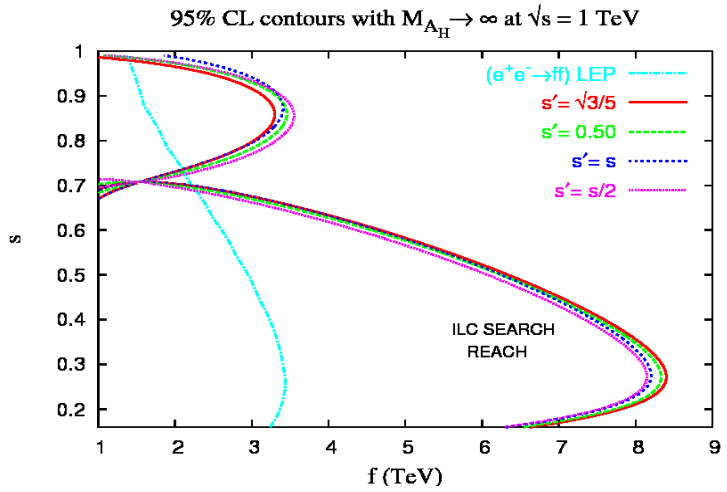

Figure 2.14: Same as Fig. 2.13, but for $\sqrt{s} = 1\,\text{TeV}$.

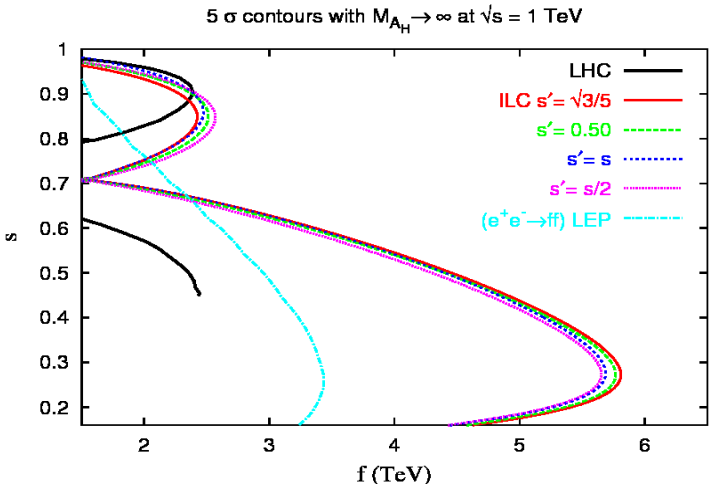

Figure 2.15: Comparison of ILC and LHC search reach in the $Z_H \to Zh$ channel. The LHC curve was read from Fig. 22 of [1].

One could hope to improve the sensitivity by adding the measurement of the Higgs branching ratios as additional observables. It turns out, however, that the LH deviations of the branching ratios from their SM values are at most 1-2%, which is smaller than or equivalent to the experimental sensitivity at the ILC.

Lastly, we again compare the reach obtainable at the ILC from this process to that of the LHC in $pp \to Z_H \to Z_L + h$. We display the 5σ results from the ATLAS based analysis [1] of this process in the LH using the final state $\ell^+\ell^- b\bar{b}$ in Fig. 2.15. We also show our results, again adjusted for 5σ rather than 95% statistical significance. This figure shows that the ILC overwhelms the capability of the LHC in this channel. In fact, our analysis of $e^+e^- \to f\bar{f}$ shows that for $s \lesssim 0.8$ the LEP II results already exclude the possibility of the LHC observing the $Z_L + h$ decay of the Z_H.

2.5 Summary

Little Higgs models provide an interesting mechanism for addressing the hierarchy problem. They contain a single light Higgs boson which is a pseudo-Goldstone boson with a small mass generated at the two-loop level. The quadratically divergent

loop contributions to the mass of this Higgs are canceled by contributions from new particles appearing at the TeV scale. These cancellations take place between contributions from particles which have the same spin. Measurement of the couplings of these new particles to the light Higgs would verify the structure of these cancellations and establish the Little Higgs mechanism.

Here, we have investigated the extended gauge boson sector within these theories. Numerous Little Higgs models, based on various global symmetries, have been proposed. However, the existence of an enlarged gauge sector, with rather generic features, is endemic to all these scenarios. We choose to work in the framework of the simplest model of this type, known as the Littlest Higgs, based on an SU(5)/SO(5) nonlinear sigma model. This scenario contains the new heavy gauge bosons $W_H^{\pm}$, Z_H, and A_H in addition to the SM gauge fields. The masses of these additional gauge bosons are expected to be of order the global symmetry breaking scale of $f \sim$ TeV. (It is expected that $f \lesssim 10$ TeV in order for this scenario to be relevant to the hierarchy.) However, due to the group theory structure, the A_H can be significantly lighter resulting in stringent constraints from precision electroweak data. Phenomenologically viable Littlest Higgs models must thus decouple the A_H and we have examined two such approaches in our analysis. One, where we choose the model parameters such that the fermion couplings of the A_H vanish, and another where we artificially take $M_{A_H} \to \infty$.

We study the effects of the new neutral gauge bosons in e^+e^- annihilation. These particles can participate in $e^+e^- \to f\bar{f}$ and $e^+e^- \to Zh$ via s-channel exchange, and their effects can be felt indirectly for center of mass energies well below their masses. We find that fermion pair production is more sensitive to Little Higgs effects than Zh associated production. We perform a thorough investigation of the model parameter space and find that observables at LEP II exclude the region $f \lesssim 1-3$ TeV, which is consistent with the constraints obtained from precision electroweak data. The search reach of the proposed International Linear Collider, operating at $\sqrt{s} = 500$ GeV, covers essentially the entire parameter region where this model is relevant to the hierarchy, *i.e.*, $f \lesssim 6-10$ TeV. In the case of a 1 TeV ILC, the search region probes slightly larger values of the mixing parameter s, but similar values of f.'

We have also demonstrated that once a signal is observed in these channels, accurate measurements of the couplings of the heavy gauge fields can be obtained from fermion pair production at the ILC. These couplings are related to the mixing angles in the extended gauge sector and we show that experiments at the ILC can determine the fundamental parameters of the theory. For illustration, we performed a fit to generated data for sample points in the Littlest Higgs parameter space, and found that the fundamental parameters can be determined to the precision of a few percent, provided that the LHC measures the mass of the heavy neutral gauge field. If information on the new boson masses is not available from the LHC, then the parameter determination at the ILC deteriorates. Additionally, the couplings of the extra gauge bosons to the light Higgs can separately be determined from $e^+e^- \to Zh$ for a significant region of the parameter space. This enables ILC experiments to test the consistency of the theory and verify the structure of the Higgs quadratic divergence cancellations.

In summary, we find that the ILC has the capability to discover the effects of the Littlest Higgs model over the entire theoretically interesting range of parameters, and to additionally determine the couplings of the heavy gauge bosons to the precision of a few percent.

Bibliography

[1] G. Azuelos *et al.*, Eur. Phys. J. **C39S2**, 13 (2005), hep-ph/0402037.

[2] N. Arkani-Hamed, A. G. Cohen, E. Katz, and A. E. Nelson, JHEP **07**, 034 (2002), hep-ph/0206021.

[3] N. Arkani-Hamed, A. G. Cohen, and H. Georgi, Phys. Lett. **B513**, 232 (2001), hep-ph/0105239.

[4] N. Arkani-Hamed *et al.*, JHEP **08**, 021 (2002), hep-ph/0206020.

[5] I. Low, W. Skiba, and D. Tucker-Smith, Phys. Rev. **D66**, 072001 (2002), hep-ph/0207243.

[6] D. E. Kaplan and M. Schmaltz, JHEP **10**, 039 (2003), hep-ph/0302049.

[7] S. Chang and J. G. Wacker, Phys. Rev. **D69**, 035002 (2004), hep-ph/0303001.

[8] W. Skiba and J. Terning, Phys. Rev. **D68**, 075001 (2003), hep-ph/0305302.

[9] S. Chang, JHEP **12**, 057 (2003), hep-ph/0306034.

[10] E. Katz, J.-y. Lee, A. E. Nelson, and D. G. E. Walker, JHEP **10**, 088 (2005), hep-ph/0312287.

[11] D. E. Kaplan, M. Schmaltz, and W. Skiba, Phys. Rev. **D70**, 075009 (2004), hep-ph/0405257.

[12] J. L. Hewett, F. J. Petriello, and T. G. Rizzo, JHEP **10**, 062 (2003), hep-ph/0211218.

[13] M.-C. Chen and S. Dawson, Phys. Rev. **D70**, 015003 (2004), hep-ph/0311032.

[14] W.-j. Huo and S.-h. Zhu, Phys. Rev. **D68**, 097301 (2003), hep-ph/0306029.

[15] C.-x. Yue and W. Wang, Nucl. Phys. **B683**, 48 (2004), hep-ph/0401214.

[16] C. Csaki, J. Hubisz, G. D. Kribs, P. Meade, and J. Terning, Phys. Rev. **D68**, 035009 (2003), hep-ph/0303236.

[17] C. Csaki, J. Hubisz, G. D. Kribs, P. Meade, and J. Terning, Phys. Rev. **D67**, 115002 (2003), hep-ph/0211124.

[18] E. Ros, Eur. Phys. J. **C33**, s732 (2004).

[19] C.-x. Yue, W. Wang, and F. Zhang, Nucl. Phys. **B716**, 199 (2005), hep-ph/0409066.

[20] G.-C. Cho and A. Omote, Phys. Rev. **D70**, 057701 (2004), hep-ph/0408099.

[21] S. C. Park and J. Song, Phys. Rev. **D69**, 115010 (2004).

[22] J.-J. Liu, W.-G. Ma, G. Li, R.-Y. Zhang, and H.-S. Hou, Phys. Rev. **D70**, 015001 (2004), hep-ph/0404171.

[23] C.-x. Yue, S.-z. Wang, and D.-q. Yu, Phys. Rev. **D68**, 115004 (2003), hep-ph/0309113.

[24] Z. Sullivan, (2003), hep-ph/0306266.

[25] G. Burdman, M. Perelstein, and A. Pierce, Phys. Rev. Lett. **90**, 241802 (2003), hep-ph/0212228.

[26] W. Kilian and J. Reuter, Phys. Rev. **D70**, 015004 (2004), hep-ph/0311095.

[27] T. Han, H. E. Logan, B. McElrath, and L.-T. Wang, Phys. Rev. **D67**, 095004 (2003), hep-ph/0301040.

[28] T. Han, H. E. Logan, and L.-T. Wang, JHEP **01**, 099 (2006), hep-ph/0506313.

[29] T. Gregoire, D. Tucker-Smith, and J. G. Wacker, Phys. Rev. **D69**, 115008 (2004), hep-ph/0305275.

[30] C. Kilic and R. Mahbubani, JHEP **07**, 013 (2004), hep-ph/0312053.

[31] OPAL, G. Abbiendi *et al.*, Eur. Phys. J. **C33**, 173 (2004), hep-ex/0309053.

[32] ECFA/DESY LC Physics Working Group, J. A. Aguilar-Saavedra *et al.*, (2001), hep-ph/0106315.

[33] J. L. Hewett and T. G. Rizzo, Phys. Rept. **183**, 193 (1989).

[34] M. Cvetic and S. Godfrey, (1995), hep-ph/9504216.

[35] T. G. Rizzo, (1996), hep-ph/9612440.

[36] LHC/LC Study Group, G. Weiglein *et al.*, Phys. Rept. **426**, 47 (2006), hep-ph/0410364.

[37] American Linear Collider Working Group, T. Abe *et al.*, (2001), hep-ex/0106057.

[38] S. Riemann, LC-TH-2001-007.

[39] T. G. Rizzo, Phys. Rev. **D55**, 5483 (1997), hep-ph/9612304.

[40] J. L. Hewett and T. G. Rizzo, Contribution to Proc. of Workshop on Physics and Experiments with Linear Colliders, Saariselka, Finland, Sep 9-14, 1991.

[41] M. Dittmar, A.-S. Nicollerat, and A. Djouadi, Phys. Lett. **B583**, 111 (2004), hep-ph/0307020.

[42] F. del Aguila, M. Cvetic, and P. Langacker, Phys. Rev. **D48**, 969 (1993), hep-ph/9303299.

[43] J. L. Hewett and T. G. Rizzo, Phys. Rev. **D45**, 161 (1992).

Chapter 3

Supersymmetry Without Prejudice at the LHC

3.1 Introduction

The LHC has recently begun operations, providing our first direct glimpse of the Terascale in a laboratory setting, and new physics discoveries are widely expected. Supersymmetry (SUSY) is one of the most attractive candidates out of a litany of potential theories beyond the Standard Model (SM) as it contains a natural dark matter candidate, addresses the weak hierachy problem, and provides a framework for unification of the forces [1, 2]. However, evidence for Supersymmetry has yet to be observed [3]; hence it cannot exist in its most fundamental form and must be a broken symmetry. Various mechanisms for the breaking of Supersymmetry have been proposed [4, 5, 6, 7, 8, 9, 10], each predicting a characteristic sparticle spectrum leading to distinctive signatures in colliders and other experiments. Of these, gravity mediated Supersymmetry breaking (mSUGRA) is the most often studied; it contains 5 parameters at the unification scale and thus greatly simplifies the exploration of the vast Supersymmetric parameter space. In particular, most searches for Supersymmetry at the Tevatron [11] and the planned search strategies at the LHC [12] have been designed solely in the context of mSUGRA.

The question then arises of how well mSUGRA describes the true breadth of the

Minimal Supersymmetric Standard Model (MSSM) and its possible collider signatures. It is well-known [13, 14, 15] that the D0 constraints on squark and gluino production do not hold within a broader class of SUSY models and that much lighter sparticles ($\sim$ 150 GeV) can easily evade these searches. This poses a potentially worrisome prospect for the LHC search strategies and their effectiveness needs to be checked on an extended class of SUSY models. This provides the motivation for our work.

In particular, we base our analysis on the recent study published by the ATLAS detector collaboration [12]. Here, the collaboration performed an extensive examination of a set of 7 SUSY benchmark points, all of which are based on mSUGRA, and constructed most of their SUSY search analysis suite from these investigations. In this work, we will simulate the ATLAS search analyses, pass an extensive set of broad-based SUSY models through each search channel, and determine their observability. We believe that the results will be indicative of the robustness of the ATLAS SUSY search analysis suite. In order to perform this test, we follow the analyses as presented by ATLAS in the reference. Numerous, and perhaps improved, SUSY collider search techniques have been discussed in the literature [16, 17] and may be utilized by ATLAS in the future. However, to be concrete we will only employ the analyses described in [12].

We make use of a recent comprehensive bottom-up exploration of the MSSM performed by Berger *et al.*[13]. In this work, no reference was made to theoretical assumptions at the high scale or to the mechanism of Supersymmetry breaking. The theoretical assumptions were minimal and included only CP conservation, Minimal Flavor Violation, that the lightest supersymmetric particle (LSP) be identified with the lightest neutralino and be a thermal relic, and that the first and second sfermion generations be degenerate in mass with negligible Yukawa couplings. Enforcing this minimal list of assumptions results in the pMSSM (phenomenological MSSM) with 19 real weak-scale parameters. A scan of 10^7 points in this 19-dimensional parameter space was performed over ranges chosen to ensure large sparticle production cross sections at the LHC. Each model (or point in the 19-dimensional space) was subjected to a global set of constraints from spectrum requirements, electroweak precision data,

heavy flavor physics, cosmological considerations, and LEP and Tevatron collider searches. Approximately 70,000 models in the pMSSM scan survived all of the restrictions and were found to be phenomenologically viable. (Interestingly, subjecting the seven ATLAS mSUGRA benchmark points to these same constraints results in only one of the points being consistent with the global data set.) A wide variety of properties and characteristics were found in this model sample, with features that imply a very large range of possible predictions for collider signatures.

Specifically, we set up an analysis for each of the 11 search channels studied in the ATLAS CSC book[12] and ensure that we reproduce the CSC results for each of the ATLAS benchmark points in each channel. We will then run the ∼70k pMSSM points of Berger et. al. through each analysis channel and perform a statistical test to ascertain the observability of each model. We will find that several pMSSM models cannot be detected by the ATLAS SUSY analysis suite and we will further examine these special cases and ascertain which characteristics in the sparticle spectrum render then unobservable. In many cases we find that the systematic errors associated with the SM backgrounds are the main cause of the lack of a statistically viable discovery signal and note that a reduction in these errors would greatly improve the likelihood of discovering SUSY. We will also look at a qualitatively different collider signature, that of stable supersymmetric particles. Our model set contains a large number of models with stable sparticles of various identities, and we will evaluate the prospects of observing these stable sparticles at the LHC.

The next section describes the generation of our model set, Section 4.2 discusses our procedure and analysis set-up, Section 3.4 contains our main results, Section 3.5 discusses stable particles in our model set, and our conclusions can be found in Section 3.6.

3.2 Review of Model Generation

In this section we provide a brief overview of our previously performed model generation procedure; full details and all original references are given in Refs.[13, 18, 19].

3.2.1 Parameter scans

In performing our exploration of the 19 soft-breaking parameters of the pMSSM, we first determine the ranges that we scan over for these parameters as well as how their specific values are selected within these ranges. Recall, as discussed above, that these parameters are defined at the TeV scale. In our analysis, we employed two independent scans of the pMSSM parameter space with the ranges being fixed such that large production cross sections for SUSY particles are likely at the 14 TeV LHC. This means that we will have two independent sets of models to examine for LHC SUSY signatures employing the ATLAS analyses. In the model set generated by the first scan, denoted here as the FLAT prior set, 10^7 n-tuples of the (n=)19 parameters were randomly generated, assuming flat priors, where the parameter values were chosen *uniformly* throughout the ranges:

$$\begin{aligned} 100\,\text{GeV} \leq m_{\tilde{f}} \leq 1\,\text{TeV}\,, \\ 50\,\text{GeV} \leq |M_{1,2}, \mu| \leq 1\,\text{TeV}\,, \\ 100\,\text{GeV} \leq M_3 \leq 1\,\text{TeV}\,, \\ |A_{b,t,\tau}| \leq 1\,\text{TeV}\,, \\ 1 \leq \tan\beta \leq 50\,, \\ 43.5\,\text{GeV} \leq m_A \leq 1\,\text{TeV}\,. \end{aligned} \tag{3.2.1}$$

Here the absolute value signs are present to allow the soft-breaking parameters to have arbitrary sign. To generate the models for the second scan, denoted here as the LOG prior set, 2×10^6 n-tuples of the (n=)19 parameters were generated, assuming

log priors for (*only*) the mass parameters with the modified ranges:

$$\begin{aligned} 100\,\mathrm{GeV} \leq m_{\tilde{f}} \leq 3\,\mathrm{TeV}\,, \\ 10\,\mathrm{GeV} \leq |M_{1,2}, \mu| \leq 3\,\mathrm{TeV}\,, \\ 100\,\mathrm{GeV} \leq M_3 \leq 3\,\mathrm{TeV}\,, \\ 10\,\mathrm{GeV} \leq |A_{b,t,\tau}| \leq 3\,\mathrm{TeV}\,, \\ 1 \leq \tan\beta \leq 60\,, \\ 43.5\,\mathrm{GeV} \leq m_A \leq 3\,\mathrm{TeV}\,. \end{aligned} \tag{3.2.2}$$

It is important to note that the parameter $\tan\beta$, being a dimensionless quantity, is still being scanned in a flat prior manner, unlike the other parameters, when we generate this model set. The expanded parameter range in this case allows for some access to both very light as well as some heavy sparticle states that may only be observed at the SLHC. The primary goal of this second scan was to compare these results to those of the flat prior study in order to determine the degree that the resulting model properties depend on the scan assumptions and whether any possible bias was introduced. We found that both scans yield qualitatively similar results, but that the detailed predictions in the two cases can be quantitatively different in several aspects. The physical spectra for the sparticles themselves were generated in all cases using the code SuSpect2.34[20].

3.2.2 Constraints

We now turn to a discussion of the theoretical and experimental constraints that we imposed on the set of models generated from these two scans. Each observable is required to separately lie within the experimental errors; we do not attempt to perform a global fit. We employ the 95% C.L. bounds in all cases, except for the anomalous magnetic moment of the muon and the 5-yr WMAP measurement of the relic density. These special cases are discussed in more detail below.

Theoretical constraints

The theoretical restrictions we included are standard and were applied while generating the sparticle spectrum with the SuSpect code: (*i*) the spectrum must be tachyon free, (*ii*) the spectrum cannot lead to color or charge breaking minima, (*iii*) electroweak symmetry breaking must be consistent, and (*iv*) the Higgs potential is bounded from below. Furthermore, we employed the assumption that (*v*) the WIMP LSP is a conventional thermal relic and is identified as the lightest neutralino. We also imposed the requirement of (*vi*) Minimal Flavor Violation (MFV) [21] at the TeV scale to reduce the impact of Supersymmetry on flavor physics. In this case, the SUSY contributions to flavor physics are mostly controlled by the Yukawa couplings and the CKM matrix.

Constraints from precision measurements

We then imposed experimental constraints from precision electroweak observables, flavor physics, astrophysical measurements, and collider searches for SUSY particles. The code micrOMEGAs2.21 [22, 23, 24, 25, 26] takes the MSSM spectrum output from SuSpect and implements the restrictions arising from a number of precision and flavor measurements: we required that the precision electroweak constraints obtained via possible shifts in the ρ parameter, $\Delta\rho$, as well as the rare decays $b \to s\gamma$ and $B_s \to \mu^+\mu^-$ be consistent with their measured values. Given the current theoretical and experimental uncertainties for the value of the $g-2$ of the muon, we implemented the loose requirement that $(-10 \leq \Delta(g-2)_\mu \leq 40)\cdot 10^{-10}$ in our analysis. In addition to these constraints which are essentially built into the micrOMEGAs2.21 code, we demanded consistency with the measured value of the branching fraction for $B \to \tau\nu$ and required that the ratio of first/second to the third generation squark soft breaking masses (of a given charge and helicity) differ from unity by no more than a factor of ~ 5 to satisfy the bounds from meson-anti-meson mixing.

Dark matter constraints

We employed two constraints that arise from the Dark Matter (DM) sector: first, we required that the calculated DM relic density not exceed the limit obtained from the 5 year WMAP measurement, thus allowing for the possibility that the DM sector consists of multiple components besides the lightest neutralino.[1] Second, we imposed the search constraints from the DM direct detection experiments, allowing for a factor of 4 uncertainty in the calculation of the cross section from possible variations in the input parameters and matrix elements. These calculations were also performed with the micrOMEGAs2.21 code.

Tevatron constraints

Collider searches, of course, play an important role in placing constraints on the pMSSM parameter space. Since the Tevatron searches for SUSY are closer in spirit to the LHC analysis we present below, we discuss them in more detail than the corresponding investigations from LEP. We first consider the restrictions imposed on the squark and gluino sectors arising from the null result of the multijet plus missing energy search performed by D0 [11] that is based on mSUGRA. In our study, we generalized their analysis to render it model independent. For each of our pMSSM models, we computed the NLO SUSY cross sections for squark and gluino production using PROSPINO2.0 [27, 28, 29, 30, 31, 32]. The decays for these sparticles were computed via SDECAY/HDECAY (*i.e.*, SUSYHIT1.1)[33] to obtain the relevant decay chains and branching fractions and these results were then passed to PYTHIA6.4[34] for hadronization and fragmentation. We then used PGS-74[35] to simulate the D0 detector and impose the kinematic cuts for the analysis; PGS-74 was tuned to reproduce the results and efficiencies for the three benchmark mSUGRA points employed by D0 in their published multijet study. For an integrated luminosity of 2.1 fb^{-1}, we found that the 95% CL upper limit on the number of signal events from combining all of the production channels was 8.34, where we employed the statistical method of Feldman and Cousins[36]. Models with event rates larger than this were then removed

[1] Note that although we did *not* require the WMAP bound to be saturated this condition is satisfied in a reasonable subset of our resulting models.

from further consideration. Interestingly, light squarks and gluinos (masses of order 150-200 GeV) with small mass splittings with the LSP survive this analysis[14, 15].

Analogously, we employed constraints from the CDF search for trileptons plus missing energy[37], which we also generalized to the pMSSM using essentially the same method as in the jets plus plus missing energy analysis described above. Here, we employed a CDF tune for PGS-74 which we obtained by reproducing the CDF benchmark point results. We used the leading order cross section together with a universal K-factor of 1.3 to mimic the full NLO cross section. Specifically in this case, we only made use of the '3 tight lepton' analysis from CDF as it is the easiest to implement with PGS-74. The 95% CL upper bound on a possible SUSY signal in this channel was then found to be 4.65 events assuming a luminosity of 2.02 fb^{-1} as used in the CDF analysis. Again, pMSSM parameter sets leading to larger event rates were dropped from the remainder of our analysis.

In order to satisfy the large number of stop and bottom searches at the Tevatron[38, 39, 40, 41, 42], we simply required that the masses of the lightest stop and sbottom be larger than that of the top quark, $\simeq 175$ GeV. However, an examination of the various sparticle spectra *a posteriori* reveals that this cut makes very little impact on our final model set.

Both CDF[43] and D0[44] have placed limits on the direct production of heavy stable charged particles. In our analysis we employed the stronger D0 constraint which can be taken to have the form $m_{\chi^+} \geq 206|U_{1w}|^2 + 171|U_{1h}|^2$ GeV at 95% CL in the case of chargino production. Here, the matrix U determines the Wino/Higgsino content of the lightest chargino and was used to interpolate between the separate purely Wino or Higgsino results quoted by D0. This resulted in a *very* powerful constraint on the pMSSM since chargino-LSP mass degeneracies are common in our model sample, particularly when the LSP is nearly a pure Wino or Higgsino or a combination of these two cases.

LEP constraints

We imposed a large number of constraints arising from the direct searches for both SUSY partners and the extended MSSM Higgs sector from LEP data. As for the

Tevatron, most of the LEP analyses have been carried out in the mSUGRA framework and thus need careful reconsideration when they are extended to cover the more general pMSSM scenario considered here. For brevity, we will only mention the details of a few of these here, with a complete discussion of all these constraints being given in our previous work[13]. Two of these restrictions arise from Z-pole data: (i) we required that the Higgs boson as well as all new charged particles have masses in excess of $M_Z/2$ and also that all new (detector) stable charged particles have masses in excess of 100 GeV[45]. Furthermore, (ii) we required that Z decays into stable and long-lived neutralinos not contribute more than 2 MeV[46] to the invisible width of the Z boson.[2]

ALEPH[47] has placed a lower limit of 92 GeV on the light squark masses, assuming that the gluino is more massive than the squarks, via their decay to a jet+LSP (*i.e.*, jet + missing energy) provided that the mass difference between the squark and the LSP (Δm) is $\geq$ 10 GeV to avoid very soft jets. We employed this constraint directly, including the Δm cut. For light sbottoms, the same sort of decay pattern results in a lower bound of 95 GeV on their mass. Lower bounds have been placed[48] on the masses of right-handed sleptons decaying to leptons plus missing energy of $m \gtrsim 100(95, 90)$ GeV for the selectron(smuon,stau). This is, however, only applicable if the slepton masses are at least a few percent larger than that of the LSP, otherwise the final state leptons will again be too soft. Our analysis allows for the appearance of this small mass gap. These constraints are also applicable to left-handed sleptons provided the corresponding Wino $t-$channel exchange contribution is not very important, an assumption made in our analysis. An analogous situation applies to chargino production. If the LSP-chargino mass splitting is $\Delta m > 2$ GeV, a direct lower limit of 103 GeV on the chargino mass is obtained from LEPII data. However, if this splitting is $\Delta m < 2$ GeV, the bound degrades to 95 GeV, *provided* that also $\Delta m > 50$ MeV, otherwise the chargino would appear as a stable particle in the detector and would then be excluded by the stable particle searches discussed above. In the case where the lightest chargino is dominantly Wino, this limit is found

[2]We note that for the range of sfermion mass soft breaking parameters we consider, Z decay to pairs of sneutrinos is not kinematically allowed so that this final state cannot contribute in any way to the invisible width.

to be applicable only when the electron sneutrino is more massive than 160 GeV.

For constraints on the Higgs sector, we imposed the five sets of bounds on the MSSM Higgs sector masses and couplings provided by the LEP Higgs Working Group[49]. To do this, we employed the SUSY-HIT routine, recalling that the uncertainty on the calculated mass of the lightest Higgs boson is approximately 3 GeV[50] as determined by SuSpect.

Surviving models

After all of these constraints were imposed, we found that $\sim 68.5 \cdot 10^3$ models out of our original sample of 10^7 pMSSM points in the flat prior set satisfied all of the restrictions. In the log prior sample of $2 \cdot 10^6$ pMSSM points, only $\sim 2.8 \cdot 10^3$ models survived the same constraints. As mentioned above, the properties and characteristics of the surviving sets of models from the two scans are qualitatively similar. We will now examine the production of these $\sim 71.3 \cdot 10^3$ viable pMSSM models at the LHC considering the two model sets independently. We remind the reader that we refer to each of these points in the pMSSM parameter space as a model.

A wide variety of properties and characteristics were found in this 70k model sample. In some instances, surprisingly light sparticles (*e.g.*, $\sim 180\,\mathrm{GeV}$ squarks and gluinos) are still allowed by the data. The most favored identity of the next-to-lightest supersymmetric particle (nLSP) was the lightest chargino, followed by the second lightest neutralino. However, ten other sparticles (including the right-handed selectron, the gluino and the up squark) can also play the role of the nLSP with roughly equal probabilities. The mass splitting between the LSP and nLSP, a crucial parameter for collider signals, was found to have a large range spanning seven orders of magnitude from approximately 100 keV to 100's of GeV. Over 1100 distinct classification patterns[51] were found for the content and ordering of the four lightest sparticles in the spectrum. These features imply a very large range of possible predictions for collider signatures within the pMSSM.

3.3 Analysis Procedure for Inclusive SUSY Production at the LHC

As discussed in the Introduction, the single, most important goal of this study is to explore how well the inclusive SUSY searches formulated by the ATLAS collaboration, designed with mSUGRA in mind, perform when they are applied to the larger and much more general pMSSM parameter space. To that end, we attempt to follow these analyses as presented by ATLAS itself in detail in Ref.[12] as closely as possible. The justification for the choices of specific analysis cuts, the size and nature of SM backgrounds and the associated systematics as well as the use of the statistical tests for discovery employed here are the *same* as those employed by ATLAS and are thus all given and discussed in detail in this reference. These are necessary choices if we are to make a direct comparison to the ATLAS mSUGRA study.

In particular, we examine the eleven search channels as detailed by ATLAS in this reference: at least 4(2) jets + $E_T^{\rm miss}$ [4(2)j0l], at least 4(3,2) jets + exactly one lepton + $E_T^{\rm miss}$ [4(3,2)j1l], opposite-sign dileptons + at least 4 jets + $E_T^{\rm miss}$ [OSDL], same-sign dileptons + at least 4 jets + $E_T^{\rm miss}$ [SSDL], three leptons + at least one jet + $E_T^{\rm miss}$ [3lj], three leptons + $E_T^{\rm miss}$ inclusive [3lm], at least one τ + 4j + $E_T^{\rm miss}$ [τ], and at least 4 jets with at least two b-tags + $E_T^{\rm miss}$ [b]. Here, the term listed in brackets for each channel is the 'nickname' that we will use throughout the paper for that analysis. We considered 85 SUSY production processes that contribute to these 11 signatures.

In order to perform our analysis, we must first determine the size and properties of the SM backgrounds to the various analysis signatures listed above. To this end, we obtained more details of the results and distributions for the SM backgrounds that were generated by ATLAS itself and was presented in Ref. [12] from the ATLAS SUSY Group [52]. This essentially allowed us to directly employ the ATLAS computed backgrounds in our analysis and we did not need to generate any of the SM background ourselves. Provided with these backgrounds we were thus able to perform a better direct comparison of our results with the ATLAS mSUGRA studies and this permitted us to concentrate on generating the expected signal rates for each

of these eleven searches for all of the parameter space points in our $\sim$ 71k pMSSM model sample.

It is worth noting that these cuts will most likely change as a function of luminosity in order to maximize the search reach. In addition, other search variables, such as M_{T2} and α_T, have already been employed by ATLAS and CMS in analyzing their first 35 pb^{-1} data sample [53, 54], and other new variables are likely to be invented (such as the Razor [55] search). These will likely increase the experiments' sensitivity to SUSY production.

3.3.1 Generation of the Signal Events

Several steps were employed in the generation of the signal events for the ATLAS search strategies for our set of pMSSM models. First, the SUSY spectra and corresponding sparticle and Higgs boson decay tables were generated using a modified version of SUSY-HIT. As phase space issues can be very important in our model set, due to the large number of sparticle near-degeneracies, our modifications included the incorporation of the light quark (u,d,s,c) and lepton (e and μ) masses in the calculation of branching fractions and lifetimes for the various sparticles. For two body decays, we implemented the expressions for the decay with the masses included, while for three-body decays, we only modified the phase-space cutoff to take into account the mass effects. We note that in the case of the light quarks, the hadronization products of the quarks have significantly higher masses than the corresponding bare masses of the quarks. We therefore included the mass of the lightest meson of the appropriate type in the relevant phase space cut-offs. Since it is not uncommon for the mass splitting between $\tilde{b}_1$ and the LSP to be below the B meson mass, $\simeq$ 5.3 GeV, we also included the 1-loop processes $\tilde{b}_1 \rightarrow (d, s)$+LSP in the decay tables. Also, since there are many models that have charginos which are close in mass to the LSP, we included the full expressions for the chargino decays in the $e\nu$, $\mu\nu$, and 1-3 pion plus LSP final states [56, 57]. These were employed for mass splittings below 1 GeV.

We also included CKM-suppressed decays of sbottoms, which, as discussed again

later, allowed for the decay of bottom squarks with close mass splittings with the LSP. Another set of modifications was necessary to correctly include four-body final states in the decays of stop squarks with small mass splittings. SUSY-HIT includes formulae for the decay $\tilde{t} \to \tilde{\chi}_1^0\ b\ f\ f'$, where f, f' are assumed to be massless fermions. We modified the code to compute the decay width to a specific pair of fermions, including phase-space cutoffs, using the appropriate fermion masses.

In addition, in some cases, the QCD corrections to particular partial widths, most commonly for stop and sbottom decays to Higgs/gauginos and heavy quarks, were turned off as they led to negative branching fractions. This occurred due to a poor choice of scale and/or a lack of resummation of large QCD correction terms. Yet another set of corrections to the decay tables was necessary in order to resolve PYTHIA errors that occurred; see the discussion below for more details.

Next, the NLO cross sections for the ~ 85 SUSY production processes we considered were computed using a modified version of PROSPINOv.2.1 [28, 29, 30, 31, 32] that avoided potentially negative K-factors due to sign issues associated with the neutralino masses. This modification is now implemented in the current version of the code. Processes involving τ-sneutrinos or charged Higgs production are not supported by the current version of Prospino, so their K-factors are not included. We note that these processes tend to have very small cross sections at the LHC, so this has a negligible effect on our results. We employed the CTEQ6.6M parton distribution functions [58] when performing these calculations, as well as in our event generation.

PYTHIAv.6.418 was employed for event generation, fragmentation/showering, and hadronization. In order to apply the K-factors calculated with PROSPINO, we generated individual event samples for each of the 85 SUSY production processes and scaled each by its K-factor. In some subset of the models, problems with PYTHIA arose, *e.g.*, it could not handle the final state hadronic fragmentation in the decays of colored sparticles with small mass splittings. To address this, we implemented an additional modification to the decay tables. For any sparticle with an unboosted decay length longer than ~ 20 m, so that it does not decay within the detector, we set the decay width to zero so that PYTHIA treats the sparticle as absolutely stable and does not attempt the decay. In addition, we attempted to force a larger decay

width in the case of any colored sparticle with a width less than 1 GeV to alleviate issues with hadronizing long-lived colored states, but this exacerbated the problem and led to more frequent serious PYTHIA errors and so this approach was dropped.

We are left with roughly 1% of our pMSSM model sample where PYTHIA errors occur that are serious enough to lead to a PYSTOP, *i.e.*, a halt in the event generation. In these models, the production cross sections can thus be seriously underestimated. Therefore, in the remainder of this work, these "PYSTOP models" are generally excluded from our results, except where noted otherwise. Note that since this is only a very tiny fraction of the models we consider, dropping this small set has essentially no impact on the results we quote below. This was explicitly verified for all of the ATLAS analyses we consider below for both flat and log prior model samples.

Events were then passed through an ATLAS-tuned version of PGS-74 [35] for fast detector simulation, employing the kinematic cuts for the eleven inclusive search analyses described in detail by ATLAS in Ref. [12] and given below. Here, we matched as closely as possible the set of definitions that ATLAS employed [12] for their final state 'objects' such as jets, leptons, τ's, b's and $E_T^{\rm miss}$. In particular, we replaced the default PGS-7 object isolation routine with an analysis-level routine which mimics as much as possible the published ATLAS object identification and isolation procedure.

3.3.2 Analysis Cuts

In the interest of completeness, we here provide a list of the full set of kinematic cuts for each analysis channel that we employ as given by ATLAS[12]:

- 4-jet + $E_T^{\rm miss}$:

  1. At least 4 jets with $p_T > 50$ GeV, at least one of which has $p_T > 100$ GeV.
  2. $E_T^{\rm miss} > 100$ GeV and $E_T^{\rm miss} > 0.2 M_{\rm eff}$.
  3. Transverse sphericity $S_T > 0.2$.
  4. $\Delta\phi({\rm jet}_{1,2,3} - E_T^{\rm miss}) > 0.2$.
  5. Reject events with an e or a μ.

6. $M_{\text{eff}} > 800$ GeV.

- 2-jet + E_T^{miss}:
  1. At least 2 jets with $p_T > 100$ GeV, at least one of which has $p_T > 150$ GeV.
  2. $E_T^{\text{miss}} > 100$ GeV and $E_T^{\text{miss}} > 0.3 M_{\text{eff}}$.
  3. $\Delta\phi(\text{jet}_{1,2} - E_T^{\text{miss}}) > 0.2$.
  4. Reject events with an e or a μ.
  5. $M_{\text{eff}} > 800$ GeV.
- 1 lepton + 4 jets + E_T^{miss}:
  1. Exactly one isolated lepton with $p_T > 20$ GeV.
  2. No additional leptons with $p_T > 10$ GeV.
  3. At least 4 jets with $p_T > 50$ GeV, at least one of which has $p_T > 100$ GeV.
  4. $E_T^{\text{miss}} > 100$ GeV and $E_T^{\text{miss}} > 0.2 M_{\text{eff}}$.
  5. Transverse sphericity $S_T > 0.2$.
  6. Transverse mass $M_T > 100$ GeV.
  7. $M_{\text{eff}} > 800$ GeV.
- OSDL + 4 jets + E_T^{miss}:
  1. Exactly two opposite-sign leptons with $p_T > 10$ GeV.
  2. At least 4 jets with $p_T > 50$ GeV, at least one of which has $p_T > 100$ GeV.
  3. $E_T^{\text{miss}} > 100$ GeV and $E_T^{\text{miss}} > 0.2 M_{\text{eff}}$.
  4. Transverse Sphericity, $S_T > 0.2$.
- Trilepton + jet + E_T^{miss}:
  1. At least three leptons with $p_T > 10$ GeV.
  2. At least 1 jet with $p_T > 200$ GeV.

- Trilepton + E_T^{miss}:
  1. At least three leptons with $p_T > 10$ GeV.
  2. At least one OSSF dilepton pair with $M > 20$ GeV.
  3. Lepton track isolation: $p_{T,\text{trk}}^{0.2} < 1$ GeV for electrons and < 2 GeV for muons, where $p_{T,\text{trk}}^{0.2}$ is the maximum p_T of any additional track within a $R = 0.2$ cone around the lepton.
  4. $E_T^{\text{miss}} > 30$ GeV.
  5. $M < M_Z - 10$ GeV for any OSSF dilepton pair.
- τ + jets + E_T^{miss}:
  1. At least 4 jets with $p_T > 50$ GeV, at least one of which has $p_T > 100$ GeV, and at least one τ.
  2. $E_T^{\text{miss}} > 100$ GeV.
  3. $\Delta\phi(\text{jet}_{1,2,3} - E_T^{\text{miss}}) > 0.2$.
  4. No isolated electrons or muons.
  5. At least one τ must have $p_T > 40$ GeV and $|\eta| < 2.5$.
  6. $E_T^{\text{miss}} > 0.2 M_{\text{eff}}$.
  7. $M_T > 100$ GeV, where M_T is the transverse mass of the hardest τ and E_T^{miss}.
- b jets + E_T^{miss}:
  1. At least 4 jets with $p_T > 50$ GeV.
  2. At least one of which has $p_T > 100$ GeV.
  3. $E_T^{\text{miss}} > 100$ GeV.
  4. $E_T^{\text{miss}} > 0.2 M_{\text{eff}}$.
  5. Transverse sphericity $S_T > 0.2$.
  6. At least 2 jets tagged as b jets.

7. $M_{\rm eff} > 1000$ GeV.

In addition to the 4j1l analysis we also considered 3(2)j1l analyses where the cut on the leading jet is raised to $p_T > 150$ GeV, the second(and third) jet must have $p_T > 100$ GeV, and the $E_T^{\rm miss}$ cut is harder: $E_T^{\rm miss} > \max(100 \text{ GeV}, 0.25(0.3)M_{\rm eff})$.

Furthermore, in addition to the OSDL analysis there is also an SSDL analysis with identical kinematic cuts, except that, of course, the two leptons must have the same charge and they have a somewhat harder cut: $p_T > 20$ GeV. Also in this case, the cut on transverse sphericity is dropped.

3.3.3 Statistical Procedure

In the analysis below we follow the statistical treatment of signal and backgrounds as employed by ATLAS[12] as closely as possible in determining the significance of the signal over background for each pMSSM model in the eleven different search channels. For completeness, the details of the ATLAS approach that we follow will be given here. To this end, we allowed for a 50% systematic uncertainty in the calculation of both the SM QCD and electroweak backgrounds in order to match the ATLAS analyses. However, we also considered a reduction to the case of 20% systematic errors associated with these SM backgrounds. Such a reduction, as was discussed by ATLAS, may be possible in the future using both the data itself as well as improved theoretical calculations of SM processes. Interestingly, we note that ATLAS found that these SM backgrounds for SUSY are *completely dominated* by contributions from electroweak sources as opposed to those arising from pure QCD. As we will discuss below, the former choice of background uncertainty led to better agreement with the ATLAS results for their mSUGRA benchmark models, but the latter case will be seen to substantially increase the coverage of the pMSSM model parameter space and is something that may be obtainable in the future.

Directly following the ATLAS study, we compute the signal significance as described below. We first total all background and signal events above the $M_{\rm eff}$ cut that is specific to each analysis. We then compute the probability p that the background fluctuates by chance to the total number of measured events or above, assuming

that the systematic error on the background is Gaussian and the statistical error is Poissonian. This means

$$p = A \int_0^\infty db\, G(b; N_b; \delta N_b) \sum_{i=N_{\rm data}}^{\infty} \frac{e^{-b} b^i}{i!} \,, \tag{3.3.1}$$

where N_b is the number of background events and δN_b is the associated systematic error on this number, while $N_{\rm data} = N_b + N_{\rm signal}$ is the total number of events above the $M_{\rm eff}$ cut. G is a Gaussian distribution and A is a normalization factor ensuring that the probability that the background fluctuates to any nonnegative integer is one; therefore $A = p(N_{\rm data} = 0)^{-1}$. The significance Z_n, is then given by

$$Z_n = \sqrt{2}{\rm erf}^{-1}(1 - 2p) \,. \tag{3.3.2}$$

3.3.4 Comparison with ATLAS Benchmark Models

We must first verify that our analysis for each signature can be trusted. To this end, we determine whether we can reproduce the results[12] obtained by ATLAS for their mSUGRA benchmark points (labeled here as SU1, 2, 3, 4, 6, 8.1 and 9). For each point, the ATLAS collaboration generated a large number of signal events and scaled to a luminosity of 1 fb^{-1}. We followed a similar approach in making our comparisons, generating 10 fb^{-1} of events for each ATLAS benchmark model and then scaling down to 1 fb^{-1}. Due to computing time restrictions, we put a cap of 10k generated events on any one of the 85 SUSY production processes for each benchmark model. In addition, at least 100 events were generated in every channel in order to properly evaluate potentially small cross sections; these events were then appropriately rescaled.

Here it is important to note that our SUSY signal generation, as described above, necessarily differs in detail from that performed by ATLAS. In contrast to our inclusive SUSY analysis, ATLAS determined their mSUGRA spectra and performed their sparticle decay table calculations using ISASUGRA versions 7.64-7.71. They used PROSPINOv2.0.6 [27, 28, 29, 30, 31, 32] and the CTEQ6M parton distribution

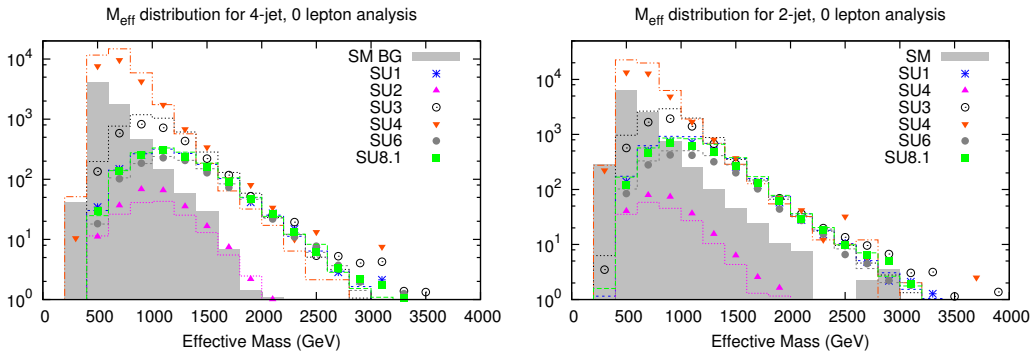

Figure 3.1: The $M_{\rm eff}$ distribution for the 4(2) jet, 0 lepton analysis on the left(right). The data points represent our analysis, while the color coded lines are the results from the ATLAS study[12].

functions [59] to obtain the NLO results for strong interaction processes, *i.e.*, squark and gluino pair production as well as squark-gluino associated production. NLO corrections were not included for the other channels. Event generation, fragmentation/showering, and hadronization were performed using HERWIG [60, 61, 62] and the results were then passed through the full ATLAS GEANT detector simulation.

The results of our comparison benchmark study, as can be seen in Figures 3.1-3.3, suggest that we are indeed able to faithfully reproduce those obtained by ATLAS in the case of their mSUGRA benchmark models for all of the various inclusive analyses. The one possible exception occurs in the tails of the $M_{\rm eff}$ distributions, where statistics are poor and large fluctuations are to be expected. This is an important check to perform, and pass, before we embark on computing these signature channels for our large model set.

We should also note that the agreement between our τ analysis results and that of ATLAS is somewhat suspect because of an issue with the PGS-74 τ fake rate and efficiency. We find that this fake rate is much higher, and the efficiency much lower, than the values quoted for the ATLAS τ reconstruction algorithm. The agreement between our results and those of ATLAS for this analysis are therefore due to some compensation between these two factors. In what follows, we will generally show results without the τ analysis, as we believe its validity is in question.

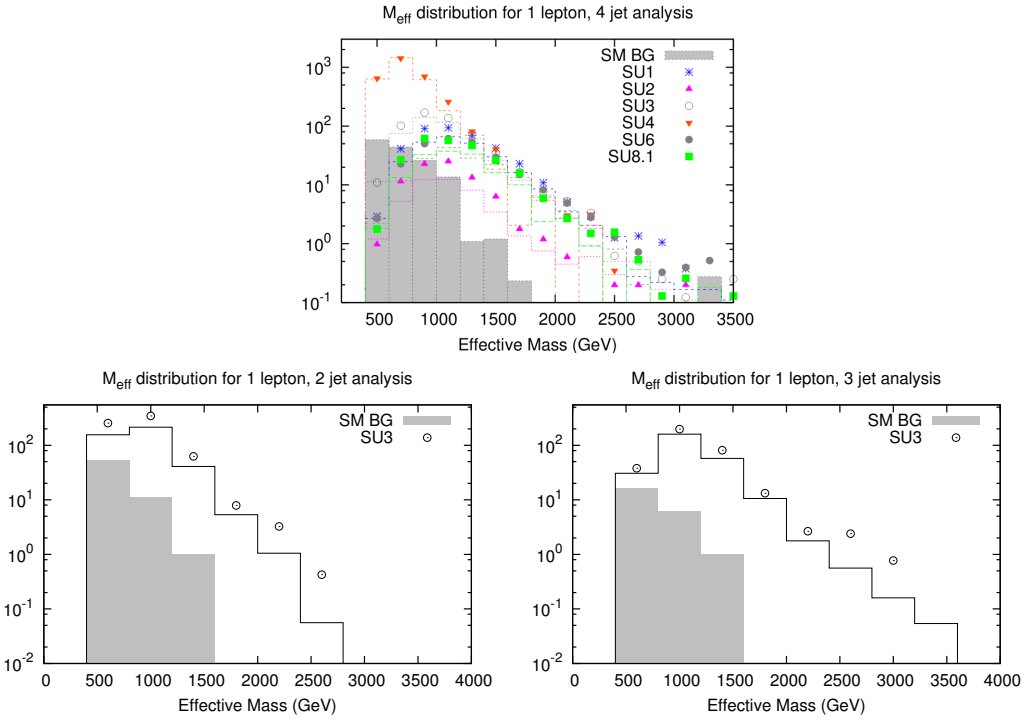

Figure 3.2: The M_{eff} distribution for the 1 lepton, 4(2,3) jet analysis on the top(bottom left, bottom right). The data points represent our analysis, while the lines are the results from the ATLAS study[12].

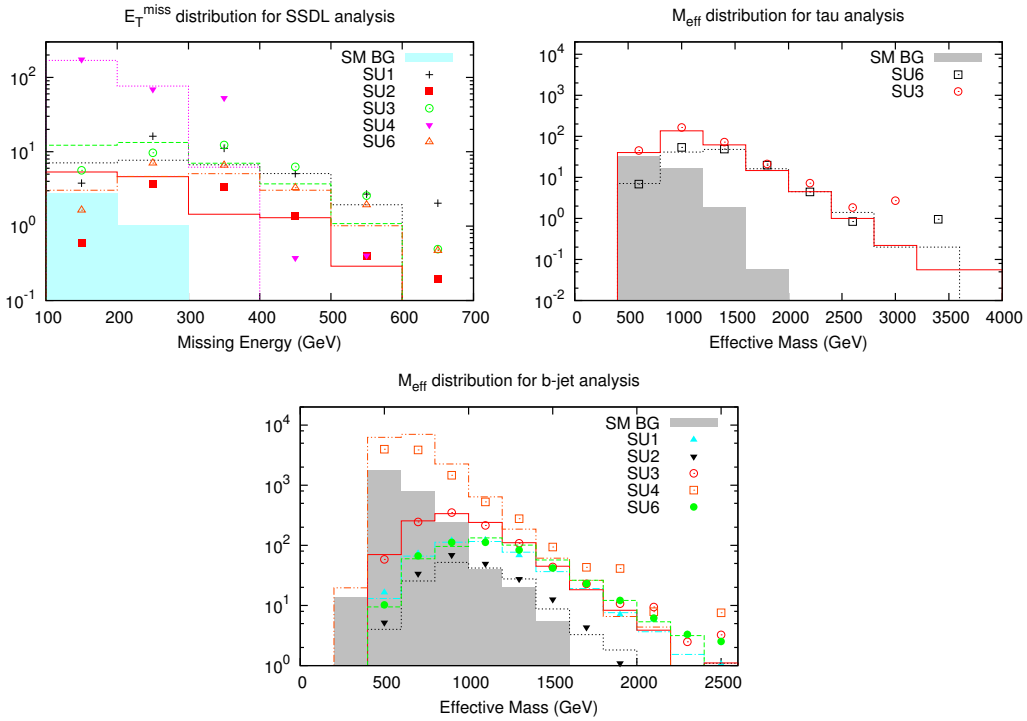

Figure 3.3: The M_{eff} (E_T^{miss} for SSDL) distribution for the same-sign dilepton(τ,b-jet) analysis on the top(bottom left, bottom right). The data points represent our analysis, while the lines are the results from the ATLAS study[12].

For easy comparison, in Table 3.1 we present a comparison of the number of events passing the $M_{\rm eff}$ cut for each analysis.

Having verified the reliability of our event generation, detector simulation, and data analysis procedure, the last ingredient to check is the statistical procedure described above. The primary issue is how large a systematic error one should assign to the SM background due to theoretical uncertainties associated with, *e.g.*, higher order perturbative calculations. In [12], ATLAS assigns a 50% error to QCD backgrounds and 20% to electroweak backgrounds, and combines these two errors in quadrature. What is important, however, is that the systematic error represent the true uncertainty in these background predictions at the time of LHC data analysis. It is likely that the theoretical uncertainties on the computation of relevant electroweak backgrounds will continue to be quite high, especially for processes with additional jets, and could easily be of order 50%[63]. We therefore adopt a 50% systematic error on both electroweak and QCD backgrounds as a conservative default assumption for most of our results that follow. In many cases, however, we will also show for comparison the effect of reducing the background systematic error to 20% for both background samples. We will return to this point of discussion in more detail below.

3.4 Results: ATLAS Inclusive MET Analyses

Now that we have convinced the reader that we can do a reasonable job at reproducing the analyses performed by ATLAS for their mSUGRA benchmark points, we turn to a discussion of the corresponding analyses for our 71k pMSSM model set.

3.4.1 Global Results

We first consider some global results. The first, and most important, question we address is what fraction of the two pMSSM model sets would be discovered by each of the various inclusive ATLAS analyses assuming an integrated luminosity of 1 fb^{-1}. This will give us a good feel for how good a job the various ATLAS MET analyses, designed for mSUGRA, will do at discovering SUSY in the more general pMSSM

Analysis	Model	Us	ATLAS
4j0l	SU1	1228.8	1144.7
4j0l	SU2	131.6	197.8
4j0l	SU3	3349.1	2430.4
4j0l	SU4	8511.4	7260.5
4j0l	SU6	955.8	912.0
4j0l	SU81	1284.1	1154.1
2j0l	SU1	3195.5	2479.4
2j0l	SU2	90.4	138.1
2j0l	SU3	6431.8	4590.8
2j0l	SU4	9418.1	8088.7
2j0l	SU6	1986.6	1566.7
2j0l	SU81	3067.0	2324.4
1l4j	SU1	232.3	334.9
1l4j	SU2	39.6	74.8
1l4j	SU3	363.6	458.7
1l4j	SU4	895.8	962.0
1l4j	SU6	147.9	221.5
1l4j	SU81	136.3	232.1
1l2j	SU3	262.3	418.6
1l3j	SU3	230.6	298.0
SSDL	SU1	28.5	40.9
SSDL	SU2	13.0	9.7
SSDL	SU3	37.4	37.0
SSDL	SU4	251.8	297.5
SSDL	SU6	16.8	20.9
tau	SU3	259.1	315.2
tau	SU6	118.9	135.5
b	SU1	375.7	392.2
b	SU2	137.6	165.6
b	SU3	764.8	766.3
b	SU4	3179.2	2462.9
b	SU6	435.9	396.8

Table 3.1: The number of events above the M_{eff} cut for each benchmark model and each analysis, as computed by us and by ATLAS.

Analysis	Flat priors	Log priors
4j0l	88.3	48.2
2j0l	87.6	47.4
4j1l	41.7	18.4
3j1l	64.1	36.6
2j1l	62.9	33.5
OSDL	6.1	3.8
SSDL	14.8	8.9
3lj	13.5	8.6
3lm	2.7	2.9
τ	83.5	44.0
b	74.0	42.9

Table 3.2: The percentage of the pMSSM model set that passes each analysis, for the flat and log prior model sets. This assumes a systematic error of 50% on the SM background.

parameter space. The answer to this question for both the flat and log prior model samples can be found in Table 3.2. Note that throughout this paper, when we say a model "passes" a given analysis, we mean the significance S (Z_n in the ATLAS notation) satisfies $S \geq 5$. Similarly, we say the model is missed or 'fails' if $S < 5$.

This Table shows us that the ATLAS MET analyses do a very reasonable job at probing the more general pMSSM parameter space and that some searches perform better at this than do others. Specifically, here in this Table we observe a number of interesting results: (i) The ATLAS search capabilities for the flat and log prior samples are different. Clearly, we see that a greater fraction of our pMSSM model points are observable in each of the analyses in the case of flat priors than in the case of log priors; there are two obvious reasons for this result. First, in the case of the log prior sample, the sparticle spectra generally extend out to far larger masses, ~ 3 TeV, rendering them less kinematically accessible at the LHC. Second, the models generated by the log prior scan tend to have mass spectra which are somewhat compressed, *i.e.*, more sparticles lie in a given mass interval, making it in principle somewhat more difficult to produce trigger particles with sufficient E_T to pass the various analysis cuts. We will discuss this issue further below.

(*ii*) The (2,4)j0l analyses are, overall, found to be the most powerful of the set of MET analyses in the sense that they lead to a discovery for the greatest fraction of our model points for either prior set. We note that the 4j0l analysis is found to perform only slightly better than the 2j0l one for both sets of priors when the background systematic error is taken to be 50%. This is not overly surprising as ATLAS also found the 4j0l analysis to be the most powerful in the case of mSUGRA [12] at $\sqrt{s} = 14$ TeV. In comparison to our results, ATLAS found that for mSUGRA models the reach of the 2j0l analysis was much more degraded with respect to the 4j0l case than that found here.[3]

(*iii*) The (2,3,4)j1l channels do not play as important a role in the present study as they did for ATLAS in their analysis of the mSUGRA parameter space. ATLAS determined that these three searches were all found to give a somewhat comparable discovery reach in their coverage of the $m_0 - m_{1/2}$ plane. Here we see that the (2,3)j1l analyses are the relatively more powerful ones in this set of single lepton searches, but are still somewhat degraded in relative importance in comparison to the coverage provided by the (2,4)j0l channels. Of course, these two classes of signatures provide complementary coverage of most of the model set since the (4,2)j0l search requires the *absence* of leptons.

(*iv*) The τ analysis appears to provide almost as large a reach as do the (2,4)j0l channels; here we must recall the warning from the previous section that PGS-7 has simultaneously a low τ efficiency and a high fake rate. It is thus likely that the model coverage offered by this channel is somewhat overestimated. However, we note that for large $\tan\beta$, ATLAS found the τ analysis to be a reasonably powerful channel in the case of mSUGRA.

(*v*) Neither the SSDL nor the OSDL searches do particularly well at detecting many models; this is primarily due to the relatively small number of dilepton final states in our model sample. We will return to this issue further below. The 3lj and 3lm analyses are also seen to provide poor model coverage (as might then be expected due to the low number of final state leptons). The less inclusive 3lj channel appears

[3]We remind the reader that these two analyses are not completely mutually exclusive since they are actually requiring *at least* 4j and 2j, respectively. ATLAS typically found that $\sim 35\%$ of their 2j0l sample also appeared in the corresponding 4j0l sample [12].

to do somewhat better than the more inclusive 3lm case, most likely due to reduced SM background.

What are the reasons that the ATLAS SUSY search analysis channels fail to observe the full pMSSM model sample? One reason could be the rather low luminosity, 1 fb^{-1}, assumed in this study. However, recall that we need to overcome not only the possible low statistics available in the signal channel but also the large systematic error associated with the uncertainties in the SM backgrounds. If these are large, as we'll see below is the case for the 4j0l and 2j0l analyses, then increasing the integrated luminosity will actually be of minimal use and in such circumstances it is more important to get a better handle on the size of the backgrounds from either direct measurements or refined theoretical calculations. To address the issue of how useful increasing the integrated luminosity would be for the cases at hand, we display in Table 3.3 our results (analogous to those in Table 3.2 above) for an integrated luminosity of 10 fb^{-1} while maintaining a 50% systematic error on the SM backgrounds. Clearly, for all analyses, and for both flat and log priors, the fraction of models that could be discovered increases. However, in most cases this increase is seen to be quite modest (in particular, for the (2,4)j0l channels) compared to what one might expect, although some channels show a more significant improvement than others. Although increased luminosity is always helpful to some extent, many pMSSM models are clearly missed for physics reasons and not just due to insufficient statistics; certainly some of this is due to the large uncertainties in the SM backgrounds.

3.4.2 Impact of Background Uncertainties

We now further quantify the effect of systematic uncertainties on the observability of a SUSY signal. Figure 3.4 shows how the significance of several of the ATLAS $E_T^{\rm miss}$ searches will scale (in the Gaussian limit) when the integrated luminosity is increased from 1 fb^{-1} to 10 fb^{-1} as a function of the systematic error on the associated SM backgrounds. Here we see that for channels with large backgrounds, significant improvement in the signal significance is prevented by sizable systematic errors when the luminosity is increased by a factor of 10, *i.e.*, analyses which have large SM

Analysis	Flat priors	Log priors
4j0l	88.6	48.1
2j0l	87.8	47.4
4j1l	44.9	20.4
3j1l	70.9	46.0
2j1l	68.4	40.5
OSDL	6.7	4.2
SSDL	25.5	15.9
3lj	17.4	11.1
3lm	2.9	3.0
τ	86.5	45.6
b	76.9	44.6

Table 3.3: Same as Table 3.2 but for an integrated luminosity of 10 fb^{-1}.

backgrounds lead to searhes which are already essentially *systematics dominated* at luminosities of order 1 fb^{-1}. In particular, we note that substantial gains in significance for the (4,2)j0l channel are not possible unless the associated systematic errors are substantially reduced. This is one of the main reasons why a significantly larger fraction of our models are not captured by the most powerful (4,2)j0l analyses when the luminosity is increased. We also see that analyses with lower SM backgrounds, however, are more statistics limited and will find their search reaches improved as the intergrated luminosity increases.

We can understand these results more clearly by examining Table 3.4 which shows the number of expected background events for each of the MET analyses assuming an integrated luminosity of 1 fb^{-1}. This table also shows the corresponding number of signal events required to reach the $S = 5$ level for each channel assuming a systematic error of 50(20)% in the estimation of the associated background. Here we clearly see that channels with a larger number of expected background events benefit the most from a reduction of the corresponding background systematic error, while the reverse is true for analyses with smaller backgrounds.

Correspondingly, the number of signal events required to reach the $S = 5$ level for each of the analyses is shown as a function of the corresponding background

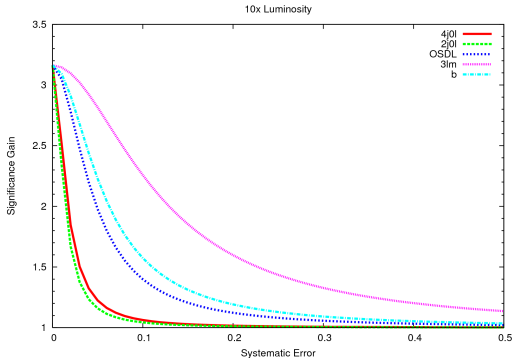

Figure 3.4: The relative gain in significance due to a tenfold increase in integrated luminosity, as a function of the systematic error (in percent) on the background cross section for several analysis channels. For example, if the gain is '2' then the significance doubles. Here we see that analyses with large SM backgrounds are essentially systematics dominated at 1 fb^{-1} and that there reaches can only be improved significantly by the reduction of the background systematic errors.

Analysis	N_B	$N_S^{\delta B=50\%}$	$N_S^{\delta B=20\%}$
4j0l	709	1759	721
2j0l	1206	2778	1129
4j1l	41.6	121	62
3j1l	7.2	44	28
2j1l	18.2	61	36
OSDL	84.7	230	108
SSDL	2.3	17	13
3lj	12	44	28
3lm	72.5	198	94
τ	51	144	72
b	69	178	86

Table 3.4: Expected number of background events for each of the ATLAS analyses and the corresponding number of events (N_S) required to observe a signal with $S = 5$ assuming a background uncertainty of either $\delta B = 50\%$ or 20%. The integrated luminosity is taken to be 1 fb^{-1}.

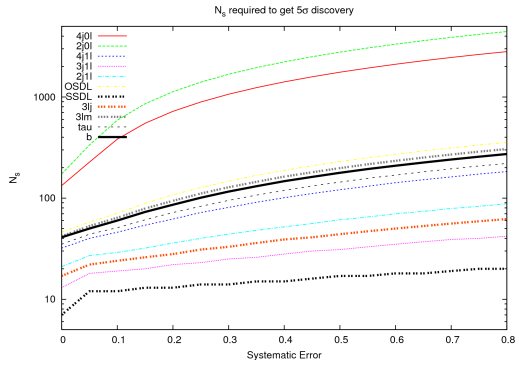

Figure 3.5: How the number of signal events required to reach $S = 5$ changes within each analysis as a function of the assumed systematic uncertainty in the SM background.

systematic error in Fig 3.5. These results show that a significant gain in the overall model space coverage can likely be obtained through even modest reductions in the background systematic errors.

To further quantify the importance of the background systematic errors in each of the analysis channels, we examine the change in the fraction of pMSSM models that are observable in a given analysis when the systematic uncertainty on the SM background is modified. As discussed in the previous section, in most of the results we present, including those in Tables 3.2 and 3.3 above, we have assumed a default 50% systematic uncertainty in both the QCD and electroweak background rates. We now study the effect of reducing the systematic error on these backgrounds to 20%, which may be possible using both the data itself as well as by improving theoretical calculations of the SM backgrounds.

The left panel of Figure 3.6 shows the distribution of the significance variable S across our flat-prior model set for the 4j0l analysis. In this figure, we compare this distribution for different values of the systematic error on the SM background and integrated luminosity. For this analysis we see that increasing the integrated luminosity from 1 fb^{-1} to 10 fb^{-1} has very little effect on this distribution; in particular, the number of pMSSM models for which $S > 5$ hardly changes. On the other hand, reducing the systematic error on the SM background from 50% to 20% shifts the peak

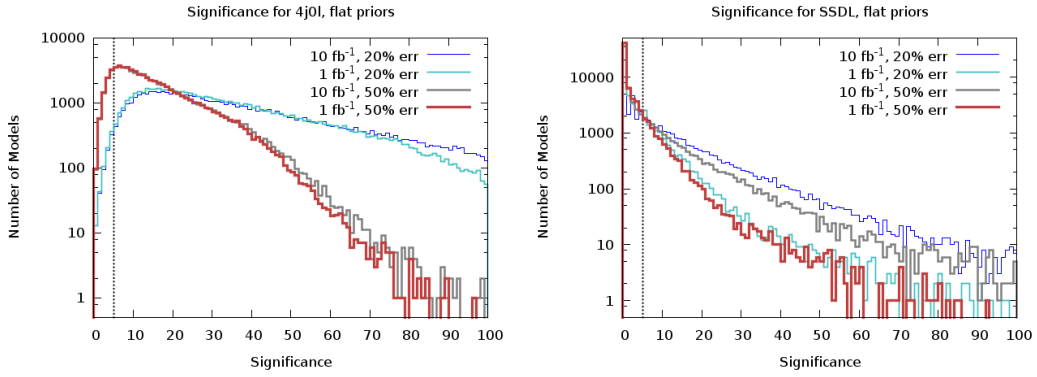

Figure 3.6: Significance distributions for the 4j0l and SSDL analyses of the flat prior model set for 4 different combinations of integrated luminosity and SM background errors. The dashed vertical line is located at $S = 5$.

in the distribution to much higher values of S, such that many more pMSSM models have $S \geq 5$. Clearly, then, the 4j0l search channel is already systematics-dominated at 1 fb^{-1}, and further theoretical and experimental work on improving the QCD background determination would be extremely fruitful.

However, for an analysis with a much smaller number of background events, such as SSDL, we find that a reduction of the systematic error has a smaller impact. In the right panel of Figure 3.6 we show the significance distribution for the flat prior model set for this analysis with the same four luminosity-error combinations. In this case, one can see that the distribution shifts to higher significance values for 10 fb^{-1}, while a change in the systematic error has relatively little effect on the distribution.

We can study the effect of varying the integrated luminosity and systematic error on the remaining analysis channels in the same way. In Table 3.5, we summarize these results by comparing the fraction of pMSSM models that pass each search analysis for all choices of the luminosity and systematic error. Here we see that, for most analyses, a reduction in the background uncertainty goes much further in increasing our model space coverage than does increased luminosity alone. Clearly, then, many of the standard SUSY searches at the LHC are systematics limited.

We now ask the very important question of whether or not our pMSSM models are discovered in one, more than one, or even in multiple, searches. Furthermore, and

Analysis	50% 1 fb^{-1}	50% 10 fb^{-1}	20% 1 fb^{-1}	20% 10 fb^{-1}
4j0l	88.3	88.6	98.9	99.0
2j0l	87.6	87.8	98.8	98.8
1l4j	41.7	44.9	56.8	63.0
1l3j	64.1	70.9	69.7	81.1
1l2j	62.9	68.4	70.6	80.6
OSDL	6.1	6.7	15.3	18.7
SSDL	14.8	25.5	18.5	32.9
3lj	13.5	17.4	19.3	29.0
3lm	2.7	2.9	4.9	5.8
tau	83.5	86.5	96.9	98.7
b	74.0	76.9	91.7	94.9

Table 3.5: The percentage of our pMSSM models that are observable in each analysis for the flat prior model set with both 1 fb^{-1} and 10 fb^{-1} of integrated luminosity and both 50% and 20% error assumed for the SM background.

perhaps even more importantly, we also want to know if there are any pMSSM models which are *missed entirely* by the suite of ATLAS inclusive $E_T^{\rm miss}$ searches. In such cases, though kinematically accessible sparticles are produced at the LHC, they are not discovered by the ATLAS searches. The answers to these questions will give us another good handle on how well the ATLAS $E_T^{\rm miss}$ searches, designed for mSUGRA, will do at covering the much more general pMSSM parameter space. The answers are to be found in Table 3.6 which shows the results for both flat and log prior model samples and for both integrated luminosities of 1 and 10 fb^{-1} assuming 50% background uncertainties. We note that the results for both prior sets are substantially different. Specifically, this table shows the fraction of the pMSSM models that have lead to a significance $S \geq 5$ in n different ATLAS analysis channels. For example, we see that for the flat prior model set with a luminosity of 1 fb^{-1}, $\sim 13.2(15.2)\%$ of the models are found by 3(6) different ATLAS analyses. As the integrated luminosity is increased, we see that for both the flat and log prior model sets the fraction of models found by a larger number of analyses increases as one would expect. Perhaps even more interesting, we observe that a respectable fraction of models are missed by *all*

N_A	F_1	F_{10}	L_1	L_{10}
0	0.6	0.4	31.8	27.0
1	1.3	1.0	6.3	6.5
2	3.4	2.5	9.0	10.1
3	13.2	10.6	11.8	11.1
4	22.0	18.5	16.5	16.3
5	9.6	10.3	5.7	6.6
6	15.2	16.9	6.1	7.1
7	20.1	17.7	6.7	6.2
8	7.6	11.8	3.0	4.4
9	3.9	6.4	1.5	2.6
10	2.1	2.8	1.1	1.1
11	1.0	1.2	0.6	0.8

Table 3.6: The percentage of models that are observable in N_A analyses, for each of the flat (F) and log (L) model sets, for 1 and 10 fb^{-1} luminosity assuming a 50% background uncertainty.

of the ATLAS inclusive MET search analyses, even for the larger value of integrated luminosity. Of course, as expected, a higher fraction of models are missed in the log prior case due to the reasons discussed above, *e.g.*, many of the sparticles may be significantly more massive. Some significant fraction of these models which are missed may be due to the large background systematic errors discussed previously. We note that if we remove the tau signature from this set of inclusive MET analysis channels, the results in the table are not appreciably modified. Why are some models missed by the various analyses and not others? We will return to address this question below as the causes are not always simple and obvious.

It is also of interest to ask 'if SUSY signatures are found in *only* one of the ATLAS searches, which one is it?'; this can be important for any number of reasons including questions about the strict validity of any given analysis. For example, for the flat prior models with 1 fb^{-1} of integrated luminosity we find that the 2j0l search is this lone analysis in 75.7%(84.9%) of the cases assuming a SM background uncertainty of 50%(20%) with the b analysis coming in as a distant second at 8.7%(7.5%), respectively. These results are thus seen to be somewhat sensitive to the assumed systematic

Analysis	$f_{\rm FLAT}^{\delta B=50\%}$	$f_{\rm FLAT}^{\delta B=20\%}$	$f_{\rm LOG}^{\delta B=50\%}$	$f_{\rm LOG}^{\delta B=20\%}$
4j0l	0.43	0	0.56	0
2j0l	75.7	84.6	44.1	59.9
4j1l	0	0	0	0
3j1l	3.4	0	18.4	11.8
2j1l	3.6	5.8	10.6	11.2
OSDL	0	0	0	0
SSDL	0.56	0	0	0
3lj	0.11	0	10.1	9.9
3lm	0	0	0	0
τ	8.0	1.9	3.4	1.3
b	8.7	7.7	12.3	5.9

Table 3.7: The identity of the single analysis discovering SUSY signals at the $S = 5$ level assuming an integrated luminosity of 1 fb^{-1}. Shown is the fraction (f), in percent, of models found by a given analysis, for both the flat and log prior model sets and for 50% and 20% background systematic error.

error on the SM background and are also found to be sensitive to the choice of the flat or log prior set. Detailed answers to this question can be found in Table 3.7.

We can further quantify the effect of reducing the systematic errors by reproducing Table 3.6 and taking the systematic error on the SM background to be 20%. This is shown in Table 3.8. As we can see, this smaller systematic error significantly reduces the number of models that are missed in all of the analyses, *e.g.*, only a relatively small number of models from the flat prior sample would now remain undiscovered by any analysis. Even the log prior sample experiences a significant reduction in the fraction of models which are missed entirely. To emphasize the power of reduced systematic errors, we compare the number of flat prior models that are missed by all analysis channels with a luminosity of 1(10) fb^{-1} and a systematic error on the background of 50%, *i.e.*, 369(239), to the case with a 20% systematic error, *i.e.*, 11(4). We conclude that reducing the systematic error is a very powerful way to increase Supersymmetric parameter space coverage.

N_A	F_1	F_{10}	L_1	L_{10}
0	0.02	0.006	18.7	12.6
1	0.08	0.04	5.4	4.2
2	0.6	0.2	7.3	8.1
3	4.9	2.6	9.4	8.1
4	22.1	13.7	21.8	17.3
5	5.9	6.1	6.2	8.8
6	11.2	14.8	7.2	10.4
7	30.1	24.2	11.7	10.5
8	9.4	13.2	4.6	8.1
9	6.1	10.6	3.0	4.8
10	6.6	10.2	2.9	4.3
11	3.1	4.4	1.8	2.7

Table 3.8: As in Table 3.6, but now assuming a 20% systematic error on the SM background instead of 50%.

3.4.3 Properties of Unobservable Models

These results now suggest the more specific issue of how and why any of the pMSSM models are not observable in the various ATLAS SUSY search analyses. Of course with so many models under discussion finding specific reasons in every case is not possible. However, in the detailed discussion below we will endeavour to find all of the most important culprits which will cover the vast majority of the missed model cases. Since in some cases some subtle issues are involved and the physics is more complex than that encountered in, *e.g.*, mSUGRA models, a thorough discussion of all the issues is mandated.

A useful piece of information in addressing the question of why models are unobservable is what are the various individual SUSY contributions to the the relevant signals for any given analysis. For example, in the conventional mSUGRA scenario, apart from events which originate from hard ISR, the common wisdom is that gluino pair production is almost exclusively the source of the 4j0l signal since the gluinos are usually more massive than the squarks and each gluino essentially decays to the 2j+MET final state. This assumption, *e.g.*, forms the basis of the Tevatron squark

and gluino searches discussed above. However, in the pMSSM models we consider here, we find that the situation is far more complicated since the sparticle spectra do not follow any particular pattern. Figure 3.7 shows the origin of the 4j0l and 2j0l signals for both prior cases. Here we see, *e.g.*, in the flat prior case, that associated squark-gluino production can easily be the major contributor among the various sources for both of these signatures in many of the models. This can easily happen when squarks are more massive than gluinos, which they very often are in this model set. In such a case, gluinos can commonly decay to 2j+MET while squarks will decay to 3j+MET. Note, however, that in the log prior case the fractions of the initial SUSY states contributing to these same signatures is now completely different as, among other reasons, the sparticle spectra are somewhat more compressed. Thus the squark-gluino mass ordering, spectrum degeneracy, the number of steps in the decay cascade, as well as the amount of ISR can all play a role in generating the (4,2)j0l final states.

Perhaps the obvious question to ask about the models which are not found by the ATLAS analyses is 'how much does the overall SUSY mass scale contribute to preventing these pMSSM models from being found?' Are, *e.g.*, the gluinos and squarks, which are most commonly at the top of SUSY decay chains, just too heavy to be produced with sufficient rates to yield a viable signal that is large enough to pass selection cuts? As we will see, large squark and/or gluino masses, while playing a role in the signal significances, are not always the most important determining factor as to whether or not a given pMSSM model is discovered. Figures 3.8, 3.9 and 3.10 address this issue for the specific case of the gluino mass, *i.e.*, perhaps if the gluinos are too massive models will be completely missed. In Figures 3.8 and 3.9 we see the significance of the 4j0l and 2j0l analyses, respectively, as a function of the gluino mass for both the flat and log prior model sets assuming an integrated luminosity of 1 fb^{-1} and a 50% background systematic. Both analyses show a qualitatively similar behavior. Overall, we see that S tends to decrease as the gluino mass increases. This is not a surprise and is especially noticeable in the log prior case as the gluino mass range extends out to ~ 3 TeV. We note, however, that for any given value of the gluino mass, the range of values of S can extend over two orders of magnitude,

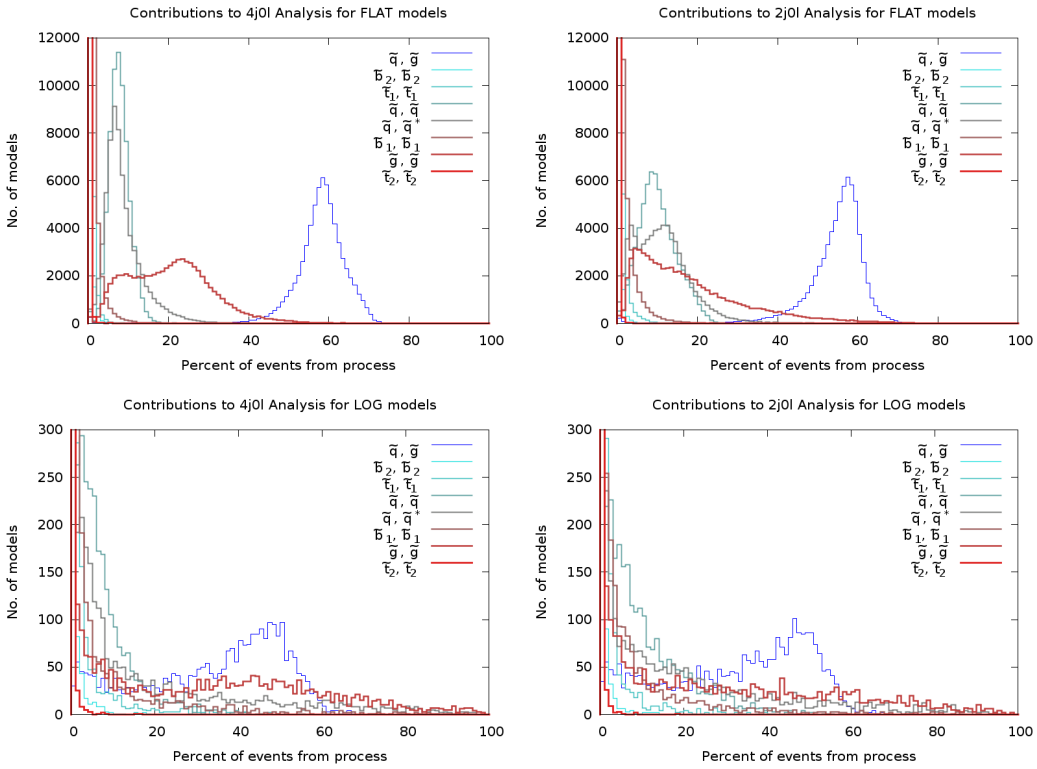

Figure 3.7: Contributions to the events passing the 4j0l and 2j0l analysis cuts from various SUSY production processes as indicated for both flat and log priors.

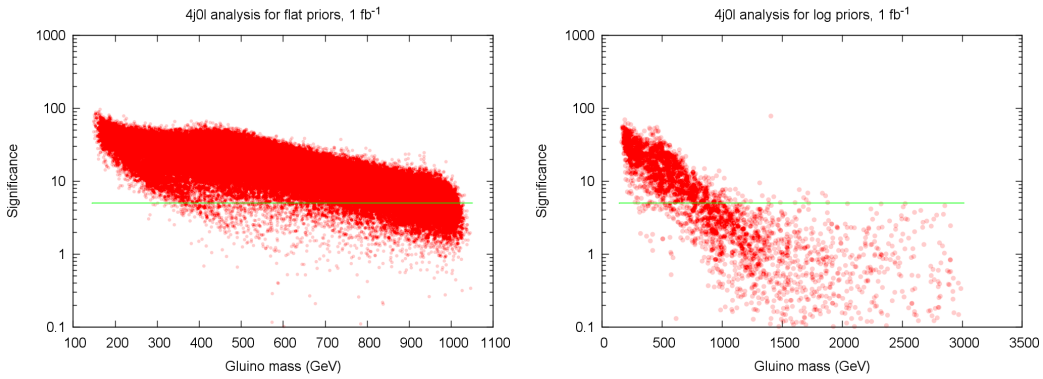

Figure 3.8: The significance of the 4j0l analysis as a function of gluino mass for the flat(log) prior set in the left(right) panel. The horizontal line denotes $S = 5$.

so, clearly, the gluino mass itself is not the sole determining factor for the overall signal significance. Does this situation change as more luminosity is accumulated? Figure 3.10 shows how the values of S respond to an increase in the integrated luminosity for the case of flat priors for both the 4j0l and 2j0l channels. We see that there is only a marginal increase in the typical value of S, indicating that increasing the integrated luminosity will not necessarily lead to the analyses capturing all of the missed models; this is as expected from the discussion of the background systematic errors above.

One thing to note about these figures is that there are a number of models whose significance value, S, lies rather close to either side of the $S = 5$ boundary. Clearly for such models variations in the signal generation process, or even statistical fluctuations, may push their significance either below or above this boundary. Thus, these models near the observation boundary may or may not be observable; in this paper we will strictly assume that the resulting values for S as will be seen by ATLAS is exactly as generated here. Another thing to note is the gluino mass reach implied by the log prior results. Here we see that the 2j0l analysis appears to be sensitive to gluino masses even as large as 3 TeV for some pMSSM model cases these models, however, may have lighter squarks which are being observed rather than the heavy gluinos.

Does a similar result hold for the squarks? Is the squark mass scale an important

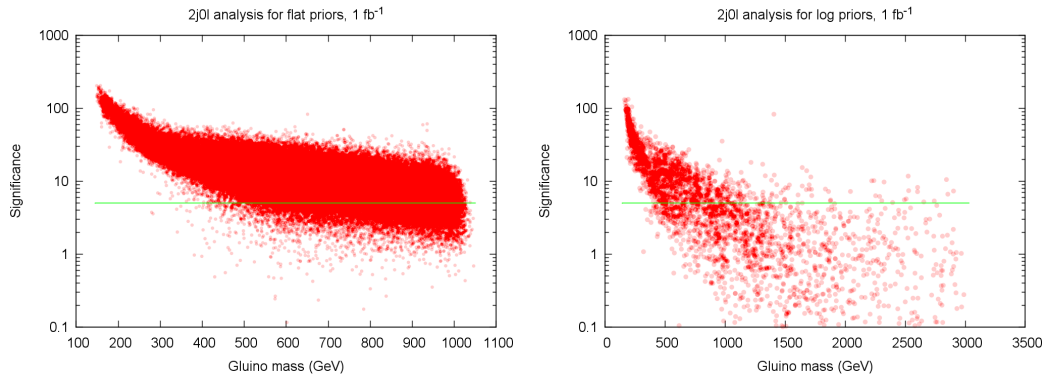

Figure 3.9: The significance of the 2j0l analysis as a function of gluino mass for the flat(log) prior set in the left(right) panel.

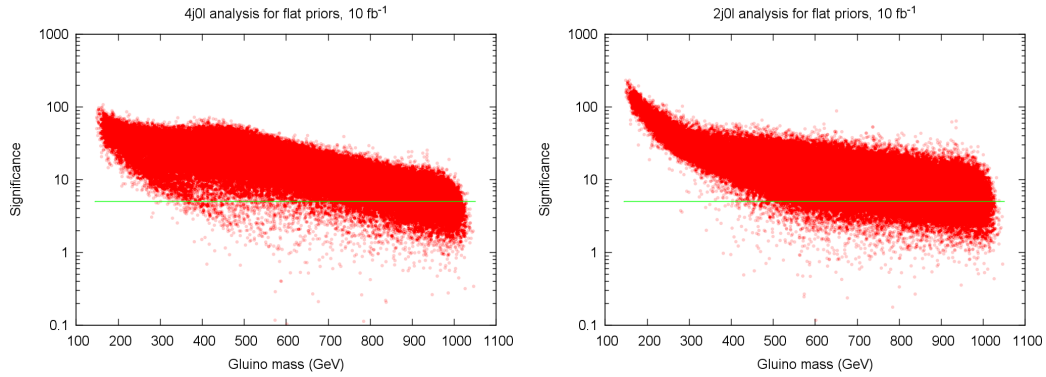

Figure 3.10: The significance as a function of gluino mass for 10 fb^{-1} luminosity for the 4(2)j0l analysis in the left(right) panel.

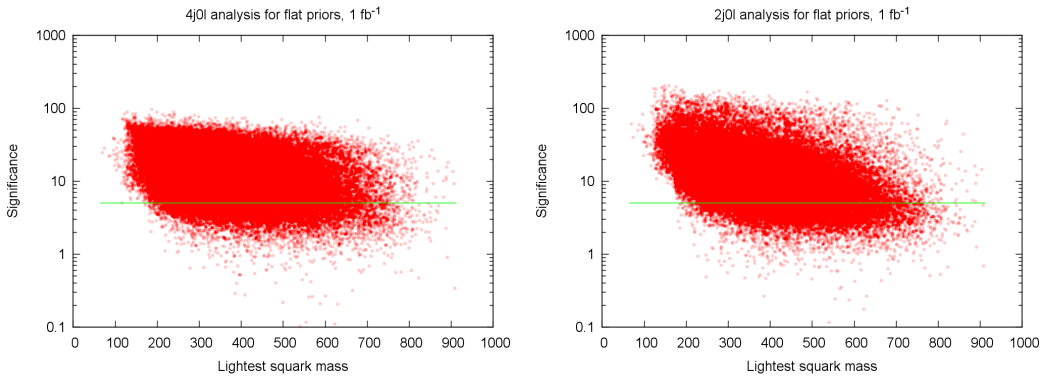

Figure 3.11: The significance versus the lightest 1st or 2nd generation squark mass for the 4(2)j0l analysis in the left(right) panel.

factor in model observability? Figure 3.11(3.12) shows a comparison of the values of significance, S, for both the 4j0l and 2j0l analyses with flat priors assuming an integrated luminosity of 1 fb^{-1} as a function of the lightest(average) squark mass within the first two squark generations. As anticipated, S in this case shows only a weak decrease as the squarks become more massive. We also see, as was the case for gluinos, that for any particular value of the squark mass, the range of values of S spans more than an order of magnitude. This supports our suspicion that effects other than just the overall squark mass scale play a major role in determining the signal significance and in preventing models from being discovered by these analyses.

At this point it is instructive to consider the relative distributions of pMSSM models which are observed (or not) by the 4j0l and 2j0l ATLAS analyses in the gluino mass versus average light squark mass plane. This is relevant as squark and gluino production will generate all of these MET signals. These results are shown for the flat prior model sample with both low and high integrated luminosities in Figures 3.13 and 3.14. In these figures, the models that are observable in the respective analyses are represented as green points whereas those that are missed by the analyses are shown in red. Examining these figures we see that most, but not all, of the missed models lie in the upper right-hand corner of this plane where both the squark and gluino masses are large. This is just what we would naively expect since in this case

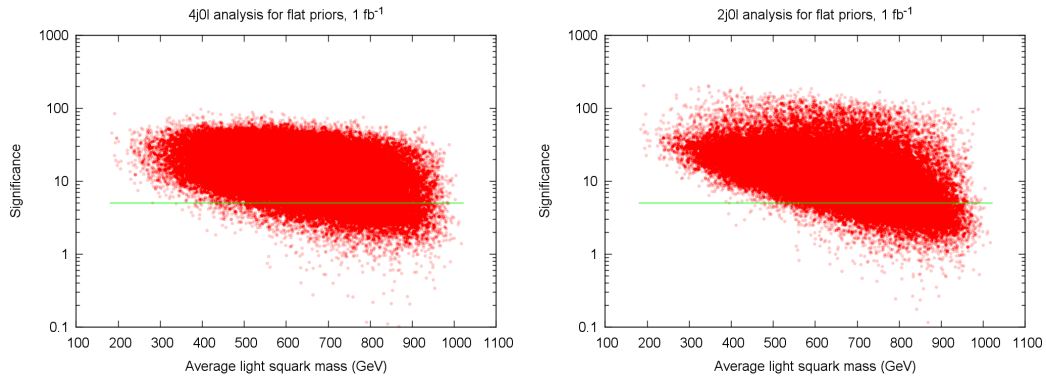

Figure 3.12: The significance versus the average 1st and 2nd generation squark mass for the 4(2)j0l analysis in the left(right) panel.

both squark and gluino production would be kinematically suppressed and a smaller number of events would result. It is important to note, however, that there are also a significant number of obviously interesting models that have relatively light squark and gluino masses but which are not detected in either of these analyses. Here we again observe that increasing the integrated luminosity does not particularly help in most of these cases, even those with rather light squark and/or gluino masses due to the large SM background systematic errors.

Interestingly, these figures show, *e.g.*, that a particular pair of models (model numbers 19933 and 53105) have gluino masses below 300 GeV and light squarks and yet they are missed by both the 4j0l and 2j0l analyses. The reason for this is that these models have unusual spectra where the gluinos mostly decay through the $\tilde{d}_R$ which then, in turn, universally decays via $\tilde{\chi_2}^0$ (which is mostly bino in these cases) finally yielding the $2jl^+l^-$+MET final state. Since leptons essentially must always appear in the cascade decays of these two models, the 4j0l and 2j0l analysis requirement of there being no isolated leptons can never be met. These two models are, however, found to be observable in the lepton plus jets analyses. To see this more clearly, Fig. 3.15 shows the set of models which fail the 4(2)j0l analyses and *simultaneously* indicates whether or not they pass the corresponding 4(2)j1l analysis. Here we see that the two specific models under discussion, as well as others, which are missed by

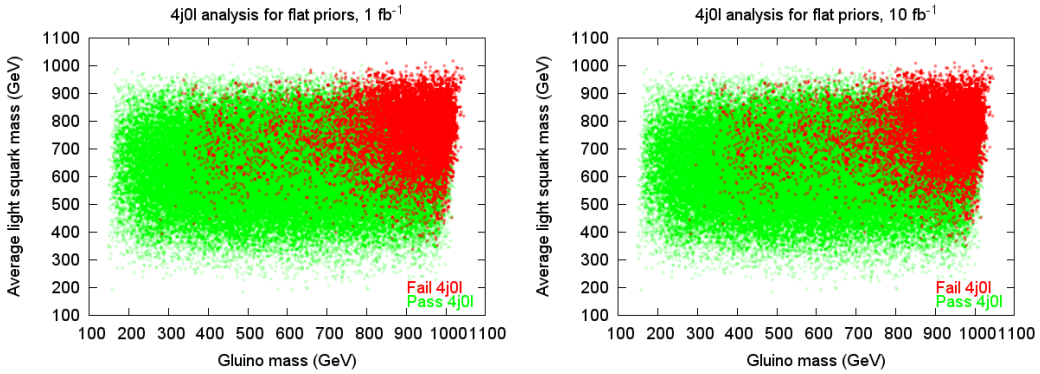

Figure 3.13: The pMSSM models from the flat prior set in the gluino mass - average 1st and 2nd generation squark mass plane. The models that pass (fail) the 4j0l analysis are shown in green(red). The left(right) panel corresponds to an integrated luminosity of 1(10) fb^{-1}.

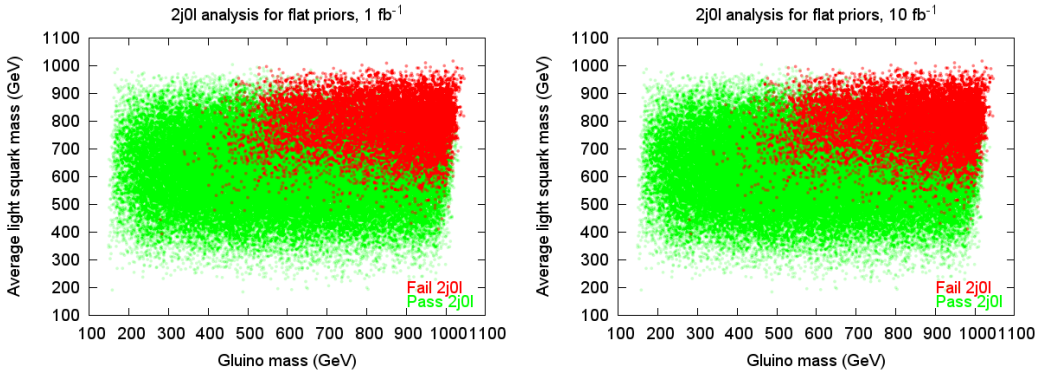

Figure 3.14: The same as in Figure 3.13, but for the 2j0l analysis.

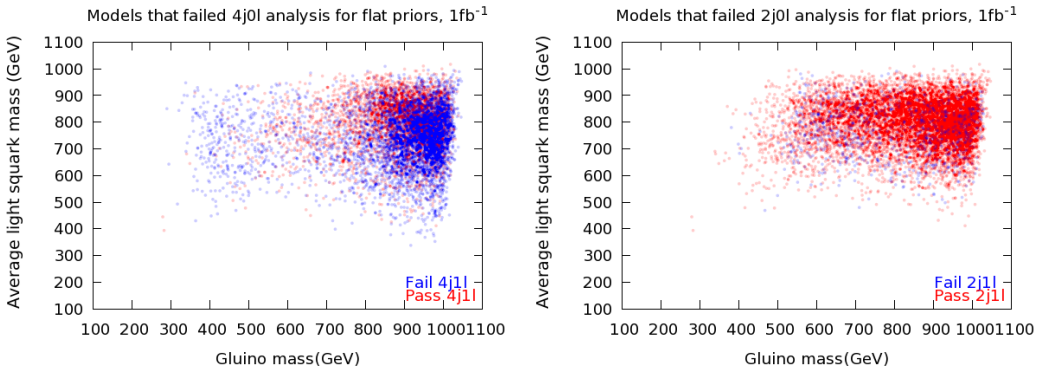

Figure 3.15: The set of flat prior models that fail the 4(2)j0l analyses and whether they are detected or not in the corresponding 4(2)j1l analyses.

the 4(2)j0l analyses are indeed subsequently captured by the corresponding leptonic analyses.

As alluded to in the previous section on model generation, many of our models satisfy the Tevatron search constraints even though the squarks and gluinos are fairly light; this occurs when the mass splittings between the squarks and/or gluinos and the LSP are relatively small. This configuration easily leads to rather soft jets in the final state and clearly some models will be unobservable in the (4,2)j0l analysis channels at the LHC for the same reasons. To see this, it is worth examining which models pass and fail the (4,2)j0l analyses as the gluino/squark-LSP mass splittings are varied. This is shown for the case of gluinos with flat priors in Figure 3.16 (always assuming an integrated luminosity of 1 fb^{-1} and 50% systematic background errors). Here we see, particularly in the case of the 4j0l channel, that many models with light gluinos which are unobservable have small mass splittings with the LSP, hence producing rather soft jets. This occurs mainly for gluino masses $m_{\tilde{g}} \gtrsim 350$; gluinos lighter than this have large production cross sections associated with hard radiated jets which can compensate for the soft jets in the decay and pass the kinematic cuts for this channel (we note that squark production could also be contributing to this channel). Of course some of these models will again be missed by the 4j0l and 2j0l analyses due to the presence of high E_T leptons as mentioned above. To see how this impacts

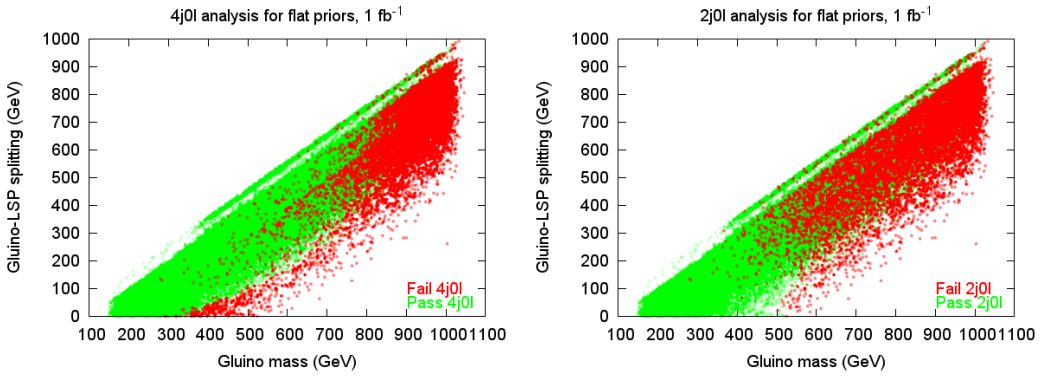

Figure 3.16: The mass splitting between the gluino and LSP as a function of the gluino mass for the flat prior model sample. The models that pass the 4(2)j0l analysis for 1 fb^{-1} are shown in green, while the ones that fail are displayed in red. The 4(2)j0l channel is shown in the left(right) panel.

us more clearly, Fig. 3.17 shows the set of flat prior models that are unobservable in *both* of the 4(2)j0l analyses as well as the corresponding 4(2)j1l analyses in red while the green points label models passing the $S = 5$ significance requirements of *either* analysis. Still, it is clear that many models are unobservable in the (4,2)j0l channel due to the small mass splittings and not due to the presence of leptons.

Figure 3.18 shows an analogous behavior to that discussed above for gluinos in the case of the lightest first or second generation squark mass splitting with the LSP for both the 4j0l and 2j0l channels in the flat prior case. As was found for the gluinos, a respectable number of models which fail these analyses are observed to have light squarks with small mass splittings with the LSP leading to soft jets in their decay products. Certainly, a sizable fraction of such models will not be observed in the (4,2)j0l analyses for this reason but others again may be missed due to the presence of leptons in their cascade decays as is shown in Fig. 3.19.

So far we have found three 'obvious' reasons why some of our pMSSM model points fail to be observed by the 4j0l/4j1l and 2j0l/2j1l analysis channels: (*i*) low signal cross sections for particular channels which can be correlated with (*ii*) heavy colored states at the top of decay chains causing kinematic suppression or unexpected decay patterns. The fact that these characteristics render the models unobservable

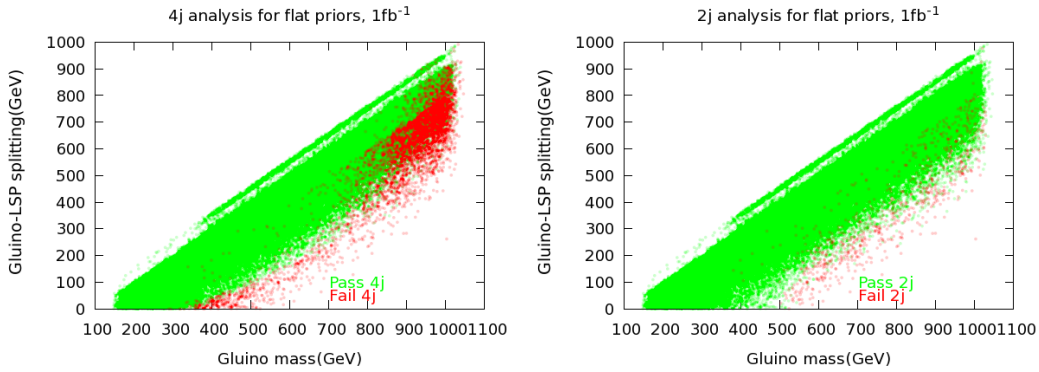

Figure 3.17: The mass splitting between the gluino and LSP as a function of the gluino mass for the flat prior model sample. The models that fail *both* of the 4(2)j0l and 4(2)j1l analyses in shown in red, while the green points label those models passing *either* analysis. The 4(2)j0l channel is shown in the left(right) panel.

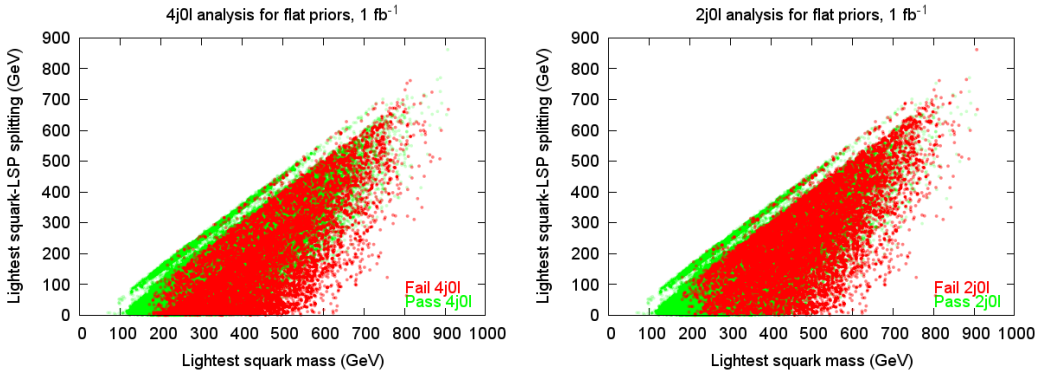

Figure 3.18: The mass splitting between the lightest first/second generation squark and the LSP as a function of the lightest squark mass for the flat prior model sample. The models that pass the 4(2)j0l analysis for 1 fb^{-1} are shown in green, while the ones that fail are displayed in red. The 4(2)j0l channel is shown in the left(right) panel.

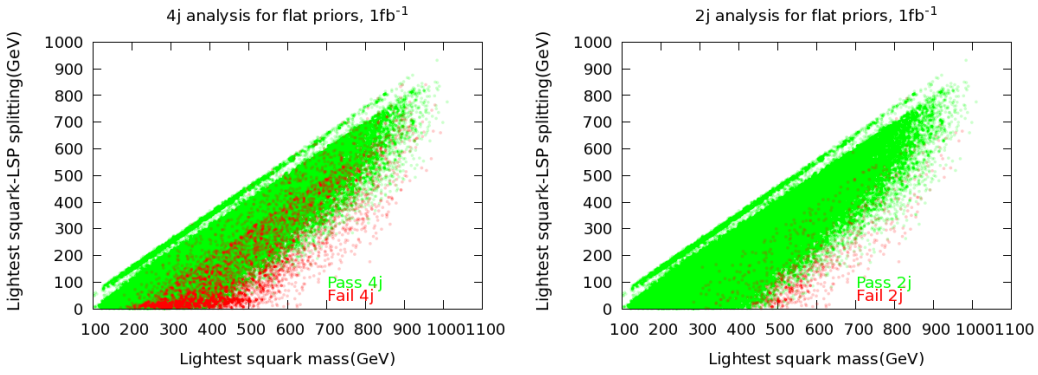

Figure 3.19: The set of flat prior models failing *both* of the 4(2)j0l and 4(2)j1l analyses are shown in red, while green points label models passing *either* analysis. The results are shown in the plane of the mass splitting between the lightest first/second generation squark and the LSP and the lightest squark mass.

can also in large part be attributed to the rather large systematic errors associated with the sizable SM backgrounds in both the 4j0l and 2j0l analyses. As we saw above, a larger systematic uncertainty associated with the SM background requires a greater number of signal events to reach the $S = 5$ discovery level. The size of this SM background uncertainty was found to play a *major* role in models being missed by the 4j0l and 2j0l analyses. (*iii*) Furthermore, small mass splittings between the various colored states in the spectrum and the LSP can lead to the production of significantly softer final state objects that have a more difficult time passing the various analysis thresholds.

Let us now turn to other search channels. Figure 3.20 shows the set of flat prior models that *fail* the 4j1l and 2j1l analyses assuming an integrated luminosity of 1 fb^{-1} and the standard 50% background systematic error. Here we have examined whether a given model fails because of the jet cut requirements (as in the corresponding 4j0l and 2j0l analyses) or because of the leptonic cuts for these specific analyses. As we would expect, most of the models failing the jet criteria correspond to cases with large squark and/or gluino masses, particularly so for the 4j1l case where the jet requirements are somewhat stronger. For either analysis, however, we see that most of the models are missed due to their failure to pass the leptonic cuts and are observed

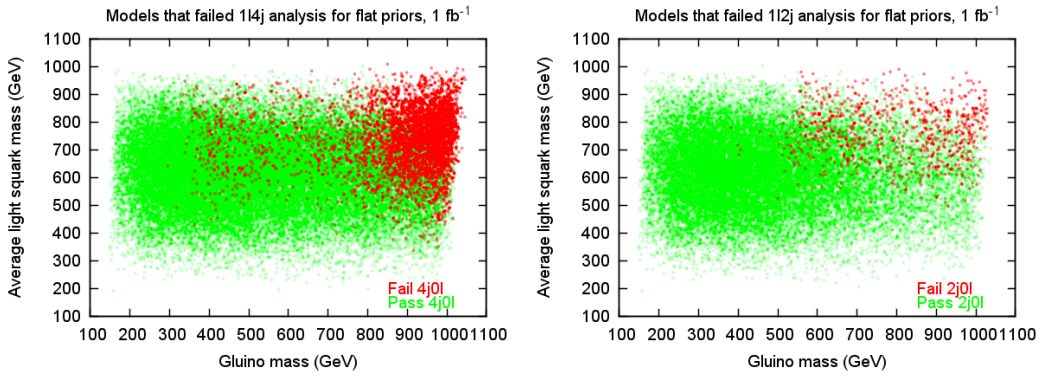

Figure 3.20: The set of pMSSM models which are unobservable in the 4(2)1l analysis channel in the left(right) panel shown in the plane of the average 1st/2nd generation squark mass and the gluino mass. The models which are observed in the corresponding 4(2)j0l channel are shown in green, while those that fail these analyses are shown in red.

in the zero lepton channels; in many cases this is simply due to the absence of the required lepton with either sufficient E_T or lack of isolation from the final state jets.

3.4.4 The Effect of Cuts

It is instructive to consider how our pMSSM model samples 'respond' as each of the individual experimental cuts are applied for a given analysis. This provides another direct indicator of why models are observable or not. For each analysis and each model, we keep track of the number of signal events after each cut is applied in sequence. With these event numbers, and the number of background events after all the cuts have been applied, we compute a significance at each step and check if it is greater than 5. Since we compare the number of signal events after each kinematic cut to the number of background events after all cuts (as this is the only result for the background we were provided), this significance is somewhat artificial. Nonetheless it is still illustrative in showing the relative impact of the cuts. Note that for the analyses that have a M_{eff} cut, we apply that cut to the signal at each step, and only consider the effect of the remaining cuts here.

The accompanying Tables 3.9–3.19 show the results of these considerations for

both the flat and log prior model samples assuming an integrated luminosity of either 1 or 10 fb^{-1} and a 50% systematic error on the SM background as usual. Note that some care must be used in reading these Tables as in many cases the effectiveness of a given cut may strongly depend upon the order in which it has been implemented. Here the cuts are applied in the order as given by the ATLAS SUSY study [12]. The cut numbers listed in the Tables correspond to those in Section 3.2. Further note that the flat and log prior model sets can respond somewhat differently to any particular cut or set of cuts so it is important to study both of these cases seperately in what follows.

We see in Tables 3.9 and 3.10 that the models easily pass the jet cuts for both the familiar 4j0l and 2j0l searches but requiring the absence of isolated leptons (cuts number 5 and 4, respectively) takes a respectable toll on the fraction of models found. In the 2j0l case, the stronger cut on $E_T^{\rm miss}$ (cut 2) is also seen to lead to a significant weakening in the model space reach. The cut study for the 4(3,2)j1l analysis channels is shown in Table 3.11(3.12,3.13). In all three cases the combined requirements of (only) a single isolated lepton, multiple high E_T jets as well as $E_T^{\rm miss}$ are all seen to lead to significant reductions in the signal events for these separate analyses.

In the case of the OSDL search, as shown in Table 3.14, the simultaneous requirement of opposite sign dileptons and four hard jets (cuts 1 and 2) eliminates more than $\sim 80\%$ of the model set. In addition, the $E_T^{\rm miss}$ and transverse sphericity cuts (cuts 3 and 4) are seen to reduce the signal further by another factor of $\simeq 2$. In the SSDL analysis shown in Table 3.15, we again see that the lepton and jet requirements remove almost $\sim 80\%$ of the model set, but here the $E_T^{\rm miss}$ requirements (cut 3) are more easily met in the surviving model subset. For the trilepton analyses, shown in Tables 3.16 and 3.17 the 3 lepton requirement alone (cut 1) is seen to eliminate most of flat prior model sample. Requiring an extra high-E_T jet (cut 2) in the 3lj analysis and removing dilepton pair masses near the Z (cut 5) in the 3lm analysis both reduce the number of remaining models to rather small numbers in these channels. For the τ analysis presented in Table 3.18, the transverse mass cut (cut 7) is seen to be the most restrictive. In the case of the b analysis shown in Table 3.19, the double b-tagging requirements (cut 6) has by far the most impact.

Cut	F_1	F_{10}	L_1	L_{10}
4j0l 1	99.7	99.7	70.1	69.8
4j0l 2	98.6	98.6	62.3	62.1
4j0l 3	94.7	94.9	53.0	52.9
4j0l 4	93.4	93.5	51.5	51.3
4j0l 5	88.3	88.6	48.2	48.1

Table 3.9: The percent of models that pass the 4 jet 0 lepton analysis after each subsequent cut is applied. "F" refers to the flat priors model set and "L" to the log priors set, and the subscript "1" or "10" refers to the luminosity in fb^{-1}. Note that the background after all cuts is used to determine significance.

Cut	F_1	F_{10}	L_1	L_{10}
2j0l 1	99.5	99.5	68.1	67.7
2j0l 2	95.0	95.1	53.8	53.7
2j0l 3	94.2	94.3	52.2	51.9
2j0l 4	87.6	87.8	47.4	47.4

Table 3.10: Same as in Table 3.9 but for the 2 jet 0 lepton analysis channel.

Cut	F_1	F_{10}	L_1	L_{10}
4j1l 1	84.6	86.2	65.3	67.7
4j1l 2	84.1	85.8	64.2	66.6
4j1l 3	69.6	71.7	45.8	48.0
4j1l 4	61.4	63.9	35.2	37.7
4j1l 5	53.3	56.1	27.7	29.9
4j1l 6	41.7	44.9	18.4	20.4

Table 3.11: Same as Table 3.9 but for the 4 jet, 1 lepton, analysis channel.

Cut	F_1	F_{10}	L_1	L_{10}
3j1l 1	97.0	98.8	87.2	92.4
3j1l 2	96.9	98.7	86.8	92.0
3j1l 3	86.9	91.2	73.5	80.1
3j1l 4	79.0	84.4	56.7	66.6
3j1l 5	73.5	79.3	48.1	57.4
3j1l 6	64.1	70.9	36.6	46.0

Table 3.12: Same as Table 3.9 but for the 3 jet, 1 lepton, analysis channel.

Cut	F_1	F_{10}	L_1	L_{10}
2j1l 1	92.8	95.4	80.5	84.9
2j1l 2	92.5	95.1	79.7	84.2
2j1l 3	88.8	91.8	75.5	80.1
2j1l 4	81.6	85.6	59.6	66.4
2j1l 5	72.2	77.0	46.0	52.5
2j1l 6	62.9	68.4	33.5	40.5

Table 3.13: Same as Table 3.9 but for the 2 jet, 1 lepton, analysis channel.

Cut	F_1	F_{10}	L_1	L_{10}
OSDL 1	49.6	51.3	39.5	40.9
OSDL 2	17.6	18.6	11.4	12.2
OSDL 3	8.2	8.9	5.0	5.8
OSDL 4	6.1	6.7	3.8	4.2

Table 3.14: Same as Table 3.9 but for the OSDL analysis channel.

Cut	F_1	F_{10}	L_1	L_{10}
SSDL 1	40.2	50.8	26.9	38.4
SSDL 2	21.3	32.0	13.7	21.2
SSDL 3	14.8	25.5	8.9	15.9

Table 3.15: Same as Table 3.9 but for the SSDL analysis channel.

Cut	F_1	F_{10}	L_1	L_{10}
3lj 1	24.2	29.2	19.4	23.7
3lj 2	13.5	17.4	8.6	11.1

Table 3.16: Same as Table 3.9 but for the trilepton + jet analysis channel.

Cut	F_1	F_{10}	L_1	L_{10}
3lm 1	7.6	8.1	6.5	7.1
3lm 2	6.6	7.0	5.6	6.3
3lm 3	6.6	7.0	5.6	6.3
3lm 4	6.4	6.8	5.2	5.6
3lm 5	2.7	2.9	2.9	3.0

Table 3.17: Same as Table 3.9 but for the trilepton + missing energy analysis channel.

Cut	F_1	F_{10}	L_1	L_{10}
tau 1	100.0	100.0	81.4	82.4
tau 2	100.0	100.0	79.8	80.9
tau 3	99.9	100.0	78.6	79.4
tau 4	99.7	99.8	75.1	76.6
tau 5	96.0	96.9	59.4	61.3
tau 6	90.9	92.9	51.5	53.1
tau 7	83.5	86.5	44.0	45.6

Table 3.18: Same as Table 3.9 but for the τ analysis channel.

Cut	F_1	F_{10}	L_1	L_{10}
b 1	100	100	95.0	95.5
b 2	100	100	95.0	95.5
b 3	100	100	94.8	95.1
b 4	100	100	92.6	92.9
b 5	100	100	89.6	90.3
b 6	74.0	76.9	42.9	44.6

Table 3.19: Same as Table 3.9 but for the b jet analysis channel.

3.4.5 Discussion of 'Difficult' Models

It is interesting to understand why some specific models are unobservable in *all* of the ATLAS MET search channels. A good sample of such cases to study is provided by the set of 11 models from the flat prior scan that are missed by all of the analysis channels, assuming an integrated luminosity of 1 fb^{-1} with a 20% SM background systematic error.[4] To this end, we display and discuss some of the details of the mass spectra for these 11 specific models. Four of these models (labeled as model number 14602, 43704, 62912, and 63694) are undetected due to the presence of long-lived charginos, resulting in a correspondingly small E_T^{miss} signature (the spectra for the latter three models are shown in Figure 3.21). Three more models (7888, 17158, and 47787) are unobservable due to their compressed sparticle spectra (the spectrum of one of these is also shown in Figure 3.21). The remaining four models (5700, 7105, 25692, and 35678) are missed for more subtle reasons described below.

One way to better understand why a specific model is unobservable is to try to find a 'sister' model (or models) within our pMSSM set that has as similar a spectrum as possible to the missed model and yet is observable in at least one of the ATLAS MET analyses. Comparisons between the failed and passed models may then reveal the underlying cause that renders the model to be undiscoverable. Model 14602 provides a good example of this approach and Figure 3.22 compares the spectrum of this model and its sister, 43001. Both of these models have qualitatively similar cross sections for the production of squarks and gluinos which initiate the long decay cascades. However, a side-by-side comparison of these two models shows that 14602 has consistently lower values of S for each of the analyses and yet both models have similar preselection jet and lepton spectra as well as having long-lived charginos (which are Higgsino-like and Wino-like, respectively).

The only significant difference between the two models is in their preselection E_T^{miss} distributions as can be seen in Figure 3.23. Here we see that this distribution peaks at much lower values for model 14602 and has a correspondingly diminished high energy tail in comparison to model 43001. Due to the presence of large branching

[4]Note that only 4 of these specific models remain undiscovered when the integrated luminosity is increased by a factor of 10.

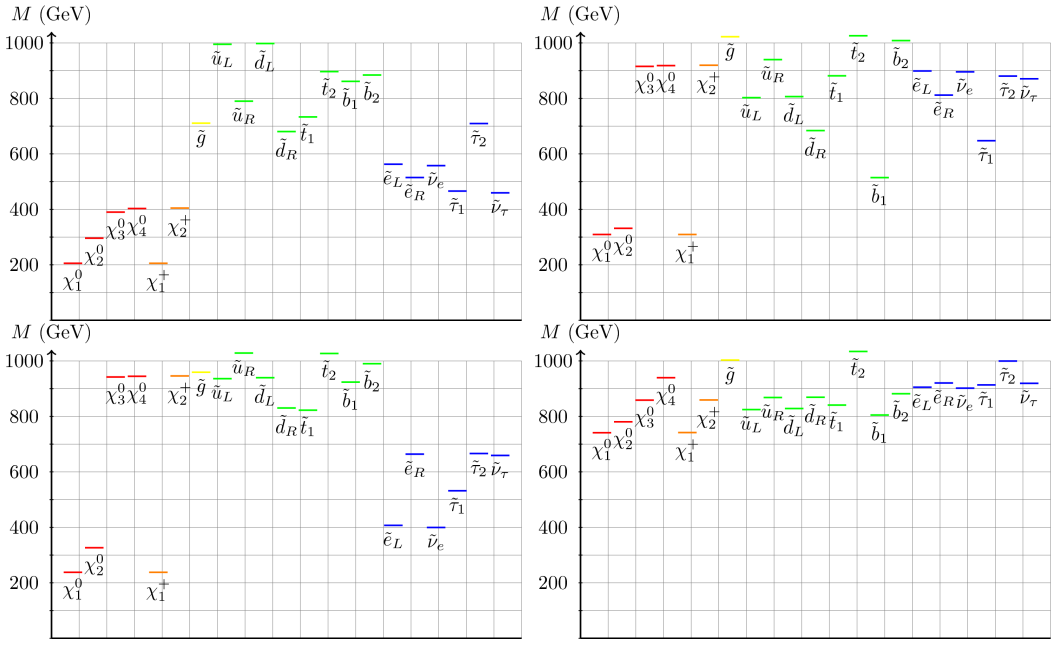

Figure 3.21: The spectra for four of the eleven models that are unobservable in all analysis channels. The first three (from left to right, top to bottom: 43704, 62912, and 63694) are missed due to the presence of long-lived charginos, while the last (bottom right: 17158) is missed due to a compressed spectrum. The colored balls represent masses for (left to right) $\tilde{\chi}_1^0$, $\tilde{\chi}_2^0$, $\tilde{\chi}_3^0$, $\tilde{\chi}_4^0$, $\tilde{\chi}_1^+$, $\tilde{\chi}_2^+$, $\tilde{g}$, $\tilde{u_L}$, $\tilde{u_R}$, $\tilde{d_L}$, $\tilde{d_R}$, $\tilde{t}_1$, $\tilde{t}_2$, $\tilde{b}_1$, $\tilde{b}_2$, $\tilde{e_L}$, $\tilde{e_R}$, $\tilde{\nu}_e$, $\tilde{\tau}_1$, $\tilde{\tau}_2$, $\tilde{\nu}_\tau$.

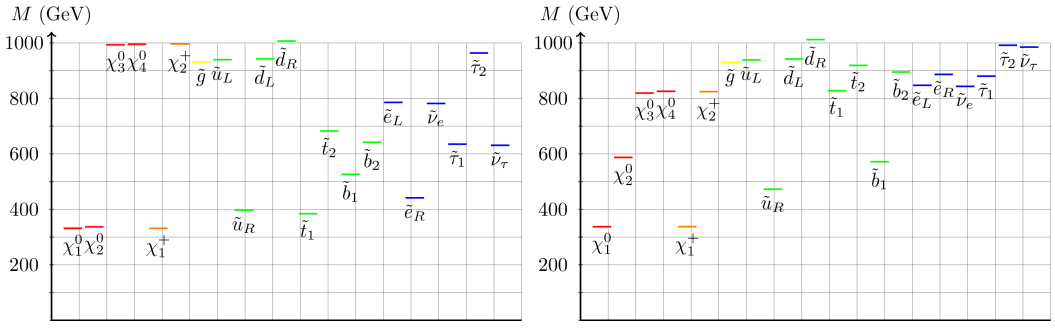

Figure 3.22: A comparison of the spectra of sister models 14602 (left) and 43001 (right).

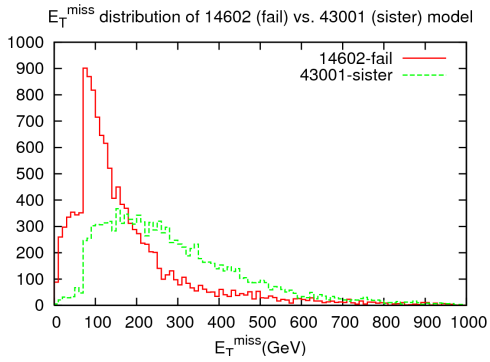

Figure 3.23: A comparison of the $E_T^{\rm miss}$distributions of model 14062 and its sister 43001.

fractions in the gluino cascades that lead to a stable chargino in model 14602, there is insufficient $E_T^{\rm miss}$ to pass the ATLAS analysis cuts. This is related to the suppressed couplings of the first and second generation squarks to light Higgsinos. However, model 14602, with 20% background systematics, has reasonable values of S in some of the search analyses and a factor of 10 or so increase in the integrated luminosity allows this model to be discovered in the 3j1l, τ and b channels. The corresponding examination of the other 3 models with long-lived charginos yields somewhat similar results.

Undiscovered models 7888 and 47787, as well as their discovered co-sister 42790 (Figure 3.24), all show a relatively heavy and compressed sparticle spectrum except that the gluino is slightly more massive and well-separated from the squarks in model 42790 and the squarks are more degenerate with the LSP for the two undetected models. Interestingly, the missed models both have larger cross sections for squark and gluino production (due to their lighter gluinos) than does their sister model by over a factor of 2. Thus the initial, pre-cut event rates for the missed model are not an issue here. However, the larger gluino-squark mass splitting for model 42790 allows for a higher p_T jet from the decay $\tilde{g} \to \tilde{q} + j$ than do the two missed models and so it is found by the 2j0l analysis. The degeneracy of the squarks with the LSP makes it difficult for any of these models to generate additional high p_T jets. Nonetheless, model 7888 would pass the 2j0l analysis at 10 times higher integrated luminosity. In

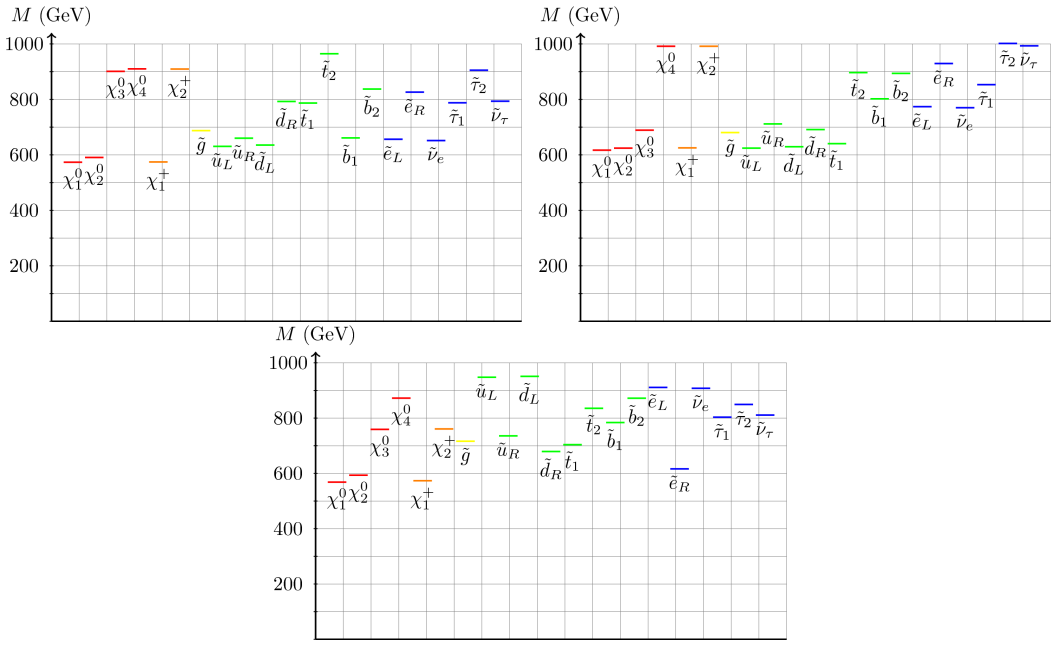

Figure 3.24: A comparison of the spectra of models 7888 (top left) and 47787 (top right) with their sister 42790 (bottom).

addition, model 17158 is seen to have a very massive and highly compressed spectrum and fails the MET searches for qualitatively similar reasons.

The remaining undetected models are somewhat more difficult to analyze. Model 5700 (with its sister model 28575 shown in Figure 3.25) is the most straightforward case to study and the gluino is sandwiched between the squarks in the mass spectrum. The resulting mass splitting between the heavier $\tilde{u}_{L(R)}$ and the gluino is only about half of that of the sister model. The essential difference between these two models is the placement of the lightest squark in the spectrum and the relative splittings between this squark, the gluino, and the LSP. The model cannot produce 3rd or 4th jets with sufficient E_T to pass the 4j0l selection. Note that the splittings are somewhat larger for the sister model. In addition, the sister sparticle spectrum makes the decay products arising from stop and sbottom production easier to observe. This is another case where a luminosity increase to 10 fb^{-1} leads to a discovery for a missed model.

Comparing the undetected model 25692 with its sister 1446 (see Figure 3.26), we

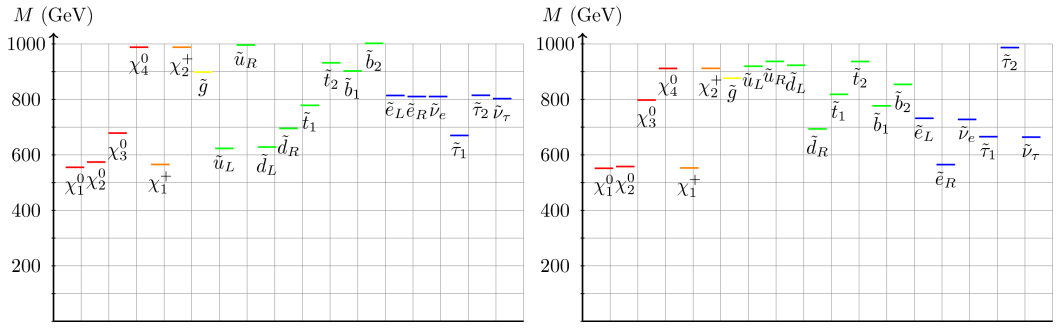

Figure 3.25: A comparison of the spectra of sister models 5700 (left) and 28575 (right).

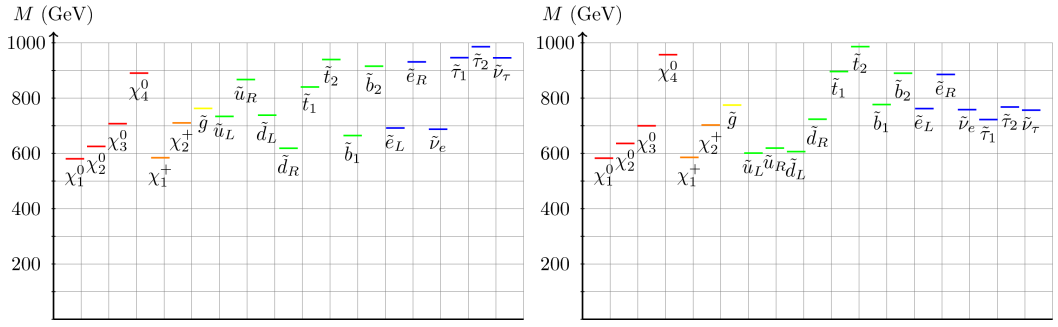

Figure 3.26: A comparison of the spectra of sister models 25962 (left) and 1446 (right).

see that the squarks are somewhat lighter in the sister case allowing for both larger production cross sections as well as more gluino decay modes with larger branching fractions into final states that can populate the 2j0l channel. We find that increased luminosity would be useful in this case as well.

For model 35678 and its sister model 9396, shown in Figure 3.27, the electroweak gaugino sectors are almost identical. However, the gluino is heavier than all the first- and second-generation squarks in the sister case while the $(\tilde{u}_L, \tilde{d}_L)$ are heavier than the gluino for model 35678. The lighter slepton spectrum in the sister model allows for an enhancement in the number of high p_T leptons produced so that this model can be found in the lepton plus jets channels (but does not do as well in the 4(2)j0l analyses as does 35678). Both the 4(2)j0l analyses would allow model 35678 to be

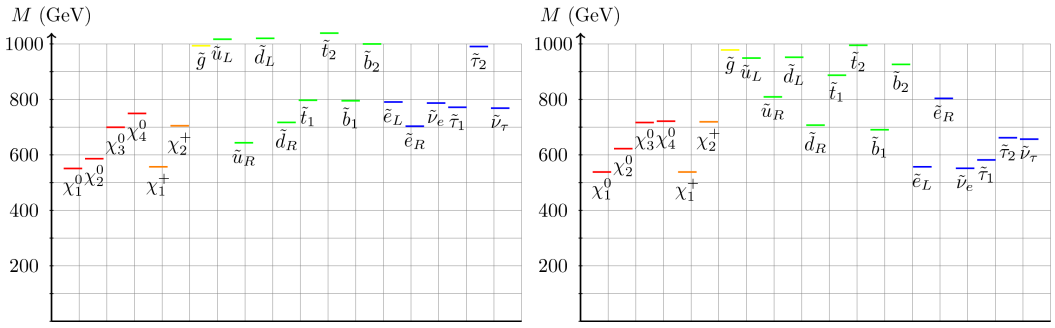

Figure 3.27: A comparison of the spectra of sister models 35678 (left) and 9396 (right).

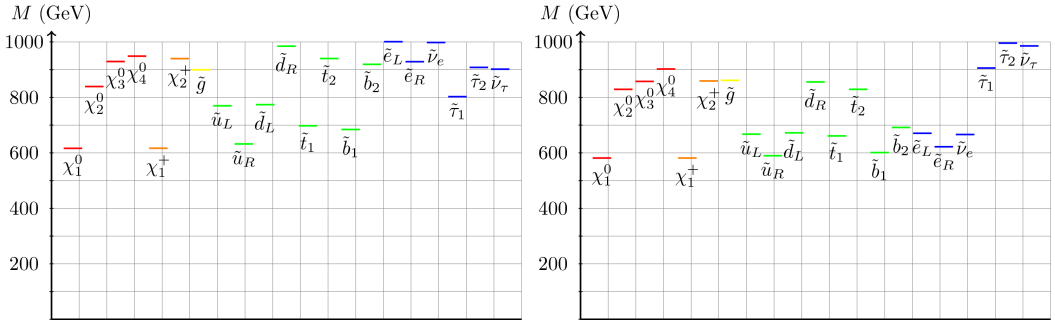

Figure 3.28: A comparison of the spectra of sister models 7105 (left) and 53923 (right).

discovered with an integrated luminosity of 10 fb^{-1}.

Model 7105 has a sister model 53923 whose spectrum is shown in Figure 3.28; the sister has somewhat larger gluino and squark production rates. This sister model also has lighter sleptons which produce a larger fraction of final states with higher E_T leptons. Both models are found to fail the 4j0l analysis yet the sister model passes the 2j0l channel. It has a higher amount of E_T^{miss} since all the squarks are lighter than the gluino and have substantial branching fractions into the LSP. Increased luminosity would be useful in this case as well.

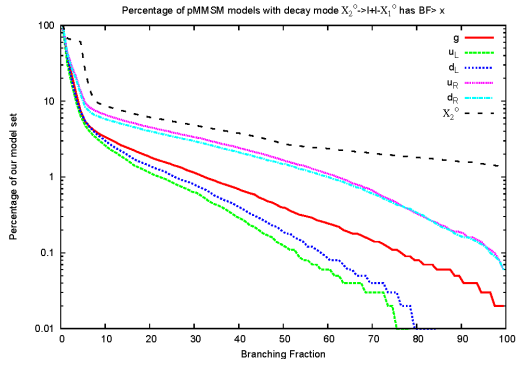

Figure 3.29: The fraction of pMSSM models that lead to the $X+(j)l^+l^-$+MET signature, passing through the second neutralino, as a function of the minimum branching fraction for this final state. The various sparticle initial states are color coded as indicated.

3.4.6 Classic Decay Modes and the SUSY Mass Scale

There are a number of other interesting questions that we can address with this large data set. For example, a final state that has received much attention for its usefulness in determining sparticle masses [64] is jl^+l^-+MET which originates from the cascade decay of an initial colored sparticle, usually with the second neutralino and a slepton appearing in the chain. One can ask how often this specific final state occurs in the decays of the various initial squarks and gluinos in our pMSSM model sets; the results are shown in Figure 3.29 for both the flat and log prior model sets combined. This figure shows the fraction of the model sample that leads to this particular final state as a function of the minimum value for the branching fraction for this decay. For example, the fraction of the models in our set that have a $\tilde{u}_R$ initiated decay to an Xjl^+l^-+MET final state with a branching fraction of at least 20(5)% is only $\sim$ 5(9)%! For $\tilde{u}_L$ cascades, which are commonly studied in this regard, we see that the branching fraction for this final state is significantly smaller, only $\sim$ 1.5(5)%. Clearly, unlike the case of mSUGRA, this final state does not appear to occur very frequently with a large branching fraction in the decays of squarks or gluinos in our pMSSM model sample. From this we can conclude that other final states would need to be employed in most cases for measuring sparticle masses.

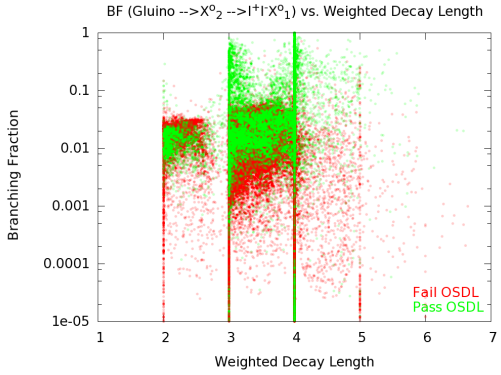

Figure 3.30: The average branching fraction as a function of the weighted decay length to reach the $l^+l^-\tilde{\chi}_1^0$ final state via the $\tilde{\chi}_2^0$ in decays of the gluino. The models that pass the OSDL analysis cuts are shown in green, while those that fail are in red.

Another question we address is what are the number of steps in the decay topology necessary to reach a specific final state such as, *e.g.*, Xl^+l^-+MET, from a given initial colored sparticle at the top of the decay chain. For the case of the gluino, this result is shown in Figure 3.30. In this figure, branching fraction of the gluino into this inclusive final state is shown as a function of the number of decay chain steps (weighted by the branching fraction so not necessarily an integer) necessary to reach this specific final state. The colors reflect model points which do(green) or do not(red) pass the OSDL analysis requirements; note that most of the models which pass the OSDL analysis have large branching fractions. While this final state may be reached in as few as 2 steps (via gluino loop decay to $g\tilde{\chi}_2^0$ followed by the 3-body decay $\tilde{\chi}_2^0 \rightarrow l^+l^-\tilde{\chi}_1^0$), it is interesting to see that there are some model points where 6 or 7 steps are required. This demonstrates that the decay topologies in the pMSSM framework can be much more complex than those found in mSUGRA, with implications for SUSY searches and mass measurements at the LHC.

Finally, we investigate whether certain global observables can be used to determine the effective SUSY mass scale. Long ago[65, 66], it was observed within mSUGRA that the M_{eff} variable can be used to determine the overall scale of the colored sparticles in the SUSY mass spectrum. In particular, it was observed that within these

models $M_{\rm eff} \simeq 1.5 M_{\rm min} \pm (10-15)\%$ where $M_{\rm min}$ is the mass of the lightest sparticle in the set $\tilde{g}, \tilde{u}_{L,R}, \tilde{d}_{L,R}$, which are the dominant sources of jets and MET. We can now see whether this sort of relationship holds in the much more general context of the pMSSM. The answer to this question is shown in Fig. 3.31 which displays $M_{\rm eff}$ as a function of both $M_{\rm min}$ and $M_{\tilde{g}}$. The data generated when performing the 4j0l analysis (before imposing the $M_{\rm eff}$ cut itself) was used to obtain the results shown in these figures for the $\sim$ 68k pMSSM flat prior model set. The points are also color-coded to show whether they passed (green) or failed (red) the 4j0l analysis for an integrated luminosity of 1 fb^{-1} and an assumed 50% SM background uncertainty. Indeed, we see that there is a reasonably strong correlation between $M_{\rm eff}$ and $M_{\rm min}$ though somewhat less so in the case of $M_{\rm eff}$ and $M_{\tilde{g}}$. There are, however, several differences with the mSUGRA results: (*i*) our range of sparticle masses extends to significantly lower values than one finds in mSUGRA due to the strong Tevatron constraints on $m_{\tilde{g},\tilde{q}}$ in the mSUGRA framework. For small values of $M_{\rm min}$ we see that $M_{\rm eff}/M_{\rm min} \simeq 3$ which is quite far from the expected value of $\simeq 1.5$. However, for significantly larger values of $M_{\rm min} \gtrsim 600$ GeV, we do find that the relation $M_{\rm eff}/M_{\rm min} \simeq 1.5$ holds. (*ii*) The relationship between $M_{\rm eff}$ and $M_{\rm min}$ is thus not quite linear over the entire mass range of our model set. However, since $M_{\rm eff} \geq 350$ GeV is *required* to pass the 4j0l selection criteria before the $M_{\rm eff}$ cut is actually applied (and the points at low values of $M_{\rm min}$ are seen to mostly pass this analysis) we can obtain the approximate linear relationship $M_{\rm eff} \simeq 1.2 M_{\rm min} + 350$ GeV. (*iii*) The spread in values of $M_{\rm eff}$ at any given value for $M_{\rm min}$ is significantly wider than would be expected in mSUGRA with many pMSSM models falling quite far from the middle of the range. Note also that the unobservable models tend to have $M_{\rm eff}$ values somewhat further away from the mid-range. (*iv*) At small values of $M_{\rm min}$ we see that there is a sort of a gap or bifurcation in the distribution. This is connected to the identity of the lightest colored sparticle with the lower(upper) lobe corresponding to light gluinos(squarks). A study of other kinematic variables[66] used to determine the SUSY mass scale with this pMSSM model set could prove interesting.

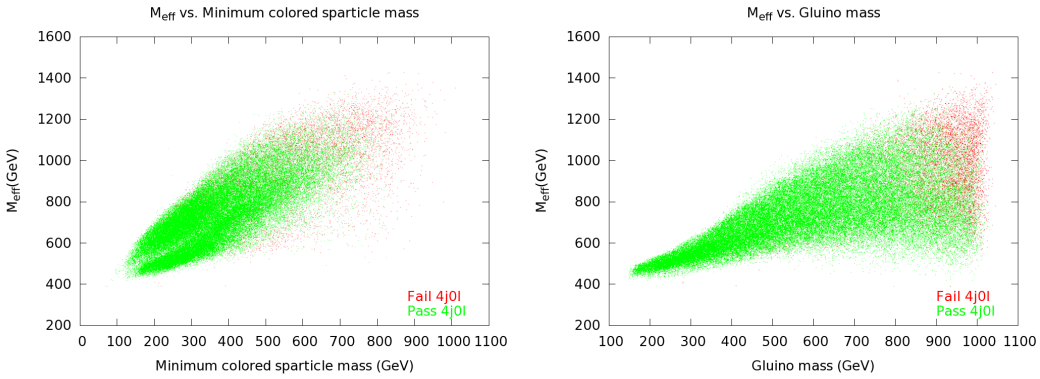

Figure 3.31: Values of M_{eff}as a function of the lightest colored sparticle mass (left) and the mass of the gluino (right) as described in the text.

3.5 Detector-Stable Sparticles

"Long-lived", "metastable", or "detector-stable" particles, *i.e.*, those particles which generally decay outside the detector when produced at colliders, can provide a striking signal of new physics (see [67] and references therein).

These detector-stable particles are found to be quite prevalent in both of our pMSSM model sets (to an extent that will be quantified below), but are not considered in the inclusive search analyses above. Given the nature of the analysis below, we can conveniently combine both the flat and log prior samples together to make a single common study.

Therefore we now discuss the phenomenological consequences of these detector-stable sparticles; the subsequent discussion, however, will be quite heuristic in comparison with the investigation of the inclusive SUSY search analyses discussed above. We will first explain our criteria for "detector-stability". We will then discuss the various species of sparticles, when, if ever, such sparticles can be detector-stable, and the prospects for discovering these detector-stable sparticles at the LHC. We will not discuss specific analyses, *e.g.*, searches for R-hadrons in the analysis presented below. Our main point here is that such long-lived states are relatively common in our model sets and that suches for long-lived states are an important supplement to the E_T^{miss} searches discussed above.

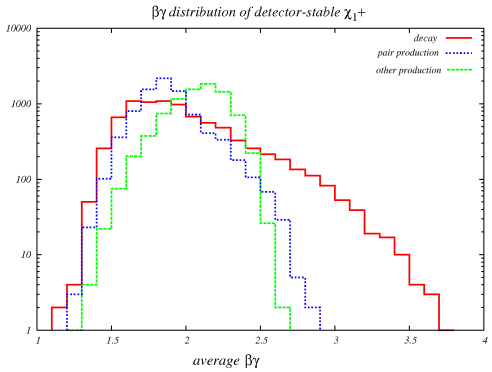

Figure 3.32: The distribution of $\beta\gamma$ for detector-stable charginos in our model set. The curve labeled "decay" refers to charginos produced in the cascade decay chains of other sparticles. "Pair production" refers to charginos directly produced in the $pp \to \tilde{\chi}_1^+ \tilde{\chi}_1^-$ hard process; "other production" refers to charginos produced in all other hard processes.

3.5.1 Criteria for Stability

A necessary first step is to specify what precisely qualifies as a "long-lived" or "detector-stable" particle. We note that for a particle at rest, its lifetime is given by $\frac{\hbar}{\Gamma}$ where Γ is the total width of the particle. This translates to the particle traveling a distance of $c\tau \sim \frac{c\beta\gamma\hbar}{\Gamma}$ in the detector.

There are several issues in determining a value of Γ, below which a particle will be considered (in this discussion) to be stable. Perhaps the most obvious is that the energy of the particle, and hence γ, will vary from event to event. Figure 3.32 shows the distribution of $\beta\gamma$ for detector-stable charginos in our pMSSM model set; this distribution is, of course, also sensitive to the mass distribution of the detector-stable charginos. We see that $\beta\gamma$ is $\lesssim 4$ for charginos in this model set; we expect this condition to hold at least roughly for the other species of stable particles as well. Therefore, we define a particle with width Γ to be "long-lived", or "detector-stable" if

$$\Gamma < \Gamma_{\text{stable}}, \text{ with } \Gamma_{\text{stable}} = 10^{-17}\,\text{GeV}. \tag{3.5.1}$$

For this value of Γ_{stable}, $\frac{c\hbar}{\Gamma} \sim 20$ m, and $\frac{c\beta\gamma\hbar}{\Gamma_{\text{stable}}} \sim 20 - 60$ m. The effect on our

quantitative results from adjusting the definition of Γ_{stable} will be discussed below.

We also note, from Figure 3.32, that the distribution of $\beta\gamma$ is quite different for charginos produced in cascade decay chains, compared with charginos produced directly in the hard process. In particular, these charginos may be more highly boosted, and, of course, be produced in events without an accompanying stable chargino. Such considerations may be very important for stable particle searches at the LHC.

Additional complications in assigning a threshold for stability arise from the probabilistic nature of decays; a full analysis taking such effects into account is beyond the scope of this work. Rather we discuss the prevalence of various detector-stable particles in our pMSSM model set in the next section, as well as the physics responsible for these sparticles' long lifetimes. Next, we will quantify the prospects for discovering or ruling out the detector-stable sparticles in our model set at the LHC.

It may be worthwhile to note that while we have considered models with absolutely stable charged particles (*i.e.*, charginos when the mass splitting with the LSP is less than the electron mass) to be excluded, we did not implement any constraints based on the effect a long-lived sparticle could have on BBN (see, for instance [67], [68], or [69]) when we generated our model sample.

3.5.2 Detector-Stable Sparticles and R-Hadrons

Table 3.20 shows the number of detector-stable sparticles of each type for different choices of Γ_{stable}; elsewhere we will always take $\Gamma_{\text{stable}} = 10^{-17}$ GeV as noted above. In what follows we will discuss the physics that can lead to detector-stable sparticles or R-hadrons, discussing gauginos first, and then sfermions.

If colored sparticles are long-lived, they can hadronize to form R-hadrons[67, 68, 70, 71, 72, 73, 74, 75, 76, 77, 78, 79, 80, 81, 82, 83, 84], a color singlet state carrying one unit of R-parity. We expect R-hadrons to form when the width of a colored particle is roughly $\Gamma \lesssim \Lambda_{\text{QCD}}$. In what follows, we will give the number of models in which various colored sparticles have total widths less than 100 MeV, taking this to be a rough indication of the number of models which would have significant R-hadron production. As the colored sparticles in our pMSSM model set have masses $\gg \Lambda_{QCD}$,

$\tilde{x}$	10^{-15}	10^{-16}	10^{-17}	10^{-18}	10^{-19}
$\tilde{\chi}_1^{\pm}$	9853	9728	8642	7683	6658
$\tilde{\tau}_1$	179	179	179	179	179
$\tilde{t}_1$	67	66	66	65	65
$\tilde{c}_R$	49	49	49	49	49
$\tilde{\chi}_2^0$	78	40	19	11	4
$\tilde{\mu}_R$	17	17	17	17	17
$\tilde{b}_1$	12	12	11	9	9
$\tilde{c}_L$	8	8	8	8	8
$\tilde{s}_R$	8	8	8	8	8
$\tilde{g}$	17	10	5	2	0

Table 3.20: The number of models in our pMSSM model set in which the specified sparticle ($\tilde{x}$) has a width less than the value given at the head of each column (in GeV). This gives some idea of the effect of the specific choice of $\Gamma_{\text{stable}} = 10^{-17}$ GeV.

the lifetime of the produced R-hadron should be roughly that of its constituent long-lived colored sparticle[67, 78, 81], so it is reasonable to use the same criterion for detector stability for colored and uncolored sparticles.

3.5.3 Detector Stability of Gauginos

Charginos

The most prevalent detector-stable particles in this pMSSM model set are charginos. This is due to the large number of models for which the lightest neutralino (the LSP) is mostly Higgsino or Wino, as is shown in Table 3.21. As is well known (see, for example, [85, 86, 87, 16, 88, 1, 2]) the Wino-like neutralino (with mass $\approx M_2$) is nearly degenerate with a Wino-like chargino. Likewise there are two nearly degenerate Higgsinos (with mass $\approx |\mu|$) which are in turn nearly degenerate with a Higgsino-like chargino. There are no models in our sample where the heavier of the two chargino species is stable.

As discussed above, we use a more detailed treatment than is given in SUSY-HIT to describe sparticle decay. In particular, for the case of close mass charginos that have small mass splittings with the LSP (Δm), we utilize expressions from [56, 57]

LSP Type	Definition	Fraction of Models
Bino	$\|Z_{11}\|^2 > 0.90$	0.156
Wino	$\|Z_{12}\|^2 > 0.90$	0.186
Higgsino	$\|Z_{13}\|^2 + \|Z_{14}\|^2 > 0.90$	0.393
All other models		0.265

Table 3.21: The majority of models in our pMSSM sample have LSPs which are relatively pure gaugino/Higgsino eigenstates. The fraction which are of each type is given here; with the definition of each type given in terms of the modulus squared of elements of the neutralino mixing matrix in the SLHA convention. See [89] for details.

to compute their decays exactly. We find that charginos generally fit our definition of detector-stability when $\Delta m = m_{\tilde{\chi}_1^\pm} - m_{\rm LSP} < 112$ MeV. The distribution of the $\tilde{\chi}_1^\pm$ width as a function of the $\tilde{\chi}_1^\pm$ LSP mass splitting is shown in Figure 3.33 for our pMSSM model set.

One sees from the figure that there is very little scatter in $\tilde{\chi}_1^\pm$ widths at low values of Δm and that the widths lie along a curve in this case. This is to be expected, as both the $\tilde{\chi}_1^\pm$ and the $\tilde{\chi}_1^0$ are nearly pure Higgsino and Wino eigenstates, and the widths are not dependent at this level on the rest of the SUSY spectrum. One can also see from Figure 3.33 where the three body chargino decay to $\mu^+\nu_\mu\tilde{\chi}_1^0$ turns on, and where the width becomes highly suppressed due to electron mass effects. The longest-lived chargino in our model set has $\Delta m = 512$ keV and a $c\tau$ of $\approx 5 \times 10^5$ light years, which is large even compared with the size of the ATLAS detector.

Neutralinos

There are 19 models in our pMSSM sample in which the second lightest neutralino is detector-stable. There are no models for which the third or fourth neutralino is detector-stable. Most, though not all, of the detector-stable second neutralinos are nearly Higgsino eigenstates, with the LSP being essentially the other neutral Higgsino eigenstate. In all cases where the second neutralino is detector-stable, the mass splitting of this neutralino with the LSP is less than ~ 650 MeV as can be seen

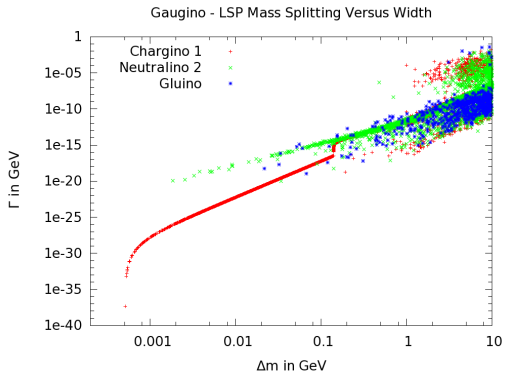

Figure 3.33: The width as a function of its mass splitting with the LSP (Δm) for the light chargino mass eigenstate (red), eigenstate, the second lightest neutralino mass eigenstate (green), and the gluino (blue). Heavier mass eigenstates for charginos and neutralinos tend to have larger mass splittings with the LSP and correspondingly large widths.

from Figure 3.33. From this figure it is clear that for low Δm, the neutralino width is basically a function of Δm. We also observe that unlike the case of charginos, the neutralino width as a function of Δm is a power law; *i.e.*, there are no obvious effects from the masses of decay products other than the LSP.

Gluinos

There are only 5 models for which the gluino width is less that Γ_{stable}; we take this to be a rough estimate of the number of cases for which the R-hadrons produced by such gluinos would be detector-stable. All of these models have a mass splitting between the gluino and LSP of $\lesssim 300$ MeV. There are, however, 12598 models where the gluino width is less than 100 MeV as shown in Table 3.22; these would be expected to form R-hadrons. The mass splitting between the LSP and the gluino is not necessarily small for these models as can be seen in Figure 3.33. Note also that there is a large spread in gluino widths, which is probably due to different patterns of squark masses, for the gluinos at any given Δm.

3.5.4 Detector Stability of Sfermions

The widths of the various species of sfermions as a function of the sparticle-LSP mass splitting are presented in Figures 3.34, 3.35, 3.36, 3.37, 3.38, and 3.39. Here, we will discuss salient aspects of the physics that leads to detector-stable sfermions in our pMSSM model set.

Close Mass Sparticles, Degeneracies, and Important Decay Modes

We remind the reader that in our pMSSM model set, the masses of the first and the corresponding second generation sparticle (such as left selectron and left smuon) are degenerate. In addition, these sparticles have the same couplings, except for Yukawa couplings that are generally negligible. Thus the first and corresponding second generation sfermion also have degenerate widths. Hence, for example, a point in Figure 3.34 for the left smuon lies on top of the point for the left selectron for all models.

The exception to this picture occurs when, for some sfermion, $\Delta m \lesssim m_f$, where f is the corresponding fermion. This is because for Δm slightly greater than m_f, the decay $\tilde{f} \rightarrow \tilde{\chi}_1^0 f$ is kinematically suppressed, and when $\Delta m < m_f$, this decay is forbidden. As this decay is generally very important for close mass sfermions, this leads to large suppressions of the sfermion decay widths. We note that the suppression due to small Δm may occur for the second generation sfermion but not the first generation sfermion when $m_{f_1} < \Delta m < m_{f_2}$. We do not find many models where charged current decays such as $\tilde{c} \rightarrow \tilde{\chi}_1^+ s$ have a large effect on the widths of close mass sfermions. The exception is in models where the stau has $\Delta m < m_\tau$, and is not detector-stable due to the decay $\tilde{\tau} \rightarrow \nu_\tau + \tilde{\chi}^+$.

Generally, in fact, we set the decay width to be zero for first and second generation sfermions when $\Delta m < m_f$ since we do not include four-body decays for these sfermions, or CKM suppressed decays in the case of first and second generation squarks. This has an important consequence for Figures 3.34, 3.35, 3.36, 3.37, 3.38,

and 3.39 as a sparticle not appear in the figures if its width is zero. A stable second generation sparticle can be identified by noting where one sees a point for the first generation sparticle with out a nearly degenerate point for the second generation sparticle.

For third generation squark decays, some of these additional decay modes were included in calculating the widths as discussed above. CKM suppressed and four-body stop decays are included in SUSY-HIT[33]. SUSY-HIT does not, however, incorporate these decays for sbottoms and we added the CKM suppressed decays (though not the four-body decays) for sbottoms.

We should note that our analysis may somewhat overstate the prevalence of detector-stable second generation sfermions in the model set. If the mixing between right and left sfermions were not precisely zero, the mass of the lighter eigenstate would be raised, possibly so that the decay $\tilde{f} \rightarrow \tilde{\chi}_1^0 f$ would not be significantly suppressed. A full understanding of this effect would have required the inclusion of trilinear coupling terms for the first two generations.

Like gluinos, squarks are colored sparticles and hence can form R-hadrons as discussed above. The number of squarks of each flavor which have widths < 100 MeV $\approx \Lambda_{QCD}$ is shown in Table 3.22.

Sum Rules and the Effect on which Sparticles are Stable

The 17 right-handed smuons with $\Delta m < m_\mu$ are the only charged sleptons that we find to be detector stable. The fact that it is right-handed rather than left-handed smuons which are detector stable in this model set is in part a consequence of the tree-level slepton mass sum rule (see for example [85, 86, 1, 2])

$$m_{\tilde{l}_L}^2 - m_{\tilde{\nu}_l}^2 = -\cos(2\beta) m_W^2. \tag{3.5.2}$$

When $\tan\beta > 1$, as in our pMSSM model set, the electron (muon) sneutrino is always lighter than the left-handed selectron (smuon). This means the left-handed selectron (smuon) is at best the third lightest sparticle and thus generically has a sufficient value of Δm to decay promptly. In fact, the minimum width for such particles in the

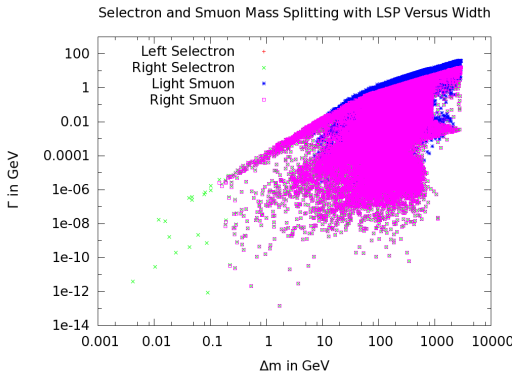

Figure 3.34: The width as a function of the mass splitting with the LSP (Δm) for the left- and right-handed selectrons and smuons. Note that as we do not include four-body smuon decays, when $\Delta m < m_\mu$ the smuon width is set to zero; thus for small Δm we see points corresponding to right-handed selectrons without the corresponding smuon point.

model set is ~ 2 keV, far greater than Γ_{stable}. As the right-handed sleptons are $SU(2)$ singlets, there is no similar effect, and they can have arbitrarily small Δm; models with cosmologically stable right-handed sleptons were excluded when our pMSSM model set was generated. A similar situation holds for squarks, where there are fewer models where $\tilde{d}_L$ or $\tilde{s}_L$ have close mass splittings.

3.5.5 Detector-Stable Sparticle Prospects

In Table 4.5 the approximate 14 TeV LHC reach for each sparticle, using [68], is presented for the specified integrated luminosities. These bounds are somewhat conservative, as they only take pair production into account; it is difficult to determine a model independent reach including detector stable particles produced in cascade decays. We assume this reach is generation independent. (This may not necessarily be the case for stable up-squarks, for example, as in such a case there could be significant contributions from t channel production.) Further, we make the conservative assumption that we can neglect the ≈ 1 fb^{-1} of data that will be collected at 7 TeV. Nonetheless, one can obtain a qualitatively accurate picture of the prospects for LHC discovery for detector-stable sparticles in this pMSSM model set.

$\tilde{g}$	12598
$\tilde{u}_L$	9628
$\tilde{c}_L$	9629
$\tilde{u}_R$	22667
$\tilde{c}_R$	22668
$\tilde{d}_L$	13595
$\tilde{s}_L$	13595
$\tilde{d}_R$	27996
$\tilde{s}_R$	27998
$\tilde{b}_1$	13355
$\tilde{b}_2$	431
$\tilde{t}_1$	5695
$\tilde{t}_2$	1

Table 3.22: The number of squarks or gluinos of the indicated species with widths < 100 MeV. This gives a rough idea of the number of models where R-hadrons would be formed; however in most cases the R-hadrons decay promptly in the detector.

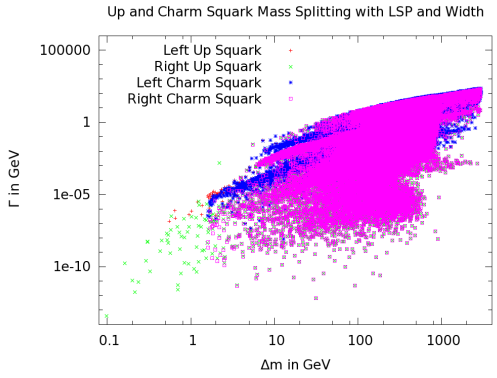

Figure 3.35: The distribution of widths for up and charm squarks as a function of Δm, the mass splitting between the sparticle and the LSP.

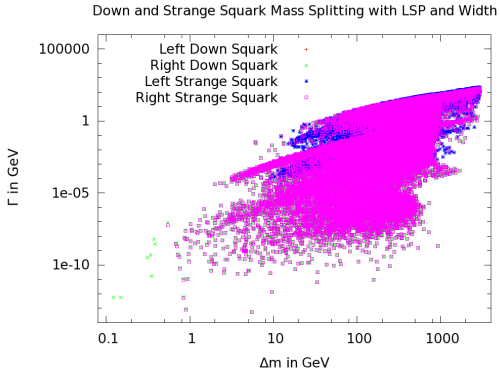

Figure 3.36: The distribution of widths for down and strange squarks as a function of Δm, the mass splitting between the sparticle and the LSP.

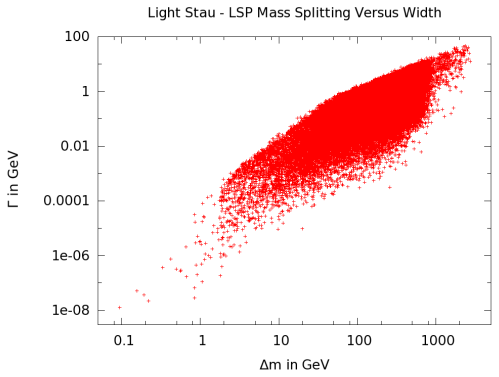

Figure 3.37: The distribution of widths for the lighter stau mass eigenstate as a function of Δm, the mass splitting between the sparticle and the LSP.

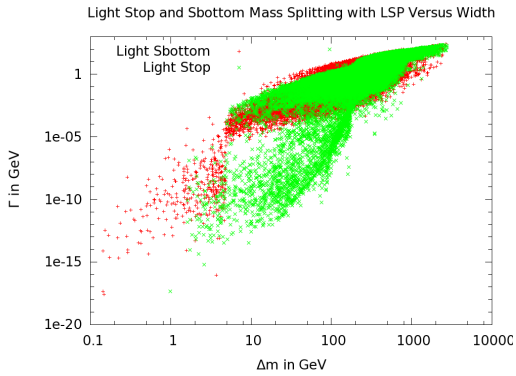

Figure 3.38: The distribution of widths for the lightest stop and sbottom as a function of Δm, the mass splitting between the sparticle and the LSP. Note: in 65 models the calculated light stop width is zero, representing nearly all of the detector-stable stops in the model set. Likewise there are 9 models in which the calculated light sbottom width is zero.

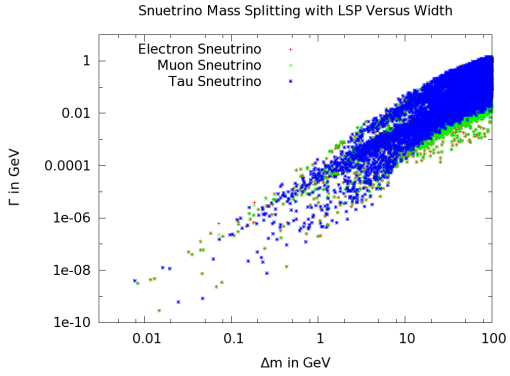

Figure 3.39: The distribution of widths for the three species of sneutrinos as a function of Δm, the mass splitting between the sparticle and the LSP. The minimum width for the electron or smuon sneutrinos in our model set is $\approx 3 \times 10^{-10}$ GeV.

Sparticle	LHC Reach 1 fb^{-1}	LHC Reach 10 fb^{-1}
$\tilde{\chi}^+$ ($\tilde{W}$-like)	365 GeV	467 GeV
$\tilde{\chi}^+$ ($\tilde{H}$-like)	280 GeV	376 GeV
$\tilde{\tau}$ (or $\tilde{\mu}$)	145 GeV	198 GeV
$\tilde{t}$ (or $\tilde{c}$)	562 GeV	681 GeV
$\tilde{b}$ (or $\tilde{s}$)	562 GeV	681 GeV
$\tilde{g}$	$>$ 1000 GeV	$>$ 1000 GeV

Table 3.23: The approximate 14 TeV LHC search reach for stable particles of a given type with 1 and 10 fb^{-1}[68]. These search reaches assume the sparticles are produced in the hard subprocess, rather than in cascade decays. For simplicity, we take the LHC reach for sbottoms to be equal to that for stops.

Table 4.6 shows the number of detector-stable ($\Gamma < 10^{-17}$ GeV) sparticles of various species in the model set, as well as the number of such sparticles which would have evaded discovery at the LHC with 1 and 10 fb^{-1} of integrated luminosity, following [68]. In addition, the LHC search reach for charginos, and its effectiveness in discovering or excluding detector-stable charginos in our model set, is shown in Figure 3.40.

Complementarity with Astrophysics

Since detector-stable particles are nearly degenerate with the LSP, they provide important channels for co-annihilation in the early universe. Thus, we expect models with detector-stable particles to have lower values for the relic density. In our pMSSM model set, there are no models with a detector stable particle with a relic density greater than $\Omega h^2 = 0.089$. Thus, the subset of these models considered in special detail in [90], all of which have $\Omega h^2 > 0.1$, do not have detector-stable particles. This suggests that the discovery of a detector-stable particle at the LHC would have important consequences for cosmology, as well as for particle physics.

$\tilde{x}$	Total	LHC-1	LHC-10
$\tilde{\chi}_1^+$	8642	560	72
$\tilde{\tau}_1$	179	179	179
$\tilde{t}_1$	66	4	0
$\tilde{c}_R$	49	0	0
$\tilde{\mu}_R$	17	16	16
$\tilde{b}_1$	11	0	0
$\tilde{c}_L$	8	0	0
$\tilde{s}_R$	8	0	0
$\tilde{g}$	5	0	0

Table 3.24: The number of stable particles of various types ($\tilde{x}$) present in our pMSSM model set (under "Total") and the number that would not have been discovered with 1 (under LHC-1) and 10 (under LHC-10) fb^{-1} at 14 TeV, following [68]. Note that the LHC will be more efficient at discovering or excluding stable squarks, gluinos, or charginos than sleptons.

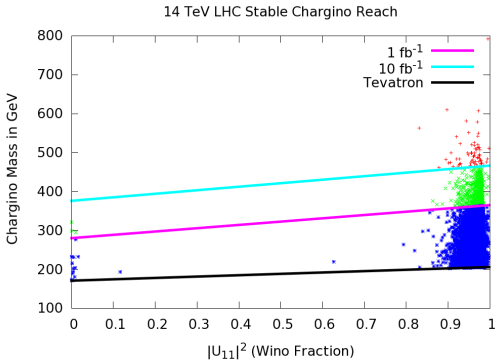

Figure 3.40: The 14 TeV LHC search reach for stable wino-like charginos with 1 and 10 fb^{-1} of integrated luminosity following [68]. As noted above, these reaches assume pair production of the charginos. We also show the Tevatron reach after 1.1 fb^{-1} [44].

3.6 Conclusions

In this paper we have investigated the robustness of the ATLAS SUSY searches prepared for the 14 TeV LHC. We passed an extensive set of broad-based SUSY models through the full planned SUSY analysis suite, following the analysis procedure designed by ATLAS in detail. We employed our previously generated $\sim$ 71k model points in the 19-dimensional pMSSM parameter space. We simulated the eleven ATLAS SUSY $E_T^{\rm miss}$ analyses, as well as the stable charged particle search, which were originally designed for an exploration of mSUGRA-based models. To test our approach, we first applied our analysis to the set of ATLAS mSUGRA model benchmark points and successfully reproduced the published results obtained previously by ATLAS. We found that for the case of the $\sim$ 68k models from the flat prior scan, where the squarks and gluinos have masses below $\lesssim$ 1 TeV, essentially all of the pMSSM points ($> 99\%$) were observable in at least one of the ATLAS $E_T^{\rm miss}$ analyses allowing for an uncertainty of 50% in the SM background with 1 fb^{-1} of integrated luminosity. Even this excellent level of parameter space coverage was seen to improve when these systematic errors were reduced to 20%. Furthermore, most of these pMSSM models were found to give significant signals in several of these $E_T^{\rm miss}$ analysis channels simultaneously. In the log prior model sample, totalling $\sim$ 3k models, the success rate for discovery fell to approximately $\sim$ 68(81)% for an assumed 50(20%) SM background error. This is also quite impressive since the sparticle masses could be as large as 3 TeV in this model set. We emphasize that these statistics apply only to our pMSSM model set, but believe they are indicative of the performance of the LHC SUSY searches in a broader SUSY parameter space. In summary, although they were designed for mSUGRA, we found that the ATLAS SUSY search analyses are quite powerful in their ability to cover the points in the pMSSM model space. This is quite reassuring!

Model points that were *not* observable by any of the ATLAS search analyses were found to be relatively few in number, *i.e.*, below $\sim$ 0.57(0.02)% in the case of the flat prior sample assuming a 50(20)% systematic uncertainty in the background. The main reasons why these models were missed can be summarized as follows: (i) In

the most trivial cases, the colored sparticles, which have the largest production cross sections, were found to have kinematically suppressed production rates since these particles were heavy. This was a much more common occurrence in the case of the log prior model set where the masses of the squarks and gluinos were allowed to be as large as ~ 3 TeV.

(*ii*) Many models contain charginos that are close in mass to the LSP due to the high proportion of the occurrence of Higgsino-like or Wino-like LSPs in our model set, unlike in most mSUGRA models. For some models there were substantially large branching fractions for squarks to decay to these charginos. In such cases, essentially stable charginos were then found to occur at the end of most decay chains thus leading to a reduction in the average amount of $E_T^{\rm miss}$ that was produced in typical events. Since the ATLAS analyses required a fairly large amount of $E_T^{\rm miss}$ to obtain significant observable signals, these models were more easily undetected. Reducing the ATLAS $E_T^{\rm miss}$ requirements might allow access to some of these models at the expense of increased SM backgrounds; this requires further study. Also for such cases, searches for stable charged particles become of great importance, particularly when these states appear, as they more commonly do, at the end of long SUSY cascade decay chains and are not simply pair produced in isolation. We found that that the $\beta\gamma$ distribution was quite different for stable charginos produced in cascade decays than for those directly produced in hard processes; the observability of such stable particles requires further study.

(*iii*) Some models in our pMSSM set have a rather compressed mass spectra. This results in a significant reduction in phase space which is available in the various decays and, hence, in a corresponding decrease in the values of p_T available for the final state jets and leptons. These final state objects were then too soft to satisfy the necessary analysis cuts.

(*iv*) Processes with large backgrounds have an associated correspondingly large systematic uncertainty of $\delta B = (50\%, 20\%)$. In order to reach a significance of 5 or more, a requirement for discovery, a substantially larger number of signal events must be produced. For example, the 4j0l(2j0l) analysis requires 1759(2778) signal events to reach the $S = 5$ level assuming a luminosity of 1 fb^{-1} provided $\delta B = 50\%$. However,

a reduction in the background uncertainty to $\delta B = 20\%$, substantially decreases the required number of signal events to only 721(1129) to reach $S = 5$. Thus it is clear that a reduction in the systematic uncertainty in the SM background is very important in order to increase the coverage of the pMSSM model space. In cases where the large background uncertainties were important, we found that increasing the luminosity by a factor of 10 was not very useful in increasing the parameter space coverage. This is expected due to the corresponding dominance of the background systematic errors.

The study presented in this paper suggests a number of areas for future work. In light of the current status of the LHC, repeating this analysis with a 7 TeV center-of-mass energy and perhaps somewhat lower luminosities is an obvious next step [91]; such a study is now underway.

The preliminary study of stable particles in the MSSM presented here makes it clear that more work could be performed in this area. A more detailed modeling of the interactions and decays of R-hadrons, for example, is necessary to accurately predict their signatures at the LHC. Searches for stable particles produced in decay chains, rather than pair-produced in the hard process, also deserves significant study.

As always, it would be interesting to explore ways to optimize the kinematic cuts or otherwise modify the search analyses to obtain a better performance across the general MSSM. This would require generating the actual background events, so that various distributions could be examined.

In summary, we found that the standard SUSY search analyses, taken together, provide excellent coverage of the MSSM parameter space at the LHC with relatively small luminosity, at least for sparticle masses up to $\sim$ TeV. We conclude that the prospects for observing Supersymmetry in the early running of the LHC are quite good!

Bibliography

[1] M. Drees, R. Godbole, and P. Roy, Hackensack, USA: World Scientific (2004) 555 p.

[2] H. Baer and X. Tata, Cambridge, UK: Univ. Pr. (2006) 537 p.

[3] Particle Data Group, C. Amsler *et al.*, Phys. Lett. **B667**, 1 (2008).

[4] E. Cremmer, P. Fayet, and L. Girardello, Phys. Lett. **B122**, 41 (1983).

[5] G. F. Giudice and R. Rattazzi, Phys. Rept. **322**, 419 (1999), hep-ph/9801271.

[6] M. Dine, A. E. Nelson, Y. Nir, and Y. Shirman, Phys. Rev. **D53**, 2658 (1996), hep-ph/9507378.

[7] L. Randall and R. Sundrum, Nucl. Phys. **B557**, 79 (1999), hep-th/9810155.

[8] G. F. Giudice, M. A. Luty, H. Murayama, and R. Rattazzi, JHEP **12**, 027 (1998), hep-ph/9810442.

[9] Z. Chacko, M. A. Luty, A. E. Nelson, and E. Ponton, JHEP **01**, 003 (2000), hep-ph/9911323.

[10] D. E. Kaplan, G. D. Kribs, and M. Schmaltz, Phys. Rev. **D62**, 035010 (2000), hep-ph/9911293.

[11] D0, V. M. Abazov *et al.*, Phys. Lett. **B660**, 449 (2008), 0712.3805.

[12] The ATLAS, G. Aad *et al.*, (2009), 0901.0512.

[13] C. F. Berger, J. S. Gainer, J. L. Hewett, and T. G. Rizzo, JHEP **02**, 023 (2009), 0812.0980.

[14] J. Alwall, M.-P. Le, M. Lisanti, and J. G. Wacker, Phys. Lett. **B666**, 34 (2008), 0803.0019.

[15] J. Alwall, M.-P. Le, M. Lisanti, and J. G. Wacker, Phys. Rev. **D79**, 015005 (2009), 0809.3264.

[16] L. Pape and D. Treille, Rept.Prog.Phys. **69**, 2843 (2006).

[17] LHC/LC Study Group, G. Weiglein *et al.*, Phys.Rept. **426**, 47 (2006), hep-ph/0410364.

[18] R. C. Cotta, J. S. Gainer, J. L. Hewett, and T. G. Rizzo, New J. Phys. **11**, 105026 (2009), 0903.4409.

[19] R. C. Cotta, J. S. Gainer, J. L. Hewett, and T. G. Rizzo, Nucl. Phys. Proc. Suppl. **194**, 133 (2009), 0909.4088.

[20] A. Djouadi, J.-L. Kneur, and G. Moultaka, Comput. Phys. Commun. **176**, 426 (2007), hep-ph/0211331.

[21] G. D'Ambrosio, G. F. Giudice, G. Isidori, and A. Strumia, Nucl. Phys. **B645**, 155 (2002), hep-ph/0207036.

[22] G. Belanger, F. Boudjema, A. Pukhov, and A. Semenov, Comput. Phys. Commun. **177**, 894 (2007).

[23] G. Belanger, F. Boudjema, A. Pukhov, and A. Semenov, Comput. Phys. Commun. **180**, 747 (2009), 0803.2360.

[24] G. Belanger, F. Boudjema, A. Pukhov, and A. Semenov, Comput. Phys. Commun. **149**, 103 (2002), hep-ph/0112278.

[25] G. Belanger, F. Boudjema, A. Pukhov, and A. Semenov, Comput. Phys. Commun. **174**, 577 (2006), hep-ph/0405253.

[26] G. Belanger, F. Boudjema, A. Pukhov, and A. Semenov, Comput. Phys. Commun. **176**, 367 (2007), hep-ph/0607059.

[27] W. Beenakker, R. Hopker, and M. Spira, (1996), hep-ph/9611232.

[28] W. Beenakker, R. Hopker, M. Spira, and P. M. Zerwas, Nucl. Phys. **B492**, 51 (1997), hep-ph/9610490.

[29] W. Beenakker, M. Kramer, T. Plehn, M. Spira, and P. M. Zerwas, Nucl. Phys. **B515**, 3 (1998), hep-ph/9710451.

[30] W. Beenakker *et al.*, Phys. Rev. Lett. **83**, 3780 (1999), hep-ph/9906298.

[31] M. Spira, (2002), hep-ph/0211145.

[32] T. Plehn, Czech. J. Phys. **55**, B213 (2005), hep-ph/0410063.

[33] A. Djouadi, M. M. Muhlleitner, and M. Spira, Acta Phys. Polon. **B38**, 635 (2007), hep-ph/0609292.

[34] T. Sjostrand, S. Mrenna, and P. Z. Skands, JHEP **05**, 026 (2006), hep-ph/0603175.

[35] J. Conway, Pgs4, `Mhttp://www.physics.ucdavis.edu/~conway/research/software/pgs/pgs.html`.

[36] G. J. Feldman and R. D. Cousins, Phys. Rev. **D57**, 3873 (1998), physics/9711021.

[37] CDF, T. Aaltonen *et al.*, Phys. Rev. Lett. **101**, 251801 (2008), 0808.2446.

[38] CDF, T. Aaltonen *et al.*, Phys. Rev. Lett. **101**, 071802 (2008), 0802.3887.

[39] D0, V. M. Abazov *et al.*, Phys. Rev. Lett. **97**, 171806 (2006), hep-ex/0608013.

[40] CDF and D0, V. Buescher *et al.*, (2005), hep-ex/0504004.

[41] D0, V. M. Abazov *et al.*, Phys. Lett. **B665**, 1 (2008), 0803.2263.

[42] CDF, T. Aaltonen *et al.*, Phys. Rev. **D76**, 072010 (2007), 0707.2567.

[43] CDF, F. Abe *et al.*, Phys. Rev. **D46**, 1889 (1992).

[44] D0, V. M. Abazov *et al.*, Phys. Rev. Lett. **102**, 161802 (2009), 0809.4472.

[45] G. Benelli, UMI-31-09638.

[46] LEP Electroweak Working Group, Mhttp://www.cern.ch/LEPEWWG.

[47] ALEPH, R. Barate *et al.*, Phys. Lett. **B469**, 303 (1999).

[48] LEP SUSY Working Group, Mhttp://lepsusy.web.cern.ch/lepsusy.

[49] LEP Higgs Working Group,Mhttp://lephiggs.web.cern.ch/LEPHIGGS/www/Welcome.html.

[50] S. Heinemeyer, W. Hollik, and G. Weiglein, Phys. Rept. **425**, 265 (2006), hep-ph/0412214.

[51] D. Feldman, Z. Liu, and P. Nath, JHEP **04**, 054 (2008), 0802.4085.

[52] We would like to thank the various members of the ATLAS SUSY group with providing us with this information on SM backgrounds as well as for many discussions during the course of this analysis.

[53] Atlas Collaboration, G. Aad *et al.*, (2011), 1102.5290, * Temporary entry *.

[54] CMS Collaboration, V. Khachatryan *et al.*, Phys.Lett. **B698**, 196 (2011), 1101.1628, * Temporary entry *.

[55] (2011).

[56] C. H. Chen, M. Drees, and J. F. Gunion, Phys. Rev. **D55**, 330 (1997), hep-ph/9607421.

[57] C. H. Chen, M. Drees, and J. F. Gunion, (1999), hep-ph/9902309.

[58] P. M. Nadolsky *et al.*, Phys. Rev. **D78**, 013004 (2008), 0802.0007.

[59] D. Stump *et al.*, JHEP **10**, 046 (2003), hep-ph/0303013.

[60] G. Corcella *et al.*, JHEP **01**, 010 (2001), hep-ph/0011363.

[61] G. Corcella *et al.*, (2002), hep-ph/0210213.

[62] S. Moretti, K. Odagiri, P. Richardson, M. H. Seymour, and B. R. Webber, JHEP **04**, 028 (2002), hep-ph/0204123.

[63] Lance J. Dixon, private communication.

[64] A. J. Barr and C. G. Lester, (2010), 1004.2732.

[65] I. Hinchliffe, F. E. Paige, M. D. Shapiro, J. Soderqvist, and W. Yao, Phys. Rev. **D55**, 5520 (1997), hep-ph/9610544.

[66] See for a recent overview of these various observables and original references, T. Robens, talk given at SUSY2010, Bonn, Germany, 23-28 Aug. 2010.

[67] M. Fairbairn *et al.*, Phys. Rept. **438**, 1 (2007), hep-ph/0611040.

[68] A. R. Raklev, (2009), 0908.0315.

[69] F. D. Steffen, JCAP **0609**, 001 (2006), hep-ph/0605306.

[70] G. R. Farrar and P. Fayet, Phys. Lett. **B76**, 575 (1978).

[71] M. S. Chanowitz and S. R. Sharpe, Phys. Lett. **B126**, 225 (1983).

[72] J. L. Hewett, T. G. Rizzo, and M. A. Doncheski, Phys. Rev. **D56**, 5703 (1997), hep-ph/9612377.

[73] G. R. Farrar, Phys. Rev. Lett. **53**, 1029 (1984).

[74] F. Buccella, G. R. Farrar, and A. Pugliese, Phys. Lett. **B153**, 311 (1985).

[75] G. R. Farrar, Phys. Rev. **D51**, 3904 (1995), hep-ph/9407401.

[76] H. Baer, K.-m. Cheung, and J. F. Gunion, Phys. Rev. **D59**, 075002 (1999), hep-ph/9806361.

[77] E. L. Berger *et al.*, Phys. Rev. Lett. **86**, 4231 (2001), hep-ph/0012001.

[78] T. Sjostrand and P. Z. Skands, Nucl. Phys. **B659**, 243 (2003), hep-ph/0212264.

[79] J. L. Hewett, B. Lillie, M. Masip, and T. G. Rizzo, JHEP **09**, 070 (2004), hep-ph/0408248.

[80] A. C. Kraan, Eur. Phys. J. **C37**, 91 (2004), hep-ex/0404001.

[81] W. Kilian, T. Plehn, P. Richardson, and E. Schmidt, Eur. Phys. J. **C39**, 229 (2005), hep-ph/0408088.

[82] R. Mackeprang and A. Rizzi, Eur. Phys. J. **C50**, 353 (2007), hep-ph/0612161.

[83] R. Mackeprang, AIP Conf. Proc. **1200**, 746 (2010), 0909.5104.

[84] M. R. Buckley, B. Echenard, D. Kahawala, and L. Randall, (2010), 1008.2756.

[85] H. E. Haber and G. L. Kane, Phys. Rept. **117**, 75 (1985).

[86] S. P. Martin, (1997), hep-ph/9709356.

[87] D. J. H. Chung *et al.*, Phys. Rept. **407**, 1 (2005), hep-ph/0312378.

[88] H. K. Dreiner, H. E. Haber, and S. P. Martin, Phys. Rept. **494**, 1 (2010), 0812.1594.

[89] P. Z. Skands *et al.*, JHEP **07**, 036 (2004), hep-ph/0311123.

[90] R. C. Cotta, J. A. Conley, J. S. Gainer, J. L. Hewett, and T. G. Rizzo, (2010), 1007.5520.

[91] ATLAS has performed a preliminary study with a fraction of our pMSSM model set for center-of-mass energies of 10 TeV in ATL-PHYS-PUB-2009-084, July 2009.

Chapter 4

Supersymmetry Without Prejudice at the 7 TeV LHC

4.1 Introduction and Background

The LHC has had an initial run at 7 TeV with both the ATLAS and CMS experiments collecting $\sim 35 - 45$ pb^{-1} of useful data. Even with this low integrated luminosity these experiments have been able to extend searches far beyond the reach of the Tevatron for many new physics scenarios with, so far, null results [1, 2]. This clearly demonstrates the power of increasing the center of mass energy in the search for new physics at hadron colliders. Starting soon, the LHC is to begin a longer run at 7 TeV and is expected to collect of order $1 - 7$ fb^{-1} of data over the next 2 years. Such a data set will allow for a first exploration of the TeV mass scale, and if new strongly interacting particles exist in this kinematic regime, they should be observed.

A well-motivated, and perhaps most popular, possibility for new physics that may be discovered during this coming LHC run is Supersymmetry (SUSY) [3]. Both ATLAS [4] and CMS [5] have designed detailed searches for many of the SUSY partners of the Standard Model (SM) particles; these are mostly (but not exclusively) based on the assumption of mSUGRA/CMSSM-like soft breaking within the Minimal Supersymmetric Standard Model (MSSM) framework. This assumption greatly simplifies the exploration of the vast Supersymmetric parameter space. While these searches

are designed to well cover the parameter space of these SUSY-breaking scenarios it is important to ascertain their discovery potential in a more general MSSM context. This is particularly worrisome in light of results from the Tevatron, where it has been realized [6, 7] that relatively light gluinos may have escaped undetected. The question then arises whether these specific scenarios and associated searches adequately describe the true breadth of the MSSM and its possible collider signatures, and whether the LHC searches as presently designed could fail to observe sparticle production. This has prompted several studies of more model independent search strategies as well as the development of simplified models [8].

Recently, we have addressed [9] this question by investigating the capability of the 14 TeV LHC to explore a more general MSSM model parameter space, i.e., that of the pMSSM (phenomenological MSSM) [7], to be described below, from the point of view of the ATLAS detector. In particular, we examined the performance of the planned ATLAS SUSY searches in exploring this more general MSSM scenario. This analysis provides insight into general features of the MSSM without reference to a particular SUSY breaking scenario or any other assumptions at the GUT scale. We found that the ATLAS mSUGRA-inspired searches, based on missing E_T, did surprisingly well at covering the kinematically accessible portions of this model space; we also found that some interesting exceptions can arise in these more general models. Given the lower-energy run of the LHC over the next 2 years it behooves us to determine how well the corresponding mSUGRA motivated searches designed by ATLAS would perform under these conditions, since this is the situation presently before us. This is the goal of the present paper. We note that recently there have been several mSUGRA-based studies evaluating the capability of the 7 TeV LHC run to probe that parameter space [10]

As is well known, soft SUSY breaking within the MSSM in all generality leads to a theory with over ~ 100 a priori free parameters which prohibits a detailed study of this theory. A number of theoretically possible scenarios exist which describe the breaking of Supersymmetry; maybe even multiple mechanisms are simultaneously responsible. Practically speaking, there are two ways to approach reducing this large number of a priori unknown parameters to something more manageable. One approach is to

consider only specific, well-motivated SUSY breaking scenarios, such as mSUGRA or others. This leads to a drastic reduction in the number of free parameters (to only $\sim 3-5$) so that detailed analyses of the resulting parameter space can be easily achieved. A problem with performing such studies is that they may result in a bias as to the nature of SUSY signals when searching for collider or other SUSY signatures. An alternative approach is to be less prejudicial and to instead follow a bottom-up analysis which we have employed in a number of recent works [9, 11] and will make use of here. By imposing a set of theoretically and experimentally well-motivated constraints on the general MSSM (to be described below), without making any reference to the specific mechanism of SUSY breaking, we arrive at a theory with 19 TeV-scale parameters. This is known as the pMSSM, which is significantly more manageable than the full Supersymmetric parameter space, and yet allows for more breadth than is present in , *e.g.*, mSUGRA.[1] These parameters will then completely define and describe all aspects of TeV-scale SUSY phenomenology. Such an approach has the advantage of being more general than any given (or given set of) specific SUSY breaking scenario(s) and allows one to be in some sense agnostic about the SUSY mass spectrum.

To this end, we examine the $E_T^{\rm miss}$-based SUSY searches developed by the ATLAS collaboration for the 7 TeV LHC [12]. We simulate the pMSSM signal for roughly 71k pMSSM models (hereafter 'model' refers to a point in the 19-dimensional pMSSM parameter space) that we generated in our previous work [7]. We employ SM backgrounds provided by the ATLAS Collaboration. In Section 2, we describe our SUSY model generation and LHC analysis procedure. It is important to note that we strictly adhere to the analyses as designed by ATLAS. While numerous, and perhaps improved, SUSY collider search techniques have been discussed in the literature [13], it is not our present purpose here to discuss or employ them. Section 3 contains our main results. We find the systematic error in determining the SM background to SUSY production is a limiting factor in the potential discovery of these models; in fact, some channels become systematics limited at larger luminosities. In this section

[1] Even in such a case a full exploration of this large parameter space is at best difficult if not impossible with present computing power.

we determine the fraction of our pMSSM model set that is discoverable at the 7 TeV LHC. We then examine the model characteristics in some detail that render some of the models undetectable. We find that the observability of models depends on the precise details of the sparticle spectrum and that a blanket statement of constraints on the mass of, say the gluino or squarks, cannot be made. In this Section, we also explore potential modifications to the kinematic cuts in these analyses that may improve model observability. In Section 4, we examine the implications of a null SUSY search during this run with respect to the degree of fine-tuning present in these models, as well as the implications for sparticle production at a high energy e^+e^- Linear Collider. A summary and our conclusions can be found in Section 5.

4.2 Analysis Procedure for Inclusive SUSY Production

The purpose of this work is to explore how well mSUGRA-inspired inclusive SUSY searches (in particular the set proposed by the ATLAS collaboration [12]) apply to the larger and much more general pMSSM parameter space for the 7 TeV run of the LHC. This is similar in spirit to to Ref. [9], which explored this question for the more powerful 14 TeV LHC. The pMSSM model sample that we study was generated in Ref. [7]; here, we briefly review the procedure employed to generate this sample. We then describe our procedure for generating the signal events, comparing to background, and determining the statistical criteria for discovery. We will show that we faithfully reproduce the ATLAS results in each analysis channel for their benchmark SUSY model.

As stated above, we study the 19-dimensional parameter space of the pMSSM. This set of parameters was arrived at [14] by imposing the following set of requirements onto the general R-Parity conserving MSSM: (*i*) the soft parameters are taken to be real so that there are no new CP-violating sources beyond those in the usual CKM matrix; (*ii*) Minimal Flavor Violation(MFV) [15] is assumed to be valid at the

TeV scale; (*iii*) the first two generations of sfermions having the same quantum numbers are taken to be degenerate and to have negligible Yukawa couplings and (*iv*) the lightest neutralino is assumed to be the Lightest Supersymmetric Particle(LSP) and is a stable thermal WIMP. Most of these assumptions are applied in order to avoid issues associated with flavor physics constraints. With these conditions, the remaining 19 free soft-breaking parameters are given by the three gaugino masses, $M_{i=1-3}$, the ten sfermion masses $m_{\tilde{f}}$, the three A-terms for the third generation fermions ($A_{b,t,\tau}$), and the usual Higgs sector parameters μ, M_A and $\tan\beta$.

To generate the specific pMSSM parameter points that we study below (hereafter referred to as our set of models), we performed numerical scans over the space formed by these 19 parameters. This required both a selection of the parameter range intervals as well as an assumption about the nature of the scan prior for how points are chosen within these intervals. These issues are both described in detail in our previous works [7, 9, 11] and the interested reader should refer to them directly. Here, we simply note that two scans were performed: one employing a flat prior beginning with 10^7 points and one with a log prior (that is, flat in the logarithm of the mass parameters) employing 2×10^6 points. The main distinctions between these two scans directly relevant to our analysis here are that (a) all SUSY mass parameters were restricted to be ≤ 1 TeV for the flat prior case, while for the log case the upper limit on mass parameters was raised to 3 TeV, and (b) the choice of the log prior generally leads to a more compressed sparticle spectrum than does the flat prior case. Note that the restriction on the upper limit for the mass parameters ensures relatively large production cross sections at the LHC for the case of the flat prior model sample. For

convenience, we repeat here the parameter ranges used for the flat scan,

$$\begin{aligned} 100\,\mathrm{GeV} \leq m_{\tilde{f}} \leq 1\,\mathrm{TeV}\,, \\ 50\,\mathrm{GeV} \leq |M_{1,2}, \mu| \leq 1\,\mathrm{TeV}\,, \\ 100\,\mathrm{GeV} \leq M_3 \leq 1\,\mathrm{TeV}\,, \\ |A_{b,t,\tau}| \leq 1\,\mathrm{TeV}\,, \\ 1 \leq \tan\beta \leq 50\,, \\ 43.5\,\mathrm{GeV} \leq m_A \leq 1\,\mathrm{TeV}\,; \end{aligned} \tag{4.2.1}$$

and for the log scan,

$$\begin{aligned} 100\,\mathrm{GeV} \leq m_{\tilde{f}} \leq 3\,\mathrm{TeV}\,, \\ 10\,\mathrm{GeV} \leq |M_{1,2}, \mu| \leq 3\,\mathrm{TeV}\,, \\ 100\,\mathrm{GeV} \leq M_3 \leq 3\,\mathrm{TeV}\,, \\ 10\,\mathrm{GeV} \leq |A_{b,t,\tau}| \leq 3\,\mathrm{TeV}\,, \\ 1 \leq \tan\beta \leq 60\,, \\ 43.5\,\mathrm{GeV} \leq m_A \leq 3\,\mathrm{TeV}\,. \end{aligned} \tag{4.2.2}$$

It is important to note that in the log scan the parameter $\tan\beta$, being a dimensionless quantity, was still scanned in using a flat prior.

Once these points were generated, we demanded that they be consistent with a large number of both theoretical and experimental constraints in order to ensure that the model sets are valid to study. We mention the most important of these restrictions here[2]: (*i*) The spectrum is required to be tachyon free, color and charge breaking minima must be avoided, a bounded Higgs potential must be obtained and electroweak symmetry breaking must be consistent. (*ii*) We impose a number of flavor and electroweak constraints arising from $g-2$, $b \to s\gamma$, $B \to \tau\nu$, $B_S \to \mu^+\mu^-$, meson–anti-meson mixing, the invisible width of the Z and $\Delta\rho$. (*iii*) We demand that the LSP contribution to the dark matter density not exceed the upper bound determined

[2]For full details, see Ref. [7]

by WMAP; note that the LSP is not required to saturate the measured relic density, leaving room for the existence of other dark matter candidates. Constraints from dark matter direct detection searches are also applied. (*iv*) We then include the restrictions imposed from the numerous direct searches for both the SUSY particles themselves as well as the extended SUSY Higgs sector at LEP. Here, some care was required as some of these searches needed to be re-evaluated in some detail due to particular SUSY model-dependent assumptions present in the analysis which we needed to remove. (*v*) Finally, the null results from a number of Tevatron searches are imposed. In addition to the Higgs searches, the most restrictive searches were found to be those hunting for stable charged particles [16] and those looking for an excess of multijet plus MET events [17]. We note that in the latter case, the search strategies were designed for kinematics expected in mSUGRA-like models. We thus were forced to simulate them in some detail, at the level of fast Monte Carlo, for our full model set. At the end of this analysis chain, $\sim 68.4k$ models from the flat prior set survived this set of constraints, as well as a corresponding set of $\sim 2.9k$ log prior models. These are the models that we will consider in our following analysis.

We now turn our attention to the analysis procedure that we followed in generating and analyzing the signal events from sparticle production at the 7 TeV LHC. Throughout our analysis, we adhere to the search strategies developed by ATLAS [12] as closely as possible. In this reference, ATLAS considers 10 MET search channels, including selections where the minimum number of jets is 2, 3, or 4 and the number of leptons is 0, 1, or 2. In the dilepton case, opposite-sign (OSDL) and same-sign (SSDL) pairs are considered separately, with SSDL only being considered in association with 2 jets. Note that flavor tagged final states are not considered here. We consider 85 SUSY production processes that contribute to these 10 signatures.

Accurate estimates of the SM backgrounds for the various channels are crucial to the validity of this study. We obtained details of the background distributions presented in Ref. [12] directly from the ATLAS SUSY Group [18]. These backgrounds were produced with state-of-the-art Monte Carlo event generators and the full ATLAS detector simulation. Employing these ATLAS computed backgrounds in our analysis allows us to concentrate on generating and analyzing signal events for each of the

$\sim$71k parameter space points in our pMSSM model sample.

4.2.1 Generation of the Signal Events

The steps involved in the generation of the signal events are very similar to those detailed in Ref. [9]. Here we will briefly summarize the procedure and point out any differences in the present analysis. For the generation and analysis of events for a single model, the workflow is:

1. The spectrum and decay table was generated with a modified [9] version of SUSY-HIT [19].

2. The NLO cross sections for the 85 distinct SUSY production processes considered were computed using Prospino2.1 [20] and the CTEQ6.6M parton distribution functions [21] (which were also used in the event generation).

3. Using PYTHIA 6.418, events were generated, fragmented, showered, and hadronized for each of 85 SUSY production processes, with each process being weighted by its K-factor.

4. Detector effects were simulated using an ATLAS-tuned version of the fast detector simulation PGS-3-7-7-74 [22] with the default isolation cuts removed.

5. The simulated events were then analyzed using the analysis cuts for the 10 ATLAS analyses listed above, as well as the isolation cuts described in Ref. [12].

We note that as in our previous work, a subset (about 1%) of the models suffered serious enough errors that the Pythia event generation halted. These "PYSTOP" models are excluded from our results.

4.2.2 Analysis Cuts

For the reader's convenience, we provide here the full set of kinematic cuts for each analysis channel, summarizing the information given in Section 4 of Ref. [12]. All channels have a missing energy cut of $E_T^{\rm miss} > 80$ GeV, and all analyses except the

Number of jets	≥ 2	≥ 3	≥ 4
Leading jet p_T (GeV)	> 180	> 100	> 100
Other jets p_T (GeV)	> 50	> 40	> 40
min. $\Delta\phi(\text{jet}_i, E_T^{\text{miss}})$	$0.2, 0.2$	$0.2, 0.2, 0.2$	$0.2, 0.2, 0$
$E_T^{\text{miss}} > f \times M_{\text{eff}}$	$f = 0.3$	$f = 0.25$	$f = 0.2$

Table 4.1: The kinematic cuts employed in the event selection: the cut on the p_T of the leading jet, the p_T of the other selected jets, the azimuthal angle between the selected jets and the missing transverse energy, and the missing energy as a fraction of the effective mass.

SSDL channel have a transverse sphericity cut of $S_T > 0.2$. Table 4.1 summarizes the cuts for the searches with $n = 2, 3, 4$ jets which are independent of the choice of lepton channel except for SSDL, which will be described below.

We complete the description of the kinematic cuts by specifying the additional cuts that are specific to the various lepton channels. For the case with zero leptons, events are rejected that have at least one lepton with $p_T > 20$ GeV. For the one-lepton channels, one lepton with $p_T > 20$ GeV is required, no additional leptons with $p_T > 10$ GeV are allowed, and the transverse mass M_T of the selected lepton and the missing energy vector must satisfy $M_T > 100$ GeV. (The definition of M_T can be found in Ref. [4].) For the OSDL channel, exactly two leptons with $p_T > 10$ GeV are required, and they must have opposite charge.

As mentioned above, the SSDL channel has distinct cuts; unlike all the other analyses, the three different jet selection options specified in Table 4.1 are not employed. Instead, two jets with $p_T > 80$ GeV are required. In addition, two leptons with $p_T > 20$ GeV, same charge, and invariant mass $m_{\ell\ell} > 5$ GeV must be present, and there is a veto on additional leptons with $p_T > 10$ GeV. The transverse mass of the leading lepton and the missing energy vector must satisfy $M_T > 80$ GeV.

Lastly, when performing our statistical analysis, the M_{eff} cut is optimized for each channel, and for each pMSSM model, in steps of 400 GeV [12].

4.2.3 Statistical Procedure

To compute the significance of the signal for each search channel, we follow the statistical procedure described in detail in Refs. [9, 4], which is that employed by the ATLAS collaboration. The probability that the expected background fluctuates to the number of observed events is computed assuming that the systematic error on the background is Gaussian and the statistical error is Poissonian. In other words, we compute the probability

$$p = A \int_0^\infty db\, G(b; N_b; \delta N_b) \sum_{i=N_{\rm data}}^{\infty} \frac{e^{-b} b^i}{i!} \,, \tag{4.2.3}$$

where N_b is the number of background events and δN_b is the associated systematic error on this number, while $N_{\rm data} = N_b + N_{\rm signal}$ is the total number of events above the $M_{\rm eff}$ cut. G is a Gaussian distribution and A is a normalization factor ensuring that the probability that the background fluctuates to any nonnegative integer is one; therefore $A = p(N_{\rm data} = 0)^{-1}$. The significance, S, is then given by

$$S = \sqrt{2}{\rm erf}^{-1}(1 - 2p) \,. \tag{4.2.4}$$

A significance of $S \geq 5$ is required for the observation of a signal. As mentioned above, the $M_{\rm eff}$ cut is optimized for each channel, and for each pMSSM model, in steps of 400 GeV [12]. As was discussed in Ref. [9], and will be further demonstrated here, the accuracy of the background estimation has a profound impact on the signal significance and the resulting search reach. In order to quantify this, we will present results assuming a 20, 50, and 100% systematic error on the background. We will also consider integrated luminosities of 0.1, 1, and 10 fb^{-1}.

4.2.4 Comparison with ATLAS Benchmark Models

The ATLAS SUSY group has published signal rates for a single mSUGRA benchmark point (SU4) in their study of Supersymmetry at the 7 TeV LHC [12]. It is imperative for us to check the results of our analysis against these published results for this

benchmark model before proceeding to apply our analysis to the pMSSM model set.

Here it is important to remind the reader that our SUSY signal generation, as described in detail in Ref. [9], differs slightly from the procedure employed by ATLAS. In particular, the numerical programs used to compute the SUSY spectrum and decay tables, as well as event generation, are different. Furthermore, we use, by necessity, a fast detector simulation as opposed to the ATLAS full GEANT-based simulation. Therefore, a small degree of discrepancy can be expected. The comparisons shown in Figures 4.1-4.5, however, indicate that we are indeed able to faithfully reproduce the results obtained by ATLAS for this benchmark model for all of the various inclusive analyses.

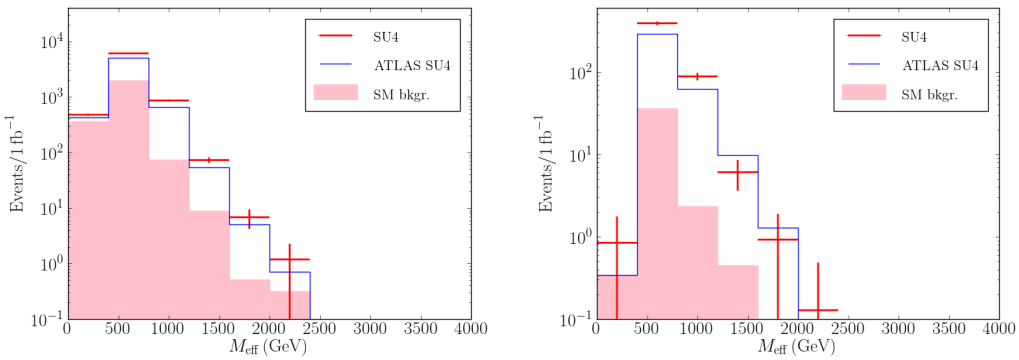

Figure 4.1: The $M_{\rm eff}$ distribution for the 4 jet, 0(1) lepton analysis on the left(right) for the SU4 benchmark model. The red data points represent our analysis (the error bars are simply $\sqrt{N}$ statistical errors), while the blue line is the result from the ATLAS study [12]. The pink shaded area represents the SM background.

4.3 Results of the 7 TeV Analysis

In this Section, we relate the results of our study on the effectiveness of the ATLAS 7 TeV $E_T^{\rm miss}$ analyses in detecting our pMSSM model sample. We first discuss the impact of the size of the background systematic errors on SUSY searches, and then turn to the discovery coverage of the pMSSM. We examine the characteristics which cause some models to be undetectable as well as study the effects of modifying the

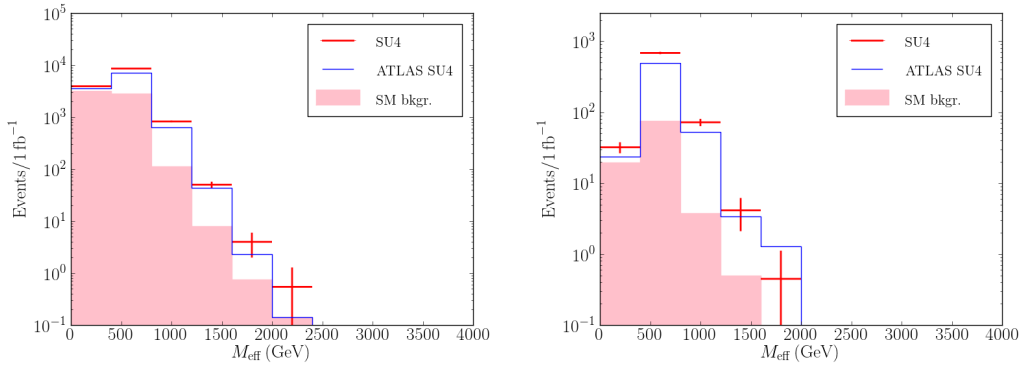

Figure 4.2: The same as Figure 4.1, except for the 3 jet, 0(1) lepton analysis on the left(right).

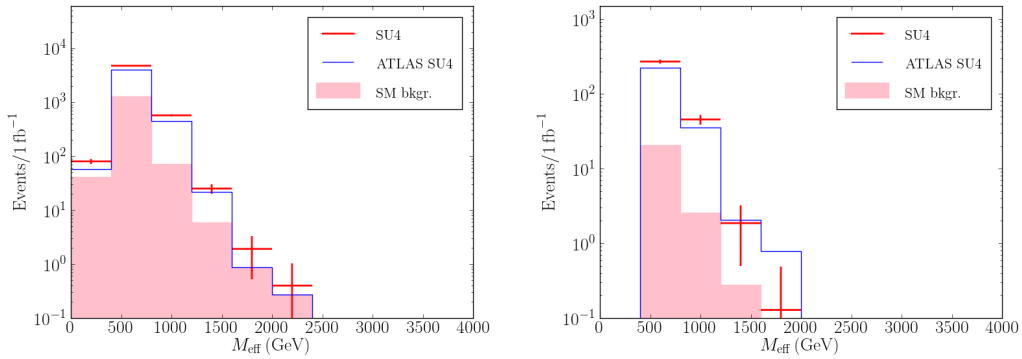

Figure 4.3: The same as Figure 4.1, except for the 2 jet, 0(1) lepton analysis on the left(right).

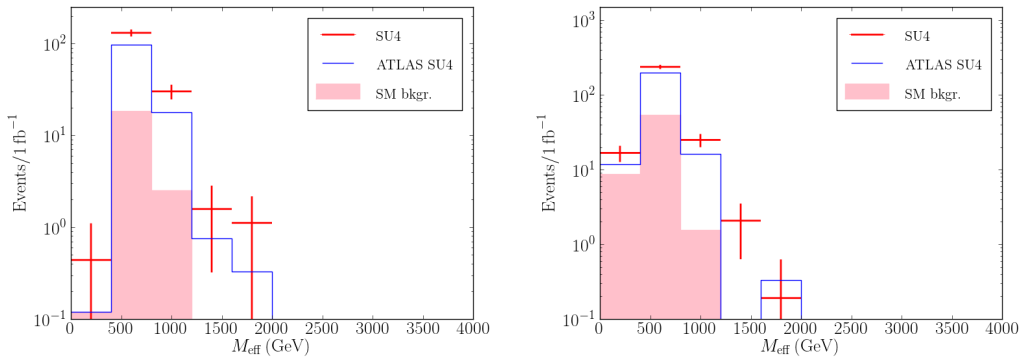

Figure 4.4: The same as Figure 4.1, except for the 4(3) jet, OSDL lepton analysis on the left(right).

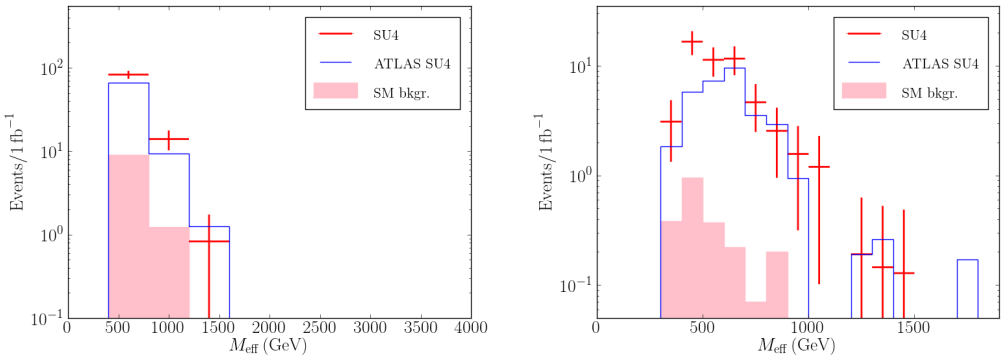

Figure 4.5: The same as Figure 4.1, except for the 2 jet, OSDL(SSDL) analysis on the left(right).

ATLAS SUSY analysis cuts. We remind the reader that our sample of $\sim$ 70k models is not intended to be a full description of the 19-dimensional pMSSM parameter space. However, the sample does contain numerous models which exhibit properties that are quite different than those expected in mSUGRA and thus provides insight into general features of the full MSSM.

4.3.1 Influence of Background Systematic Errors

As mentioned above, the size of the SM background systematic errors plays an important role in the ability of the ATLAS $E_T^{\rm miss}$ searches to discover Supersymmetry, including the pMSSM. This is not surprising as the number of signal events necessary to reach $S = 5$ critically depends upon both the size of the estimated background itself as well as the background uncertainty. For a fixed systematic uncertainty, search channels with large backgrounds clearly require a large number of signal events in order to claim a discovery. To get a feel for this in the case of the ATLAS $E_T^{\rm miss}$ analyses studied here, we determine the necessary number of signal events to reach the $S = 5$ level in each analysis as function of the fractional background uncertainty. We remind the reader that the SM backgrounds for each channel were supplied to us by the ATLAS SUSY working group [18]. In performing these calculations we exactly follow the discussion as given by ATLAS in Ref. [4]. Our results are displayed in Figs. 4.6 and 4.7 for the ten ATLAS $E_T^{\rm miss}$ channels assuming 1 fb^{-1} of integrated

luminosity. Here, we see the number of signal events that are required to obtain the discovery criterion of $S = 5$ for various values of the final $M_{\rm eff}$ cut. In the case of the nj0l channel, which has the largest SM background, we note that the required number of signal events is particularly large and is quite sensitive to the value of the $M_{\rm eff}$ cut. Note that as the systematic error increases, the number of required signal events can rise drastically, in some cases by an order of magnitude or more. In particular, the difference between a reasonably low 20% systematic error and taking a 0% error (i.e., ignoring this effect) is substantial and theoretical analyses that do not include this error are thus wildly optimistic.

We will use these numerical results in our subsequent analyses of the pMSSM model coverage in these $E_T^{\rm miss}$-based searches in the next subsection. They indicate the importance of reducing background systematic errors in order to increase the coverage of new physics parameter spaces.

4.3.2 pMSSM Model Coverage

We now run each of our pMSSM models through the analysis chain described above. The first question we address is how well do the various search analyses cover the pMSSM model sample, or, more precisely, what fraction of these models can be discovered (or not) by these searches. Further, we also determine which of the analyses provide the best model discovery capabilities. Clearly the answers to these questions will be highly sensitive to the assumed values of both the integrated luminosity and the estimated SM background uncertainty. Figure 4.8 shows the fraction of the pMSSM models that can be discovered with $S \geq 5$ in each of the ATLAS $E_T^{\rm miss}$ channels for the flat prior model set as a function of the integrated luminosity assuming three different choices for the background systematic error. The corresponding results obtained in the case of the log prior model set can be found in Fig. 4.9. Here, we again emphasize that our pMSSM sample is not meant to provide full coverage of the 19-dimensional parameter space (such coverage would be computationally prohibited). However both the very large number of models in our pMSSM sample, and the distinct characteristics they possess, make this sample an ideal testbed for this set of mSUGRA

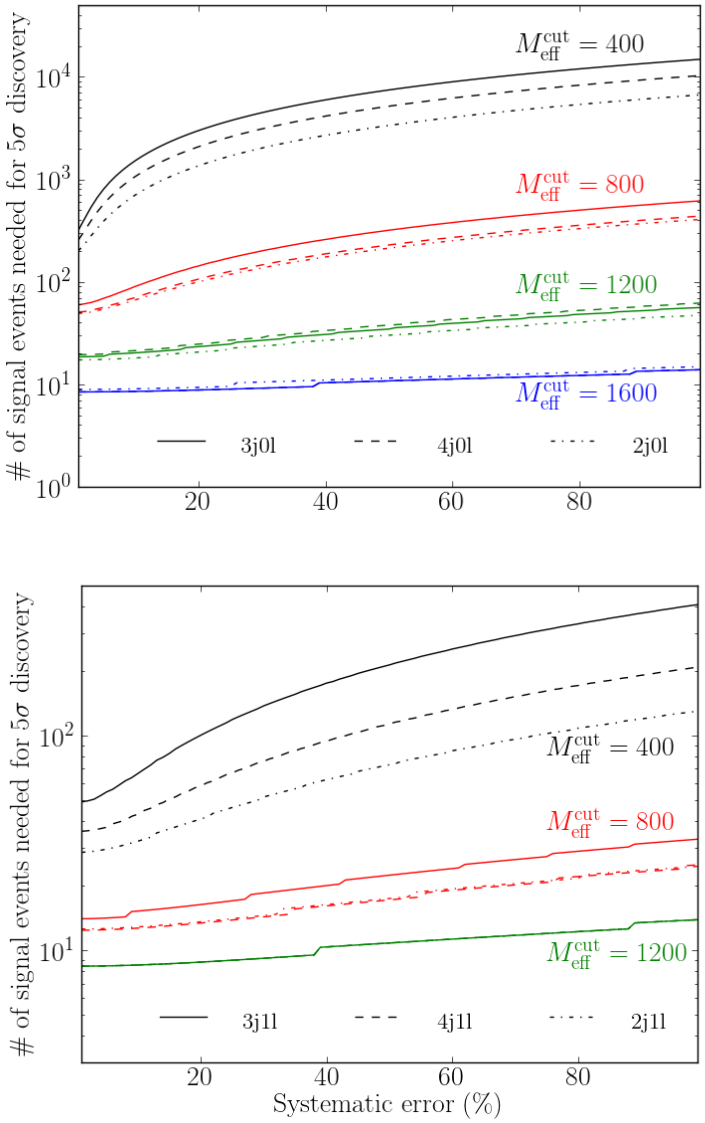

Figure 4.6: Number of events required to reach the $S = 5$ level of discovery as a function of the fractional systematic error in the SM background for the ATLAS $E_T^{\rm miss}$ searches for various values of the $M_{\rm eff}$ cut. The results for the nj0l and nj1l searches are shown in the top and bottom panels, respectively. The curves are color coded according to $M_{\rm eff}$ cut from top to bottom as indicated by the labels in the plot, and the line style indicates the number of jets in the analysis as shown in the legend. For higher values of the $M_{\rm eff}$ cut, we see that the curves are essentially indistinguishable, lying on top of one another, because the number of background events is almost zero in this case for each channel.

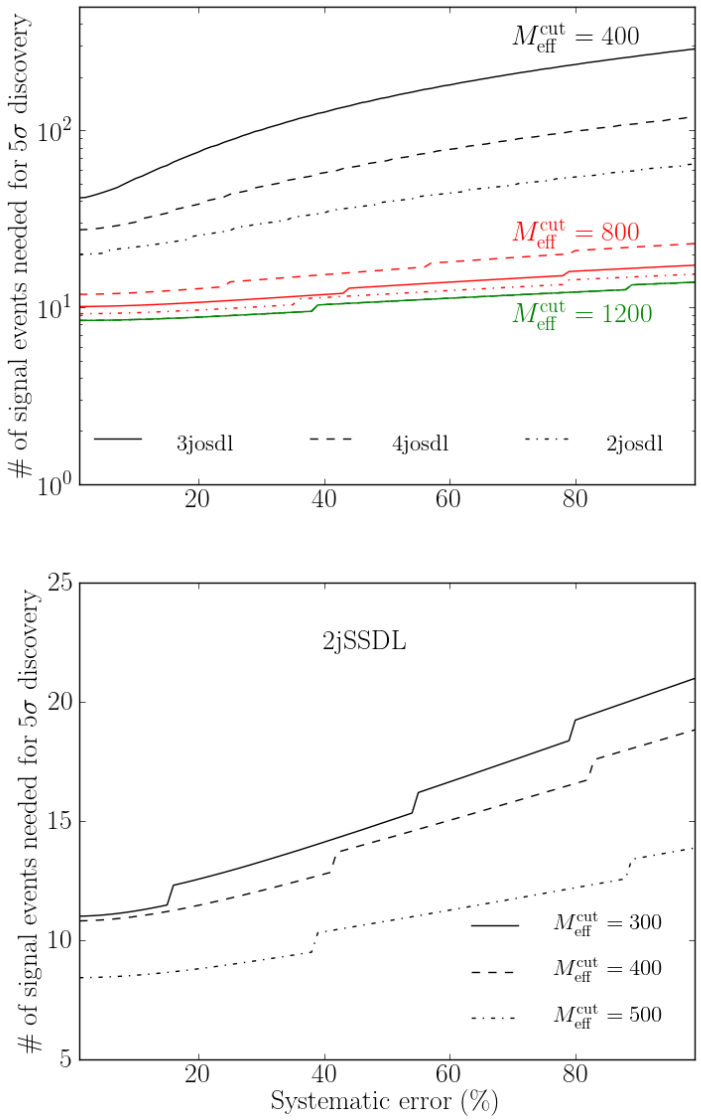

Figure 4.7: Same as the previous figure but now for the njSSDL (top) and 2jSSDL (bottom) search channels.

designed search strategies. Our fractional results based on our pMSSM model set are thus indicative of the behavior of the MSSM under these search routines.

These figures reveal a number of interesting results: (*i*) The size of the background systematic errors makes a significant impact on model coverage for all search channels and integrated luminosities. For the searches with significant SM backgrounds, i.e., the nj0l and nj1l channels, variation in the background uncertainty leads to substantial changes in the capability to observe the model sample. The search least affected by systematics is 2jSSDL since the backgrounds in this case are quite small. This behavior confirms the results of the previous subsection. (*ii*) The model coverage in almost all cases is significantly better for the flat prior model set than for the log prior sample. This, too, is not very surprising since the masses of the sparticles in the log prior case extend out to much larger values and the sparticle spectrum is generally more compressed in this set [7]. The latter leads to softer jets and leptons in the corresponding cascade decays which have a more difficult time passing the analysis cuts. (*iii*) For all values of the background systematic error, the nj0l channels yield the best model space coverage with 4j0l affording the best discovery opportunity. In fact, we see that the channels which require more jets to be present have a better chance of being observed for the nj0l and nj1l searches. For the flat prior sample, the 4j0l analysis with low background systematics is observed to cover a very large fraction of the model set by itself once significant integrated luminosities are obtained. (*iv*) As the number of leptons required to be present in the final state increases, the model coverage is found to decrease significantly, especially for smaller values of the integrated luminosity. This is due to the fact that the branching fractions for leptons to appear in squark and gluino induced cascade decays are generally not very large in our model sample, as we have seen in our earlier work [9]. (*v*) Independently of the specific $E_T^{\rm miss}$ search, as the background systematic errors become large, the pMSSM model coverage is seen to increase more slowly with the integrated luminosity. Some of the search channels nearly saturate at high luminosity due to the large background uncertainties and thus become systematics dominated.

As discussed above, the final step in the ATLAS $E_T^{\rm miss}$ analyses is to apply a cut on $M_{\rm eff}$, where the particular value of $M_{\rm eff}$ that is chosen (in units of 400 GeV) is the one

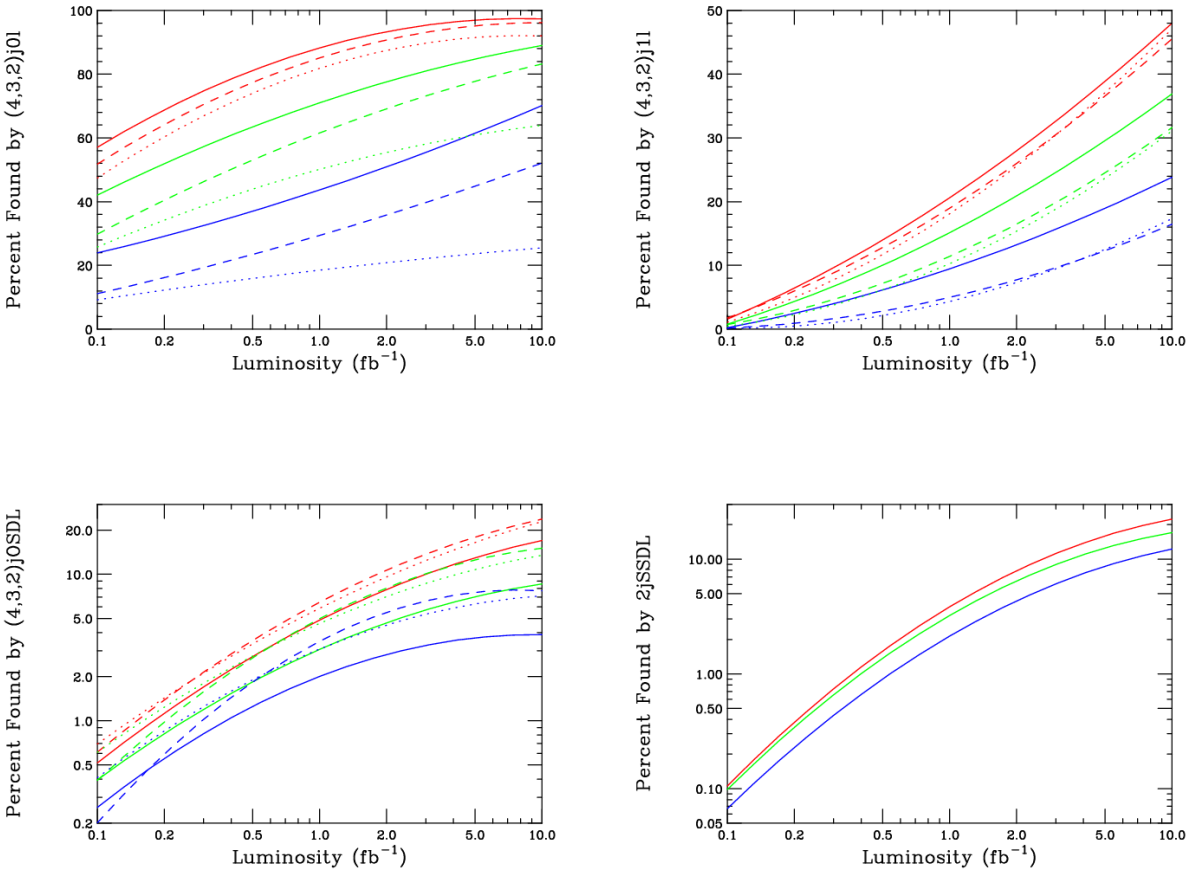

Figure 4.8: Fraction of flat prior pMSSM model set that can be observed with $S \geq 5$ in the nj0l (top-left), nj1l (top-right), njOSDL (bottom-left), and 2jSSDL (bottom) search channels as a function of the integrated luminosity. The solid(dashed, dotted) curves in each case correspond to n=4(3,2), respectively for the nj0l, nj1l, njOSDL channels. From top to bottom, the red(green, blue) curves correspond to background systematic uncertainties of 20(50, 100)%, respectively.

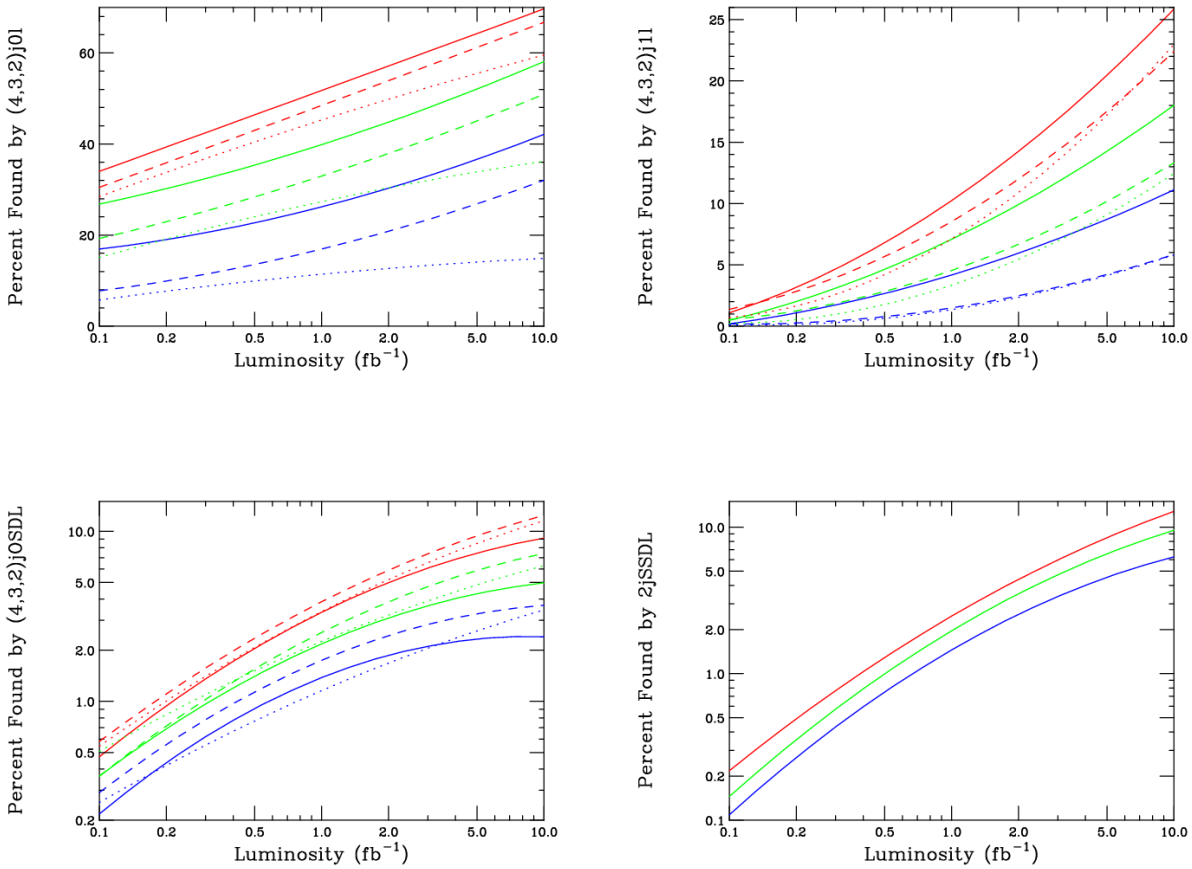

Figure 4.9: Same as Figure 4.8, except for the log prior model set.

that maximizes the signal significance given the SM background and its corresponding uncertainty. This choice not only depends upon the particular channel but also on the amount of integrated luminosity. It is important to note that if this cut is taken to be *too* large when maximizing the signal, then the analysis will be very sensitive to the detailed shape in the tails of both the signal and expected background distributions, especially with higher luminosities. This happens when there are very few events with large values of M_{eff}, e.g., 2 TeV. In this situation, small fluctuations in the SM background and/or SUSY signal expectations due to limited Monte Carlo statistics can lead to inconsistencies in whether a given model is observable in a specific analysis or even whether or not it would be detected overall. This effect only occurs in the case of the search analyses designed for the 7 TeV run, as the M_{eff} cut applied in the planned 14 TeV ATLAS analyses was fixed at relatively low values.

Figure 4.10 shows the optimized value for the M_{eff} cut for the nj0l analyses, as an example, for the flat prior model sample. The three things we see here are: (*i*) for large background systematic errors, a harder M_{eff} cut is required to optimize the search, (*ii*) as the number of required jets in the final state decreases, the strength of the cut can be reduced. Both of these results are also found to hold for the nj1l and njOSDL searches although the M_{eff} cut itself turns out to be less important as the number of required leptons in the final state increases. (*iii*) Given the warning about distribution tails in the discussion above, it is a welcome result to see that in the majority of cases only a moderately strong M_{eff} cut is required to optimize the signal significance. Note that there are some cases where the M_{eff} cut does not contribute very much to increase the significance of the SUSY signal; this happens in particular for scenarios where the background is low and the effect of systematic uncertainties is not very significant.

It is interesting to evaluate the fraction of models that can be discovered in multiple analyses. This is important to consider as, first, it is valuable to verify the discovery of new physics in more than one channel, and second, the availability of multiple discovery channels admits for the possibility of further studies that will allow for, e.g., the extraction of sparticle masses. To be specific, Tables 4.2, 4.3 and 4.4 show the fraction of pMSSM models which are observed in (exactly) n channels

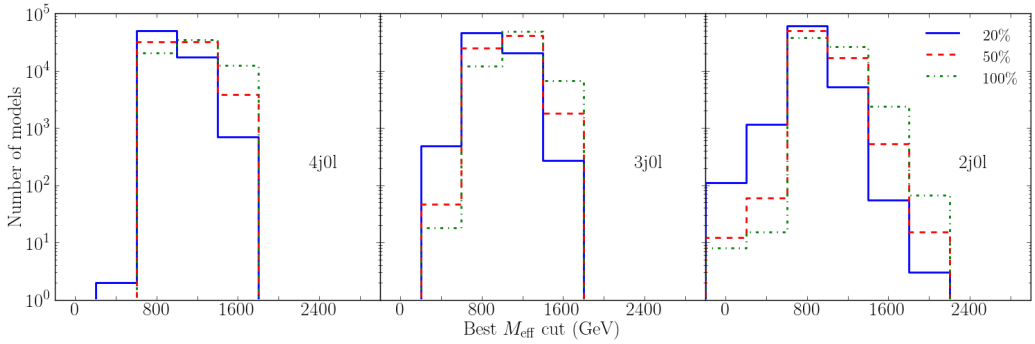

Figure 4.10: Optimized $M_{\rm eff}$ cut for the flat prior model set for the 4j0l (left), 3j0l(middle) and 2j0l (right) analyses. The blue(red, green) (solid(dashed, dot-dashed)) histograms correspond to background systematic uncertainties of 20(50, 100)%, respectively. An integrated luminosity of 1 fb^{-1} has been assumed in these figures for purposes of demonstration.

assuming a SM background systematic error of 20, 50, and 100%, respectively. Note that the distribution shifts towards more models being observed in multiple channels as the integrated luminosity increases and the background systematic error decreases, as expected.

By combining our results for these $E_T^{\rm miss}$ searches, we can also determine the fraction of pMSSM models that are undetected in *all* of the 7 TeV search analyses designed by ATLAS; this corresponds to the case of $n = 0$ in these Tables. Figure 4.11 presents the fraction of pMSSM models which are undetected in all of the search channels as a function of integrated luminosity for both the flat and log prior sets. In the flat prior case we see that as the integrated luminosity increases, the model coverage substantially improves, and approaches (or exceeds) $\sim 95\%$ for 10 fb^{-1} with SM background uncertainties of 50% or less. In the log prior case, the improvement in pMSSM model coverage as the luminosity increases is much more gradual as we might have expected from the discussion above. However, even in this case, at high integrated luminosities substantial model coverage is seen to be obtainable at 7 TeV.

This figure also shows the important playoff between increasing the integrated luminosity and decreasing the SM background systematic error in terms of pMSSM model coverage. (Of course, increased luminosity often results in decreased systematic errors, up to a point.) For example, it is interesting to compare the effectiveness of

n	Flat $\mathcal{L}_{0.1}$	Flat $\mathcal{L}_1$	Flat $\mathcal{L}_{10}$	Log $\mathcal{L}_{0.1}$	Log $\mathcal{L}_1$	Log $\mathcal{L}_{10}$
0	38.2	7.6	1.0	63.6	44.0	22.9
1	9.3	4.2	0.91	5.4	4.9	5.8
2	8.7	4.7	1.6	3.7	5.7	6.0
3	41.8	59.9	39.6	26.0	34.9	35.4
4	0.66	4.9	7.9	0.25	2.2	6.5
5	0.53	4.3	6.7	0.47	2.0	4.8
6	0.54	8.5	13.5	0.33	3.1	6.5
7	0.067	2.5	8.9	0.22	1.5	4.2
8	0.063	1.2	5.6	0.036	0.73	2.3
9	0.077	1.3	6.5	0	0.58	2.9
10	0.013	0.93	7.7	0	0.47	2.6

Table 4.2: The percentage of models that are observed in (exactly) n $E_T^{\rm miss}$ search channels assuming a SM background systematic error of 20%. The subscript of $\mathcal{L}$ represents the integrated luminosity in fb^{-1}.

n	Flat $\mathcal{L}_{0.1}$	Flat $\mathcal{L}_1$	Flat $\mathcal{L}_{10}$	Log $\mathcal{L}_{0.1}$	Log $\mathcal{L}_1$	Log $\mathcal{L}_{10}$
0	54.8	21.8	4.9	71.6	55.9	32.6
1	14.1	10.5	4.8	8.2	7.3	9.9
2	7.8	11.5	10.0	5.1	7.1	12.5
3	22.6	42.9	40.7	14.9	24.2	28.5
4	0.30	4.1	8.4	0.18	1.7	4.6
5	0.16	3.2	7.6	0	1.4	3.5
6	0.14	3.3	9.1	0.073	1.1	3.5
7	0.061	1.4	6.0	0.036	0.80	2.0
8	0.031	0.59	3.6	0.036	0.33	1.4
9	0.013	0.43	3.0	0	0.036	1.2
10	0.0015	0.25	1.9	0	0.11	0.40

Table 4.3: Same as the previous Table but now assuming a SM background systematic error of 50%.

n	Flat $\mathcal{L}_{0.1}$	Flat $\mathcal{L}_1$	Flat $\mathcal{L}_{10}$	Log $\mathcal{L}_{0.1}$	Log $\mathcal{L}_1$	Log $\mathcal{L}_{10}$
0	74.1	47.2	17.6	81.9	69.0	47.9
1	13.9	16.8	16.0	9.8	10.8	14.0
2	4.5	13.3	21.9	3.2	7.7	15.9
3	7.3	18.2	26.2	4.9	10.6	15.4
4	0.11	1.9	6.5	0.036	0.80	2.6
5	0.037	1.0	4.7	0.036	0.33	1.7
6	0.024	0.71	3.3	0	0.33	1.0
7	0.019	0.57	2.2	0.073	0.36	0.87
8	0.0030	0.17	1.0	0	0.036	0.36
9	0.0015	0.064	0.46	0	0	0.11
10	0	0.012	0.13257	0	0	0.036

Table 4.4: Same as the previous Table but now assuming a SM background systematic error of 100%.

the analyses for the flat prior set assuming $\delta B = 100\%$ and $\mathcal{L} = 5(10)$ fb^{-1} with other values. Figure 4.11 shows that taking $\delta B = 50\%$ and $\mathcal{L} = 0.65(1.4)$ fb^{-1} or $\delta B = 20\%$ with $\mathcal{L} = 0.20(0.39)$ fb^{-1} produces essentially identical model coverage. This demonstrates that small reductions in the SM background uncertainty can be worth a significant amount of increased integrated luminosity in terms of pMSSM model coverage.

Another very important message to take home from this figure is that for the integrated luminosity collected during the 2010 LHC run at 7 TeV (~ 35 pb^{-1} for ATLAS), some significant fraction of these pMSSM models should already have been observed at the $S = 5$ level. Explicitly, for a background systematic error of 20(50,100)% we find that 46(28,15)% of the flat prior model set should have been discovered; in the log prior case the corresponding results are found to be 30(24,14)%. Since these are *discovery* results, an even greater portion of the pMSSM model sample would be expected to be *excluded* by these analyses. This shows the incredible power of going from Tevatron energies up to the 7 TeV LHC in performing searches for massive objects, such as SUSY sparticles, even when only small amount of integrated luminosity is available.

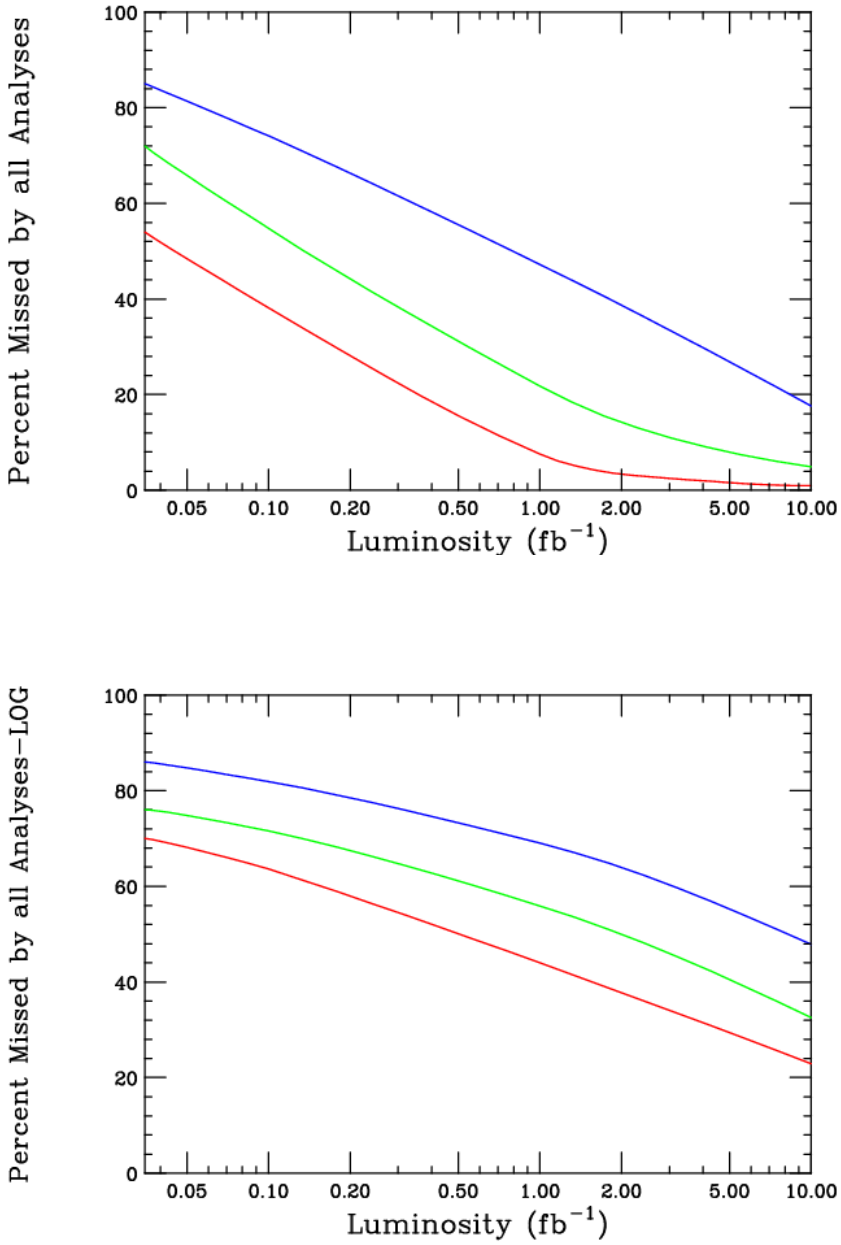

Figure 4.11: Fraction of flat prior (top) or log prior (bottom) pMSSM model sets which are undetected after combining all of the ATLAS E_T^{miss} search analyses. From bottom to top, the red(green, blue) curves correspond to background systematic uncertainties of 20(50, 100)%, respectively.

4.3.3 Why are Models not Detected by the ATLAS $E_T^{\rm miss}$ Searches?

Here, we investigate the main reasons why some pMSSM models are not discoverable in the ATLAS $E_T^{\rm miss}$ searches at 7 TeV. We addressed this question in some detail in our earlier work for the case of the analyses designed for the 14 TeV LHC [9], so our discussion here will not be as extensive. Clearly, many of our previous results will carry over qualitatively into the present 7 TeV analysis.

There are multiple explanations as to why some pMSSM models are undetected by the $E_T^{\rm miss}$ searches, the most obvious one being small production cross sections for the colored sparticles that initiate the familiar SUSY cascades. As an example, we note that for our pMSSM models in the flat prior set, the cross sections for the production of gluino and squark pairs are found to cover an enormous range of several orders of magnitude as can be seen in Fig. 4.12 (recall that the upper limit on sparticle masses in our flat model set is ~ 1 TeV). Here we see that the large (or small) values of the gluino pair cross section is completely uncorrelated with the corresponding values for first generation squarks within a particular model. Furthermore, by summing over all of the QCD production channels involving gluinos and/or first generation squarks (i.e., $\tilde{g}\tilde{g}$, $\tilde{g}\tilde{q}$, $\tilde{q}\tilde{q}$ and $\tilde{q}\tilde{q}^*$) we obtain an approximate handle on the total overall rate for SUSY production which we see ranges over four orders of magnitude. Note that for any particular value of the squark or gluino mass, the corresponding production cross section itself can vary by up to an order of magnitude or more depending upon the remainder of the pMSSM model spectrum.

While it is certainly clear from this figure that some models have too small a cross section to be discovered, the bottom-right panel indicates that this cannot be the entire explanation. Here we show the search significance, S, of the 4j0l channel (as it is the most powerful channel in terms of discovery capability) as a function of the total NLO QCD production cross section assuming $\mathcal{L} = 1$ fb^{-1} and $\delta B = 50\%$. Here we observe that (i) there are models with cross sections ~ 20 pb which are *missed* by this analysis, while (ii) there are models with cross sections ~ 100 fb which are discovered. (iii) For any given value of the cross section, the range of the significance is large and

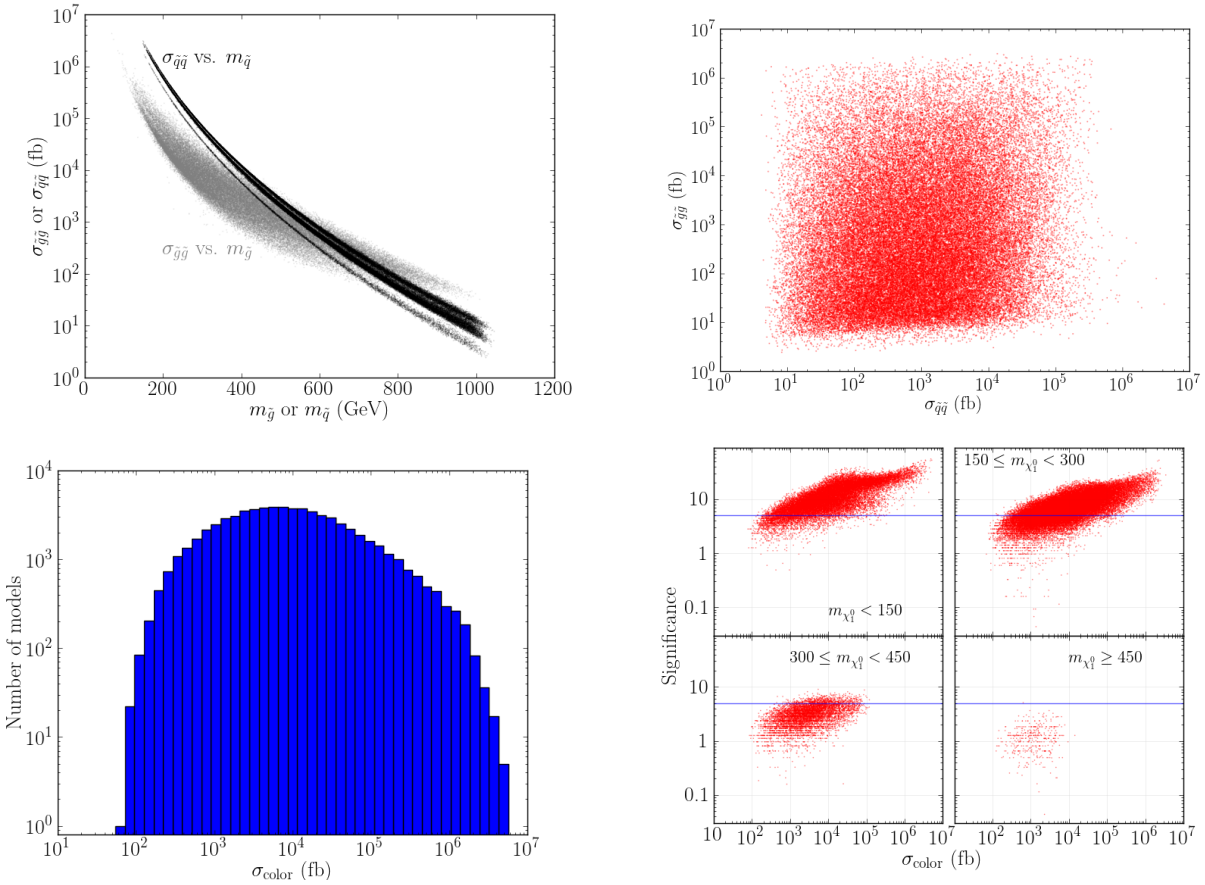

Figure 4.12: (Top left) NLO first generation squark and gluino pair production cross sections at $\sqrt{s} = 7$ TeV as a function of their masses for the flat prior model set. The gray(black) points represent the gluino(squark) cross sections. (Top right) Correlation of the squark pair and gluino pair NLO cross sections in the flat prior set. Each point represents one model. (Bottom left) Total NLO QCD production cross section distribution for the flat model set. (Bottom right) Search significance of the 4j0l analysis as a function of the total NLO QCD production cross section assuming $\mathcal{L}$=1 fb^{-1} and $\delta B = 50\%$. The solid line highlights the $S = 5$ discovery level, and each panel represents a different mass interval for the LSP.

can be up to two orders of magnitude or more. This validates the claim that there are reasons other than small production cross sections that render models unobservable by these $E_T^{\rm miss}$ analyses. (*iv*) For any given gluino mass there is a strong correlation of the signal significance with the mass of the LSP. Clearly when these two masses are close the average p_T of the jets will be softer and this will make it more difficult to pass analysis cuts. Also if the LSP mass is large then that implies even larger squark and gluino masses that will result on average in smaller production cross sections. In the case of the nj0l analyses, a larger number of signal events is required for discovery due to the sizeable SM backgrounds and hence such models will be missed by these analyses. Visibility will then require the production of leptons with significant p_T in cascade decays in order to pass the lower background nj1l, njOSDL and 2jSSDL searches. Unfortunately, lepton branching fractions are low in these cascades in our model sample (since, e.g., sleptons are heavy) and thus some models will be missed entirely. Of course, models that are lepton-rich will automatically fail all the nj0l analyses since they veto events with high p_T leptons, but will be picked up by the searches containing leptons.

Though the production cross section for SUSY particles is reasonably well correlated with their masses, we can ask more directly if larger sparticle masses lead to their non-observation in these searches. Figure 5.1 shows that, indeed, models with lighter squarks or gluinos tend to lead to signals with greater significance in the 4j0l channel. However, as we can also see from this Figure, this is not true universally, e.g., there are many models with gluino (lightest squark) masses below 300 (200) GeV that have $S < 5$, while conversely there are models with 1 TeV gluinos that have $S > 5$. We see that for any given squark or gluino mass the value of S can vary significantly. The top panel of Fig. 4.14 displays this property even more strongly where we see that these results hold even when all of the $E_T^{\rm miss}$ searches are combined. This Figure shows the set of flat prior models that are unobservable in all the search channels in average light squark mass–gluino mass plane. Note that there are a significant number of these models which contain light squarks and gluinos. Thus while the masses of the colored sparticles do play an important role in model observability clearly there are additional important factors.

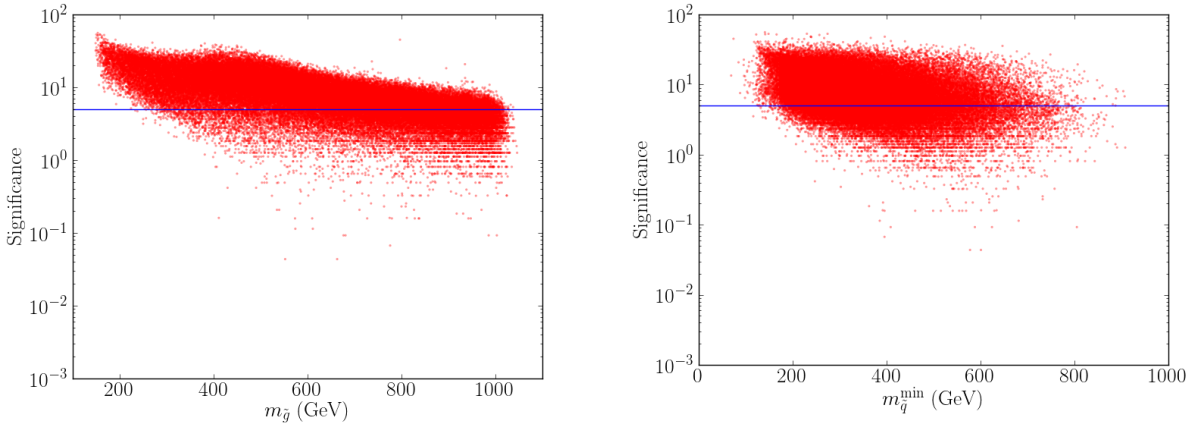

Figure 4.13: Significance of the 4j0l search for the flat prior model set as a function of the gluino (left) and lightest squark (right) masses. $\mathcal{L}$=1 fb^{-1} and $\delta B = 50\%$ have been assumed.

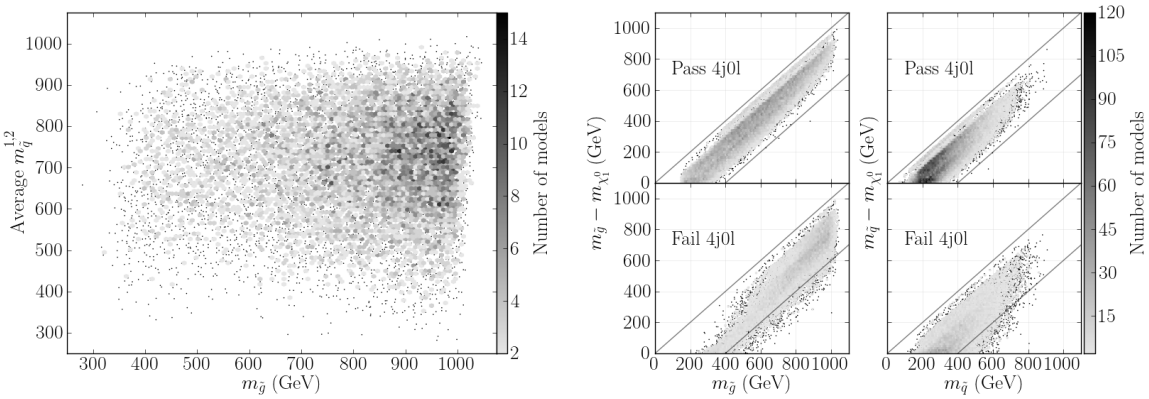

Figure 4.14: (Left) Flat prior models that are unobservable in all of the E_T^{miss}-based search analyses in the average light squark mass-gluino mass plane. (right) Flat prior models that pass(upper panels) or fail(lower panels) the 4j0l analysis in the gluino(lightest squark) mass vs gluino-LSP (lightest squark-LSP) mass splitting plane in the left (right) panels. The solid lines at $\delta m = m$ and $\delta m = m - 200$ are just to facilitate comparison between the panels. In both plots, the dots show individual models, while in the more highly-populated regions, the shaded cells show the number of models per cell $\mathcal{L}$=1 fb^{-1} and $\delta B = 50\%$ have again been assumed.

In the lower panels of Fig. 4.14 we see that the mass splitting between squarks and/or gluinos and the LSP can play an important role in determining model observability as was first noted in Ref. [6] and was seen explicitly in our earlier work on the generation of the pMSSM models [7] and the 14 TeV ATLAS SUSY analyses [9]. The obvious reasoning here is that as the degeneracy in the spectrum increases and mass splittings become smaller, the values of, e.g., the p_T of the jets, will be reduced so that it will be more difficult to satisfy any of the analysis cuts. These figures show this result explicitly. Note, however, that, e.g., in the case of light gluinos with small gluino-LSP splittings there are many models which are still discoverable in the 4j0l channel. The reason for this is that while the efficiency[3] for passing the 4j0l analysis cuts may be quite low for small mass splittings, as seen in Fig. 4.15, the cross section to produce the lighter gluinos/squarks is very large and more than compensates for these low efficiencies, especially if there are any additional hard jets in the event from ISR. However, there are numerous unobservable models that have larger raw sparticle production cross sections than observable models with somewhat similar spectra; the difference then being in their respective abilities to pass the necessary analysis cuts.

Another cause for models being undetected is the occurrence of detector-stable sparticles at the end of gluino or squark induced decay chains instead of the LSP [9]. This happens with reasonable frequency in both the 7 and 14 TeV analyses. In such cases, the amount of $E_T^{\rm miss}$ that is produced is substantially decreased which reduces the capability of the relevant models to pass any $E_T^{\rm miss}$ analysis requirements. Most commonly, these sparticles are actually long-lived charginos that are reasonably degenerate with the LSP in wino- or Higgsino-like LSP scenarios. In these cases, searches for long-lived sparticles, as discussed below, will be a important supplement to the conventional $E_T^{\rm miss}$ searches. Of course, a loss of the $E_T^{\rm miss}$ signature can happen in other ways. For example, if the initial squark or gluino produces a very long decay chain then the particles produced at the end of such a chain will be somewhat soft. In some cases this may lead to the inability to pass the necessary p_T and/or $E_T^{\rm miss}$ requirements for the various $E_T^{\rm miss}$-based searches and the model will not be observed. Such long decay chains were shown to occur with a reasonable frequency in our earlier

[3]Here, efficiency is defined as the fraction of generated signal events that pass the analysis cuts.

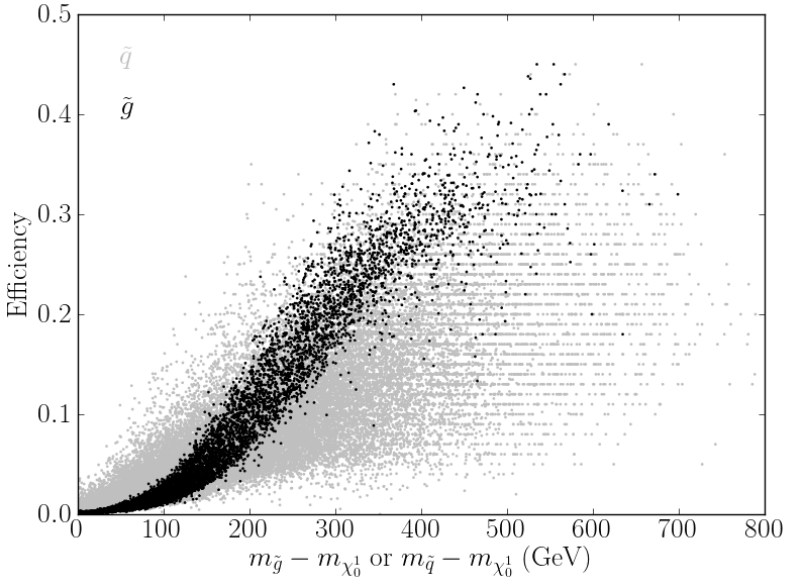

Figure 4.15: The efficiency for passing the 4j0l analysis cuts as a function of the (black)gluino- or (gray)squark-LSP mass splitting. Here, efficiency is defined as the fraction of generated signal events that pass the analysis cuts.

work [9] and can be a contributor to models failing to pass the analyses requirements.

There are, of course, other reasons that prevent models from being discovered. As noted above, subtleties in any sector of the sparticle spectrum can make a significant difference as to whether a given model is observed by various analyses. Here, we will discuss a couple of examples where this occurs. As in Ref. [9], the approach we follow is to compare a model which fails to be observed in all search channels to one with a similar spectrum (dubbed a 'sister' model) that is detected in at least one channel and then examine the difference between them. For this study, we concentrate on the more difficult cases by taking the flat prior model sample and assume $\mathcal{L} = 10$ fb^{-1} and $\delta B = 20\%$; this leaves only ~ 670 models that are not observed. In order to avoid the statistical issues associated with the tails of the $M_{\rm eff}$ distribution discussed above, and to further reduce this model set to a more manageable size, we will only consider models whose optimized $M_{\rm eff}$ value is ≤ 800 GeV. We note that a large fraction of models in this set have relatively heavy LSPs with masses in excess of 400 GeV. We now discuss two brief examples of these comparisons.

Figure 4.16 shows a comparison of two similar models, 8944 (observed in the 3,4jOSDL channels) and 21089 (missed by all analyses), that have comparable total colored sparticle production rates (3.4 and 4.6 pb, respectively). Both of these models are not observed in the nj0l searches since the lighter squarks are too close in mass to the LSP to produce hard jets. The gaugino sectors of these two models are quite similar (with the LSP and $\tilde{\chi}_2^0$ being Higgsino-like and $\tilde{\chi}_3^0$ being bino-like), while their colored sparticle spectra are somewhat different. In either model the decay of $\tilde{\chi}_3^0$ allows for the OSDL production through an intermediate slepton which has sufficient p_T to pass the analysis requirements. However, while 8944 has a $\tilde{u}_R$ with mass below that of the gluino (which is light enough to give a reasonable cross section), allowing for the decay into $\tilde{\chi}_3^0$, only $\tilde{d}_R$ is (sufficiently) heavier than the $\tilde{\chi}_3^0$ in model 21089. In this case, $\tilde{d}_R$ is also much more massive than the gluino, through which it will dominantly decay, and so it will not have a large enough branching fraction into $\tilde{\chi}_3^0$ to produce the OSDL signature.

Figure 4.17 compares models 9781 (discovered in the 2jSSDL channel) and 20875 (completely missed) that have total colored sparticle production cross sections of 1.3

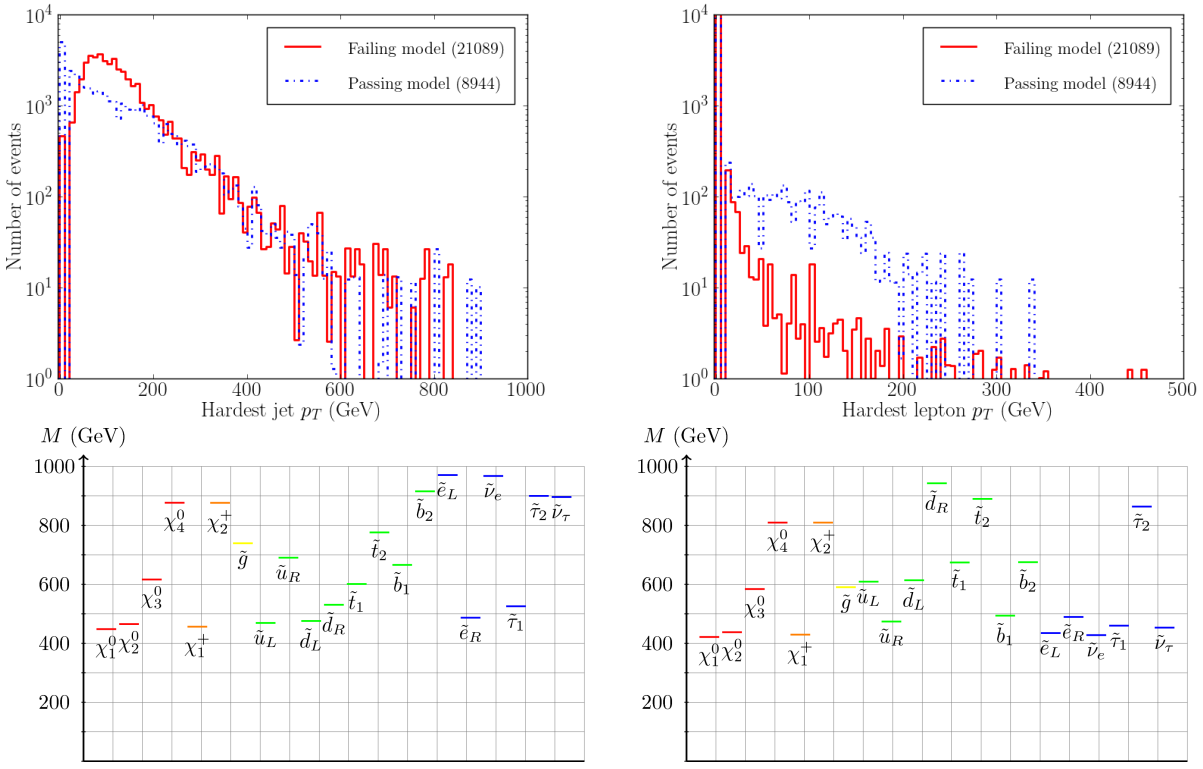

Figure 4.16: The top panels compare the leading jet (left) and leading lepton (right) p_T spectra for models 8944 (observed in 3,4jOSDL) and 21089 (missed by all analyses). The bottom panels show the sparticle spectra for models 8944 (left) and 21089 (right).

and 1.1 pb, respectively, but yet produce too few hard jet plus $E_T^{\rm miss}$ events to be found in the nj0l channels due to spectrum compression. Model 9781 is quite interesting as the charginos and lightest three neutralinos are highly mixed combinations of winos and Higgsinos. In this model, $\tilde{u}_R$ (which is relatively light) decays to $j + \tilde{\chi}_2^0$ with a $\sim 98\%$ branching fraction. Since $\tilde{\chi}_2^0$ has a large bino content, it decays $\sim 95\%$ of the time through sleptons which subsequently decay directly to the LSP with a branching fraction of $\sim 45\%$. Thus model 9781 can easily populate the leptonic final state and since the neutralinos are Majorana fermions, the 2jSSDL final state becomes accessible, a channel with an extremely small background. On the other hand, model 20875 does not allow for the generation of a typical leptonic signal. This is because the $\tilde{e}, \tilde{\mu}$ are quite heavy so that the neutralinos only allow for decay to τ leptons via an intermediate on-shell $\tilde{\tau}$. This is correlated with the relative lightness of the $\tilde{\tau}$ as well as the Higgsino-like LSP. In addition, the lightest squarks decay primarily directly to the LSP which will not produce any high-p_T leptons.

These two examples demonstrate that the full sparticle spectrum may conspire to render a model undiscoverable in the $E_T^{\rm miss}$-based analysis suite, even if the colored sparticle cross section is large. Discovery is not based on the value of the squark and/or gluino masses alone and blanket limits that claim $m_{\tilde{q},\tilde{g}}$ are ruled out below some value cannot be set.

4.3.4 Detector Stable Sparticles in Cascades

As we mentioned above, one of the reasons that some pMSSM models may not be observed in the ATLAS $E_T^{\rm miss}$ analyses is that squark and gluino cascade decays can sometimes lead to a final state with low $E_T^{\rm miss}$. In many cases this is due to the existence of long-lived sparticles, usually charginos, which appear with sizable branching fractions in such cascade chains and are essentially detector stable. Particles that decay outside the detector when produced at the LHC would provide a dramatic signal of new physics (see [23] and references therein). In fact, data from the LHC are already extending the mass limits on such detector-stable sparticles [24]. Since the inclusive $E_T^{\rm miss}$ analyses discussed above do not consider such sparticles, we will briefly

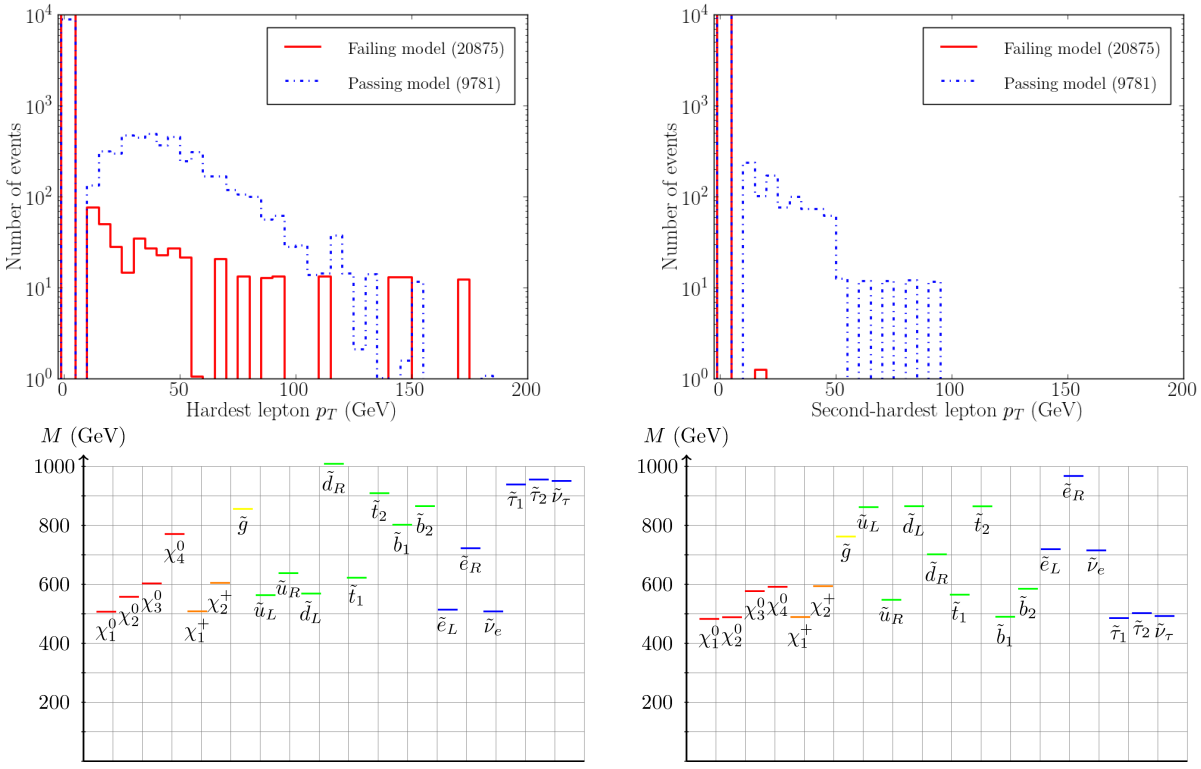

Figure 4.17: The top panels compare the leading (left) and secondary (right) lepton p_T spectra for models 9781 (observed in 2jSSDL) and 20875 (missed in all analyses). The bottom panels show the sparticle spectra for models 9781 (left) and 20875 (right).

sketch the 7 TeV discovery prospects for detector-stable sparticles in our model sets. As discussed in our earlier work [9], the existence of such long-lived states is relatively common in our pMSSM model sample as can be seen in Fig 4.18.[4]

Our estimation of the 7 TeV LHC mass reach for each long-lived sparticle is shown in Table 4.5 for the specified integrated luminosities, assuming direct pair production. These results are deduced from Figure 1 of [25] by taking the geometric mean of the search reach for a 5 and 10 TeV LHC at the specified luminosities and are interpolated to the luminosities considered here where necessary. These results are somewhat conservative as only detector-stable sparticle production in the hard process is considered; additional detector-stable sparticles could be produced through cascade decays as discussed below.

Sparticle	Reach 100 pb^{-1}	Reach 1 fb^{-1}	Reach 10 fb^{-1}
$\tilde{\chi}^+$ (Wino-like)	206 GeV	264 GeV	334 GeV
$\tilde{\chi}^+$ (Higgsino-like)	153 GeV	204 GeV	267 GeV
$\tilde{\tau}$	79 GeV	109 GeV	146 GeV
$\tilde{t}$	294 GeV	363 GeV	441 GeV
$\tilde{g}$	563 GeV	654 GeV	751 GeV

Table 4.5: Approximate 7 TeV LHC search reaches for detector-stable sparticles of the given species with 100 pb^{-1}, 1 fb^{-1}, and 10 fb^{-1} [25].

The number of detector-stable sparticles of various species in our model sample is shown in Table 4.6. This Table also shows the number of detector-stable sparticles which will not be discovered at LHC with 100 pb^{-1} and 1 fb^{-1} of integrated luminosity, using the approximate mass reaches presented in Table 4.5. We assume here that the mass reach is roughly generation-independent and that it is the same for, e.g., stops and sbottoms. This assumption is reasonable except where there could be significant t-channel production for the first or (to a lesser extent) second generation, for instance

[4]Recall that we will define a particle to be detector-stable if its unboosted decay length in at least 20m. Note that typical values of $\gamma\beta$ for long-lived particles resulting from cascade decays are in the 2-3 range. Further note that the dependence of the number of detector-stable sparticles of various species in this model set on the value of the decay width $\Gamma_{\rm stable}$ that is assumed is discussed in detail in [9].

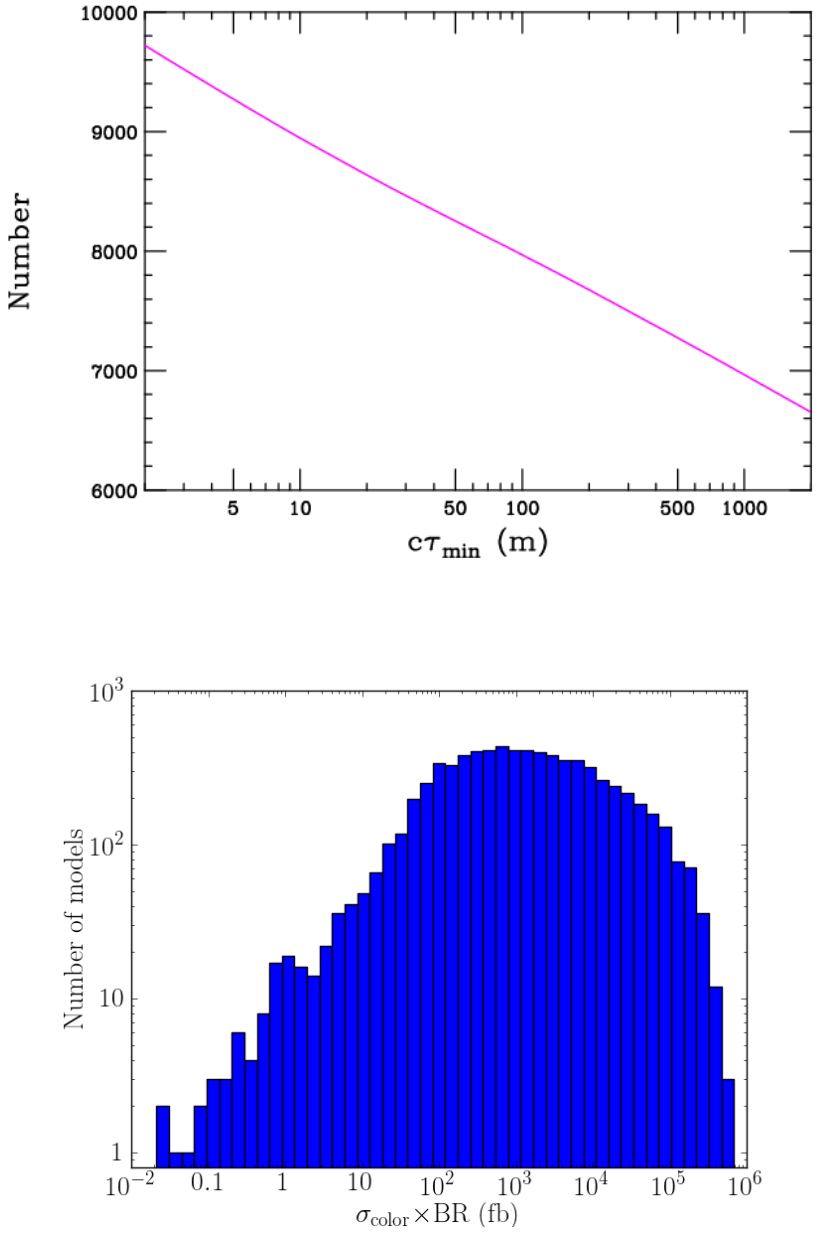

Figure 4.18: (Top) Number of models from both the log and flat prior sets combined having a charged sparticle with an unboosted decay length above a given value. (Bottom) Distribution of the estimated cross section times branching fraction for the production of detector-stable charginos in cascade decays in the flat prior model set.

in the case of up or down squarks.

Sparticle	In Model Set	Reach 100 pb^{-1}	Reach 1 fb^{-1}	Reach 10 fb^{-1}
$\tilde{\chi}_1^+$	8642	8623	3471	1024
$\tilde{\tau}_1$	179	179	174	129
$\tilde{t}_1$	66	20	9	1
$\tilde{c}_R$	49	10	4	1
$\tilde{\mu}_R$	17	17	17	11
$\tilde{b}_1$	11	0	0	0
$\tilde{c}_L$	8	0	0	0
$\tilde{s}_R$	8	3	0	0
$\tilde{g}$	5	0	0	0

Table 4.6: The second column from the left gives the number of detector-stable sparticles of various types in our model set. The next two columns show the number of such sparticles that will not be discovered after 100 pb^{-1}, 1 fb^{-1}, and 10 fb^{-1} at the 7 TeV LHC, following [25].

We now focus on the specific case of long-lived charginos, which are by far the most common long-lived sparticles in our model sets. If the production cross section for colored sparticles (times relevant branching fractions into charginos) are sufficiently large, these stable charginos should be found in searches for (effectively) stable charged particles occurring at the end of a cascade decay chain. In Fig. 4.18 we display the estimated value for σB for the production of detector-stable charginos in cascade decays in our flat prior set. (Note that this does not include the direct contribution arising from direct chargino pair production.) Here, we see that roughly $\sim 84\%$ of models with detector-stable charginos lead to σB values in excess of 10 fb at 7 TeV and so we expect them to be observable in the upcoming run of the LHC. In this estimation, we assumed the largest contribution to the production cross section arises from the production of gluino and light squark species. Using the decay tables generated for each model with detector-stable charginos, we calculated the branching fraction for the gluino and light squarks to produce a stable chargino at the end of each possible decay chain and then weighted them by their corresponding production cross-sections. Note that mass information for neither the mother particles nor the daughter chargino is used to indicate how likely it is that the chargino will pass the

trigger criteria for detection. As we used PYTHIA to compute the LO cross-section for the light squarks, we do not separately generate the production for the various light squark species. Thus in order to obtain our estimate, we make the assumption that the overall cross section is 100% dominated by that arising from the lightest squark. This assumption will break down when the squarks are nearly degenerate, especially when their branching fractions to charginos are vastly different due to the complexities in the gaugino sector. Many of our models have a large production cross-section for colored sparticles, but the relevant branching fractions to charginos can be simultaneously quite small. This can result in very small overall production rates for stable charginos well below ~ 10 fb.

4.3.5 SUSY Mass Scale From $M_{\rm eff}$

In our earlier work on the 14 TeV ATLAS $E_T^{\rm miss}$ analyses, we demonstrated that the relationship between $M_{\rm eff}$ and the mass of the lightest colored sparticle found in mSUGRA, i.e., $M_{\rm eff} \simeq 1.5 m_{\rm LCP}$ (where LCP stands for Lightest Colored Particle), proposed long ago [26] does not necessarily hold in the pMSSM. This possible relationship is important as it might be used to get the first handle on the overall mass scale of the sparticle spectrum. Here, we briefly note that this result remains valid for the 7 TeV ATLAS $E_T^{\rm miss}$ analyses as can be seen in Fig. 4.19. For both the 4j0l and 2j0l channels we see explicitly that the values of $M_{\rm eff}$ lie mostly above the expected value of $1.5 m_{\rm LCP}$, especially in the low sparticle mass region. However, for lightest colored sparticle masses in excess of $\simeq 550 - 600$ GeV we see that, indeed, the relationship $M_{\rm eff} \simeq 1.5 m_{\rm LCP}$ provides a fairly good estimate in both of these $E_T^{\rm miss}$ searches.

4.3.6 Modifying ATLAS SUSY Analysis Cuts

Given the properties of the various sparticles in our model sets, we can try to determine whether the canonical cuts employed in the ATLAS $E_T^{\rm miss}$-based search analyses can be strengthened to reduce SM backgrounds without any significant loss in the coverage of our pMSSM model space. This is certainly a non-trivial issue and the

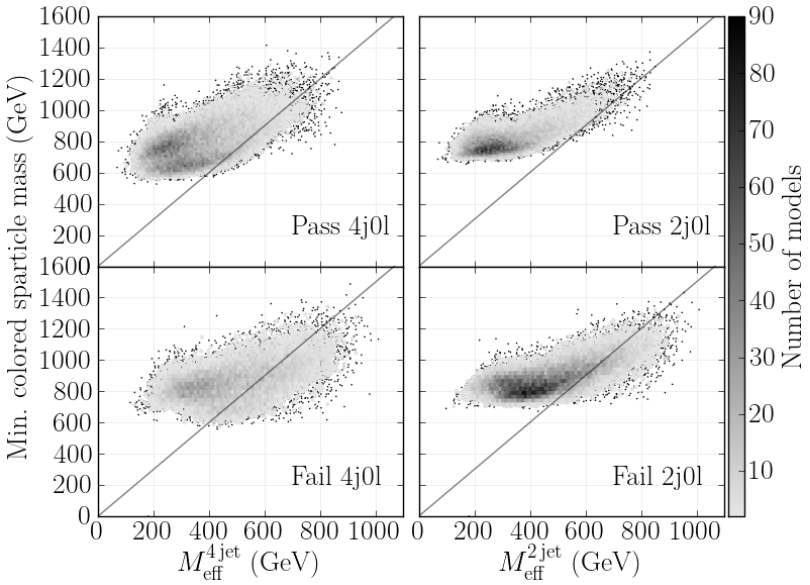

Figure 4.19: Correlation between the value of $M_{\rm eff}$ and the mass of the lightest colored sparticle for the 7 TeV 4j0l (left) and 2j0l (right) ATLAS $E_T^{\rm miss}$channels. The top (bottom) points correspond to flat prior models which are found(missed) in these two search analyses. In highly populated regions the cell shading represents how many models are in that cell.

structure of our analysis, being based on the fixed ATLAS $E_T^{\rm miss}$ analyses cuts, is not directly set up to obtain completely definitive answers. However, it is possible to make some reasonable estimates based on the information that we do have available. We will concentrate on the three nj0l analyses as they generally provide the greatest pMSSM model coverage and have large statistics. The most important kinematic quantities for these searches are the requirements on the leading jet p_T and the required amount of $E_T^{\rm miss}$. Here, we make use of the average values of the distributions in these quantities for our pMSSM model sample, as well as the corresponding fitted width of the part of the distribution below this average value for pre-selected events. This information then provides us with an estimate of where these two kinematic distributions 'turn on,' which we take to be the average value minus this width, on the low energy/momentum side below their peak average values.

First consider the cut on the leading jet, p_{T_1}, for the 2(3,4)j0l analyses; ATLAS chooses the value for this cut to be 180(100,100) GeV, respectively. Fig. 4.20 shows the distribution of the 'turn-on' p_T values for these three ATLAS analyses obtained from analyzing the flat prior model set. For the 2j0l analysis, we see that the lower edge of the 'turn-on' values lies somewhat below the cut value of 180 GeV from which we can conclude that this cut is already reasonably hard and cannot be increased without a loss of model coverage. However, for both the 3j0l and 4j0l analyses we instead observe that the 'turn-on' values lie above those of the ATLAS cuts by ~ 20 GeV suggesting that that the p_{T_1} cut in these two channels may be raised without impacting coverage rates for the pMSSM.

Similarly, the nominal $E_T^{\rm miss}$ cut imposed by ATLAS for the nj0l analyses is 80 GeV. However, there is an additional subsequent cut imposed by ATLAS based on the value of $M_{\rm eff}$, i.e., $E_T^{\rm miss} \geq f\, M_{\rm eff}$ where $f = 0.30(0.25, 0.20)$ for the $n = 2(3, 4)$ analyses. Fig. 4.21 shows the distributions for the 'turn-on' values of $E_T^{\rm miss}$ for these three channels employing the flat prior model set. Here we see that the lower edge of this distribution occurs at $\sim 160(130, 120)$ GeV for $n = 2(3, 4)$, respectively. This is suggestive that the nominal $E_T^{\rm miss}$ cut made by ATLAS may be increased for these three analyses without losing significant pMSSM model coverage.

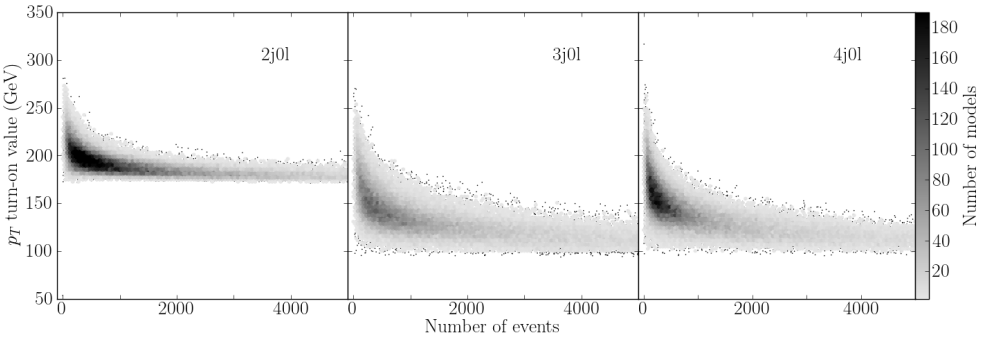

Figure 4.20: Approximate location of the lower edge of the leading jet p_T distribution as a function of the number of preselected events employing the flat prior model set for the 2j0l (left), 3j0l(middle) and 4j0l (right) ATLAS search analyses as discussed in the text. Dots represent individual models while in the highly populated regions, the shading reflects the number of models per cell.

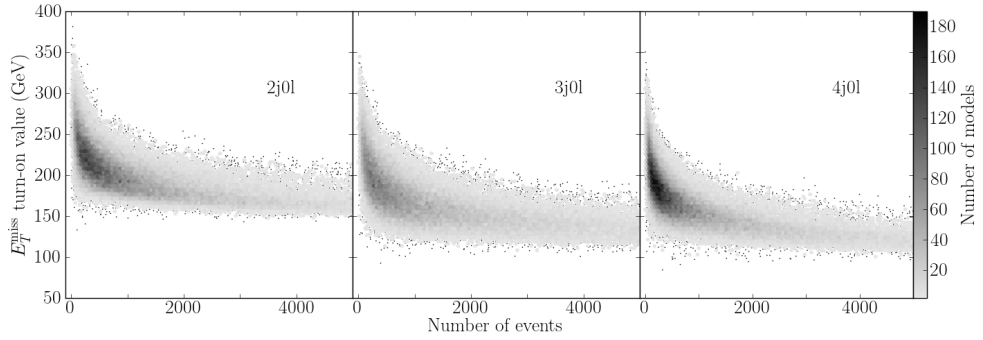

Figure 4.21: Same as in the previous figure but now for the E_T^{miss} distribution.

4.4 Implications of the 7 TeV Run

In this section, we explore some implications of a null search for Supersymmetry at the 7 TeV LHC. We examine the degree of fine-tuning that would be placed on our pMSSM model sample and we discuss the resulting expectations for sparticle production at a 500 GeV and 1 TeV Linear Collider.

4.4.1 Fine-tuning in the Undiscovered pMSSM Models

As has recently been discussed in the mSUGRA/CMSSM context [27, 28], it is apparent that if SUSY signatures are not discovered at the 7 TeV LHC as the integrated luminosity accumulates it is likely that the SUSY parameter space must become more fine-tuned, and hence more problematic as a solution to the hierarchy problem. Since we know which models in our sample are discoverable (or not) by the ATLAS $E_T^{\rm miss}$ search analyses, we can ask whether this same result also holds in the case of our pMSSM model sets.[5]

Figure 4.22 displays the results of this analysis assuming a background systematic error of 50% for both the flat and log prior model samples. Clearly, in the flat prior case, one sees that as the integrated luminosity increases and more models can be discovered by ATLAS, those remaining yet *undiscovered* tend to be more fine-tuned as expected. In other words, the fractional loss of models from the full distribution occurs more rapidly with increasing luminosity for models with smaller amounts of fine-tuning. This is not too surprising as, overall, models with less tuning tend to have lighter SUSY sparticle spectra and are thus more easily discovered at the LHC. On the other hand, the results from the log prior model set appear to be affected somewhat differently in that the overall shape of the fine-tuning distribution does not appear to change very much by removing models that should have been already been discovered by ATLAS as the luminosity increases. In this case, we see that there is not much of an increase in the amount of fine-tuning as the set of undiscovered models shrinks. This represents one of the few apparent differences between these

[5]Note that the amount of fine-tuning in both our model sets was examined in some detail in our earlier work [7].

two different model sets. This can be explained by the fact that while the log prior model set tends to have light sparticle spectra (though they extend out to larger mass values than do those for the flat prior models) and are thus less fine-tuned to begin with, these same spectra are generally compressed making these models more difficult to discover at the LHC as was discussed above. This would imply that the models missed by the ATLAS $E_T^{\rm miss}$ analyses in the log prior case are generally *not* much more fine-tuned than those appearing in the originally generated model set. Thus we find that the amount of fine-tuning that remains in the LHC-undiscovered pMSSM model sample can depend upon the prior used to generate the original model set.

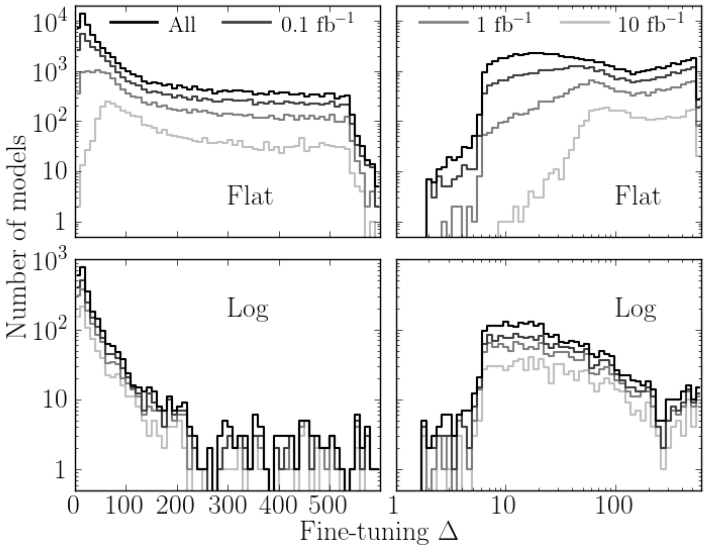

Figure 4.22: Two projections of the fine-tuning distributions for models in our flat (top panels) and log (bottom panels) prior sets. The top black histogram in all panels shows the result for the full model set while the subsequently lower and lighter gray histograms correspond to models not observed by the ATLAS $E_T^{\rm miss}$ search analyses for various values of the integrated luminosity as indicated, assuming a background uncertainty of 50%.

4.4.2 Implications of pMSSM Searches for the Linear Collider

If there are no clear SUSY signals as the 7 TeV LHC integrates more luminosity, the question arises whether the production (and study) of charged sparticles remains viable at the proposed 500 GeV Linear Collider (LC). Based on mSUGRA/CMSSM model coverage projections from both the ATLAS [12] and CMS [29] Collaborations at 7 TeV with a 1 fb^{-1} integrated luminosity (as well as their results from the 2010 SUSY searches), it would seem very unlikely that either light sleptons or gauginos (other than perhaps the LSP itself) will remain kinematically accessible at a 500 GeV LC if nothing is observed. Here, we address the question whether this expectation also remains true for our pMSSM model sets. To this end we examine the set of flat and log prior models which are not detected by *any* of the ATLAS $E_T^{\rm miss}$ search analyses for assumed values of both the integrated luminosity and background systematic error and then determine the part of the sparticle spectrum within these models which is kinematically accessible at a 500 GeV LC.[6] A similar analysis can also be performed for a 1 TeV LC. We remind the reader that, e.g., in the flat prior case we have no sparticles heavier than ~ 1 TeV.

We present the results of this analysis in various ways. Tables 4.7 and 4.8 show the number of sparticles of various species that are kinematically accessible at a 500 GeV or 1 TeV LC within the subset of ATLAS-undetected models assuming $\mathcal{L} = 1(10)$ fb^{-1} with $\delta B = 50(20)\%$, respectively. These two cases represent both a possibly conservative and a more optimistic performance for the LHC over the 2011-12 running period. Here we see several things: (*i*) In addition to the gauginos and sleptons, sparticles such as stops, sbottoms and other squarks are potentially almost as likely to also be kinematically accessible at the LC [32]. (*ii*) The number of models with kinematically accessible sparticles and their variety is significantly greater in the log prior sample as these models are more likely to have a lighter and more compressed sparticle spectrum (*iii*) The difference between the two cases presented in these Tables is quite significant; in particular, we see that for the flat prior model

[6] Note that we have not performed any analysis here to ascertain whether or not a given kinematically accessible sparticle is actually *observable* at such a LC. See, however, the work in Refs. [30, 31].

set there is a huge depletion in the number of unobserved models at higher luminosity and with lower background systematics. There are extremely few flat prior models remaining at high luminosity with any accessible sparticles at a 500 GeV LC. (*iv*) Going from a 500 GeV to a 1 TeV LC *substantially* increases the number of models with kinematically accessible sparticles, especially in the flat prior case. It is clear that, at least for the flat prior model sample with luminosities in excess of 1 fb^{-1} at the LHC, that the 500 GeV LC does not seem to be a good place to study our pMSSM models if no signal for SUSY is found at the LHC in 2011-12.

	$\sqrt{s} = 500$ GeV		$\sqrt{s} = 1$ TeV	
Sparticle	Flat	Log	Flat	Log
$\tilde{e}_L$	107	101	3052	347
$\tilde{e}_R$	260	209	3938	565
$\tilde{\tau}_1$	730	381	7431	869
$\tilde{\tau}_2$	30	36	1288	207
$\tilde{\nu}_e$	151	117	3168	356
$\tilde{\nu}_\tau$	386	236	4366	553
$\tilde{\chi}_1^0$	5487	1312	14,510	1539
$\tilde{\chi}_2^0$	2738	1035	10,714	1395
$\tilde{\chi}_3^0$	429	352	5667	903
$\tilde{\chi}_4^0$	10	18	1267	202
$\tilde{\chi}_1^\pm$	4856	1208	13,561	1495
$\tilde{\chi}_2^\pm$	94	54	3412	456
$\tilde{g}$	0	0	1088	65
$\tilde{d}_L$	35	11	2459	117
$\tilde{d}_R$	220	96	3630	526
$\tilde{u}_L$	52	16	2545	123
$\tilde{u}_R$	124	64	3581	273
$\tilde{b}_1$	289	75	5553	590
$\tilde{b}_2$	1	0	409	21
$\tilde{t}_1$	93	9	3727	217
$\tilde{t}_2$	0	0	2	0

Table 4.7: Number of kinematically accessible sparticles from our set of 14623(1546) flat(log) prior pMSSM models that are unobservable by the ATLAS $E_T^{\rm miss}$ searches assuming $\mathcal{L}$=1 fb^{-1} with $\delta B = 50\%$ for both a 500 GeV and 1 TeV LC.

In order to study these LC results in more detail we examine their dependence on

	$\sqrt{s} = 500$ GeV		$\sqrt{s} = 1$ TeV	
Sparticle	Flat	Log	Flat	Log
$\tilde{e}_L$	0	37	63	142
$\tilde{e}_R$	0	72	53	223
$\tilde{\tau}_1$	2	142	165	338
$\tilde{\tau}_2$	0	11	9	69
$\tilde{\nu}_e$	0	42	64	146
$\tilde{\nu}_\tau$	0	85	81	236
$\tilde{\chi}_1^0$	26	507	587	626
$\tilde{\chi}_2^0$	4	397	352	557
$\tilde{\chi}_3^0$	0	136	57	357
$\tilde{\chi}_4^0$	0	5	5	66
$\tilde{\chi}_1^\pm$	25	467	505	608
$\tilde{\chi}_2^\pm$	0	17	16	170
$\tilde{g}$	0	0	27	5
$\tilde{d}_L$	0	3	73	24
$\tilde{d}_R$	1	18	63	157
$\tilde{u}_L$	0	5	81	24
$\tilde{u}_R$	0	14	86	79
$\tilde{b}_1$	0	20	103	189
$\tilde{b}_2$	0	0	3	4
$\tilde{t}_1$	1	2	94	58
$\tilde{t}_2$	0	0	0	0

Table 4.8: Same as the previous Table but now corresponding to the 672(663) undetected flat(log) prior models assuming $\mathcal{L}$=10 fb^{-1} with $\delta B = 20\%$.

the LHC integrated luminosity; this is shown for the 500 GeV LC in Fig. 4.23 and for the 1 TeV LC in Fig. 4.24. Here we display the *fraction* of the unobserved set of models that have a kinematically accessible sparticle of a particular variety. At a 500 GeV LC, this fraction for charginos, stops, sbottoms, selectrons (or smuons) and staus in the flat prior model set is seen to decrease significantly as the LHC accumulates integrated luminosity without observation of a signal for SUSY. However, note that for the corresponding log prior model set, while the number of surviving models decreases with any corresponding increase in the LHC integrated luminosity (or with any decrease in the SM background uncertainty) as one would expect, the *fraction* of the surviving models with a kinematically accessible sparticle changes very little, if at all! For charginos at a 500 GeV LC this fraction is found to be quite large, $\sim 75\%$, but it is found to be somewhat smaller for the other sparticles, e.g., $\sim 25\%$ for $\tilde{\tau}_1$ and $\sim 7\%$ for $\tilde{e}_L$.

One possible explanation of this unexpected behavior in the log prior sample is as follows: As we saw in the previous discussion of fine-tuning, in the log prior case, the removal of pMSSM models from the log prior set (as they are 'discovered' by ATLAS) must affect the various sparticle mass distributions in a roughly uniform manner. Otherwise the observed amount of fine-tuning would necessarily increase. However, in the flat prior case, models with lighter sparticles are preferentially 'discovered' by ATLAS searches. This hypothesis can qualitatively explain why there is no significant reduction in the *fraction* of the log prior models with kinematically accessible sparticles at a 500 GeV (or 1 TeV) LC (especially in the case of non-colored sparticles as we have seen above). It also simultaneously explains why the apparent amount of fine-tuning does not change appreciably as the LHC covers more of the log scan parameter space. Of course, as can be seen from these figures, at a 1 TeV LC a substantial portion of both the log and flat prior model sets which remain undiscovered at the LHC have sparticles which are kinematically accessible even at high LHC integrated luminosities. We further note that the fraction of LHC-unobserved models where *no* SUSY sparticles whatsoever are accessible at a LC (not even the LSP) is quite large for the flat model set at a 500 GeV LC, but is only in the 12-20% range for the corresponding log prior model set. On the other hand, at a 1 TeV LC,

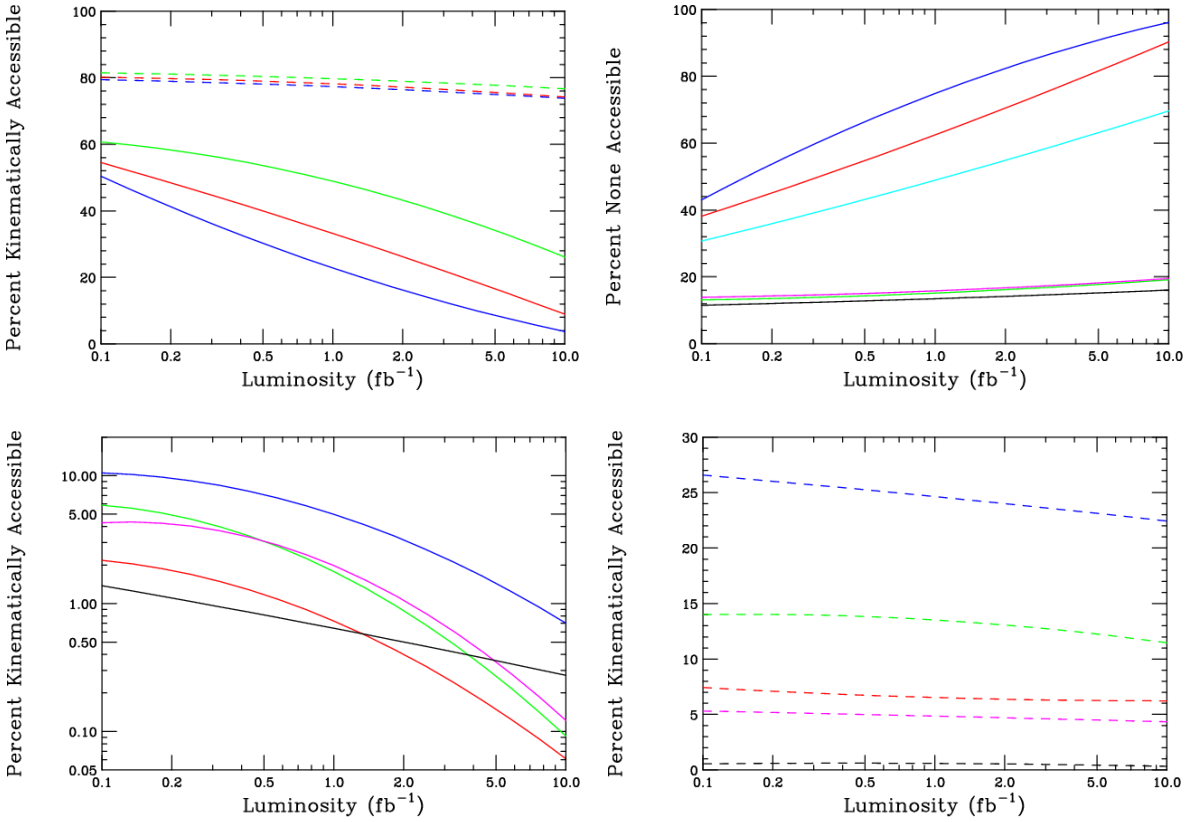

Figure 4.23: Top left: Fractional number of undetected models with kinematically accessible $\tilde{\chi}_1^{\pm}$ at a 500 GeV LC as a function of the LHC integrated luminosity for flat(solid) and log(dashed) prior models. From top to bottom, the green(red, blue) curves correspond to background systematic uncertainties of 100(50,20), respectively. Bottom left: Same as the previous panel but now for flat prior models only with $\delta B = 50$ for (from top to bottom according to the curves' intersection with the y-axis) the $\tilde{\tau}_1$(blue), $\tilde{e}_R$(green), $\tilde{b}_1$(magenta),$\tilde{e}_L$(red), and $\tilde{t}_1$(black). Bottom right: Same as the previous panel but now for log prior models, where the order of the curves, from top to bottom,is now $\tilde{\tau}_1$(blue), $\tilde{e}_R$(green), $\tilde{e}_L$(red), $\tilde{b}_1$(magenta), and $\tilde{t}_1$(black). Top right: Fraction of undetected models with *no* sparticles kinematically accessible. From top to bottom, the blue(red, cyan) curves are for flat prior models with $\delta B = 20(50, 100)\%$ while the magenta(green, black) curves are the corresponding results for the log prior set.

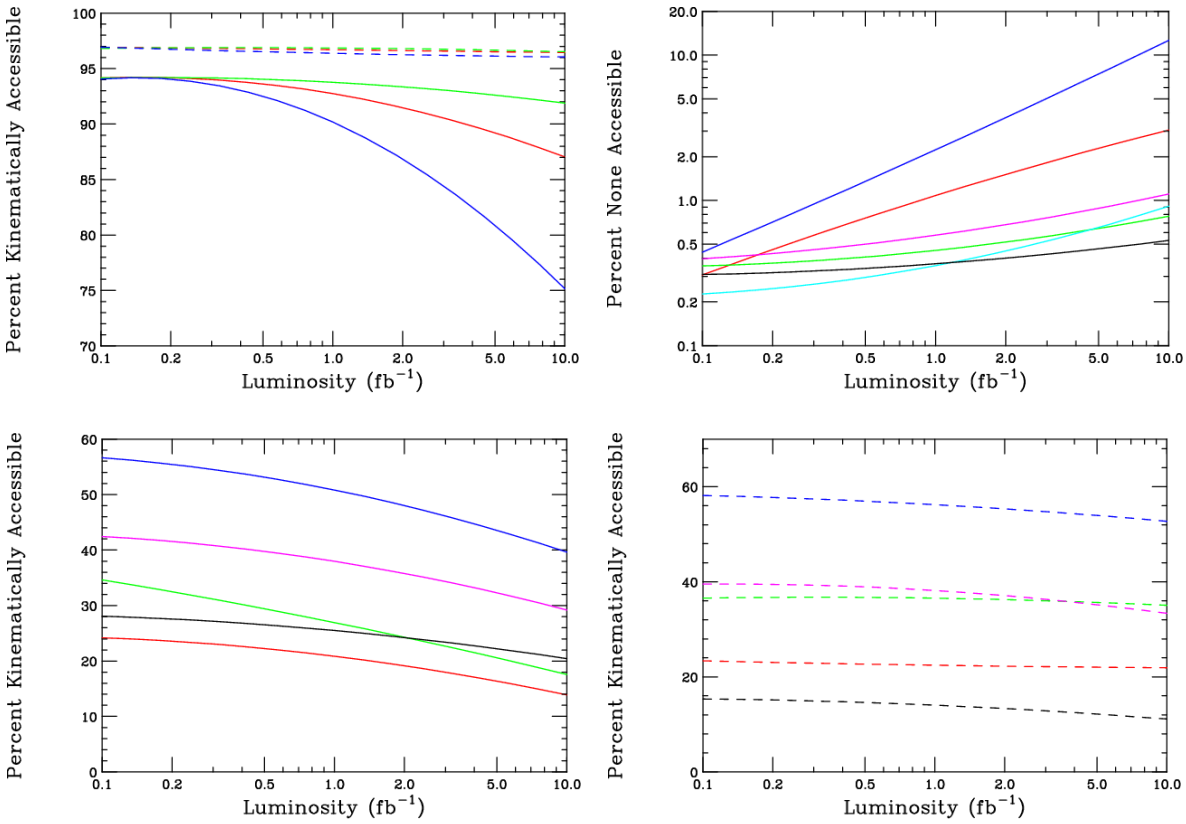

Figure 4.24: Same as in the previous Figure but now for a 1 TeV LC. The order of curves has changed for all but the first panel, so we will specify the new order here. Bottom left: From top to bottom (according to the curves' intersection with the left-hand edge of the frame) the curves are $\tilde{\tau}_1$(blue), $\tilde{b}_1$(magenta), $\tilde{e}_R$(green), $\tilde{t}_1$(black), and $\tilde{e}_L$(red). Bottom right: From top to bottom (according to the curves' intersection with the left-hand edge of the frame) the curves are $\tilde{\tau}_1$(blue), $\tilde{b}_1$(magenta), $\tilde{e}_R$(green), $\tilde{e}_L$(red), and $\tilde{t}_1$(black). Top right: From top to bottom (according to the curves' intersection with the *right*-hand edge of the frame) the curves are $\delta B = 20\%$, flat prior(blue); $\delta B = 50\%$, flat prior(red); $\delta B = 20\%$, log prior(cyan); $\delta B = 100\%$, flat prior(cyan); $\delta B = 50\%$, log prior(green); $\delta B = 100\%$, log prior(black).

this value is seen to lie below $\sim 1\%$ for the log prior models, while for the flat prior set it remains below $\sim 13\%$. Clearly, a 1 TeV LC will be far better at accessing the sparticles in our pMSSM model sets.

In order to test this hypothesis, we show the mass distributions for the $\tilde{e}_L$ and $\tilde{\chi}_2^0$ in both the flat and log prior model sets in Fig. 4.25.[7] Indeed, we see that this hypothesis is true for non-colored states: in the flat prior set, models being observed by the ATLAS analyses mostly correspond to those with lower sparticle masses. On the other hand, for the log prior case, we see that the mass distributions for non-colored sparticles approximately maintain their overall shape as the models are observed, showing not much preference for the lighter sparticle masses. Fig. 4.26 shows, however, that in the case of colored sparticles, here for the gluinos and (one of the) squarks, which are most directly sensitive to most of the ATLAS $E_T^{\rm miss}$ analyses, this same effect is somewhat less significant. In particular for the gluinos we see that even in the log prior case there is a significant loss in the fraction of models with lighter masses as the LHC integrated luminosity is increased.

4.5 Summary and Conclusions

In this paper we have analyzed the capability of the ATLAS $E_T^{\rm miss}$-based SUSY analyses to discover Supersymmetry in a model independent fashion at the 7 TeV LHC. To this end, we tested these search channels on a large set of model points, $\sim$ 71k, in the 19-dimensional parameter space of the pMSSM. This model sample contains a wide variety of properties and characteristics and provides a framework to explore the breadth of possible SUSY signatures at colliders and elsewhere. These models were generated in a previous work and comply with a set of minimal theoretical assumptions as well as the global precision electroweak, heavy flavor, collider searches, and astrophysical data sets. We simulated ten ATLAS $E_T^{\rm miss}$ search channels, which were designed in the context of mSUGRA-based SUSY, and employed the SM backgrounds as provided directly by the ATLAS SUSY working group. We first checked that our

[7] Note that there is nothing special about the choice of these two particular non-colored sparticles and the features that we will now describe are also found in the mass distributions of other sparticles.

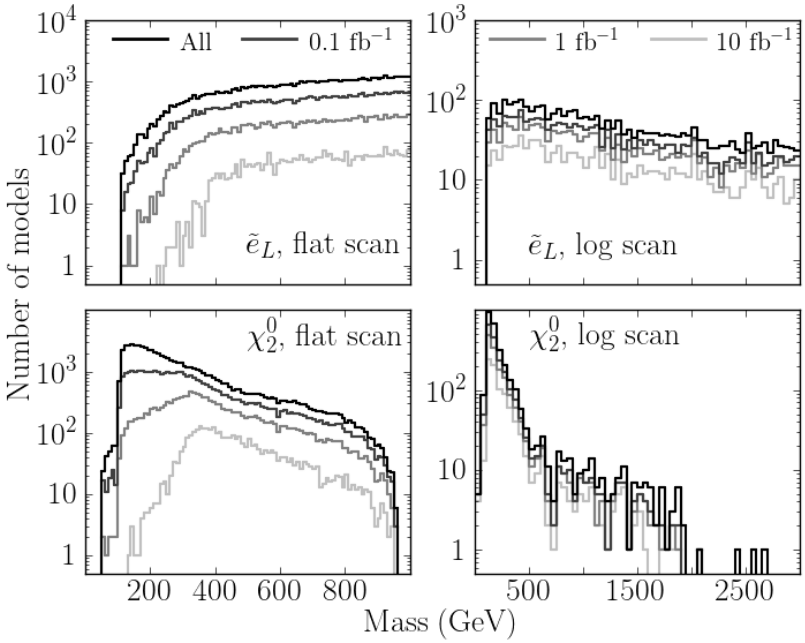

Figure 4.25: Mass distributions for $\tilde{e}_L$ (top) and $\tilde{\chi}_2^0$ (bottom) for the ATLAS-undetected flat (left) and log (right) prior models assuming $\delta B = 50\%$ for different values of the LHC integrated luminosity as indicated. The top black histogram in each case corresponds to the original model sets before any of the ATLAS analyses are considered while the subsequently lower histograms correspond to those subsets of models undetected by the ATLAS $E_T^{\rm miss}$ analyses at fixed integrated luminosities.

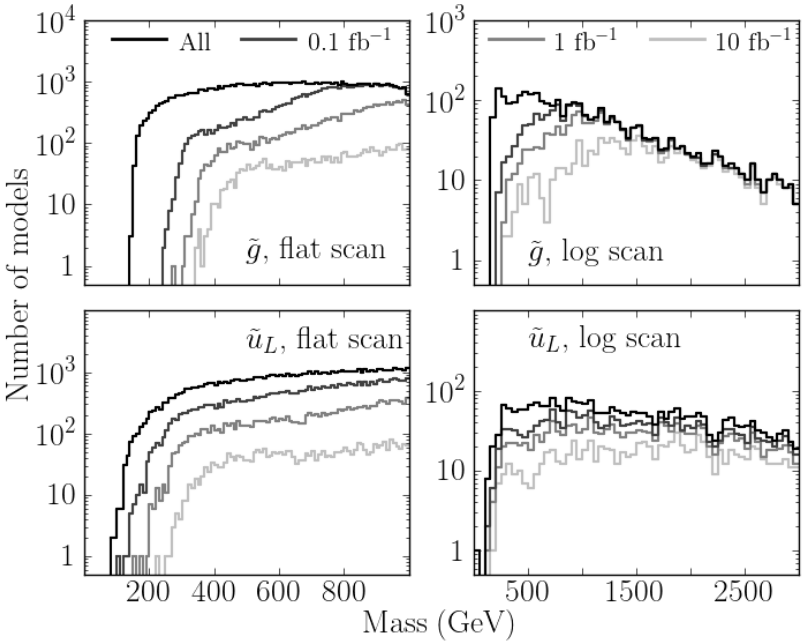

Figure 4.26: Same as the previous Figure but now for gluinos and $\tilde{u}_L$.

analyses were in agreement with ATLAS results for the mSUGRA benchmark point that the collaboration had previously simulated.

We passed our model sample through the ATLAS analysis chain and computed the significance of the signal for each model in each search channel. A significance of $S \geq 5$ was used as the criteria for discovery in each channel; we employed the same numerical technique that ATLAS does for calculating this value. We found that the systematic error due to uncertainties in the size of the expected background made a substantial impact on model discovery for the range of expected integrated luminosities. In fact, some channels become systematics dominated at luminosities of order $5 - 10$ fb^{-1}. Overall, for 1(10) fb^{-1} of integrated luminosity roughly 80(95)% of the flat prior model sample is discoverable, assuming a 50% background systematic error. Larger (or smaller) systematic errors greatly reduce (or increase) this model coverage. We found that the 4j0l channel is the most powerful in terms of observing a signal, whereas the leptonic channels had a much reduced model coverage. This is due to the suppression of leptonic cascade decays appearing in our model sample

compared to expectations from *e.g.*, mSUGRA. The model coverage was worse for the log prior sample due to kinematic reasons.

We explored the characteristics that caused a model to not be observed in these search channels. While production cross section values as related to the sparticle mass obviously plays a role, it does not tell the whole story. There are cases with low mass gluinos and/or squarks with large cross sections that are missed by these search analyses, while models with heavy masses and small cross sections are sometimes observed. We found that the mass splitting between the gluino/squarks and the LSP plays an important role in detecting models, and that this can sometimes be compensated by very large production rates or ISR. We also saw that subtleties in the sparticle spectrum can conspire to render a model to not be detected. A fraction of our model set contains detector-stable sparticles which appear at the end of their cascade decay chains and hence are not detected by the $E_T^{\rm miss}$-based searches. We studied the effectiveness of the planned stable charged particle searches in these cases and found that some, but not all, of these models will be discovered.

We briefly considered potential modifications to the ATLAS kinematic cuts in these $E_T^{\rm miss}$ analyses that would improve their discovery potential. We studied the optimal cut on M_{eff} as well as for the p_T of the leading jet and overall $E_T^{\rm miss}$. Our results indicate that the cuts for both the leading jet transverse momentum and the $E_T^{\rm miss}$ could be increased from their nominal value without seriously impacting model coverage.

Lastly, we studied the implications of a null result from the 7 TeV LHC run. We found that the degree of fine-tuning that would be imposed on the pMSSM depended on the choice of priors which generated the model sample, but overall would not be as large as in the case of mSUGRA. However, the expectations for sparticle production at a high energy Linear Collider would be greatly impacted if Supersymmetry is not discovered during this LHC run. Basic kinematics would essentially exclude sparticle production at a 500 GeV Linear Collider, and would point towards the need for a higher energy machine in order to study Supersymmetry.

In summary, we find that the mSUGRA motivated $E_T^{\rm miss}$-based searches for Supersymmetry perform well over a larger and more complicated SUSY parameter space

such as the pMSSM. However, there are some exceptions and coverage is not perfect. The details of the full sparticle spectrum play a very important role in the observability of a model. There are no blanket statements regarding the potential for discovery, or in setting a mass limit, that that can honestly be made.

We anxiously await the discovery of Supersymmetry in the near future.

Bibliography

[1] For recent overviews of LHC searches for new physics, see E. Gross (ATLAS) and H. Flaecher (CMS), talks given at LaThuile-7-7-7 2011, Les Rencont res de Physique de la Valle d'Aoste, 27 Feb-5 Mar, 2011.

[2] V. Khachatryan *et al.* [CMS Collaboration], [arXiv:1101.1628 [hep-ex]]; CMS Collaboration, [arXiv:1103.0953 [hep-ex]]; CMS Collaboration, [arXiv:1103.1348 [hep-ex]]; G. Aad *et al.* [Atlas Collaboration], [arXiv:1102.2357 [hep-ex]]; ATLAS Collaboration, [arXiv:1102.5290 [hep-ex]].

[3] H. E. Haber and G. L. Kane, Phys. Rept. **117**, 75 (1985); S. P. Martin, arXiv:hep-ph/9709356; D. J. H. Chung, L. L. Everett, G. L. Kane, S. F. King, J. D. Lykken and L. T. Wang, Phys. Rept. **407**, 1 (2005) [arXiv:hep-ph/0312378]; L. Pape and D. Treille, Rept. Prog. Phys. **69**, 2843 (2006); H. K. Dreiner, H. E. Haber, S. P. Martin, Phys. Rept. **494**, 1-196 (2010); M. Drees, R. Godbole and P. Roy, *Hackensack, USA: World Scientific (2004) 555 p*; H. Baer and X. Tata, *Cambridge, UK: Univ. Pr. (2006) 537 p.*

[4] G. Aad *et al.* [The ATLAS Collaboration], [arXiv:0901.0512 [hep-ex]].

[5] G. L. Bayatian *et al.* [CMS Collaboration], J. Phys. G **G34**, 995-1579 (2007).

[6] J. Alwall, M. -P. Le, M. Lisanti, J. G. Wacker, Phys. Lett. **B666**, 34-37 (2008). [arXiv:0803.0019 [hep-ph]].

[7] C. F. Berger, J. S. Gainer, J. L. Hewett *et al.*, JHEP **0902**, 023 (2009). [arXiv:0812.0980 [hep-ph]].

[8] J. Alwall, P. Schuster, N. Toro, Phys. Rev. **D79**, 075020 (2009). [arXiv:0810.3921 [hep-ph]]; N. Arkani-Hamed, P. Schuster, N. Toro, J. Thaler, L. -T. Wang, B. Knuteson, S. Mrenna, [hep-ph/0703088 [HEP-PH]].

[9] J. A. Conley, J. S. Gainer, J. L. Hewett *et al.*, [arXiv:1009.2539 [hep-ph]].

[10] S. Akula, N. Chen, D. Feldman, M. Liu, Z. Liu, P. Nath, G. Peim, [arXiv:1103.1197 [hep-ph]]; S. Heinemeyer, [arXiv:1103.0952 [hep-ph]]; B. C. Allanach, T. J. Khoo, C. G. Lester, S. L. Williams, [arXiv:1103.0969 [hep-ph]]; P. Athron, S. F. King, D. J. Miller, S. Moretti, R. Nevzorov, [arXiv:1102.4363 [hep-ph]]; O. Buchmueller, R. Cavanaugh, D. Colling, A. De Roeck, M. J. Dolan, J. R. Ellis, H. Flacher, S. Heinemeyer *et al.*, [arXiv:1102.4585 [hep-ph]]; S. Scopel, S. Choi, N. Fornengo, A. Bottino, [arXiv:1102.4033 [hep-ph]]; B. C. Allanach, [arXiv:1102.3149 [hep-ph]]; D. Feldman, K. Freese, P. Nath, B. D. Nelson, G. Peim, [arXiv:1102.2548 [hep-ph]]; O. Buchmueller, R. Cavanaugh, D. Colling, A. De Roeck, M. J. Dolan, J. R. Ellis, H. Flacher, S. Heinemeyer *et al.*, Eur. Phys. J. **C71**, 1583 (2011). [arXiv:1011.6118 [hep-ph]].

[11] R. C. Cotta, J. A. Conley, J. S. Gainer, J. L. Hewett, T. G. Rizzo, JHEP **1101**, 064 (2011). [arXiv:1007.5520 [hep-ph]]; R. C. Cotta, J. S. Gainer, J. L. Hewett, T. G. Rizzo, Nucl. Phys. Proc. Suppl. **194**, 133-144 (2009). [arXiv:0909.4088 [hep-ph]]; R. C. Cotta, J. S. Gainer, J. L. Hewett, T. G. Rizzo, New J. Phys. **11**, 105026 (2009). [arXiv:0903.4409 [hep-ph]].

[12] ATLAS Note, *Prospects for Supersymmetry discovery based on inclusive searches at a 7 TeV centre-of-mass energy with the ATLAS detector*, Tech. Rep. ATL-PHYS-PUB-2010-010, CERN, Geneva (2010).

[13] L. Pape, D. Treille, Rept. Prog. Phys. **69**, 2843-3067 (2006); G. Weiglein *et al.* [LHC/LC Study Group Collaboration], Phys. Rept. **426**, 47-358 (2006). [hep-ph/0410364].

[14] A. Djouadi, J. -L. Kneur, G. Moultaka, Comput. Phys. Commun. **176**, 426-455 (2007). [hep-ph/0211331].

[15] G. D'Ambrosio, G. F. Giudice, G. Isidori, A. Strumia, Nucl. Phys. **B645**, 155-187 (2002). [hep-ph/0207036].

[16] F. Abe *et al.* [CDF Collaboration], Phys. Rev. **D46**, 1889-1894 (1992); V. M. Abazov *et al.* [D0 Collaboration], Phys. Rev. Lett. **102**, 161802 (2009). [arXiv:0809.4472 [hep-ex]].

[17] V. M. Abazov *et al.* [D0 Collaboration], Phys. Lett. **B660**, 449-457 (2008). [arXiv:0712.3805 [hep-ex]].

[18] We would like to thank the members of the ATLAS SUSY Physics Group for providing us with this information.

[19] A. Djouadi, M. M. Muhlleitner, M. Spira, Acta Phys. Polon. **B38**, 635-644 (2007). [hep-ph/0609292].

[20] W. Beenakker, R. Hopker, M. Spira, P. M. Zerwas, Nucl. Phys. **B492**, 51-103 (1997). [hep-ph/9610490]; W. Beenakker, M. Kramer, T. Plehn, M. Spira, P. M. Zerwas, Nucl. Phys. **B515**, 3-14 (1998). [hep-ph/9710451]; W. Beenakker, M. Klasen, M. Kramer, T. Plehn, M. Spira, P. M. Zerwas, Phys. Rev. Lett. **83**, 3780-3783 (1999). [hep-ph/9906298]; M. Spira, [hep-ph/0211145]; T. Plehn, Czech. J. Phys. **55**, B213-B220 (2005). [hep-ph/0410063].

[21] P. M. Nadolsky, H. -L. Lai, Q. -H. Cao, J. Huston, J. Pumplin, D. Stump, W. -K. Tung, C. -P. Yuan, Phys. Rev. **D78**, 013004 (2008). [arXiv:0802.0007 [hep-ph]].

[22] J. Conway, *PGS-3-7-7-74*, http://www.physics.ucdavis.edu/ conway/research/software/pgs/pgs.html

[23] M. Fairbairn, A. C. Kraan, D. A. Milstead, T. Sjostrand, P. Z. Skands, T. Sloan, Phys. Rept. **438**, 1-63 (2007). [hep-ph/0611040].

[24] V. Khachatryan *et al.* [CMS Collaboration], [arXiv:1101.1645 [hep-ex]].

[25] A. R. Raklev, Mod. Phys. Lett. **A24**, 1955-1969 (2009). [arXiv:0908.0315 [hep-ph]].

[26] I. Hinchliffe, F. E. Paige, M. D. Shapiro, J. Soderqvist and W. Yao, Phys. Rev. D **55**, 5520 (1997) [arXiv:hep-ph/9610544].

[27] A. Strumia, [arXiv:1101.2195 [hep-ph]].

[28] S. Cassel, D. M. Ghilencea, S. Kraml *et al.*, [arXiv:1101.4664 [hep-ph]].

[29] CMS Note 2010/008.

[30] C. F. Berger, J. S. Gainer, J. L. Hewett *et al.*, Phys. Rev. **D80**, 095018 (2009). [arXiv:0712.2965 [hep-ph]].

[31] C. F. Berger, J. S. Gainer, J. L. Hewett *et al.*, Phys. Lett. **B677**, 48-53 (2009). [arXiv:0711.1374 [hep-ph]].

[32] T. G. Rizzo, [arXiv:1005.4626 [hep-ph]].

Chapter 5

Higgs Properties in the Fourth Generation MSSM: Boosted Signals Over the 3G Plan

5.1 Introduction and Background

Although the Standard Model (SM) provides an excellent starting point from which to understand almost all experimental data, it provides an incomplete picture of TeV scale physics as there are many questions it leaves unanswered. Four of the most troubling of these questions are (*i*) how is the hierarchy between the weak and Planck mass scales generated and stabilized, (*ii*) what is the nature of dark matter, (*iii*) what generates the observed matter, anti-matter asymmetry, and (*iv*) why are there three chiral fermion families? In order to address these issues, clearly some larger theoretical framework will be required.

Numerous theoretical scenarios have been suggested over the years to address these shortcomings of the SM, all of which have striking experimental signatures at the TeV scale[1]. Supersymmetry (SUSY), in the guise of the Minimal Supersymmetric Standard Model (MSSM)[2], provides one of the best motivated (and most popular) frameworks in which to address both the hierarchy and dark matter problems and predicts a rich, testable phenomenology. The addition of a fourth family of

chiral fermions remains attractive as a potential new source for the observed baryon asymmetry generated in the early universe[3] and as a way to address a number of potential issues in the heavy flavor sector[4]. Although the MSSM with 3 chiral families of fermions (the 3GMSSM) has been relatively well explored, the four generation MSSM has received relatively little attention except in the very recent literature[5, 6] where it has been found to have several interesting features. In particular, it has been noted[7] that the 4GMSSM with $\tan\beta$ near unity yields a strong first order phase transition.

In some ways, due to the totality of experimental constraints, the 4GMSSM parameter space is somewhat more restricted than the corresponding one of the 3GMSSM. Only relatively recently has it been realized[8] that a fourth chiral family of SM fermions remains allowed by the simultaneous requirements imposed by precision electroweak data[9], theoretical constraints on Yukawa coupling perturbativity[6, 10] and the direct search limits for the ν', l' leptons from LEP[11] as well as the b', t' quarks from both the Tevatron[12] and now the LHC[13]. Given these multiple constraints, the parameter space of allowed particle masses, particularly for the b', t', is relatively restricted, and generally requires the b', t' masses to lie in the 300-600 GeV range with mass splittings of order 50-100 GeV. A recent study of the 4GMSSM [6], shows that the experimental lower bounds on the b', t' masses constrains the value of $\tan\beta$ such that it cannot differ very much from unity due to perturbativity requirements[14]. Specifically $\tan\beta$ is required to lie in the range $1/2 \lesssim \tan\beta \lesssim 2$. One of the attractive features of the 4GMSSM is that the very large radiative corrections induced from loops involving the heavy fourth generation fermion masses allows one to push the lightest CP-even Higgs (h) mass far above the ~ 130 GeV conventional 3GMSSM upper bound, thus simultaneously relieving both fine-tuning issues as well as the direct Higgs search constraints.

In this paper we will examine the properties of the 4GMSSM Higgs fields (such as mass spectrum, couplings and decay modes) and will begin to explore the collider physics of this Higgs sector. In particular we note the very interesting possibility that while large radiative corrections necessarily drive the CP-even (h, H) and charged Higgs $(H^{\pm})$ masses to large values $\gtrsim 350 - 400$ GeV, the CP-odd field (A) can

remain relatively light with a mass in the 100-300 GeV range. Thus A may be the lightest, and possibly, the first observable part of the Higgs sector of the 4GMSSM. Interestingly, such a light state easily avoids the usual LEP, Tevatron and LHC MSSM Higgs searches[15] since: (i) A, unlike h, does not couple to WW^* or ZZ^*, so that searches for, *e.g.*, $W + b\bar{b}$, l^+l^-+MET, or $\gamma\gamma$+MET are trivially evaded, (ii) the sum of the h and A masses is forced to be rather large, $\gtrsim 400 - 500$ GeV, so that associated production is absent or highly suppressed at colliders and (iii) since $\tan\beta$ is required to be close to unity in the 4GMSSM, constraints arising from searches for the $A \to \tau^+\tau^-$ final state are relatively easy to avoid. (iv) Furthermore, for low $\tan\beta$ and large $H^\pm$ masses, constraints from both $B \to \tau\nu$[16] as well as top quark decays[17] are also easily satisfied. The state A might, however, be observable in the $A \to \gamma\gamma$ decay mode at either the Tevatron or LHC if it is sufficiently light, especially as the values for both branching fractions $B(A \to gg, \gamma\gamma)$ can be significantly enhanced by the presence of the heavy fourth generation loop contributions. In addition, we find that the h and H bosons are highly mixed states and become non-SM-like with atypical values for their branching fractions into various final states.

The paper is organized as follows. In the next Section, we review the effects of the fourth generation on the radiative corrections for the MSSM Higgs sector and examine the resulting Higgs mass spectrum. We also perform a global fit of the 4GMSSM to the precision electroweak data by analyzing the oblique electroweak parameters S, T, and U and determine the allowed range of parameter space for the special case of a light pseudoscalar Higgs. We then study the collider phenomenology of the 4GMSSM Higgs sector, namely the Higgs production cross sections and branching ratios to various final states in Section 3. We compare these to present constraints from experiment and explore future detection prospects. In particular, we find that $gg \to A \to \gamma\gamma$ is a promising channel for early discovery. Finally, we present our conclusions in Section 4.

5.2 Radiative Corrections

We begin our analysis by reviewing the effect of the radiative corrections to the Higgs sector arising from the fourth generation in the 4GMSSM. As noted by Ref.[6], since the fourth generation masses are so large, it suffices for our purposes to employ the one-loop, leading log effective potential approximation in performing these calculations[18]. In these computations, we must use as input the values of the b', t', ν' and l' masses as well as the values of both M_A and $\tan\beta$. In our analysis we take $\tan\beta$ to lie in the approximate range $1/2 \lesssim \tan\beta \lesssim 2$, as dictated by consistency with perturbative Yukawa couplings for fourth generation masses in the $\sim 300 - 500$ GeV range. In the limit where we neglect sfermion mixing and set all SUSY sfermion masses to a common value of ~ 1 TeV, only two further parameters must be specified: the common sfermion mass, m_S, and a common colorless gaugino mass, m_χ. Under these assumptions, we find that our conclusions are not much impacted by variations in these two parameters as our results are only logarithmically dependent on m_S, and the gaugino can potentially make only a rather small contribution to the rates for loop decays to the $\gamma\gamma$ final state for large masses. We note that the values of these input parameters must be chosen so as to satisfy all of the existing bounds from direct searches, precision electroweak data and the requirements of perturbative Yukawa couplings. The results presented below can, of course, be easily generalized to allow for both sfermion mixing as well as non-degenerate sparticle masses, but this will only modify the results we obtain in detail and not in any qualitative way.

To calculate the radiative corrections to the Higgs mass spectrum due to the addition of fourth generation fermions and their superpartners, we closely follow the work of Barger *et al.* in Ref. [19]. We stress that in performing these calculations both M_A and $\tan\beta$ are to be treated as input parameters along with the masses of the fourth generation fermions and all the superpartners. In the general case, the masses associated with the CP-even Higgs fields are obtained by diagonalizing the matrix

$$
\begin{aligned}
M &= \frac{1}{2}\begin{pmatrix} \cot\beta & -1 \\ -1 & \tan\beta \end{pmatrix} M_Z^2 \, \sin 2\beta \\
&\quad + \frac{1}{2}\begin{pmatrix} \tan\beta & -1 \\ -1 & \cot\beta \end{pmatrix} M_A^2 \, \sin 2\beta + \frac{g^2}{16\pi^2 M_W^2}\begin{pmatrix} \Delta_{11} & \Delta_{12} \\ \Delta_{12} & \Delta_{22} \end{pmatrix} , \qquad (5.2.1)
\end{aligned}
$$

where the Δ_{ij} are given by

$$
\begin{aligned}
\Delta_{11} &= \sum_{(u,d)=(t',b'),(\nu',e')} \frac{N_c m_u^4}{\sin^2\beta} \, g_u C_u^2 \mu^2 \\
&\quad + \frac{N_c m_d^4}{\cos^2\beta}\left[\ln\left(\frac{\tilde{m}_{d1}^2 \tilde{m}_{d2}^2}{m_d^4}\right) + A_d C_d \left(2 \, \ln\left(\frac{\tilde{m}_{d1}^2}{\tilde{m}_{d2}^2}\right) + A_d C_d g_d\right)\right] , \\
\Delta_{22} &= \Delta_{11}\left(\text{with } \mathrm{u} \leftrightarrow \mathrm{d}, \ \mathrm{fi} \rightarrow \frac{ß}{2} - \mathrm{fi}\right) , \qquad (5.2.2) \\
\Delta_{12} &= \sum_{(u,d)=(t',b'),(\nu',e')} \frac{N_c m_u^4}{\sin^2\beta} \, \mu C_u \left[\ln\left(\frac{\tilde{m}_{u1}^2}{\tilde{m}_{u2}^2}\right) + A_u C_u g_u\right] \\
&\quad + \left(u \leftrightarrow d, \ \mathrm{fi} \rightarrow \frac{ß}{2} - \mathrm{fi}\right) .
\end{aligned}
$$

$\tilde{m}_i$ are the physical sfermion masses, and the mixing parameters, C_u and C_d, as well as the loop parameter g_f, are defined as

$$
\begin{aligned}
C_u &\equiv \frac{(A_u + \mu \, \mathrm{cotfi})}{(\tilde{m}_{u1}^2 - \tilde{m}_{u2}^2)} , \\
C_d &\equiv \frac{(A_d + \mu \, \mathrm{tanfi})}{(\tilde{m}_{d1}^2 - \tilde{m}_{d2}^2)} , \qquad (5.2.3) \\
g_f &\equiv 2 - \frac{(\tilde{m}_{f1}^2 + \tilde{m}_{f2}^2)}{(\tilde{m}_{f1}^2 - \tilde{m}_{f2}^2)} \ln\left(\frac{\tilde{m}_{f1}^2}{\tilde{m}_{f2}^2}\right) .
\end{aligned}
$$

In writing these expressions, we have assumed that there is no mixing between

the fourth generation fermions or sfermions with their counterparts in the other three generations. In particular, we specialize further to the case where the fourth generation squark/slepton mass eigenstates are the same as their interaction eigenstates, corresponding to $\mu = 0$ and $A_{t',b',\nu',e'} = 0$, wherein the mass matrix simplifies considerably. In our numerical results, we assume that all of the sfermions are degenerate with a mass of $m_S = 1$ TeV. From these general expressions, we can obtain not only the contributions from the fourth generation, but also those from the usual top and bottom quarks.

For the corresponding charged Higgs sector, we must diagonalize the analogous matrix

$$\begin{aligned} M &= \frac{1}{2}\begin{pmatrix} \tan\beta & 1 \\ 1 & \cot\beta \end{pmatrix} M_W^2 \ \sin 2\beta \\ &+ \frac{1}{2}\begin{pmatrix} \tan\beta & 1 \\ 1 & \cot\beta \end{pmatrix} M_A^2 \ \sin 2\beta + \frac{1}{2}\begin{pmatrix} \tan\beta & 1 \\ 1 & \cot\beta \end{pmatrix} \widetilde{\Delta} \ \sin 2\beta \,, \end{aligned} \tag{5.2.4}$$

where

$$\begin{aligned} \widetilde{\Delta} &\equiv \frac{g^2}{64\pi^2 \ \sin^2\beta \ \cos^2\beta \ M_W^2} \\ &\times \sum_{(u,d)=(t',b'),(\nu',e')} N_c \left(\frac{(m_d^2 - M_W^2 \ \cos^2\beta)(m_u^2 - M_W^2 \ \sin^2\beta)}{\tilde{m}_{u1}^2 - \tilde{m}_{d1}^2} \left[f(\tilde{m}_{u1}^2) - f(\tilde{m}_{d1}^2) \right] \right. \\ &\left. + \frac{m_u^2 m_d^2}{\tilde{m}_{u2}^2 - \tilde{m}_{d2}^2} \left[f(\tilde{m}_{u2}^2) - f(\tilde{m}_{d2}^2) \right] - \frac{2 m_u^2 m_d^2}{m_u^2 - m_d^2} \left[f(m_u^2) - f(m_d^2) \right] \right), \end{aligned} \tag{5.2.5}$$

with the function f being given by $f(m^2) = 2m^2 \ [\ln(m^2/M_W^2) - 1]$. Removing the Goldstone field $G^{\pm}$ leaves us with the desired mass (squared) of the charged Higgs field. As in the case of the neutral CP-even Higgs fields above, it is trivial to include the contributions from the ordinary third generation.

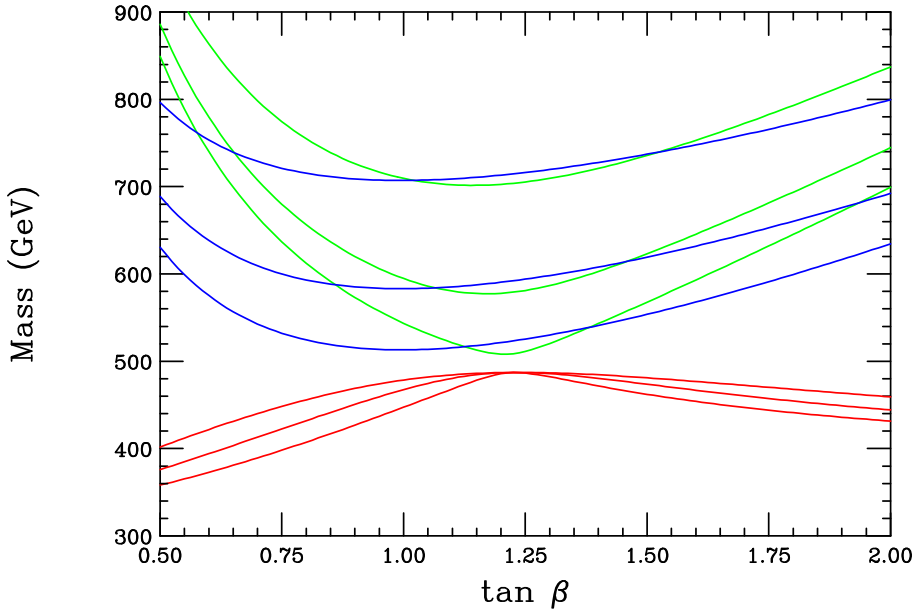

Figure 5.1: Masses of the h(red), H(green) and $H^{\pm}$(blue) Higgs fields as functions of $\tan\beta$. The lower(middle, top) curve in each case corresponds to $M_A = 115(300, 500)$ GeV, respectively. Here $m_{t'} = 400$ GeV, $m_{b'} = 350$ GeV, and $m_{l',\nu'} = 300$ GeV with $m_S = 1$ TeV have been assumed for purposes of demonstration.

The primary results of this analysis are the masses of the h, H and $H^{\pm}$ fields as functions of the input parameters. Figure 5.1 shows a representative sample mass spectrum for these particles as a function of $\tan\beta$ for three different values of M_A (115, 300, and 500 GeV) and taking $m_{t'} = 400$ GeV, $m_{b'} = 350$ GeV and $m_{\ell',\nu'} = 300$ GeV. As can be seen in the formulae given above, the CP-even Higgs masses are expected to grow approximately quadratically with the fourth generation mass scale (with the other parameters being held fixed). This expectation was verified explicitly in [6] where the sensitivity to variations in the fourth generation fermion masses was examined and we obtain similar results here. In this Figure, we observe that (*i*) the mass of h is not particularly sensitive to the value of either M_A or $\tan\beta$ and is primarily driven only by the masses of the fourth generation particles. (*ii*) The values of M_H are found to be sensitive to both of the input parameters. (*iii*) On the other hand, $M_H^{\pm}$, while not particularly sensitive to the value of $\tan\beta$, does vary with M_A. For these choices of fourth generation masses we see that the CP-even states h and H are quite heavy and thus it is easy for A to be the lightest member of the Higgs spectrum and so it, perhaps, might be most easily observed at the Tevatron or LHC. Note that in all cases the $H^{\pm}$ boson is too heavy to play much of a role in flavor physics, particularly since $\tan\beta$ is always near unity.

As the 4GMSSM includes many new electroweak states beyond those of the SM, one must carefully consider the effect that these states will have on the precise measurements of the electroweak interactions that are seen to be consistent with the SM (with a light SM Higgs, $m_h \sim 100\,\mathrm{GeV}$). 4GMSSM scenarios with a light A boson (*i.e.*, $M_A < 300$ GeV) and/or $\tan\beta < 1$ have not been previously considered so it behooves us to re-examine these cases. Here we focus on oblique corrections to the S, T and U parameters[20] from the 4GMSSM with $M_A = 115\,\mathrm{GeV}$ and $0.6 < \tan\beta < 1.8$; a broader and more detailed investigation of such corrections in the context of the 4GMSSM has been presented in [6].

We compute the fourth generation fermion and Higgs sector contributions to the $S\,, T$ and U parameters following the formulae in [21]. We neglect sfermion contributions as we assume all sfermions are heavy and degenerate, having $M_{\mathrm{SUSY}} \sim 1\,\mathrm{TeV}$, and hence their contributions are negligible. Fermion and Higgs contributions to the

U parameter, while non-zero, are also negligibly small in the parameter space considered here. The contributions due to the fermions alone were found to be numerically consistent with the results [8].

Constraints on new corrections to the $S\,, T$ and U parameters are experimentally determined to be [22]

$$\begin{aligned} \Delta S = S - S_{SM} &= -0.08 \pm 0.10 \\ \Delta T = T - T_{SM} &= 0.09 \pm 0.11 \\ \Delta U = U - U_{SM} &= 0.01 \pm 0.10, \end{aligned} \tag{5.2.6}$$

where the values above correspond to subtracting SM contributions which are calculated at the reference scale* $m_{h,ref} = 300\,\mathrm{GeV}$. The corrections ΔS, ΔT and ΔU come purely from new physics, *i.e.*, the SM contributions (with $m_h = 300\,\mathrm{GeV}$) to ΔS, ΔT and ΔU are zero, in reasonable agreement with the above experimental ranges. We determine a χ^2 value for points in 4GMSSM space, following [6],

$$\chi^2 = \sum_{ij} (\Delta X_i - \Delta \widehat{X}_i)(\sigma_{ij})^{-1}(\Delta X_j - \Delta \widehat{X}_j), \tag{5.2.7}$$

where the $\Delta \widehat{X}_i$ are the central values ΔS, ΔT and ΔU of Eqn. (5.2.6), the ΔX_i are the fourth generation fermion and Higgs contributions to ΔS, ΔT and ΔU from the particular 4GMSSM model and $\sigma_{ij} = \sigma_i \rho_{ij} \sigma_j$ is the covariance matrix built from the errors σ_i in Eqn. (5.2.6) and from

$$\rho = \begin{pmatrix} 1.0 & 0.879 & -0.469 \\ 0.879 & 1.0 & -0.716 \\ -0.469 & -0.716 & 1.0 \end{pmatrix}. \tag{5.2.8}$$

Viewed as a goodness of fit test on 3 degrees of freedom (ΔS, ΔT and ΔU), the

*We note that while m_h can vary between approximately 360-500 GeV as the 4GMSSM parameter space is varied, we observe that the use of data values centered around the reference point $m_{h,ref}$=300 GeV does not lead to any significant shift in the allowed regions displayed in the figure below.

ellipsoid defined by $\chi^2 = 7.815$ in the space of oblique parameters defines the 95% C. L. region. 4GMSSM models lying outside of this ellipsoid would be excluded by electroweak precision measurements at the 95% C. L. and those lying inside cannot be excluded at the 95% C. L..

In Figure 5.2 we display points in the $(m_{t'} - m_{b'})$ vs. $(m_{\nu'} - m_{e'})$ plane that are allowed by precision electroweak measurements and consistent with unitarity (for $m_{t'} = 400\,\mathrm{GeV}$ and $m_{e'} = 300\,\mathrm{GeV}$, this means $m_{b'} < 525\,\mathrm{GeV}$ and $m_{\nu'} < 750\,\mathrm{GeV}$ [6]). The model dependence of the fits in the $(m_{t'} - m_{b'})$ vs. $(m_{\nu'} - m_{e'})$ plane is most pronounced as the contributions to ΔT are sensitively dependent on isospin violating mass splittings in the fourth-generation fermion sector ($i.e.$, $\Delta T \sim (\delta m)^4/m_W^2 m^2$ for new fermions with masses m and $m + \delta m$ where $\delta m \ll m$ and $m \gg m_W$,$\mathrm{m_Z}$) and rather less so on the mass spectrum of the higgs sector (via tanβ). We observe that for tan$\beta \sim 1$, there is a relatively tuned set of fourth generation doublet splittings that are consistent with precision constraints, while, for somewhat larger and smaller values of tanβ, small splittings (or even degenerate doublets) are required for the 4GMSSM to be consistent with the precision electroweak data.

Note that since the t' and ℓ' masses as well as M_A are being held constant in these figures, the variation with $\tan\beta$ arises from only two unique sources: the changes in the Higgs couplings to the fermions and gauge bosons described above and the corresponding changes in the various Higgs boson mass splittings entering the loop functions. Since the mass splitting between the Higgs fields is greatest at the two ends of the allowed $\tan\beta$ range, we see that in such cases the allowed region in the fourth generation mass splitting plane then reduces to a solid ellipse. Furthermore, when these mass splittings are minimized for $\tan\beta \simeq 1 - 1.2$ we see that the allowed arc-shaped region in this plane has its maximal radial extent.

5.3 Collider Phenomenology

We next examine the collider phenomenology of the 4GMSSM Higgs sector, paying particular attention to the region of parameter space that results in different signatures from the three generation case. Throughout this section we shall assume

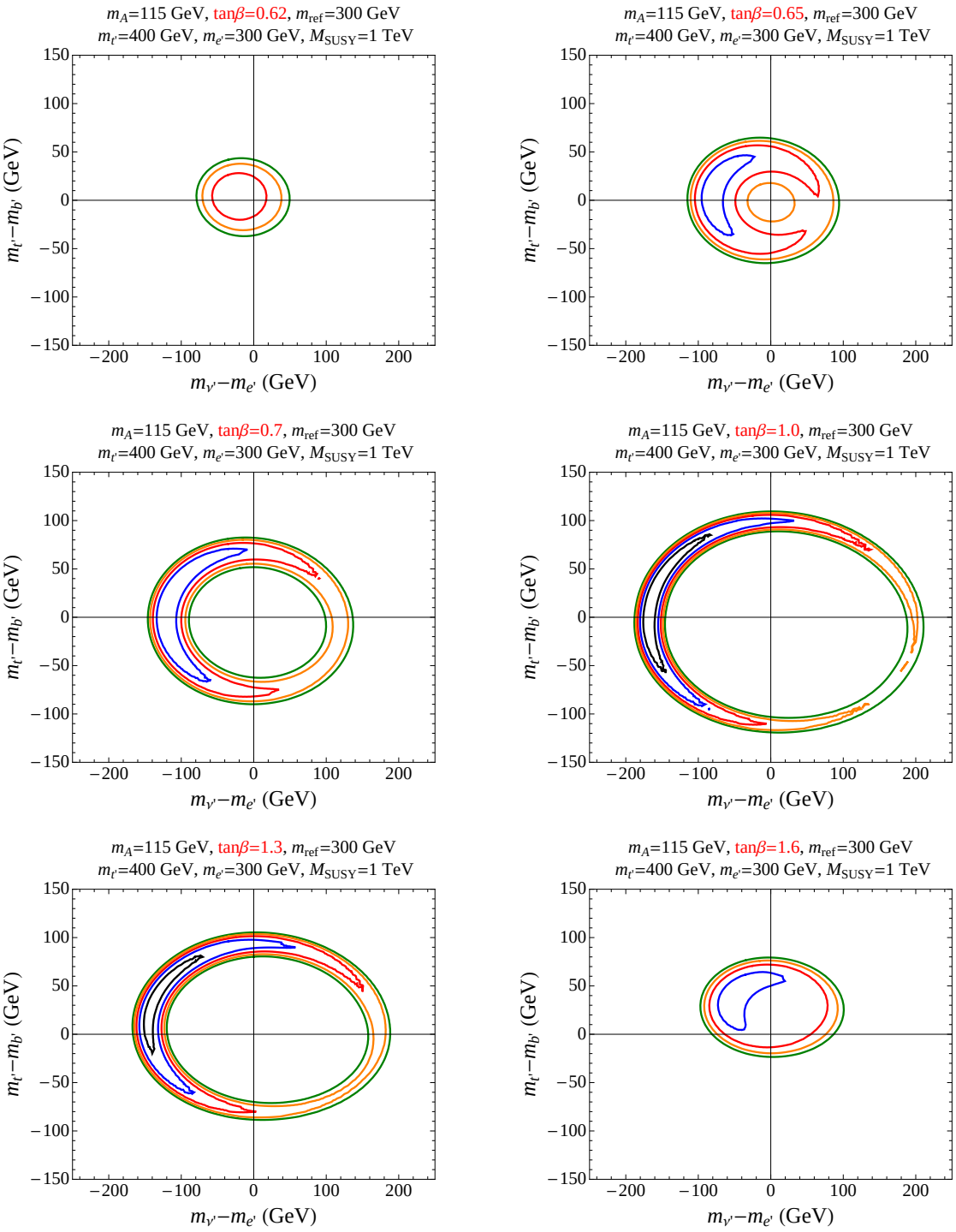

Figure 5.2: We display iso-χ^2 contours describing the goodness of fit (using Eqn. 5.2.7) to measured precision electroweak data (Eqn. 5.2.8) for 4GMSSM models in the $(m_{t'}-m_{b'})$ vs. $(m_{\nu'}-m_{e'})$ plane. In all cases we take $m_A = 115\,\text{GeV}$, $M_{\rm SUSY} \sim 1\,\text{TeV}$, $m_{t'} = 400\,\text{GeV}$ and $m_{e'} = 300\,\text{GeV}$. Points in the different panels correspond to models with distinct values of $\tan\beta$, as denoted in the figure. Models inside of the red contour have $\chi^2 < 8.0$ and are consistent with ΔS, ΔT and ΔU at the $\sim 95\%$ C. L. (for a goodness of fit test with 3 degrees of freedom). Adjacent contours represent a difference of 2.0 units of χ^2, with black, blue, red, orange and green contours

$m_{t'} = 400$ GeV, $m_{b'} = 350$ GeV, $m_{\ell',\nu'} = 300$ GeV and $m_S = 1$ TeV in presenting our results. We find that varying the fourth generation fermion masses within their allowed ranges does not qualitatively modify our conclusions.

Our first step is to determine the various coupling coefficients for the h, H bosons to the u, d-type fermions and SM gauge bosons as functions of $\tan\beta$ and M_A for our fixed values of the other input parameters. The corresponding couplings of the pseudoscalar A boson to the fermions are simply given by $\tan\beta$ and its inverse, and VVA-type couplings are absent. The form of these couplings follow directly from the equations describing the radiative corrections to the Higgs sector in the previous section with the diagonalization of the CP-even Higgs mass matrix then determining the mixing angle α. Figure. 5.3 shows these various couplings as functions of $\tan\beta$ for three different values of M_A. These couplings display a strong $\tan\beta$ dependence in the range of interest, while showing only a somewhat mild dependence on M_A except for an overall broadening of the peak observed in the center of the figures near $\tan\beta \sim 1.2$ as the value of M_A is increased. Interestingly, we find that for a substantial fraction of the range of $\tan\beta$, the CP-even Higgs fields have significant mixing so that neither h nor H are SM-like. This is in contrast to the usual scenario in the 3GMSSM. Note that generally $h(H)$ has stronger(weaker) couplings to $u\bar{u}$-type quarks than does the SM Higgs while the reverse is found to be true for the corresponding $d\bar{d}$-type couplings. Also note that it is possible for both h and H to simultaneously have substantially large couplings to the SM W, Z bosons.

Once the couplings of the various Higgs states are determined, we can calculate their respective branching fractions. Here, we first pay special attention to the CP-odd field A since it may be the lightest of the Higgs states. Figure 5.4 shows these branching fractions as a function of M_A for three different values of $\tan\beta$ taking the fourth generation masses as above. Note that the channel $A \to gg$ is greatly enhanced for $M_A < 2m_t$, and is the dominant decay mode for $\tan\beta < 1$. The $\gamma\gamma$ partial width is also found to be enhanced by up to a factor of two over that of the SM Higgs, but this increase is found to wash out in the branching fraction. Together, this can lead to large signal rates for $gg \to A \to \gamma\gamma$ as will be discussed below. Note that the size of the b, c, τ branching fractions are particularly sensitive to the value of $\tan\beta$. For

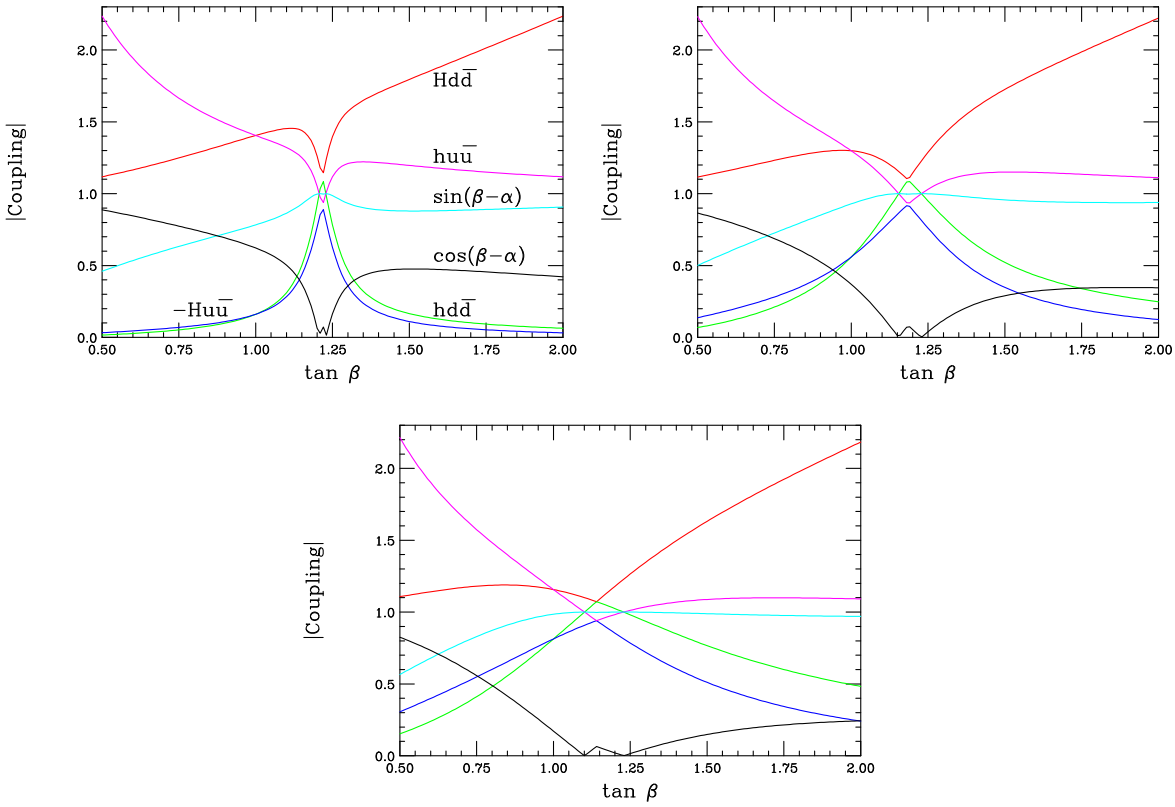

Figure 5.3: CP-even Higgs boson coupling factors, normalized to the corresponding SM Higgs couplings, as a function of $\tan\beta$ for $M_A = 115(300, 500)$ in the top left(top right, bottom) panel. Here $m_{t'} = 400$ GeV, $m_{b'} = 350$ GeV, and $m_{l',\nu'} = 300$ GeV with $m_S = 1$ TeV have been assumed for purposes of demonstration. All curves are as labeled in the upper left-hand panel.

larger values of M_A, the $\tau^+\tau^-$ and $\gamma\gamma$ channels are roughly comparable.

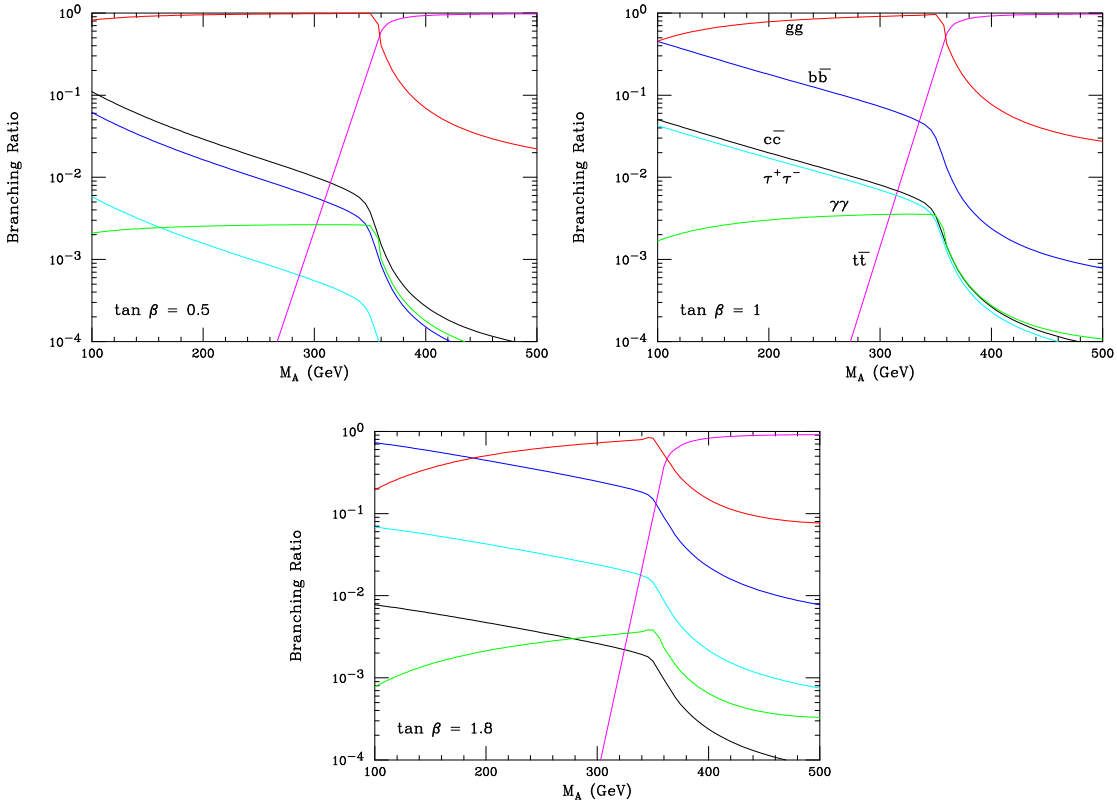

Figure 5.4: Branching fractions of the CP-odd state A as a function of M_A for the same input masses as in the previous figure. The top left(right) panel assumes $\tan\beta = 0.5(1)$ while the bottom panel assumes $\tan\beta = 1.8$. All curves are as labeled in the upper right-hand panel.

Turning to the CP-even Higgs bosons, Fig. 5.5 shows the relevant branching fractions. Here, we have assumed for simplicity that decays to pairs of fourth generation fermions are not kinematically allowed.† As expected, h and H decays to VV (with V being either the SM W or Z boson) can dominate over most of the parameter space. In the case of h, the $t\bar{t}$ mode is of comparable importance. For $\tan\beta \sim 1.2$, as can be seen from Fig. 5.3, h becomes more SM-like and, hence, H nearly decouples from VV

†Decays to fourth generation fermions are not kinematically allowed for the lightest Higgs boson h. However, for fixed M_A, as $\tan\beta$ is varied, decay channels to the fourth generation may open up for the heavier H boson if the 4G fermion masses are light enough. Here we will ignore such decays for simplicity.

in this region. This is reflected in the dip in the $H \to VV$ branching fractions near this particular $\tan\beta$ value. Similarly, since the $Hu\bar{u}$ coupling is usually suppressed relative to the corresponding SM value (except again near $\tan\beta \sim 1.2$), the $H \to t\bar{t}$ decay is generally found to be sub-dominant. h, H branching fractions to both $b\bar{b}$ and $\tau^+\tau^-$ are seen to be rather small throughout this $\tan\beta$ interval while the gg branching fraction remains relatively large, being in the 10^{-3} to few $\times 10^{-2}$ range. A very important mode in almost all cases (except where it is suppressed by phase space) is $h, H \to AZ$. The reason for this large branching fraction is the relative enhancement in the effective $(h, H)AZ$ coupling by a factor of $\sim (M_{h,H} - M_A)/M_Z$ as can be seen from taking the Z Goldstone boson limit. In particular, when A is light we see that the mass splitting in the numerator can be quite large ($\sim 500 - 800$ GeV) relative to M_Z.

For our choice of parameters, the decays of the charged Higgs bosons are more straightforwardly understood than those of the corresponding neutral Higgs. Clearly, if $M_{H^\pm}$ is in excess of any appropriate pair of fourth generation masses, then these decay modes will dominate, while below this threshold decays to $t\bar{b}$ will be found to dominate. The corresponding partial decay rates to other fermionic final states will be highly suppressed. A possibly competing decay mode is $H^\pm \to (h, H, A)W^\pm$ provided phase space is available since it too is somewhat enhanced by the same mechanism discussed above in the case of $(h, H) \to AZ$ decay although the mass splittings among the h, H and $H^\pm$ are not always large.

Since A is possibly the lightest member of the Higgs spectrum, we first discuss its production signatures at the Tevatron and LHC. Since the $A \to gg$ partial width is generally large, $\tan\beta$ is close to unity and the VVA coupling is absent, the $gg \to A$ process is the most important one for A production at hadron colliders. These ggA couplings are sufficiently loop-enhanced that one may worry about $gg \to A \to gg$ being seen above the dijet background at hadron colliders. Existing searches at the LHC[23],[24] are only constraining for values of M_A beyond our region of interest while those from the Tevatron[25],[26] and at lower energies[27] are found to be rather weak.

For $\tan\beta \gtrsim 1$, we see from Fig. 5.4 that the $A \to \tau\tau$ process is a relatively important mode but is still subdominant in comparison to both gg and $b\bar{b}$. However,

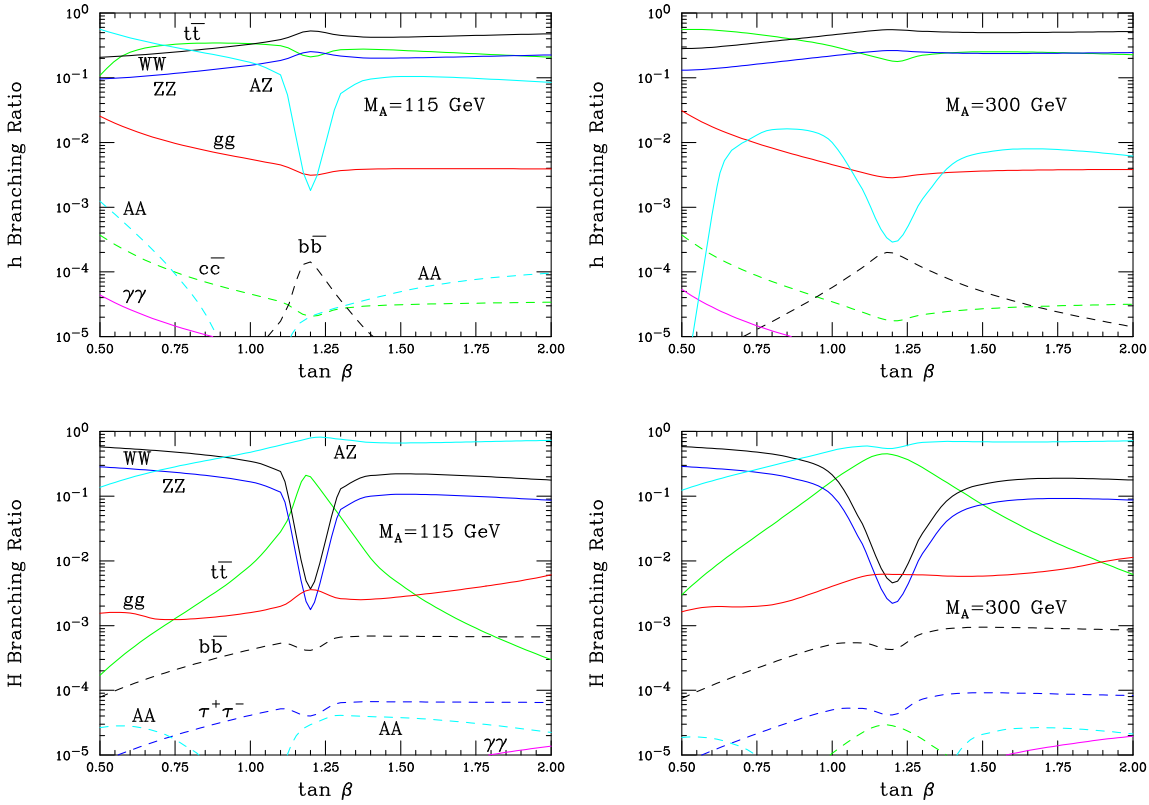

Figure 5.5: Branching fractions for the h(top) and H(bottom) as functions of $\tan\beta$ for $M_A = 115(300)$ GeV in the left(right) panels. The other input masses are taken to be those as employed above. The curves in the right panels correspond to the same decays as the ones in the left panels.

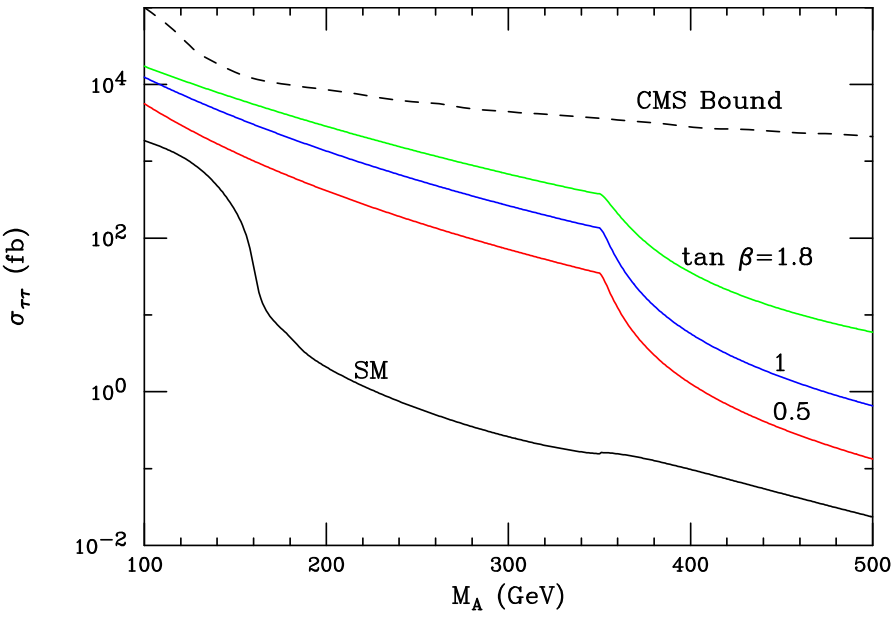

Figure 5.6: Cross section times branching fraction for $gg \to A \to \tau\tau$ as a function of M_A for $\tan\beta$ =0.5(red), 1(blue) and 1.8(green) at the 7 TeV LHC and a comparison to the bound obtained by CMS.

the latter two channels are swamped by QCD backgrounds. The production cross section for the subprocess $gg \to A \to \tau^+\tau^-$ is shown in Fig. 5.6 for $\sqrt{s} = 7$ TeV using the CTEQ6.6M parton distribution functions [28][‡]. For light A and $\tan\beta \gtrsim 1$ the resulting cross section is found to be not too far below the (somewhat model-dependent[29]) upper bound recently placed by CMS[30] as can be seen in Fig. 5.6. However, we note that for smaller values of $\tan\beta$ the $gg \to A \to \tau^+\tau^-$ cross section is found to be rather small.

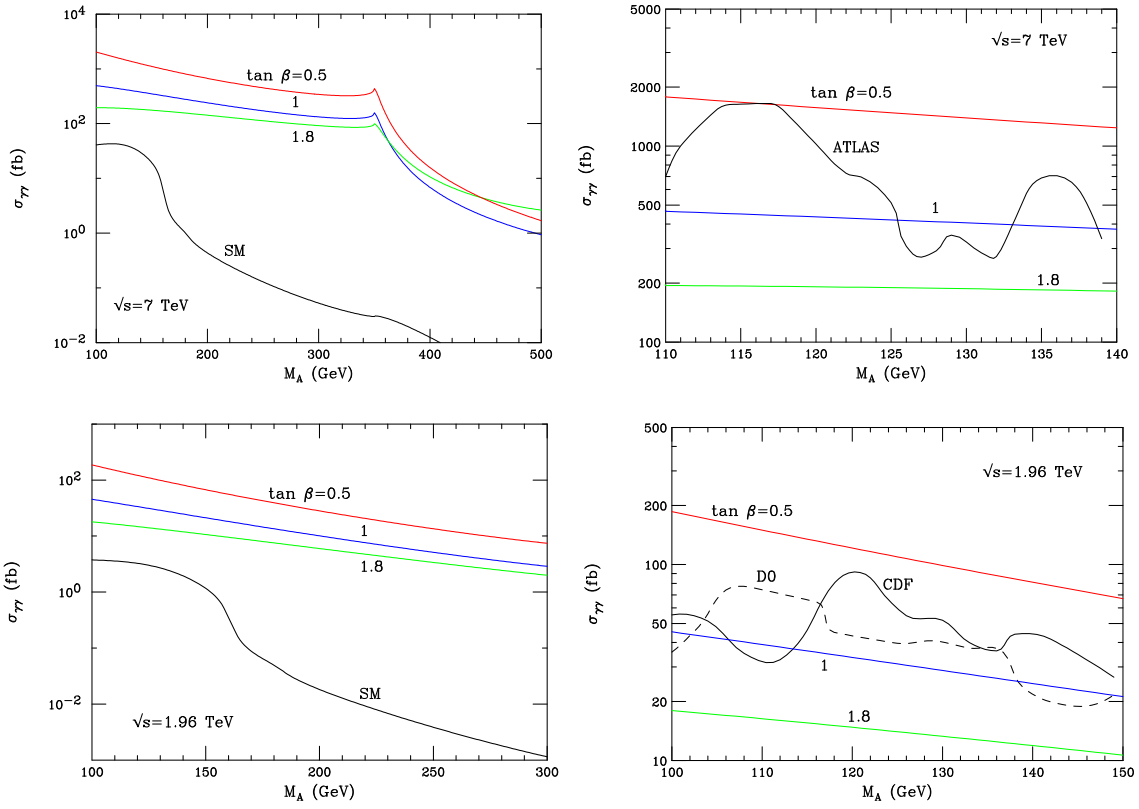

Figure 5.7: Cross section times branching fraction for $gg \to A \to \gamma\gamma$ as a function of M_A for $\tan\beta$ =0.5(red), 1(blue) and 1.8(green) at the 7 TeV LHC(upper left) and Tevatron(lower left). The upper right(lower right) panels explicitly show the limits obtained by CMS at the LHC and by CDF and D0 at the Tevatron. The lower solid curve in both left hand panels is the corresponding result for the SM Higgs.

Perhaps the cleanest mode for the observation of a light A boson is in the $\gamma\gamma$

[‡]See the discussion below on how these cross sections are calculated.

final state; the 7 TeV LHC cross section is shown in Fig. 5.7 in comparison to the bound obtained by ATLAS[31]. We also show in the lower panels the corresponding expectations for the Tevatron along with the constraints obtained by both CDF[32] and D0[33]. For this cross section, at either the Tevatron or the LHC, we see a significant enhancement for $\tan\beta \lesssim 1$. Note that the results shown in this and the previous Figure have assumed a constant NNLO K-factor of $\simeq 2$, with the LO cross section renormalized to that for NNLO A, h production for light A, h masses employing the results in Ref.[34]. In this approximation our results will give very reasonable overall estimates of the $gg \to A, h, H$ cross sections. In this Figure we see that that ratio of cross sections for $gg \to A \to \gamma\gamma$ in comparison to that for the corresponding conventional SM Higgs process can be as large as an order of magnitude at lower Higgs masses at hadron colliders. For example at the LHC, taking M_A=100-150 GeV and $\tan\beta \sim 0.7 - 1$ results in a factor $\sim 10 - 30$ times larger cross section via the A in this mode than for a SM Higgs boson of the same mass. Thus for light A bosons in the range $\sim 100 - 150$ GeV the $\gamma\gamma$ decay mode may provide the earliest observable collider signature. Note, however, that an update of the null ATLAS $h \to \gamma\gamma$ search presented in Ref. [35] would seem to favor values of $\tan\beta \gtrsim 0.7$ as would the Tevatron results.

	$\tan\beta$		
M_A (GeV)	0.5	1.0	1.8
115	33.1 (358)	6.5 (447)	4.2 (441)
300	28.9 (375)	6.3 (467)	4.4 (454)

Table 5.1: Gluon fusion production cross section at the 7 TeV LHC for the lightest Higgs scalar, $gg \to h+X$, in pb for various values of M_A and $\tan\beta$. Fourth generation masses are taken to be $m_{l',\nu'} = 300$ GeV, $m_{b'} = 350$ GeV, and $m_{t'} = 400$ GeV. The numbers in parenthesis indicate the corresponding values of the lightest scalar Higgs mass in GeV, m_h, for these input values of M_A and $\tan\beta$.

Tables 5.1 and 5.2 show the expected gg fusion total cross sections for h, H production obtained by appropriately rescaling the NNLO results found in Ref.[34] for some sample values of M_A and $\tan\beta$. While H production in this channel is

relatively weak due to the larger masses and the reduced effective ggH couplings, h on the other hand is seen to have a substantial cross section with a correspondingly respectable branching fraction into both W^+W^- and ZZ. For some ranges of these parameters these final states have cross sections that are not very far below the present bounds obtained from the 2010 run of the LHC[36, 37].

	$\tan\beta$		
M_A (GeV)	0.5	1.0	1.8
115	0.14 (849)	0.58 (543)	0.78 (645)
300	0.09 (885)	0.63 (594)	0.69 (693)

Table 5.2: Gluon fusion production cross section at the 7 TeV LHC for the heaviest Higgs scalar, $gg \to H+X$, in pb for various values of M_A and $\tan\beta$. Fourth generation masses are taken to be $m_{l',\nu'} = 300$ GeV, $m_{b'} = 350$ GeV, and $m_{t'} = 400$ GeV. The numbers in parenthesis indicate the corresponding values of the heaviest scalar Higgs mass in GeV, m_H, for these input values of M_A and $\tan\beta$.

5.4 Summary and Conclusions

In this paper we have examined the properties of the Higgs fields in the 4GMSSM with an eye toward their production signatures at the Tevatron and the LHC. The couplings and corresponding branching fractions for these various fields were examined in detail. In particular we have noted the strong possibility that the CP-odd field A may be the lightest member of the Higgs spectrum as well as the possibility that the region $\tan\beta \lesssim 1$ is now physically allowed. We further verified that such a light A scenario is consistent with the usual constraints imposed by the electroweak data on the oblique parameters for the entire range of perturbatively allowed values of $\tan\beta$. As such, the CP-odd state, A, may be the first part of the 4GMSSM Higgs spectrum to be discovered at hadron colliders. We find that while $gg \to A$ may soon lead to a potential signal in the $\tau^+\tau^-$ channel at the LHC, A is more likely to be first observed in the $\gamma\gamma$ mode due to its highly fourth generation loop-enhanced cross section which

can be more than an order of magnitude larger than that of the SM Higgs for a mass of $\sim 100 - 150$ GeV provided that $\tan\beta \lesssim 1$. If such a scenario is correct new signals might soon be observable at the LHC.

Bibliography

[1] D. E. Morrissey, T. Plehn, T. M. P. Tait, [arXiv:0912.3259 [hep-ph]].

[2] M. Drees, R. Godbole, P. Roy, Hackensack, USA: World Scientific (2004) 555 p; H. Baer, X. Tata, Cambridge, UK: Univ. Pr. (2006) 537 p.

[3] W. -S. Hou, Chin. J. Phys. **47**, 134 (2009). [arXiv:0803.1234 [hep-ph]]; Y. Kikukawa, M. Kohda, J. Yasuda, Prog. Theor. Phys. **122**, 401-426 (2009). [arXiv:0901.1962 [hep-ph]].

[4] E. Lunghi, A. Soni, [arXiv:1104.2117 [hep-ph]]; E. Lunghi, A. Soni, Phys. Lett. **B697**, 323-328 (2011). [arXiv:1010.6069 [hep-ph]]; W. -S. Hou, C. -Y. Ma, Phys. Rev. **D82**, 036002 (2010). [arXiv:1004.2186 [hep-ph]]; W. -S. Hou, Y. -Y. Mao, C. -H. Shen, Phys. Rev. **D82**, 036005 (2010). [arXiv:1003.4361 [hep-ph]]; M. Bobrowski, A. Lenz, J. Riedl, J. Rohrwild, Phys. Rev. **D79**, 113006 (2009). [arXiv:0902.4883 [hep-ph]]; S. K. Garg, S. K. Vempati, [arXiv:1103.1011 [hep-ph]]; see also A. Soni, A. K. Alok, A. Giri, R. Mohanta and S. Nandi, Phys. Lett. B **683**, 302 (2010) [arXiv:0807.1971 [hep-ph]] and decays," Phys. Rev. D **82**, 033009 (2010) [arXiv:1002.0595 [hep-ph]].

[5] S. Litsey, M. Sher, Phys. Rev. **D80**, 057701 (2009). [arXiv:0908.0502 [hep-ph]].

[6] S. Dawson, P. Jaiswal, Phys. Rev. **D82**, 073017 (2010). [arXiv:1009.1099 [hep-ph]]. For an earlier discussion of the perturbativity constraints and the possibility of Landau poles in the 4GMSSM, see R. M. Godbole, S. K. Vempati, A. Wingerter, JHEP **1003**, 023 (2010). [arXiv:0911.1882 [hep-ph]].

[7] R. Fok, G. D. Kribs, Phys. Rev. **D78**, 075023 (2008). [arXiv:0803.4207 [hep-ph]].

[8] G. D. Kribs, T. Plehn, M. Spannowsky, T. M. P. Tait, Phys. Rev. **D76**, 075016 (2007). [arXiv:0706.3718 [hep-ph]]; M. S. Chanowitz, Phys. Rev. **D**, 035018 (2010). [arXiv:1007.0043 [hep-ph]]. See also O. Eberhardt, A. Lenz, J. Rohrwild, Phys. Rev. **D82**, 095006 (2010). [arXiv:1005.3505 [hep-ph]]. Fo earlier work in this area, see H. -J. He, N. Polonsky, S. -f. Su, Phys. Rev. **D64**, 053004 (2001). [hep-ph/0102144].

[9] LEP Electroweak Working Group, http://lepewwg.web.cern.ch/LEPEWWG/

[10] E. De Pree, G. Marshall, M. Sher, Phys. Rev. **D80**, 037301 (2009). [arXiv:0906.4500 [hep-ph]].

[11] P. Achard *et al.* [L3 Collaboration], Phys. Lett. B **517**, 75 (2001) [arXiv:hep-ex/0107015].

[12] A. Lister [CDF Collaboration], PoS **ICHEP2010**, 402 (2010). [arXiv:1101.5992 [hep-ex]]. T. Aaltonen *et al.* [The CDF Collaboration], $p\bar{p}$ collisions at $\sqrt{s} = 1.96$ TeV," Phys. Rev. Lett. **106**, 141803 (2011). [arXiv:1101.5728 [hep-ex]].

[13] S. Chatrchyan *et al.* [CMS Collaboration], [arXiv:1102.4746 [hep-ex]]; ATLAS Collaboration, ATLAS-CONF-2011-022, March 2011.

[14] M. S. Chanowitz, M. A. Furman, I. Hinchliffe, Nucl. Phys. **B153** (1979) 402 and Phys. Lett. **B78** (1978) 285.

[15] See talks given by B Jayatilaka (CDF/D0), T. Scanlon (CDF/D0), M. Schumacher (ATLAS), and C. Veelken (CMS), at *Recontres de Moriond EW 2011*, March 2011, LaThuile, Italy.

[16] Heavy Flavor Averaging Group, http://www.slac.stanford.edu/xorg/hfag/; CKM Fitter, http://ckmfitter.in2p3.fr/.

[17] T. Aaltonen *et al.* [CDF Collaboration], Phys. Rev. Lett. **103**, 101803 (2009). [arXiv:0907.1269 [hep-ex]]; V. M. Abazov *et al.* [D0 Collaboration], Phys. Lett. **B682**, 278-286 (2009). [arXiv:0908.1811 [hep-ex]].

[18] M. Sher, Phys. Rept. **179**, 273-418 (1989).

[19] V. D. Barger, M. S. Berger, A. L. Stange, R. J. N. Phillips, Phys. Rev. **D45**, 4128-4147 (1992).

[20] M. E. Peskin, T. Takeuchi, Phys. Rev. **D46**, 381-409 (1992).

[21] H. J. He, N. Polonsky and S. f. Su, Phys. Rev. D **64**, 053004 (2001) [arXiv:hep-ph/0102144].

[22] K. Nakamura et al. (Particle Data Group), J. Phys. G 37, 075021 (2010); GFitter Working Group, http://gfitter.desy.de/.

[23] V. Khachatryan *et al.* [CMS Collaboration], Phys. Rev. Lett. **105**, 211801 (2010). [arXiv:1010.0203 [hep-ex]].

[24] G. Aad *et al.* [ATLAS Collaboration], [arXiv:1103.3864 [hep-ex]].

[25] T. Aaltonen *et al.* [CDF Collaboration], Phys. Rev. **D79**, 112002 (2009). [arXiv:0812.4036 [hep-ex]].

[26] V. M. Abazov *et al.* [D0 Collaboration], Phys. Rev. **D69**, 111101 (2004). [hep-ex/0308033].

[27] J. Alitti *et al.* [UA2 Collaboration], Z. Phys. **C49** (1991) 17-28 and Nucl. Phys. **B400** (1993) 3-24.

[28] P. M. Nadolsky, H. -L. Lai, Q. -H. Cao, J. Huston, J. Pumplin, D. Stump, W. -K. Tung, C. -P. Yuan, Phys. Rev. **D78** (2008) 013004. [arXiv:0802.0007 [hep-ph]].

[29] J. Baglio, A. Djouadi, [arXiv:1103.6247 [hep-ph]].

[30] S. Chatrchyan *et al.* [CMS Collaboration], [arXiv:1104.1619 [hep-ex]].

[31] ATLAS Collaboration, ATLAS-CONF-2011-025.

[32] CDF Collaboration, CDF/PUB/EXOTIC/PUBLIC/10485

[33] D0 Collaboration, D0 Note 6177-CONF.

[34] S. Dittmaier *et al.* [LHC Higgs Cross Section Working Group Collaboration], [arXiv:1101.0593 [hep-ph]].

[35] ATLAS Collaboration, ATLAS-CONF-2011-071.

[36] See ATLAS notes ATLAS-CONF-2011-048 for Higgs searches in the ZZ channel and ATLAS-CONF-2011-052 for those in W^+W^- channel.

[37] S. Chatrchyan *et al.* [CMS Collaboration], Phys. Lett. **B699**, 25-47 (2011). [arXiv:1102.5429 [hep-ex]].

Chapter 6

Searching for Directly Decaying Gluinos at the Tevatron

6.1 Introduction

In many theories beyond the Standard Model, there is a new color octet particle that decays into jets plus a stable neutral singlet. This occurs, for example, in supersymmetry [1] and Universal Extra Dimensions [2], as well as Randall-Sundrum [3] and Little Higgs models [4]. As a result, jets plus missing transverse energy ($E_T^{\rm miss}$) is a promising experimental signature for new phenomena [5, 6, 7, 8, 9].

At present, the jets + $E_T^{\rm miss}$ searches at the Fermilab Tevatron are based upon the minimal supersymmetric standard model (MSSM) and look for production of gluinos ($\tilde{g}$) and squarks ($\tilde{q}$), the supersymmetric partners of gluons and quarks, respectively [7, 8]. Both gluinos and squarks can decay to jets and a bino ($\tilde{B}$), the supersymmetric partner of the photon. The bino is stable, protected by a discrete R-parity, and is manifest as missing energy in the detector. Different jet topologies are expected, depending on the relative masses of the gluinos and squarks.

There are many parameters in the MSSM and setting mass bounds in a multidimensional parameter space is difficult. This has lead to a great simplifying ansätz known as the CMSSM (or mSUGRA) parameterization of supersymmetry breaking [10]. This ansätz sets all the gaugino masses equal at the grand unified scale and runs

them down to the weak scale, resulting in an approximately constant ratio between the gluino and bino masses ($m_{\tilde{g}} : m_{\tilde{B}} = 6 : 1$). Thus, the mass ratio between the gluino and bino is never scanned when searching through CMSSM parameter space. Since the bino is the LSP in most of the CMSSM parameter space, the restriction to unified gaugino masses means that there is a large region of kinematically-accessible gluinos where there are no known limits.

The CMSSM parametrization is not representative of all supersymmetric models. Other methods of supersymmetry breaking lead to different low-energy particle spectra. In anomaly mediation [11], the wino can be the LSP; for instance, $m_{\tilde{g}} : m_{\tilde{W}} \simeq 9 : 1$. Mirage mediation [12], in contrast, has nearly degenerate gauginos. A more comprehensive search strategy should be sensitive to all values of $m_{\tilde{g}}$ and $m_{\tilde{B}}$. Currently, the tightest model-independent bound on gluinos is 51 GeV and comes from thrust data at ALEPH and OPAL [13].

In this paper, we describe how bounds can be placed on all kinematically-allowed gluino and bino* masses. We will treat the gluino as the first new colored particle and will assume that it only decays to the stable bino: $\tilde{g} \to \bar{q}_1 \tilde{q}^* \to \bar{q}_1 q_2 \tilde{B}$. The spin of the new color octet and singlet is not known a priori; the only selection rule we impose is that the two have the same statistics. In practice, the spin dependence is a rescaling of the entire production cross section. For our analysis, we will assume that the octet has spin 1/2, and will show how the results vary with cross section rescaling.

We show how a set of optimized cuts for $E_T^{\rm miss}$ and $H_T = \sum_{\rm jets} E_T$ can discover particles where the current Tevatron searches would not. In order to show this, we model our searches on $D0$'s searches for monojets [9], squarks and gluinos [7]. In keeping the searches closely tied to existing searches, we hope that our projected sensitivity is close to what is achievable and not swamped by unforeseen backgrounds.

*Throughout this note, we will call the color octet a "gluino" and the neutral singlet the "bino," though nothing more than the color and charge is denoted by these names.

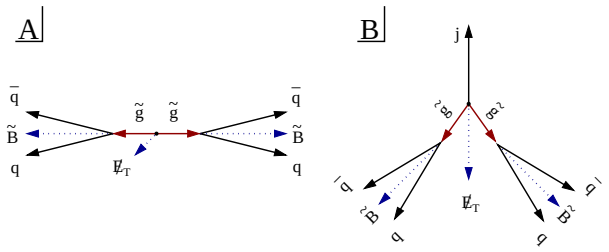

Figure 6.1: Boosted gluinos that are degenerate with the bino do not enhance the missing transverse energy when there is no hard initial- or final-state radiation. (A) illustrates the cancellation of the bino's E_T^{miss}. (B) shows how initial- or final-state radiation leads to a large amount of E_T^{miss}even if the gluino is degenerate with the bino.

6.2 Event Generation

6.2.1 Signal

The number of jets expected as a result of gluino production at the Tevatron depends on the relative mass difference between the gluino and bino, $m_{\tilde{g}} - m_{\tilde{B}}$. When the mass splitting is much larger than the bino mass, the search is not limited by phase space and four or more well-separated jets are produced, as well as large missing transverse energy. The situation is very different for light gluinos ($m_{\tilde{g}} \lesssim 200$ GeV) that are nearly degenerate with the bino. Such light gluinos can be copiously produced at the Tevatron, with cross sections $\mathcal{O}(10^2$ pb), as compared to $\mathcal{O}(10^{-2}$ pb) for their heavier counterparts ($m_{\tilde{g}} \gtrsim 400$ GeV). Despite their large production cross sections, these events are challenging to detect because the jets from the decay are soft, with modest amounts of missing transverse energy. Even if the gluinos are strongly boosted, the sum of the bino momenta will approximately cancel when reconstructing the missing transverse energy (Fig. 6.1A). To discover a gluino degenerate with a bino, it is necessary to look at events where the gluino pair is boosted by the emission of hard QCD jets (Fig. 6.1B). Therefore, initial-state radiation (ISR) and final-state radiation (FSR) must be properly accounted for.

The correct inclusion of ISR/FSR with parton showering requires generating gluino events with matrix elements. We used MadGraph/MadEvent [14] to compute

processes of the form

$$p\bar{p} \rightarrow \tilde{g}\tilde{g} + Nj, \tag{6.2.1}$$

where $N = 0, 1, 2$ is the multiplicity of QCD jets. The decay of the gluino into a bino plus a quark and an antiquark, as well as parton showering and hadronization of the final-state partons, was done in PYTHIA 6.4 [15].

To ensure that no double counting of events occurs between the matrix-element multi-parton events and the parton showers, a version of the MLM matching procedure was used [16]. In this procedure, the matrix element multi-parton events and the parton showers are constrained to occupy different kinematical regions, separated using the $k_\perp$ jet measure:

$$\begin{aligned} d^2(i,j) &= \Delta R_{ij}^2 \min(p_{Ti}^2, p_{Tj}^2) \\ d^2(i,\text{beam}) &= p_{Ti}^2, \end{aligned} \tag{6.2.2}$$

where $\Delta R_{ij}^2 = 2(\cosh\Delta\eta - \cos\Delta\phi)$ [17]. Matrix-element events are generated with some minimum cut-off $d(i,j) = Q_{\text{min}}^{\text{ME}}$. After showering, the partons are clustered into jets using the k_T jet algorithm with a $Q_{min}^{PS} > Q_{min}^{ME}$. The event is then discarded unless all resulting jets are matched to partons in the matrix-element event, $d(\text{parton}, \text{jet}) < Q_{min}^{PS}$. For events from the highest multiplicity sample, extra jets softer than the softest matrix-element parton are allowed. This procedure avoids double-counting jets, and results in continuous and smooth differential distributions for all jet observables.

The matching parameters ($Q_{\text{min}}^{\text{ME}}$ and $Q_{\text{min}}^{\text{PS}}$) should be chosen resonably far below the factorization scale of the process. For gluino production, the parameters were:

$$Q_{\text{min}}^{\text{ME}} = 20 \text{ GeV and } Q_{\text{min}}^{\text{PS}} = 30 \text{ GeV}. \tag{6.2.3}$$

The simulations were done using the CTEQ6L1 PDF [18] and with the renormalization and factorization scales set to the gluino mass. The cross sections were rescaled to the next-to-leading-order (NLO) cross sections obtained using Prospino 2.0 [19].

Finally, we used PGS [20] for detector simulation, with a cone jet algorithm with $\Delta R = 0.5$. As a check on this procedure, we compared our results to the signal point given in [7] and found that they agreed to within 10%.

6.2.2 Backgrounds

The three dominant Standard Model backgrounds that contribute to the jets plus missing energy searches are: $W^{\pm}/Z^0$ + jets, $t\bar{t}$, and QCD. There are several smaller sources of missing energy that include single top and di-boson production, but these make up a very small fraction of the background and are not included in this study.

The $W^{\pm}/Z^0 + nj$ and $t\bar{t}$ backgrounds were generated using MadGraph/MadEvent and then showered and hadronized using PYTHIA. PGS was used to reconstruct the jets. MLM matching was applied up to three jets for the $W^{\pm}/Z^0$ background, with the parameters $Q^{\rm ME}_{\rm min} = 10$ GeV and $Q^{\rm PS}_{\rm min} = 15$ GeV. The top background was matched up to two jets with $Q^{\rm ME}_{\rm min} = 14$ GeV and $Q^{\rm PS}_{\rm min} = 20$ GeV. Events containing isolated leptons with $p_T \geq 10$ GeV were vetoed to reduce background contributions from leptonically decaying $W^{\pm}$ bosons. To reject cases of $E_T^{\rm miss}$ from jet energy mismeasurement, a lower bound of 90° and 50° was placed on the azimuthal angle between $E_T^{\rm miss}$ and the first and second hardest jets, respectively. An acoplanarity cut of $< 165°$ was applied to the two hardest jets. Because the $D0$ analysis did not veto hadronically decaying tau leptons, all taus were treated as jets in this study.

Simulation of the missing energy background from QCD is beyond the scope of PYTHIA and PGS, and was therefore not done in this work. However, to avoid the regions where jet and calorimeter mismeasurements become the dominant background, a lower limit of $E_T^{\rm miss} > 100$ GeV was imposed. Additionally, in the dijet analysis, the azimuthal angle between the $E_T^{\rm miss}$ and any jet with $p_T \geq 15$ GeV and $|\eta| \leq 2.5$ was bounded from below by 40°. This cut was not placed on the threejet or multijet samples because of the large jet multiplicities in these cases.

For each of the $W^{\pm}/Z^0 + nj$ and $t\bar{t}$ backgrounds, 500K events were generated. The results reproduce the shape and scale of the $E_T^{\rm miss}$ and H_T distributions published by the $D0$ collaboration in [7] for $1{\rm fb}^{-1}$. For the dijet case, where the most statistics

are available, the correspondence with the $D0$ result is $\pm 20\%$. With the threejet and multijet cuts, the result for the $t\bar{t}$ background is similar, while the $W^{\pm}/Z^0 + nj$ backgrounds reproduce the $D0$ result to within $30 - 40\%$ for the threejet and multijet cases. The increased uncertainty may result from insufficient statistics to fully populate the tails of the $E_T^{\rm miss}$ and H_T distributions. The PGS probability of losing a lepton may also contribute to the relative uncertainties for the $W^{\pm} + nj$ background. Heavy flavor jet contributions were found to contribute 2% to the $W^{\pm}/Z^0$ backgrounds, which is well below the uncertainties that arise from not having NLO calculations for these processes and from using PGS.

6.3 Projected Reach of Searches

A gluino search should have broad acceptances over a wide range of kinematical parameter space; it should be sensitive to cases where the gluino and bino are nearly degenerate, as well as cases where the gluino is far heavier than the bino. As already discussed, the number of jets and $E_T^{\rm miss}$ depend strongly on the mass differerence between the gluino and bino. Because the signal changes dramatically as the masses of the gluino and bino are varied, it is necessary to design searches that are general, but not closely tied to the kinematics. We divided events into four mutually exclusive searches for $E_T^{\rm miss}$ plus $1j$, $2j$, $3j$ and 4^+j, respectively. For convenience, we keep the $nj + E_T^{\rm miss}$ classification fixed for all gluino and bino masses (see Table 7.1). These selection criteria were modeled after those used in $D0$'s existing search [7].[†] These exclusive searches can be statistically combined to provide stronger constraints.

Two cuts are placed on each search: $H_T^{\rm min}$ and $E_T^{{\rm miss}min}$. In the $D0$ analysis, the H_T and $E_T^{\rm miss}$ cuts are constant for each search. The signal (as a function of the gluino and bino masses) and Standard Model background are very sensitive to these cuts. To maximize the discovery potential, these two cuts should be optimized for all gluino and bino masses. For a given gluino and bino mass, the significance $(S/\sqrt{S+B})$ is maximized over $H_T^{\rm min}$ and $E_T^{{\rm miss}min}$ in each nj+$E_T^{\rm miss}$search. Due to

[†]It should be noted, however, that the $D0$ searches are inclusive because each is designed to look for separate gluino/squark production modes (i.e., $pp \to \tilde{q}\tilde{q}$, $\tilde{q}\tilde{g}$, $\tilde{g}\tilde{g}$).

	$1j + E_T^{\text{miss}}$	$2j + E_T^{\text{miss}}$	$3j + E_T^{\text{miss}}$	$4^+j + E_T^{\text{miss}}$
$E_{T\,j_1}$	≥ 150	≥ 35	≥ 35	≥ 35
$E_{T\,j_2}$	< 35	≥ 35	≥ 35	≥ 35
$E_{T\,j_3}$	< 35	< 35	≥ 35	≥ 35
$E_{T\,j_4}$	< 20	< 20	< 20	≥ 20

Table 6.1: Summary of the selection criteria for the four non-overlapping searches. The two hardest jets are required to be central ($|\eta| \leq 0.8$). All other jets must have $|\eta| \leq 2.5$.

the uncertainty in the background calculations, the S/B was not allowed to drop beneath the conservative limit of $S/B > 1$. More aggressive bounds on S/B may also be considered; $D0$, for instance, claims a systematic uncertainty of $\mathcal{O}(30\%)$ in their background measurements [7]. The resulting 95% sensitivity plot using the optimized H_T and E_T^{miss} cuts is shown in Fig. 6.2. The corresponding inset illustrates the effect of varying the production cross section.

For light and degenerate gluinos, the $1j + E_T^{\text{miss}}$ and $2j + E_T^{\text{miss}}$ searches both have good sensitivity. In an intermediate region, the $2j + E_T^{\text{miss}}$, $3j + E_T^{\text{miss}}$ and $4^+j + E_T^{\text{miss}}$ all cover with some success, but there appears to be a coverage gap where no search does particularly well. If one does not impose a S/B requirement, a lot of the gap can be covered, but background calculations are probably not sufficiently precise to probe small S/B. For massive, non-degenerate gluinos, the $3j + E_T^{\text{miss}}$ and $4^+j + E_T^{\text{miss}}$ both give good sensitivity, with the $4^+j + E_T^{\text{miss}}$ giving slightly larger statistical significance.

In the exclusion plot, the E_T^{miss} and H_T cuts were optimized for each point in gluino-bino parameter space. However, for gluino masses 200 GeV $\lesssim m_{\tilde{g}} \lesssim$ 350 GeV, where the monojet search gives no contribution, we found that the exclusion region does not markedly change if the following set of generic cuts are placed:

$$\begin{aligned}(H_T, E_T^{\text{miss}}) \;\geq\; & (150, 100)_{2j+E_T^{\text{miss}}}, \\ & (150, 100)_{3j+E_T^{\text{miss}}}, (200, 100)_{4^+j+E_T^{\text{miss}}}. \end{aligned} \tag{6.3.1}$$

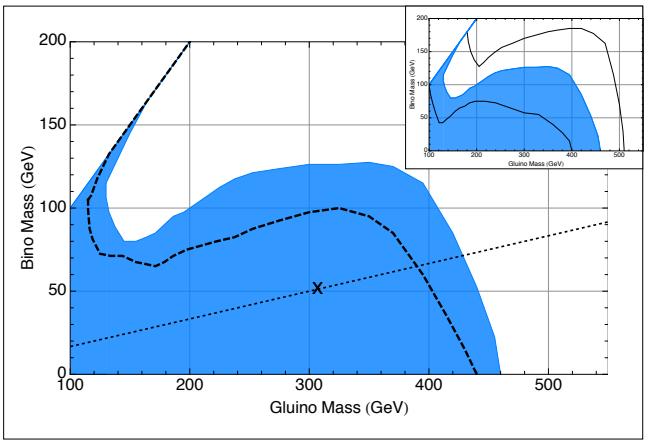

Figure 6.2: The 95% gluino-bino exclusion curve for $D0$ at 4 fb^{-1} for $S/B > 1$. The dashed line shows the corresponding exclusion region using $D0$'s non-optimized cuts. The masses allowed in the CMSSM are represented by the dotted line; the "X" marks the current $D0$ limit on the gluino mass at 2.1 fb^{-1} (see text for details) [7]. The inset shows the effect of scaling the production cross section for the case of $S/B > 1$. The solid lines show the exclusion region for $\sigma/3$ (bottom) and 3σ (top).

As a comparison, the cuts used in the $D0$ analysis are

$$\begin{aligned}(H_T, E_T^{\rm miss}) \;\geq\; & (325, 225)_{2j+E_T^{\rm miss}}, \\ & (375, 175)_{3j+E_T^{\rm miss}}, (400, 100)_{4^+j+E_T^{\rm miss}}.\end{aligned} \tag{6.3.2}$$

The lowered cuts provide better coverage for intermediate mass gluinos, as indicated in Fig. 6.2. For $m_{\tilde{g}} \lesssim 200$ GeV, we place tighter cuts on the monojet and dijet samples than $D0$ does. While $D0$ technically has statistical significance in this region with their existing cuts, their signal-to-background ratio is low. Because of the admitted difficulties in calculating the Standard Model backgrounds, setting exclusions with a low signal-to-background should not be done and fortunately can be avoided by tightening the H_T and $E_T^{\rm miss}$ cuts. Similarly, for larger gluino masses, the generic cuts are no longer effective and it is necessary to use the optimized cuts, which are tighter than $D0$'s.

6.4 Conclusions and Outlook

In this paper, we describe the sensitivity that $D0$ has in searching for gluinos away from the CMSSM hypothesis in jets + E_T^{miss} searches. It was assumed that the gluino only decayed to two jets and a stable bino. However, many variants of this decay are possible and the search presented here can be generalized accordingly.

One might, for example, consider the case where the gluino decays dominantly to bottom quarks and heavy flavor tagging can be used advantageously. Cascade decays are another important possibility. Decay chains have a significant effect upon the searches because they convert missing energy into visible energy. In this case, additional parameters, such as the intermediate particle masses and the relevant branching ratios, must be considered. In the CMSSM, the branching ratio of the gluino into the wino is roughly 80%. This is the dominant decay affecting the $D0$ gluino mass bound in CMSSM parameter space (see Fig. 2). While this cascade decay may be representative of many models that have gluino-like objects, the fixed mass ratio and branching ratio are again artifacts of the CMSSM. A more thorough examination of cascade decays should be considered.

In addition to alternate decay routes for the gluino, alternate production modes are important when there are additional particles that are kinematically accessible. In this paper, it was assumed that the squarks are kinematically inaccessible at the Tevatron; however, if the squarks are accessible, $\tilde{g}\tilde{q}$ and $\tilde{q}\tilde{q}$ production channels could lead to additional discovery possibilities. For instance, a gluino that is degenerate with the bino could be produced with a significantly heavier squark. The squark's subsequent cascade decay to the bino will produce a great deal of visible energy in the event and may be more visible than gluino pair production.[‡]

Finally, in the degenerate gluino region, it may be beneficial to use a mono-photon search rather than a monojet search [22].[§] Preliminary estimates of the reach of the mono-photon search show that it is not as effective as the monojet search. This is likely due to the absence of final-state photon radiation from the gluinos. However, it may be possible to better optimize the mono-photon search, because the Standard

[‡]We thank M. Ibe and R. Harnik for this observation.
[§]We thank F. Petriello for pointing this out

Model backgrounds are easier to understand in this case.

Ultimately, a model-independent search for jets plus missing energy would be ideal. We believe that our exclusive $nj + E_T^{\rm miss}$ searches, with results presented in an exclusion plot as a function of H_T and $E_T^{\rm miss}$, would provide significant coverage for these alternate channels [21]. This analysis should be carried forward to the LHC to ensure that the searches discover all possible supersymmetric spectra. The general philosophy of parameterizing the kinematics of the decay can be easily carried over. The main changes are in redefining the H_T and $E_T^{\rm miss}$ cuts, as well as the hard jet energy scale. We expect a similar shape to the sensitivity curve seen in Fig. 6.2, but at higher values for the gluino and bino masses. Therefore, it is unlikely that there will be a gap in gluino-bino masses where neither the Tevatron nor the LHC has sensitivity.

Bibliography

[1] S. Dimopoulos and H. Georgi, Nucl. Phys. B **193**, 150 (1981).

[2] T. Appelquist, H. C. Cheng and B. A. Dobrescu, Phys. Rev. D **64**, 035002 (2001) [arXiv:hep-ph/0012100].

[3] L. Randall and R. Sundrum, Phys. Rev. Lett. **83**, 3370 (1999) [arXiv:hep-ph/9905221];

[4] N. Arkani-Hamed, A. G. Cohen and H. Georgi, Phys. Lett. B **513**, 232 (2001) [arXiv:hep-ph/0105239]; N. Arkani-Hamed, A. G. Cohen, E. Katz, A. E. Nelson, T. Gregoire and J. G. Wacker, JHEP **0208**, 021 (2002) [arXiv:hep-ph/0206020]; E. Katz, J. y. Lee, A. E. Nelson and D. G. E. Walker, JHEP **0510**, 088 (2005) [arXiv:hep-ph/0312287].

[5] J. Alitti *et al.* [UA2 Collaboration], Phys. Lett. B **235**, 363 (1990).

[6] X. Portell [CDF Run II Collaboration], AIP Conf. Proc. **842**, 640 (2006) [arXiv:hep-ex/0609017].

[7] V. M. Abazov *et al.* [$D0$ Collaboration], [arXiv:0712.3805 [hep-ex]]; The $D0$ Collaboration, $D0$ Note 5312 (2007).

[8] The CDF Collaboration, CDF Note 9093 (2007).

[9] A. Abulencia *et al.* [CDF Collaboration], Phys. Rev. Lett. **97**, 171802 (2006) [arXiv:hep-ex/0605101]; The $D0$ Collaboration, $D0$ CONF 4400 (2007).

[10] H. P. Nilles, Phys. Rep. **110**, 1(1984).

[11] L. Randall and R. Sundrum, Nucl. Phys. B **557**, 79 (1999) [arXiv:hep-th/9810155]; G. F. Giudice, M. A. Luty, H. Murayama and R. Rattazzi, JHEP **9812**, 027 (1998) [arXiv:hep-ph/9810442].

[12] K. Choi, A. Falkowski, H. P. Nilles and M. Olechowski, Nucl. Phys. B **718**, 113 (2005) [arXiv:hep-th/0503216].

[13] D. E. Kaplan and M. D. Schwartz, [arXiv:0804.2477 [hep-ph]].

[14] J. Alwall *et al.*, JHEP **0709**, 028 (2007) [arXiv:0706.2334 [hep-ph]].

[15] T. Sjostrand, S. Mrenna and P. Skands, JHEP **0605**, 026 (2006) [arXiv:hep-ph/0603175].

[16] J. Alwall *et al.*, [arXiv:0706.2569 [hep-ph]].

[17] S. Catani, Y. L. Dokshitzer, M. H. Seymour and B. R. Webber, Nucl. Phys. B **406**, 187 (1993).

[18] J. Pumplin, D. R. Stump, J. Huston, H. L. Lai, P. Nadolsky and W. K. Tung, JHEP **0207**, 012 (2002) [arXiv:hep-ph/0201195]; D. Stump, J. Huston, J. Pumplin, W. K. Tung, H. L. Lai, S. Kuhlmann and J. F. Owens, JHEP **0310**, 046 (2003) [arXiv:hep-ph/0303013].

[19] W. Beenakker, R. Hopker, M. Spira and P. M. Zerwas, Nucl. Phys. B **492**, 51 (1997) [arXiv:hep-ph/9610490].

[20] J. Conway, *PGS: Pretty Good Simulator*, http://www.physics.ucdavis.edu/ conway/ research/software/pgs/pgs4-general.htm.

[21] Manuscript in preparation.

[22] V. M. Abazov *et al.* [$D0$ Collaboration], arXiv:0803.2137 [hep-ex].

Chapter 7

Model-Independent Jets plus Missing Energy Searches

7.1 Introduction

One of the most promising signatures for new physics at hadron colliders are events with jets and large missing transverse energy ($E_T^{\rm miss}$). These searches are very general and cover a wide breadth of potential new theories beyond the Standard Model. Jets + $E_T^{\rm miss}$ searches pose a significant challenge, however, because the Standard Model background is difficult to calculate in this purely hadronic state. The general nature of the signature motivates performing a search that only requires calculating the Standard Model background. The challenge, then, is to minimize the risk of missing new physics while still accounting for our limited understanding of the background. All experimental searches of jets + $E_T^{\rm miss}$ at hadron colliders have been model-dependent, attempting to be sensitive to specific models [1, 2, 3, 4, 5, 6]. Initial studies for the Large Hadron Collider (LHC) have been dominantly model-dependent [7, 8, 9, 10]. In this article, we explore how modest modifications to the existing jets and $E_T^{\rm miss}$ studies can allow them to be model-independent, broadening the reach of the experimental results in constraining theoretical models.

Currently, jets plus $E_T^{\rm miss}$ searches at the Tevatron are based on the Minimal Supersymmetric Standard Model (MSSM) [11] and look for production of gluinos ($\tilde{g}$) and squarks ($\tilde{q}$), the supersymmetric partners of gluons and quarks, respectively [2, 3, 4]. These particles subsequently decay into the stable, lightest supersymmetric particle

(LSP), which is frequently the bino, the supersymmetric partner of the photon. The MSSM contains hundreds of parameters and it is challenging to place mass bounds in such a multi-parameter space. To make this tractable, the CMSSM-6 (or mSUGRA) *ansatz* has been used [12]. The CMSSM-6 requires common scalar masses (m_0), gaugino masses ($m_{\frac{1}{2}}$), and trilinear scalar soft couplings (A_0) at the unification scale, in addition to electroweak symmetry breaking, gauge coupling unification, and R-parity conservation. The entire particle spectrum is determined by five parameters.

One important consequence of this theory is that the ratio of gaugino masses is fixed at approximately $m_{\tilde{g}} : m_{\widetilde{W}} : m_{\widetilde{B}} \simeq 6 : 2 : 1$, where $\widetilde{W}$ refers to the triplet of winos ($\widetilde{W}^{\pm}, \widetilde{W}^{0}$), the supersymmetric partners of the electroweak gauge bosons. Due to the number of constraints in the CMSSM-6, the bino is the LSP throughout the range of parameter space that the Tevatron has access to. Furthermore, due to the renormalization group running of the squark masses, the squarks are never significantly lighter than the gluino. Thus, the ratio in masses between the lightest colored particle and the LSP is essentially fixed. The CMSSM-6 is certainly not representative of all supersymmetric models (see, for example, [13, 14, 15, 16, 17, 18]), let alone the wider class of beyond the Standard Model theories that jets and $E_T^{\rm miss}$ searches should have sensitivity to. Verifying that a jets and $E_T^{\rm miss}$ search has sensitivity to the CMSSM-6 does not mean that the search is sensitive to a more generic MSSM.

Existing searches for gluinos and squarks make strong assumptions about the spectrum and it is unclear what the existing limits on squark-like and gluino-like particles are. Because squarks have electric charge, LEP can place limits of 92 GeV on their mass [19]; however, gluinos do not couple to either the photon or Z^0 and so limits from LEP2 are not strong. Currently, the tightest model-independent bound on color octet fermions (such as gluinos) comes from thrust data at ALEPH [20] and OPAL [21]. New colored particles should contribute at loop-level to the running of the strong coupling constant α_s. To date, the theoretical uncertainties in the value of α_s have decreased its sensitivity to new particle thresholds. Advances in Soft-Collinear Effective Theory, however, have been used to significantly reduce the uncertainties in α_s from LEP data. The current bound on color octet fermions is 51.0 GeV at 95%

confidence [22]; no limit can be set for scalar color octets.

There is no unique leading candidate for physics beyond the Standard Model; therefore, searches for new physics need to be performed in many different channels. Ideally, one should perform totally model-independent searches that only employ the Standard Model production cross section for physics with the desired channels and the correct kinematics. The goal is to be sensitive to a large number of different models at the same time so that effort is not wasted in excluding the same parts of Standard Model phase space multiple times.

Some progress on experimental model-independent searches has been made. In an ambitious program, the CDF-6 Collaboration at the Tevatron has looked at all possible new channels simultaneously (i.e., Vista, Sleuth, Bumphunter) [23, 24, 25]; however, these searches have some drawbacks over more traditional, channel-specific searches. The most important drawback is that it is difficult, in the absence of a discovery, to determine what parts of a given model's parameter space are excluded.

On the theoretical front, MARMOSET [26] is a hybrid philosophy that attempts to bridge model-independent and model-dependent searches with the use of On-Shell Effective Theories (OSETs). OSETs parameterize the most experimentally relevant details of a given model – i.e., the particle content, the masses of the particles, and the branching ratios of the decays. By using an on-shell effective theory, it is possible to easily search through all experimentally relevant parameters quickly. The on-shell approximation is not applicable in all situations, but OSETs can still give a rough idea of where new physics lies.

In this article, we will explore the discovery potential of jets and missing energy channels. In previous work [28], we presented a simple effective field theory that can be used to set limits on the most relevant parameters for jets and missing energy searches: the masses of the particles. While this approach seems obvious, existing searches at hadron colliders (Tevatron Run II, Tevatron Run I, UA2, UA1) are based on CMSSM-6-parameterized supersymmetry breaking. The previous paper studied how varying the decay kinematics changed the sensitivity of the searches and pointed out regions of parameter space where sensitivity is particularly low due to kinematics. However, this gluino-bino module was still a model-dependent analysis in that it

assumed pair-production of a new colored fermionic particle directly decaying to a fermionic LSP.

This paper will extend the analysis in two ways. First, we propose a completely model-independent analysis for jets and missing energy searches. This approach only requires knowledge of the Standard Model and places limits on differential cross sections, from which it is possible to set model-dependent limits. In the second portion of the paper, we use this approach to extend our previous analysis of a directly decaying colored particle to contain a single-step cascade and study how this altered spectrum affects the final limits on the gluino's mass.

7.2 Overview of Models

Before continuing with the main theme of the article, let us take a moment to describe the class of models that jets + E_T^{miss} searches are sensitive to. There are two general classes of particle spectra that will be covered by such searches, each of which has a stable neutral particle at the bottom of the spectrum. Typically, the stability of these neutral particles is protected by a discrete symmetry (e.g., R-parity, T-parity, or KK-parity) and, consequently, these particles are good candidates for the dark matter. In one class of models, the theory contains a new colored particle that cascade decays into the dark matter. In the other class, new electroweak gauge bosons are produced. The dark matter particle may either be produced along with the new bosons, or may be the final step in their decays.

The first class can be thought of as being generally SUSY-like where the lightest colored particle is dominantly produced through the Standard Model's strong force. The lightest colored particle then cascade decays down to the stable, neutral particle at the bottom of that sector. These cascades will either be lepton-poor or lepton-rich. Lepton-poor cascades occur when there is no state accessible in the cascades that have explicit lepton number (e.g., sleptons) and frequently occur when the cascades are mediated by $W^{\pm}$, Z^0, or Higgs bosons. A simple supersymmetric example of a lepton-poor cascade decay is a theory where the scalar masses are made heavy and only gauginos and Higgsinos are available in the decay chains. This occurs, for

instance, in PeV supersymmetry models, where the scalars are around 1000 TeV and the fermions of the MSSM are in the 100 GeV to 1 TeV range. Producing the color-neutral states of such a theory is difficult at hadron machines; consequently, the production of new particles will occur primarily through the decay of the gluino.

One potential cascade decay of the gluino, which will be considered in further detail in the second half of the paper, is

$$\tilde{g} \to \bar{q}_1 q_2 \widetilde{W} \to \bar{q}_1 q_2 \bar{q}_3 q_4 \widetilde{B}. \tag{7.2.1}$$

In this cascade, the $\widetilde{W}$ decays directly into the $\widetilde{B}$ and a $W^{\pm}, Z^0$ boson, which subsequently decays to two jets. This single-step decay is the dominant cascade if the gaugino masses are unified at high energies; in this case, the branching ratio of the gluino into the wino is $\sim 80\%$. While these cascade decays are to some degree representative, the precise mass ratio of $m_{\tilde{g}} : m_{\widetilde{W}} : m_{\widetilde{B}}$ makes a significant difference in the searches. In the limit where $m_{\widetilde{W}} \to m_{\widetilde{B}}$ the energy from $\bar{q}_3$ and q_4 is small, while if $m_{\widetilde{W}} \to m_{\tilde{g}}$ the jets from $\bar{q}_1$ and q_2 are soft. If $m_{\widetilde{W}} > m_{\tilde{g}}$, this cascade is forbidden. Interestingly, spectra with unified gaugino masses are the most difficult to see because all four jets are fairly hard and diminish the missing energy in the event in comparison to the direct decay of the gluino, $\tilde{g} \to \bar{q}_1 q_2 \widetilde{B}$.

Leptons from the decay of the $W^{\pm}$, Z^0 boson can be used in the analysis as well (see Sec. 7.5.5). However, jets + E_T^{miss} + lepton studies are better suited for lepton-rich cascades. The addition of leptons to the searches makes the experimental systematics easier to control and improves trigger efficiencies. Not all spectra of new physics can be probed with these types of searches, though, and they are thus complimentary to the jets + E_T^{miss} search.

Other cascades may produce a greater number of jets as compared to (7.2.1). In NMSSM theories where there is a new singlino at the bottom of the spectrum [27], it is possible to have cascade decays that start with the gluino, go to wino plus two jets, then bino plus two additional jets, and conclude with the singlino plus two more jets. The additional step in the decay process further diminishes the amount of missing energy in typical events, resulting in reduced limits on spectra. Other models, such as Universal Extra Dimensions (UEDs) [29] and Little Higgs models with T-parity

[30] also have new colored particles that subsequently cascade decay. The details of the exact spectra can alter the signal significantly as jets can become soft and missing energy is turned into visible energy.

It is also possible that new electroweak gauge bosons are produced, which then cascade decay, producing jets before ending with the neutral stable particle. Little Higgs models with T-parity are one such example. In such models, the new heavy bosons $W_H^{\pm}$ and Z_H^0 are produced through s-channel processes. The $W_H^{\pm}$ can decay to the $W^{\pm}$ and the dark matter A_H, while the Z_H^0 can decay to the A_H and higgs. It is also possible to produce the $W_H^{\pm}$ directly with the A_H through an s-channel $W^{\pm}$ boson. This vertex, however, is suppressed in comparison to the other two.

7.3 Proposed Analysis Strategy

At the Tevatron, the jets + E_T^{miss} channel is divided into four separate searches (monojet, dijet, threejet, and multijet), with each search defined by jet cuts $\mathcal{O}(30$ GeV). Cuts on the missing transverse energy and total visible energy* H_T of each event take place during the final round of selection cuts. The E_T^{miss} and H_T cuts are optimized for "representative" points in CMSSM-6 parameter space for each of the (inclusive) $1j - 4^+j$ searches. However, these E_T^{miss} and H_T cuts may not be appropriate for theories other than the CMSSM-6. Indeed, considering the full range of kinematically allowed phase space means accounting for many combinations of missing and visible energy. A set of static cuts on E_T^{miss} and H_T is overly-restrictive and excludes regions of phase space that are kinematically allowed.

This is explicitly illustrated in Fig. 7.1, which shows the E_T^{miss} distribution of a dijet sample passed through two different sets of E_T^{miss} and H_T cuts. The signal, a 210 GeV gluino directly decaying (i.e., no cascade) to a 100 GeV bino, is shown in white and the Standard Model background, in gray. The plot on the left shows the events that survive a 300 GeV H_T cut. While the H_T cut significantly reduces the background, it also destroys the signal above the E_T^{miss}cut of 225 GeV. These cuts were used in the $D0$ dijet search; they are optimized for a ~ 400 GeV gluino, but are

*The total visible energy H_T is defined as the scalar sum of the transverse momenta of each jet.

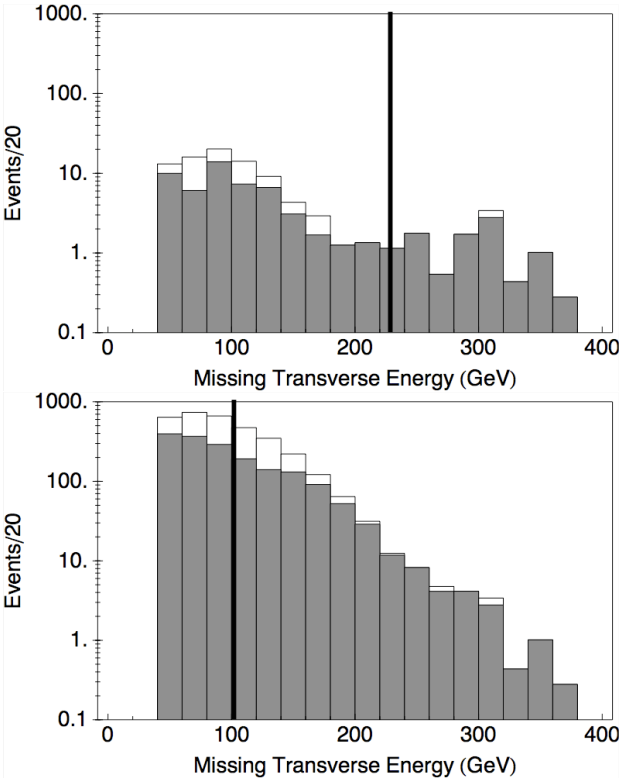

Figure 7.1: Comparison of $D0$ cuts and optimized cuts for a sample dijet signal for $m_{\tilde{g}} = 210$ GeV and $m_{\widetilde{B}} = 100$ GeV. Background distribution is shown in gray and signal distribution in white. (Left) Using the $D0$ cuts $H_T \geq 300$ GeV and $E_T^{\rm miss} \geq$ 225 GeV (Right) Using the more optimal cuts $H_T \geq 150$ GeV and $E_T^{\rm miss} \geq 100$ GeV. The optimized cuts allow us to probe regions with larger S/B.

clearly not ideal for the signal point shown here. A more optimal choice of cuts is shown on the right. While the lower H_T cut of 150 GeV keeps more background, it also keeps enough signal for a reasonable S/B ratio at low $E_T^{\rm miss}$. Therefore, with a $E_T^{\rm miss}$ cut of 100 GeV, exclusion limits on this point in parameter space can be placed.

A model-independent search should have broad acceptances over a wide range of kinematical parameter space. Ideally, searches should be sensitive to all possible kinematics by considering all appropriate $E_T^{\rm miss}$ and H_T cuts. This can be effectively done by plotting the differential cross section as a function of $E_T^{\rm miss}$ and H_T,

$$\frac{d^2\sigma}{dH_T dE_T^{\rm miss}} \Delta H_T \Delta E_T^{\rm miss}. \tag{7.3.1}$$

	$1j + E_T^{\text{miss}}$	$2j + E_T^{\text{miss}}$	$3j + E_T^{\text{miss}}$	$4^+j + E_T^{\text{miss}}$
$E_{T\,j_1}$	≥ 150	≥ 35	≥ 35	≥ 35
$E_{T\,j_2}$	< 35	≥ 35	≥ 35	≥ 35
$E_{T\,j_3}$	< 35	< 35	≥ 35	≥ 35
$E_{T\,j_4}$	< 20	< 20	< 20	≥ 20

Table 7.1: Summary of the selection criteria for the four exclusive (i.e., non-overlapping) searches. The two hardest jets are required to be central ($|\eta| \leq 0.8$). All other jets must have $|\eta| \leq 2.5$.

In this case, the results of a search would be summarized in a grid, where each box contains the measured cross section within a particular interval of E_T^{miss} and H_T.

As an example, the differential cross section grids for exclusive $1j - 4^+j$ searches (see Table 7.1 for jet selection criteria) at the Tevatron are shown in Table 7.2. The grids are made for the Standard Model background, which include $W^{\pm} + nj$, $Z^0 + nj$, and $t\bar{t} + nj$. The QCD background was not simulated; we expect the QCD contributions to be important for points in the lowest E_T^{miss} bin. For details concerning the Monte Carlo generation of the backgrounds, see Sec. 7.4.2.

From these results, it is straightforward to obtain limits on the differential cross section for any new physics signal. Consider a specific differential cross section measurement that measures N_m events in an experiment. The Standard Model predicts B events, while some specific theory predicts $B + S$ events, where S is the number of signal events.

The probability of measuring n events is given by the Poisson distribution with mean $\mu = B + S$. The mean μ is excluded to 84% such that

$$e^{-\mu^{\text{excl}}} \sum_{n=0}^{N_m} \frac{(\mu^{\text{excl}})^n}{n!} \leq 0.16. \tag{7.3.2}$$

The solution to this equation gives the excluded number of signal events

$$S^{\text{excl}}(N_m, B) = \mu^{\text{excl}}(N_m) - B. \tag{7.3.3}$$

	Simulated Background	Signal Limits
Monojet	39 | 194 | 51 | 11 | 2.1 100 150 200 250 300 350 $\not\!\!E_T$	3.1⊕20 | 7.0⊕97 | 3.6⊕26 | 1.7⊕5.5 | 1.0⊕1.1 100 150 200 250 300 350 $\not\!\!E_T$
Dijet	H_T 600 500 400 300 200 100 0.1 0.1 0 0 0 1.3 0.1 0.1 0.1 0 2.6 0.6 0.7 0.7 1.0 27 17 10 2.2 230 37 100 150 200 250 300 350 $\not\!\!E_T$	H_T 600 500 400 300 200 100 0.5⊕0.1 0.5⊕0.1 0.5⊕0.0 0.5⊕0.0 0.5⊕0.0 0.9⊕0.7 0.5⊕0.1 0.5⊕0.1 0.5⊕0.1 0.5⊕0.0 1.1⊕1.3 0.7⊕0.3 0.7⊕0.4 0.7⊕0.4 0.8⊕0.5 2.6⊕14 2.1⊕8.5 1.6⊕5.0 1.0⊕1.1 7.6⊕120 3.0⊕19 100 150 200 250 300 350 $\not\!\!E_T$
Threejet	H_T 600 500 400 300 200 100 0 0 0 0 0 0.5 0.1 0.3 0.1 0 2.5 2.4 1.0 0.5 0.1 19 7.6 1.8 0.4 17 3.0 100 150 200 250 300 350 $\not\!\!E_T$	H_T 600 500 400 300 200 100 0.5⊕0.0 0.5⊕0.0 0.5⊕0.0 0.5⊕0.0 0.5⊕0.0 0.6⊕0.3 0.5⊕0.1 0.6⊕0.2 0.5⊕0.1 0.5⊕0.0 1.1⊕1.3 1.1⊕1.2 0.8⊕0.5 0.6⊕0.3 0.5⊕0.1 2.2⊕9.5 1.4⊕3.8 1.0⊕0.9 0.6⊕0.2 2.1⊕8.5 1.2⊕1.5 100 150 200 250 300 350 $\not\!\!E_T$
Multijet	H_T 600 500 400 300 200 100 0.9 0.2 0.2 0.1 0 4.2 2.4 1.1 0.6 0.1 15 7.0 2.1 0.6 0.1 42 10 1.2 0.3 8.6 0.9 100 150 200 250 300 350 $\not\!\!E_T$	H_T 600 500 400 300 200 100 0.8⊕0.5 0.5⊕0.1 0.5⊕0.1 0.5⊕0.1 0.5⊕0.0 1.3⊕2.1 1.1⊕1.2 0.8⊕0.6 0.7⊕0.3 0.5⊕0.1 1.9⊕7.5 1.3⊕3.5 1.0⊕1.1 0.7⊕0.3 0.5⊕0.1 3.2⊕21 1.6⊕5.0 0.8⊕0.6 0.6⊕0.2 1.5⊕4.3 0.8⊕0.5 100 150 200 250 300 350 $\not\!\!E_T$

Table 7.2: Differential cross section (in fb) for the Standard Model background is shown in the left column for exclusive $1j - 4^+j$ searches. The expected signal sensitivity at 84% confidence is shown on the right (in fb). The statistical error is shown to the left of the $\oplus$ and the systematic error is on the right. For purposes of illustration, we assume a 50% systematic error on the background. The gray boxes are kinematically forbidden. These results are for 4 fb^{-1} luminosity at the Tevatron.

The expected limit on the signal is then given by

$$\langle S^{\text{excl}}(B)\rangle = \sum_{N_m=0}^{\infty} S^{\text{excl}}(N_m, B)\frac{e^{-B}B^{N_m}}{N_m!}. \tag{7.3.4}$$

In the limit of large B, the probability distribution approaches a Gaussian and we expect that

$$\lim_{B\to\infty}\langle S^{\text{excl}}(B)\rangle = \sqrt{B}. \tag{7.3.5}$$

In the limit of small B, we expect that

$$\lim_{B\to 0}\langle S^{\text{excl}}(B)\rangle = -\ln(0.16) \approx 1.8. \tag{7.3.6}$$

The right column of Table 7.2 shows the limit on the differential cross section for any new physics process. When presented in this fashion, the experimental limits are model-independent and versatile. With these limits on the differential cross section, anyone can compute the cross section for a specific model and make exclusion plots using just the signal limits shown in Table 7.2. For the comparison to be reliable, the detector simulator should be properly calibrated.

In addition to the statistical uncertainty, systematic uncertainties can also be important. Unlike the statistical uncertainties, the systematic uncertainties can be correlated with each other. One important theoretical uncertainty is the higher-order QCD correction to the backgrounds. These QCD uncertainties result in K-factors that change the normalization of the background, but do not significantly alter the background shapes with respect to H_T and E_T^{miss}. Because this uncertainty is highly correlated between different differential cross section measurements, treating the uncertainty as uncorrelated reduces the sensitivity of the searches. If a signal changes the shape of the differential cross section, e.g. causing a peak in the distribution, higher order corrections would be unlikely to explain it. To make full use of the independent differential cross section measurements, a complete error correlation matrix should be used. In practice, because the backgrounds are steeply falling with respect to H_T and E_T^{miss}, assigning an uncorrelated systematic uncertainty does not significantly hurt the resolving power of the experiment. In Table 7.2, we have assigned a systematic

uncertainty of $\epsilon_{\rm sys} = 50\%$ to each measurement, which should be added in quadrature to the statistical uncertainty. This roughly corresponds to the requirement that the total signal to background ratio is one.

The reduced chi-squared χ^2_N value for N measurements is

$$\chi^2_N = \sum_{j=1}^{N} \frac{S_j^2}{({\rm SL}_j)^2 + (\epsilon_{\rm sys} \times B_j)^2} \times \frac{1}{N}, \tag{7.3.7}$$

where S_j is the number of signal events and B_j is the number of background events in the $j^{\rm th}$ box of the grid. The statistical error ${\rm SL}_j$ and the systematic error $\epsilon_{\rm sys} \times B_j$ is read off from Table 7.2. In order to have a useful significance limit, it is necessary to only include measurements where there is an expectation of statistical significance; otherwise, the χ^2_N is diluted by a large number of irrelevant measurements. There is no canonical way of dealing with this elementary statistical question, although the ${\rm CL}_S$ method is the most commonly used [31, 32]. In this article, we take a very simple approach. If the expected significance for a single measurement is greater than a critical number, $S^{\rm crit}$, it is included in the χ^2_N, otherwise it is not.We tried several values of $S^{\rm crit}$ and the experimental sensitivity to different theories was not altered by the different choices. We chose $S^{\rm crit} = 0.5$ for the exclusion plots. This method does not maximize the reach in all cases, but because there are usually just a few measurements that give large significance, we are relatively insensitive to the exact statistical procedure.

In what follows, we will apply the general philosophy presented here to find the exclusion region for gluinos that are pair-produced at the Tevatron.† In Sec. 7.4, we will explain how the signal and background events have been generated. In Sec. 7.5, we will show how mass bounds can be placed on the gluino and bino masses using the proposed model-independent analysis and will discuss the challenges presented by cascade decays. We conclude in Sec. 7.6.

†Throughout this article, "gluino" refers to a color octet fermion, "wino" to a charged SU(2) fermion, and "bino" to a neutral singlet. These names imply nothing more than a particle's quantum numbers.

7.4 Event Generation

7.4.1 Signal

In this section, we discuss the generation of signal events for the gluino cascade decay shown in (7.2.1). The experimental signatures of this decay chain are determined primarily by the spectrum of particle masses. In particular, the mass splittings determine how much energy goes into the jets as opposed to the bino - i.e., the ratio of the visible energy to missing transverse energy. Events with large H_T and $E_T^{\rm miss}$ will be the easiest to detect; this is expected, for example, when a heavy gluino decays into a wino that is nearly degenerate with either the gluino or the bino. The reach of the searches is degraded, however, when the wino is included as an intermediate state in the decay chain. When the jets from the cascade decay are all hard, the missing energy is significantly smaller than what it would be for the direct decay case. Picking out signals with small missing transverse energy is challenging because they push us closer to a region where the dominant background is coming from QCD and is poorly understood. This happens, in particular, when the mass splitting between the gluino and bino is large and the wino mass is sufficiently separated from both. When the wino is nearly degenerate with either the gluino or the bino, then we expect to see 2 hard jets and 2 soft jets from the decay. This case begins to resemble the direct decay scenario; there is more missing energy and, therefore, the signal is easier to see. It is particularly challenging to probe regions of parameter space where the gluino is nearly degenerate with the bino. For this case, even in the light-gluino region ($m_{\tilde{g}} \lesssim 200$ GeV), the benefit of the high production cross section for the gluinos is overwhelmed by the small missing transverse momentum in each event; the jets in these events are soft and the p_T of the two binos approximately cancel when summed together [28]. Even if the gluinos are produced at large invariant mass, the situation is not markedly improved; in this case, the jets from each gluino are collinear and aligned with the $E_T^{\rm miss}$. Such events are easily mistaken as QCD events and eliminated by the cuts that are implemented to reduce the QCD backgrounds.

The inclusion of hard initial-state jets significantly increases the exclusion reach in this degenerate region of parameter space. The initial-state radiation boosts the

gluinos in the same direction, decreasing the angle between them, which in turn, enhances the $E_T^{\rm miss}$. Therefore, ISR jets allow us to capitalize on the high production cross section of light gluinos to set bounds on their masses.

To properly account for initial-state radiation (ISR) and final-state radiation (FSR), MadGraph/MadEvent [33] was used to generate events of the form

$$p\bar{p} \rightarrow \tilde{g}\tilde{g} + Nj, \tag{7.4.1}$$

where $N = 0, 1, 2$ is the multiplicity of QCD jets. Pythia 6.4 [34] was used for parton showering and hadronization. Properly counting the number of events after parton showering requires some care. In general, an $(n+1)$-jet event can be obtained in two ways: by a $(n+1)$ hard matrix-element, or by hard radiation emitted from an n-parton event during showering. It is important to understand which of the two mechanisms generates the $(n+1)$-jet final state to ensure that events are not double-counted.

In this article, a version of the so-called MLM matching procedure implemented in MadGraph/MadEvent and Pythia [35] was used for properly merging the different parton multiplicity samples. This matching has been implemented both for Standard Model production and for beyond the Standard Model processes. In this procedure, parton-level events are generated with a matrix element generator with a minimum distance between partons characterized by the $k_\perp$ jet measure:

$$\begin{aligned} d^2(i,j) &= \Delta R_{ij}^2 \min(p_{Ti}^2, p_{Tj}^2) \\ d^2(i,\text{beam}) &= p_{Ti}^2, \end{aligned} \tag{7.4.2}$$

where $\Delta R_{ij}^2 = 2[\cosh(\Delta\eta) - \cos(\Delta\phi)]$ [36]. The event is clustered using the k_T clustering algorithm, allowing only for clusterings consistent with diagrams in the matrix element, which can be done since MadGraph generates all diagrams for the process. The d^2 values for the different clustered vertices are then used as scales in the α_s value corresponding to that vertex, i.e. the event weight is multiplied by $\prod_i \frac{\alpha_s(d_i^2)}{\alpha_s(\mu_R^2)}$, where the product is over the clustered vertices i. This is done in order to treat radiation modeled by the matrix element as similarly as possible to that modeled by the parton shower, as well as to correctly include a tower of next-to-leading log

terms. A minimum cutoff $d(i,j) > Q_{\text{min}}^{\text{ME}}$ is placed on all the matrix-element multi-parton events.

After showering, the partons are clustered into jets using the standard $k_\perp$ algorithm. Then, the jet closest to the hardest parton in (η, ϕ)-space is selected. If the separation between the jet and parton is within some maximum distance, $d(\text{parton}, \text{jet}) < Q_{\text{min}}^{\text{PS}}$, the jet is considered matched. The process is repeated for all other jets in the event. In this way, each jet is matched to the parton it originated from before showering. If an event contains unmatched jets, it is discarded, unless it is the highest multiplicity sample. In this case, events with additional jets are kept, provided the additional jets are softer than the softest parton, since there is no higher-multiplicity matrix element that can produce such events. The matching pro-

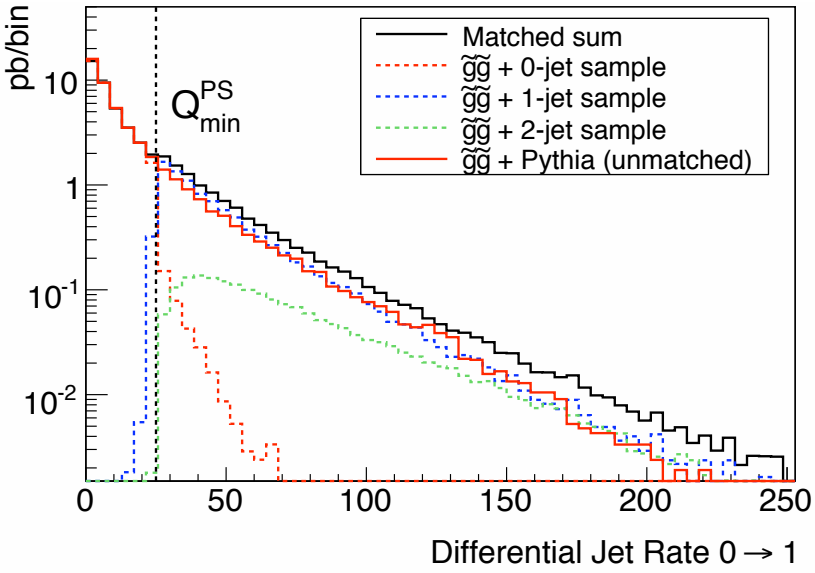

Figure 7.2: Differential $0 \to 1$ jet rate for a matched sample of light gluino production. The full black curve shows the matched distribution, and the broken curves show the contributions from different matrix element parton multiplicity samples. The matching scale $Q_{\text{min}}^{\text{PS}}$ is marked by the dashed line. The full red curve shows the result using Pythia only.

cedure ensures that jets are not double-counted between different parton multiplicity matrix elements, and should furthermore give smooth differential distributions for all jet observables. The results should not be sensitive to the particular values of the

matching parameters, as long as they are chosen in a region where the parton shower is a valid description. Typically, the matching parameters should be on the order of the jet cuts employed and be far below the factorization scale of the process. For the gluino production, the parameters were

$$Q_{\rm min}^{\rm ME} = 20 \text{ GeV} \qquad Q_{\rm min}^{\rm PS} = 30 \text{ GeV}. \tag{7.4.3}$$

Figure 7.2 shows the differential jet rate going from zero to one jets $D(1j \to 0j)$, which is the maximum $k_\perp$ distance for which a $1j$ event is characterized as a $0j$ event. Below $Q_{\rm min}^{\rm PS}$, all jets come from parton showering of the $0j$ multiplicity sample. Above $Q_{\rm min}^{\rm PS}$, the jets come from initial-state radiation. The main contributions in this region are from the $1j$ and $2j$ multiplicity samples. The sum of all the multiplicity samples is a smooth distribution, eliminating double counting between the different samples.

The simulations were done using the CTEQ6L1 PDF and with the renormalization and factorization scales set to the gluino mass [37]. The matched cross-sections were rescaled to the next-to-leading-order (NLO) cross sections obtained using Prospino 2.0. PGS-6 was used for detector simulation [39], with jets being clustered according to the cone algorithm, with $\Delta R = 0.5$. As a check on this procedure, we compared our results to the signal point given in [3] and found that they agreed to within 10%.

To emphasize the importance of properly accounting for initial-state radiation using matching, Fig. 7.3 compares the p_T distribution for the hardest jet in a matched (left) and unmatched (right) dijet sample for a 150 GeV gluino directly decaying to a bino. The colors indicate the contributions from the different multiplicity samples: $0j$ (orange), $1j$ (blue), and $2j$ (cyan). When the gluino-bino mass splitting is large enough to produce hard jets (top row), the $0j$ multiplicity sample is the main contributor. ISR is not important in this case and there is little difference between the matched and unmatched plots. The bottom row shows the results for a 130 GeV bino that is nearly degenerate with the gluino. In this case, only soft jets are produced in the decay and hard ISR jets are critical for having events pass the dijet cuts. Indeed, we see the dominance of the $2j$ multiplicity sample in the histogram of matched events. When ISR is important, the unmatched sample is clearly inadequate, with

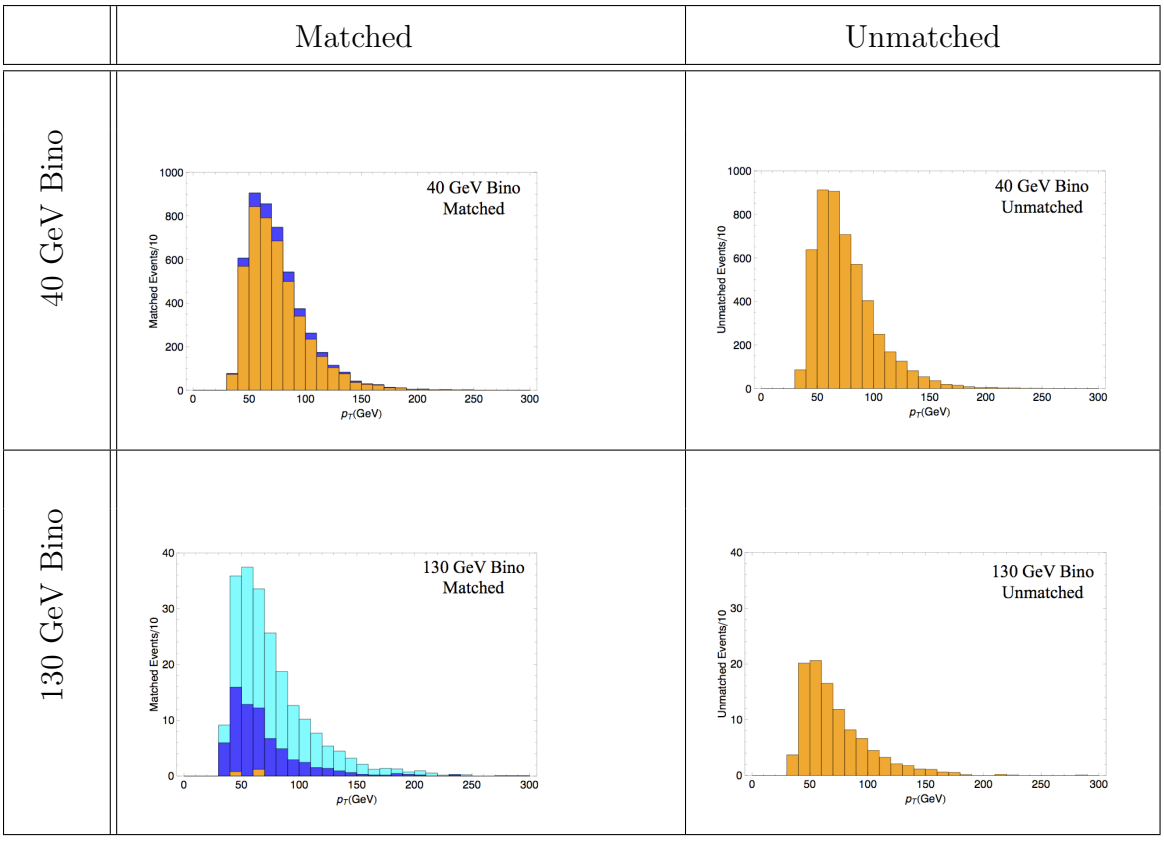

Figure 7.3: Comparison of matched and unmatched events for a dijet sample of 150 GeV gluinos directly decaying into 40 GeV (top) and 130 GeV (bottom) binos. The p_T of the hardest jet is plotted in the histograms (1 fb^{-1} luminosity). Matching is very important in the degenerate case when the contribution from initial state radiation is critical. The different colors indicate the contributions from 0j (orange), 1j (blue), and 2j (cyan).

nearly 60% fewer events than the matched sample.

7.4.2 Backgrounds

The dominant backgrounds for jets + E_T^{miss} searches are $W^{\pm}/Z^0$ + jets, $t\bar{t}$, and QCD. Additional background contributions come from single top and di-boson production (WW, WZ, ZZ), but these contributions are sub-dominant, so we do not consider them here. The missing transverse energy comes from $Z^0 \to \nu\nu$ and $W^{\pm} \to l^{\pm}\nu$, where the $W^{\pm}$ boson is produced directly or from the top quark. To reduce the $W^{\pm}$ background, a veto was placed on isolated leptons with $p_T \geq 10$ GeV. However, these cuts do not completely eliminate the $W^{\pm}$ background because it is possible to miss either the electron or muon (or misidentify them). It should be noted that muon isolation cuts were not placed by PGS-6, but were applied by our analysis software. If the muon failed the isolation cut, then it was removed from the record and its four-momentum was added to that of the nearest jet. Additionally, the $W^{\pm}$ can decay into a hadronic τ, which is identified as a jet. Because the $D0$ analysis did not veto on hadronic taus, we have treated all taus as jets in this study.

QCD backgrounds can provide a significant source of low missing energy events, but are challenging to simulate. The backgrounds can arise from jet energy mismeasurement due to poorly instrumented regions of the detector (i.e., dead/hot calorimeter cells, jet punch-through, etc.). Additionally, there are many theoretical uncertainties - for example, in the PDFs, matrix elements, renormalisation, and factorisation/matching scales - that factor in the Monte Carlo simulations of the backgrounds. For heavy-flavor jets, there is the additional E_T^{miss} contribution coming from leptonic decays of the b-quarks. It is possible, for instance, to have the b-quark decay into a lepton and a neutrino, with the neutrino taking away a good portion of the b-quark's energy. Simulation of the QCD background is beyond the scope of Pythia and PGS-6 and was not attempted in this work. To account for the QCD background, we imposed a tight lower bound on the E_T^{miss} of 100 GeV. Jet energy mismeasurement was accounted for by placing a lower bound of 90° and 50° on the azimuthal angle between the E_T^{miss} and the first and second hardest jets, respectively. In addition, an acoplanarity cut of 165° was placed between the two hardest jets. For the dijet case,

the azimuthal angle between the $E_T^{\rm miss}$ and any jet with $p_T \geq 15$ GeV and $|\eta| \leq 2.5$ was bounded from below by 40°. This cut was not placed on the threejet or multijet searches because of the greater jet multiplicity in these cases.

The $W^{\pm}/Z^0+nj$ and $t\bar{t}$ backgrounds were generated using MadGraph/MadEvent, with showering and hadronization in PYTHIA. PGS-6 was again used as the detector simulator for jet clustering. The $W^{\pm}/Z^0$ backgrounds were matched up to 3 jets using the MLM matching procedure discussed in the previous section, with matching parameters $Q_{\rm min}^{\rm ME} = 10$ GeV and $Q_{\rm min}^{\rm ME} = 15$ GeV. The $t\bar{t}$ backgrounds were matched up to 2 jets with parameters $Q_{\rm min}^{\rm ME} = 14$ GeV and $Q_{\rm min}^{\rm ME} = 20$ GeV. For each of the separate backgrounds, 500K events were generated. The results approximately reproduce the shape and scale of the $E_T^{\rm miss}$ and H_T distributions published by the $D0$ collaboration for 1 fb^{-1} [3]. In the dijet case, our results correspond to those of $D0$ within ±20%. The correspondence is similar for the $t\bar{t}$ backgrounds in the threejet and multijet cases. For the $W^{\pm}/Z^0$ backgrounds, the correspondence is within $\pm 30 - 40\%$. It is possible that this discrepancy is due to difficulties to fully populate the tails of the $E_T^{\rm miss}$ and H_T distributions with good statistics. In the case of the $W^{\pm}$ background, the modeling of the lepton detection efficiency in PGS-6 might also play a role. Heavy flavor jet contributions were found to contribute 2% to the $W^{\pm}/Z^0$ backgrounds, which is well below the uncertainties that arise from not having NLO calculations for these processes and from using PGS-6.

7.5 Gluino Exclusion Limits

7.5.1 No Cascade Decays

For the remainder of the paper, we will discuss how model-independent jets + $E_T^{\rm miss}$ searches can be used to set limits on the parameters in a particular theory. We will focus specifically on the case of pair-produced gluinos at the Tevatron and begin by considering the simplified scenario of a direct decay to the bino. The expected number of jets depends on the relative mass difference between the gluino and bino. When the mass difference is small, the decay jets are very soft and initial-state radiation is important; in this limit, the monojet search is best. When the mass difference is large,

Sample Model

Monojet

0.7	1.2	1.2	0.5	0.1

100 150 200 250 300 350

$\not{E}_T$

Dijet

0	0	0	0	0
0.2	0.2	0.1	0	0
0.6	0.7	0.6	0.4	0.1
1.4	1.9	1.6	0.3	
0.9	0.5			

H_T: 600 500 400 300 200 100

100 150 200 250 300 350

$\not{E}_T$

Threejet

0.1	0.1	0.1	0	0
0.5	0.5	0.3	0.1	0
2.2	2.5	1.4	0.4	0.1
2.9	2.7	1.4	0.2	
0.4	0.2			

H_T: 600 500 400 300 200 100

100 150 200 250 300 350

$\not{E}_T$

Multijet

0.8	0.6	0.4	0.1	0
4.0	3.0	1.3	0.4	0.1
12	10	4.7	1.0	0.1
7.9	5.8	1.8	0.2	
0.2	0.1			

H_T: 600 500 400 300 200 100

100 150 200 250 300 350

$\not{E}_T$

Table 7.3: Differential cross section (in fb) for the monojet, dijet, threejet, and multijet samples of a theoretical model spectrum with a 340 GeV gluino decaying directly into a 100 GeV bino (4 fb^{-1}). Some boxes show significant deviation from the signal limits shown in Table II: green indicates $0.5 < \chi_i \leq 2$, blue indicates $2 < \chi_i \leq 3$, and red indicates $\chi_i > 3$. All boxes with $\chi_i > 1/2$ are included in the calculation of the total χ^2 value.

the decay jets are hard and well-defined, so the multijet search is most effective. The dijet and threejet searches are important in the transition between these two limits.

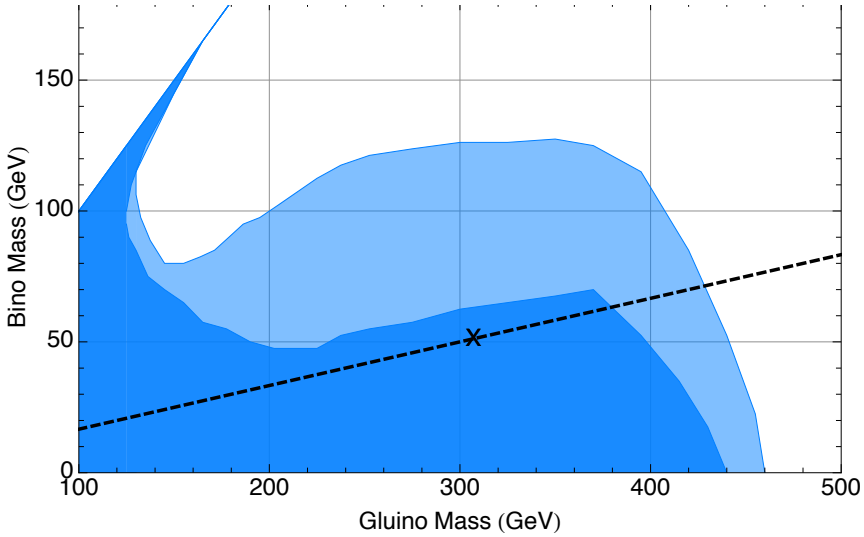

Figure 7.4: The 95% exclusion region for $D0$ at 4 fb^{-1} assuming 50% systematic error on background. The exclusion region for a directly decaying gluino is shown in light blue; the worst case scenario for the cascade decay is shown in dark blue. The dashed line represents the CMSSM-6 points and the "X" is the current $D0$ exclusion limit at 2 fb^{-1}.

As an example, let us consider the model spectrum with a 340 GeV gluino decaying directly into a 100 GeV bino. In this case, the gluino is heavy and its mass difference with the bino is relatively large, so we expect the multijet search to be most effective. Table 7.3 shows the differential cross section grids for the 1-4$^+$ jet searches for this simulated signal point. The colors indicate the significance of the signal over the limits presented in Table II; the multijet search has the strongest excesses.

Previously [28], we obtained exclusion limits by optimizing the $E_T^{\rm miss}$ and H_T cuts, which involves simulating each mass point beforehand to determine which cuts are most appropriate. This is effectively like dealing with a 1×1 grid, for which a 95% exclusion corresponds to $\chi^2 = 4$. The approach considered here considers the significance of all such cuts, and only requires that a single $n \times n$ differential cross section grid be produced for each search.

Fig. 7.4 shows the 95% exclusion limit for directly decaying gluinos at 4 fb^{-1}

luminosity and 50% systematic uncertainty on the background. The results show that such gluinos are completely excluded for masses below ~ 130 GeV.

7.5.2 Cascade Decays

In this section, we will discuss the exclusion limits for the decay chain illustrated in the inset of Fig. 7.5. In general, cascade decays are more challenging to see because they convert missing energy to visible energy.[‡] The number of jets per event is greater for cascading gluinos than directly decaying ones and the spectrum of jet energies depends on the ratio of gaugino masses. When $m_{\tilde{g}} \sim m_{\widetilde{W}}$, two hard jets are produced in the decay of the wino to the bino. In the opposite limit, when $m_{\widetilde{W}} \sim m_{\widetilde{B}}$, two hard jets are produced in the decay of the gluino to the wino. When $m_{\tilde{g}} < m_{\widetilde{W}} < m_{\widetilde{B}}$, four fairly hard jets are produced, diminishing the $E_T^{\rm miss}$ and making this region of parameter space the most challenging to see. In particular, the most difficult region to detect is when

$$m_{\widetilde{W}} = m_{\widetilde{B}} + \mathcal{O}(m_{Z^0}). \tag{7.5.1}$$

In the region of parameter space, where $m_{\widetilde{W}} \sim m_{\widetilde{B}}$, the jets from the wino to bino decay become harder as the gauge bosons go on-shell.

Fig. 7.5 shows the values of $m_{\widetilde{W}}$ and $m_{\widetilde{B}}$ that are excluded up to 95% confidence for a 240 GeV gluino (shaded region). The dark black dot, which represents the minimum bino mass for which a 240 GeV gluino is excluded for all wino masses, falls close to Eq. 7.5.1 (the dotted red line).

The exclusion region in Fig. 7.5 is not symmetric about the line $m_{\widetilde{W}} = m_{\widetilde{B}} + \mathcal{O}(m_{Z^0})$. The asymmetry is a result of the hard lepton cuts. When the gluino and wino are nearly degenerate, the leptons from the gauge boson decays are energetic, and these events are eliminated by the tight lepton cuts, reducing the significance below the confidence limit. In the opposite limit, when the wino and bino are nearly degenerate, much less energy is transfered to the leptons and fewer signal events are cut. Additionally, the jets produced in this case are color octets and give rise to a greater number of soft jets, as compared to the singlet jets emitted in the gauge boson

[‡]For additional discussion of model-independent searches of cascade decays at the Tevatron, see [40].

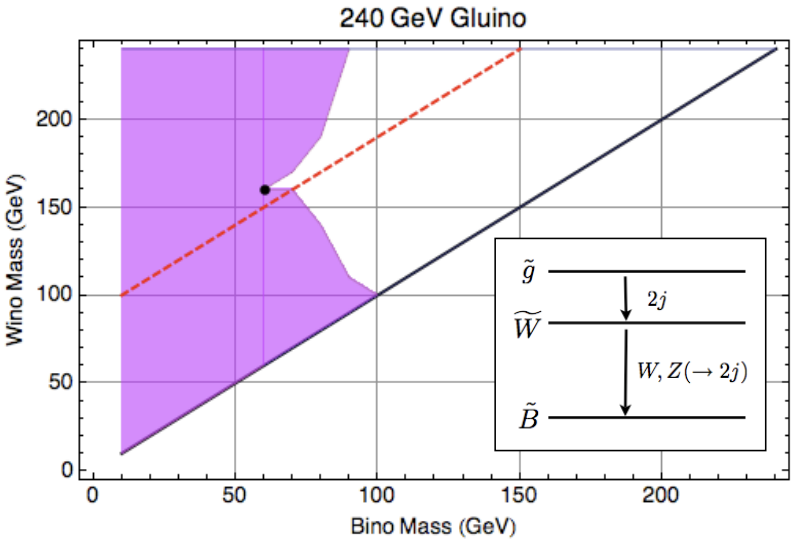

Figure 7.5: 95% exclusion region (purple) for a 240 GeV gluino decaying into a bino through a wino. The dashed line is $m_{\widetilde{W}} = m_{\widetilde{B}} + \mathcal{O}(m_{Z^0})$. The black dot at $(m_{\widetilde{B}}, m_{\widetilde{W}}) = (60, 160)$, is the minimum bino mass for which a 240 GeV gluino is excluded for *all* wino masses. The inset shows the one-step cascade considered in the paper.

decays. The presence of many soft jets may decrease the lepton detection efficiency; as a result, it may be that even fewer events than expected are being cut.

Figure 7.4 compares the 95% exclusion region for the cascade decay with that for the direct decay case. The "worst-possible" cascade scenario is plotted; that is, it is the maximum bino mass for which all wino masses are excluded. For the one-step cascade considered here, gluinos are completely excluded up to masses of ~ 125 GeV.

7.5.3 t-channel squarks

Thus far, it has been assumed that the squarks are heavy enough that they do not affect the production cross section of gluinos. If the squarks are not completely decoupled, they can contribute to t-channel diagrams in gluino pair-production. Figure 7.6 shows the production cross section for a 120 GeV (red), 240 GeV (blue), and 360 GeV (green) gluino, as a function of squark mass. When only one squark is light (and all the others are $\sim 4-5$ TeV), the production cross section is unaffected. However, when the squark masses are brought down close to the gluino mass, the production cross

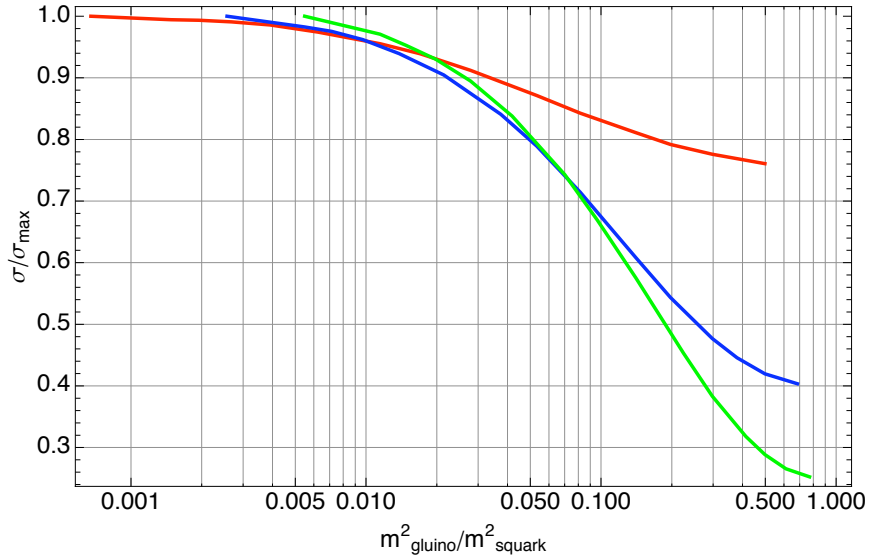

Figure 7.6: Gluino production cross section as a function of squark mass: (red) $m_{\tilde{g}} = 120$ GeV, (blue) $m_{\tilde{g}} = 240$ GeV, and (green) $m_{\tilde{g}} = 360$ GeV.

section decreases by as much as $\sim 25\%$, 60%, and 75% for 120, 240, and 360 GeV gluinos, respectively. A reduction in the production cross section alters the exclusion region in the gluino-bino mass plane; while the overall shape of the exclusion region remains the same, its size scales with the production cross section [28].

It is worthwhile to note, however, that while the inclusion of squarks reduces the exclusion region for pair-produced gluinos by decreasing the production cross section, it also provides alternate discovery channels through $\tilde{g}\tilde{q}$ or $\tilde{q}\tilde{q}$ production. For example, if a gluino and squark are produced, with the gluino nearly degenerate with the bino, the subsequent decay of the squark will produce more visible energy than the gluino decay, thereby making the event more visible.

7.5.4 Monophoton Search

Initial-state QCD radiation is important for gaining sensitivity to degenerate gluinos. Here, we will consider whether initial-state photon radiation may also be useful in the degenerate limit. Such events are characterized by small E_T^{miss} and a hard photon.

The main benefit of the monophoton search is that the Standard Model backgrounds are better understood; unlike the monojet case, QCD is no longer an important background. Instead, the primary backgrounds come from processes such as $Z^0(\rightarrow \nu\nu) + \gamma$, which is irreducible, and $W^{\pm} \rightarrow e^{\pm}\nu$ where the electron is mistaken as a photon or $W^{\pm}(\rightarrow l^{\pm}\nu) + \gamma$, where the lepton is not detected. Other backgrounds may come from $W^{\pm}/Z^0$ + jet, where the jet is misidentified as a photon, or situations where muons or cosmic rays produce hard photons in the detector.

The $D0$ Collaboration recently published results for their monophoton study, which searched for a Kaluza-Klein graviton produced along with a photon [41]. To reduce the Standard Model background, they required all events to have one photon with $p_T > 90$ GeV and $E_T^{\text{miss}} > 70$ GeV. Events with muons or jets with $p_T > 15$ GeV were rejected. They estimate the total number of background events to be 22.4 ± 2.5.

To investigate the sensitivity of monophoton searches to degenerate spectra, we consider several points and compared them against $D0$'s background measurements. We considered several benchmark values for gluino and bino masses and did a simple cuts-based comparison between the monophoton search and an optimized monojet search. For example, Figure 7.5 shows that the monojet search safely excludes the case of a 140 GeV gluino and 130 GeV bino. A monophoton search (with the cuts used in the $D0$ analysis) gives $S/B = 0.48$ and $S/\sqrt{B} = 2.3$ for this mass point; thus the monophoton search is roughly as sensitive but has a lower S/B value. Similarly, a 120 GeV gluino and 100 GeV bino is safely excluded by the monojet search, but the monophoton search only gives $S/B = 0.39$ and $S/\sqrt{B} = 1.86$.

There are several reasons why the monophoton search is not as successful as the monojet one. In the degenerate gluino region, the possibility of getting jets with a p_T above the 15 GeV threshold is significant (even though the mass difference is $\mathcal{O}(10 \text{ GeV})$) because the gluinos are boosted. The monophoton search vetoes many events with such boosted decay jets. In addition, getting photon ISR is much more difficult than getting QCD ISR for several reasons - most importantly, because $\alpha_{\text{EM}} \ll \alpha_s$ and because one is insensitive to the gluon-induced processes that contribute to the cross section. Despite these challenges, the significance of the monophoton search could still increase sensitivity. The monophoton does not fare significantly more

poorly than the monojet one with the current set of cuts. Thus, it is possible that a more optimal set of cuts may increase the effectiveness of the search, especially given that the backgrounds are better understood in this case. Finally, the above estimates do not account for the photon detection rate in PGS-6, which may be different from that used by $D0$'s full detector simulator, from which the background estimates were taken.

7.5.5 Leptons

In this section, we address whether leptons from cascades can be used to augment the sensitivity of jets + $E_T^{\rm miss}$ searches. In the gluino cascade decay considered in this paper, it is possible to get leptons from the $W^{\pm}$ and Z^0 boson decays. The 10 GeV lepton veto, however, eliminates most of these events. The exclusion limit for the gluino decay discussed in Sec. 7.5.2 is not improved by removing the lepton veto; most of the irreducible backgrounds ($W^{\pm}+nj$ and $t\bar{t}+nj$) have a lepton and dominate over the signal when the veto is removed. The exclusion limit is not improved even if we require all events to have a certain number of leptons, or place cuts on lepton p_T.

The question still remains as to whether there is any region in parameter space where the jets + $E_T^{\rm miss}$ study places no exclusion, but a jets + $E_T^{\rm miss}$ + lepton study does. The lepton signal is useful for light gluinos ($\lesssim 250$ GeV) that are nearly degenerate with the wino. The signal point, a 210 GeV gluino decaying to a 50 GeV bino through a 170 GeV wino, is not excluded by the ordinary jets + $E_T^{\rm miss}$ analysis. We find here, though, that it has a significance[§] of $\simeq 4.4$ for a p_T cut of 50 GeV, but with a $S/B \simeq 0.15$.

For high-mass gluinos, inclusion of the lepton signal does not increase the sensitivity of the search because the smaller production cross section decreases the signal significance. It might however be possible that lepton signatures are effective for high-mass gluinos in lepton-rich cascades that contain sleptons. Overall, though, these results indicate that while jets + $E_T^{\rm miss}$ + lepton searches may be useful in certain regions of parameter space, they should be combined with jets + $E_T^{\rm miss}$ searches

[§]Here, the estimate of the significance only accounts for the statistical error; it does not include the systematic uncertainty.

to provide optimal coverage.

7.6 Conclusion

In this article, we discuss how model-independent bounds can be placed on the mass of the lightest color octet particle that is pair-produced at the Tevatron. The main aspects of the analysis focus on the advantage of running exclusive $1j - 4^+j$ searches, and placing limits using the measured differential cross section as a function of the visible and missing energy. We show that the exclusion reach can be significantly extended beyond those published by $D0$ because the $E_T^{\rm miss}$ and H_T cuts used in their analysis were only optimized for points in CMSSM-6 parameter space. The proposed analysis we present here opens up the searches to all regions of parameter-space, allowing us to set limits on all kinematically-accessible gluinos. We also show how the exclusion reach is degraded when gluino cascade decays are included, focusing on the example of an intermediate wino, which decays to the dark matter candidate.

We have so far only focused on jet classification, $E_T^{\rm miss}$, and H_T as available handles for increasing the reach of jets + $E_T^{\rm miss}$ searches. However, in certain special cases, other techniques might be useful. For example, if the gluino decays dominantly to b jets, heavy flavor tagging can be used advantageously.

In our analysis of the cascade decays, we often found that the regions of highest significance in the differential cross section plot were pressed down against the 100 GeV cutoff in missing transverse energy. This lower limit was imposed to avoid regions where the QCD background dominates. If the 100 GeV limit could be reduced, then it would open up regions of high statistical significance that renders sensitivity to a larger region of parameter space. The numerous uncertainties in the theory and numerical generation of QCD events make it unlikely that precision QCD background will be generated in the near future. However, it may still be possible to reduce the cutoff by using event shape variables (i.e., sphericity).

Looking forward to the LHC, jets + $E_T^{\rm miss}$ searches are still promising discovery channels for new physics. The general analysis presented in this paper can be taken forward to the LHC without any significant changes. The primary modification will

be to optimize the jet E_T used in the classification of the $nj + E_T^{\text{miss}}$ searches. The backgrounds for the LHC are dominantly the same; however $t\bar{t}$ will be significantly larger and the size of the QCD background will also be different. Many of the existing proposals for searches at the LHC focus primarily on $4^+j + E_T^{\text{miss}}$ inclusive searches and are insensitive to compressed spectra; see [42] for further discussion on MSSM-specific compressed spectra at the LHC. By having exclusive searches over $1j + E_T^{\text{miss}}$ to $4^+j + E_T^{\text{miss}}$, the LHC will be sensitive to most beyond the Standard Model spectra that have viable dark matter candidates that appear in the decays of new strongly-produced particles, regardless of the spectrum. Additionally, having the differential cross section measurements will be useful in fitting models to any discoveries. Finally, it is necessary to confirm that there are no gaps in coverage between the LHC and Tevatron; in particular, if there is a light ($\sim$125 GeV) gluino, finding signal-poor control regions to measure the QCD background may be challenging.

Bibliography

[1] J. Alitti *et al.* [UA2 Collaboration], Phys. Lett. B **235**, 363 (1990).

[2] X. Portell [CDF-6 Run II Collaboration], AIP Conf. Proc. **842**, 640 (2006) [arXiv:hep-ex/0609017].

[3] V. M. Abazov *et al.* [D0 Collaboration], arXiv:0712.3805 [hep-ex]; The $D0$ Collaboration, $D0$ Note 5312 (2007).

[4] The CDF-6 Collaboration, CDF-6 Note 9093 (2007).

[5] A. Abulencia *et al.* [CDF-6 Collaboration], Phys. Rev. Lett. **97**, 171802 (2006) [arXiv:hep-ex/0605101]; The $D0$ Collaboration, $D0$ CONF 4400 (2007).

[6] S. Mrenna, G. L. Kane, G. D. Kribs and J. D. Wells, Phys. Rev. D **53**, 1168 (1996) [arXiv:hep-ph/9505245].

[7] H. Baer, C. h. Chen, F. Paige and X. Tata, Phys. Rev. D **52**, 2746 (1995) [arXiv:hep-ph/9503271].

[8] I. Hinchliffe, F. E. Paige, M. D. Shapiro, J. Soderqvist and W. Yao, Phys. Rev. D **55**, 5520 (1997) [arXiv:hep-ph/9610544].

[9] B. K. Gjelsten, D. J. Miller and P. Osland, JHEP **0412**, 003 (2004) [arXiv:hep-ph/0410303].

[10] B. K. Gjelsten, D. J. Miller and P. Osland, JHEP **0506**, 015 (2005) [arXiv:hep-ph/0501033].

[11] S. Dimopoulos and H. Georgi, Nucl. Phys. B **193**, 150 (1981).

[12] H. P. Nilles, Phys. Rep. **110**, 1(1984).

[13] S. Dimopoulos, S. D. Thomas and J. D. Wells, Nucl. Phys. B **488**, 39 (1997) [arXiv:hep-ph/9609434].

[14] G. F. Giudice and R. Rattazzi, Phys. Rept. **322**, 419 (1999) [arXiv:hep-ph/9801271].

[15] K. Choi, A. Falkowski, H. P. Nilles, M. Olechowski and S. Pokorski, JHEP **0411**, 076 (2004) [arXiv:hep-th/0411066]; K. Choi, A. Falkowski, H. P. Nilles and M. Olechowski, Nucl. Phys. B **718**, 113 (2005) [arXiv:hep-th/0503216].

[16] R. Kitano and Y. Nomura, Phys. Lett. B **631**, 58 (2005) [arXiv:hep-ph/0509039].

[17] T. Gherghetta, G. F. Giudice and J. D. Wells, Nucl. Phys. B **559**, 27 (1999) [arXiv:hep-ph/9904378].

[18] L. Randall and R. Sundrum, Nucl. Phys. B **557**, 79 (1999) [arXiv:hep-th/9810155]; G. F. Giudice, M. A. Luty, H. Murayama and R. Rattazzi, JHEP **9812**, 027 (1998) [arXiv:hep-ph/9810442].

[19] R. Barate *et al.* [ALEPH Collaboration], Phys. Lett. B **469**, 303 (1999).

[20] A. Heister *et al.* [ALEPH Collaboration], Eur. Phys. J. C **35**, 457 (2004).

[21] G. Abbiendi *et al.* [OPAL Collaboration], Eur. Phys. J. C **40**, 287 (2005) [arXiv:hep-ex/0503051]; P. D. Acton *et al.* [OPAL Collaboration], Z. Phys. C **59**, 1 (1993).

[22] D. E. Kaplan and M. D. Schwartz, arXiv:0804.2477 [hep-ph].

[23] T. Aaltonen *et al.* [CDF-6 Collaboration], arXiv:0712.2534 [hep-ex].

[24] T. Aaltonen *et al.* [CDF-6 Collaboration], arXiv:0712.1311 [hep-ex].

[25] C. Henderson [CDF-6 Collaboration], arXiv:0805.0742 [hep-ex]; G. Choudalakis, PhD thesis, Massachusetts Institute of Technology (2008);

[26] N. Arkani-Hamed, P. Schuster, N. Toro, J. Thaler, L. T. Wang, B. Knuteson and S. Mrenna, arXiv:hep-ph/0703088.

[27] C. Balazs, M. S. Carena, A. Freitas and C. E. M. Wagner, JHEP **0706**, 066 (2007) [arXiv:0705.0431 [hep-ph]].

[28] J. Alwall, M. P. Le, M. Lisanti and J. G. Wacker, arXiv:0803.0019 [hep-ph].

[29] T. Appelquist, H. C. Cheng and B. A. Dobrescu, Phys. Rev. D **64**, 035002 (2001) [arXiv:hep-ph/0012100].

[30] N. Arkani-Hamed, A. G. Cohen and H. Georgi, Phys. Lett. B **513**, 232 (2001) [arXiv:hep-ph/0105239]; N. Arkani-Hamed, A. G. Cohen, E. Katz, A. E. Nelson, T. Gregoire and J. G. Wacker, JHEP **0208**, 021 (2002) [arXiv:hep-ph/0206020]; E. Katz, J. y. Lee, A. E. Nelson and D. G. E. Walker, JHEP **0510**, 088 (2005) [arXiv:hep-ph/0312287].

[31] T. Junk, Nucl. Instrum. Meth. A **434**, 435 (1999) [arXiv:hep-ex/9902006].

[32] A. L. Read, "Modified frequentist analysis of search results (The CL(s) method)," Workshop on Confidence Limits, CERN (2000).

[33] J. Alwall *et al.*, JHEP **0709**, 028 (2007) [arXiv:0706.2334 [hep-ph]].

[34] T. Sjostrand, S. Mrenna and P. Skands, JHEP **0605**, 026 (2006) [arXiv:hep-ph/0603175].

[35] J. Alwall *et al.*, Eur. Phys. J. C **53**, 473 (2008) [arXiv:0706.2569 [hep-ph]].

[36] S. Catani, Y. L. Dokshitzer, M. H. Seymour and B. R. Webber, Nucl. Phys. B **406**, 187 (1993).

[37] J. Pumplin, D. R. Stump, J. Huston, H. L. Lai, P. Nadolsky and W. K. Tung, JHEP **0207**, 012 (2002) [arXiv:hep-ph/0201195]; D. Stump, J. Huston, J. Pumplin, W. K. Tung, H. L. Lai, S. Kuhlmann and J. F. Owens, JHEP **0310**, 046 (2003) [arXiv:hep-ph/0303013].

[38] W. Beenakker, R. Hopker, M. Spira and P. M. Zerwas, Nucl. Phys. B **492**, 51 (1997) [arXiv:hep-ph/9610490].

[39] J. Conway, http://www.physics.ucdavis.edu/conway/research/software/pgs/pgs4-general.htm. *PGS-6: Pretty Good Simulator*

[40] S. Chang and N. Weiner. Manuscript in preparation.

[41] V. M. Abazov *et al.* [D0 Collaboration], arXiv:0803.2137 [hep-ex].

[42] K. Kawagoe and M. M. Nojiri, Phys. Rev. D **74**, 115011 (2006) [arXiv:hep-ph/0606104].